School of Electrical Engineering, Computing and Mathematical Sciences
(EECMS)

High-temperature Materials for Thermochemical Energy Storage in Concentrated Solar Power Plants

Sruthy Balakrishnan

This thesis is presented for the Degree of
Doctor of Philosophy
of
Curtin University

March 2022

Declaration

To the best of my knowledge and belief, this thesis contains no material previously published by any other person except where due acknowledgement has been made.

This thesis contains no material which has been accepted for the award of any other degree or diploma in any university.

Signature:

Date: 09/03/2022

Dedicated to my parents Balakrishnan & Savithri, beloved husband Rajesh and our lovely girls, Shivani & Shivaga.

“Take risks in your life; if you win, you can lead! If you lose, you can guide!”

- Swami Vivekananda

Acknowledgements

I would like to acknowledge everyone who has made my PhD journey possible for me. First and foremost, my deepest gratitude goes to my principal supervisor, Prof. Craig Buckley, for offering this great opportunity and always having time to point me in the right direction.

A special thanks to Dr Veronica Sofianos for her guidance and supervision. Through all my confusion and mistakes, you are always patient with me and have taught me invaluable lessons in research. Thanks to Dr Terry Humphries for his guidance in the second half of my PhD journey. You always motivated me and gave me the confidence required for a researcher. My deep acknowledgement goes to Associate Prof. Mark Paskevicius, whose ideas, knowledge and support were essential to completing this thesis. I also thank Dr Brendan McGann for being a patient committee chair.

I would like to acknowledge Curtin University and the Curtin International Postgraduate Research (CIPRS) for the financial support.

Thanks to Dr Matthew Rowles for his assistance with XRD and *in-situ* XRD analysis, Veronica Avery for XRD lab assistance and Elaine for SEM investigations.

Sincere thanks to all my friends and researchers at HSRG: Lucas, Ali, Enrico, Diego, Amanda, Kyran, Thomas, Ainee, Simon, Lucie, Dr Yu, Dr Yurong, Dr Mauricio, Bithathia, Aneeka and Praveen. A special mention to Dr Adriana for being a great friend and supporting me greatly.

Finally, I wish to express my sincere gratitude to my family, especially my mother and father. A special mention to my husband Rajesh, and our lovely twins Shivani and Shivaga, I am so blessed to have you all in my life. Thank you for always believing and encouraging me; my PhD journey would be impossible without you guys.

Abstract

In the last two years, even while the Covid 19 pandemic has decimated the entire world's economy, the capacity of renewable energy sources, such as wind and solar, have continued to grow rapidly. Electric and H_2 vehicles set new sales records in the market. Clean energy and net-zero emissions (NZE) by 2050 are the target for many countries. Concentrated Solar Power (CSP) plants, coupled with thermal energy storage (TES) or thermal batteries, have been made dispatchable and unique among other renewable energy alternatives. Developing efficient and cost-effective thermal batteries is one of the most challenging aspects, and the future of this technology relies on its development. Over 80% of the CSP plants under construction have TES, while the efficiency and high cost still need to be addressed.

Moreover, the US Department of Energy, in their SunShot research programme, decreed three targets to develop TES: (1) Increase the operating temperature to > 600 °C; (2) ensure an exergetic efficiency of $\geq 95\%$ (3); they must cost less than \$15 per kWh_{th}. Metal hydrides have been identified as potential next-generation thermal battery materials for CSP systems. They possess high energy storage densities and have the flexibility to operate at low, medium, and high temperatures. Also, certain metal hydrides have a unique property that allows them to absorb and desorb hydrogen at a constant pressure. The concept of these materials as TES materials is that by using the sunlight to heat the metal hydrides, an endothermic thermochemical reaction takes place where H_2 is desorbed. When the Sun is unavailable, a reversible absorption of H_2 can be initiated that releases heat (exothermic reaction). The heat can then be converted to electricity using Stirling engines.

In this research, calcium hydride systems were investigated as high-temperature thermal energy storage materials. The main reasons for choosing CaH_2 are: (1) high gravimetric (4939 $kJ.kg^{-1}$) and volumetric energy densities (8396 $MJ.m^{-3}$); (2) relatively low cost (4.4 US \$/kWh-thermal) and calcium is abundant; (3) low operating hydrogen pressure at high temperature (1 - 5 bar between 1100 °C and 1400 °C); (4) high enthalpy of dehydrogenation (207.9 $kJ.mol^{-1}.H_2$); and (5) high exergetic efficiency. The melting point of both CaH_2 and Ca metal are 816 °C and 842 °C, respectively. In addition, the molten CaH_2 is highly corrosive at the operating temperature, and therefore, expensive tank materials are required, making them less feasible for TES applications. Therefore, reducing the decomposition temperature of CaH_2 (600 - 800 °C) by adding reaction destabilising additives is the best way to transform CaH_2 into a

suitable TES for next-generation CSP plants. This method is known as thermodynamic destabilisation. However, due to the complexity of the Ca - CaH_2 system, the reported thermodynamic values in the literature for pure CaH_2 varies vastly, and no studies have been published since the 1960s. Hence, Chapter 3 details the calculated thermodynamic and kinetic properties of solid and molten CaH_2 and compares them with literature values.

The primary objective of this thesis is to examine cost-effective additives to reduce the desorption temperature of CaH_2 to between 600 - 800 °C and test its feasibility as a TES for CSP application. This investigation combines the theoretical thermodynamic predictions and experimental techniques, and the entire methods used are explained in Chapter 2. Chapters 4 and 5 illustrate that adding Al_2O_3 or Zn to CaH_2 reduces the operating temperature (1 bar) from 1100 °C to 636 °C and 597 °C, respectively. The reaction between CaH_2 and Al_2O_3 occurs in one step, with $Ca_{12}Al_{14}O_{33}$ being the main reaction product. The enthalpy and entropy of the system were calculated as $\Delta H_{\text{des}} = 100 \pm 2$ kJ/mol. H_2 and $\Delta S_{\text{des}} = 110 \pm 2$ J/K. mol. H_2. When CaH_2 is mixed with Zn in a 1:3 molar ratio and heated, it produces three different alloys, $CaZn_{13}$, $CaZn_{11}$ and $CaZn_5$, at 190, 390 and 590 °C, respectively. The enthalpy and entropy of the reaction ($CaZn_{11}$ formation step) were determined as $\Delta H_{\text{des}} = 131 \pm 4$ kJ/mol. H_2 and $\Delta S_{\text{des}} = 151 \pm 4$ J/K. mol. H_2. After ten H_2 desorption/absorption cycles, the CaH_2 - 3Zn system retains 80% of the initial H_2 capacity. The evaporation of Zn from the calcium zinc alloys is the major reason for the degradation of the hydrogen capacity. These two systems (CaH_2 - Al_2O_3 and CaH_2 - Zn) provide an overview of calcium hydride's thermodynamic destabilisation, including thermodynamic and kinetic measurements, synthesis, characterisation, and thermal analysis. Each system's cost calculation and cycling stability have been studied and compared among other systems. However, the poor kinetics of CaH_2 - Al_2O_3 and volatility of Zn are the major problems that need to be addressed. The investigation of the CaH_2 - 2C system (Chapter 6) showed three different reaction pathways and the release of methane gas. The possible reaction pathways of C with gaseous $H_2(g)$ or CaH_2 to form $CH_4(g)$ make the system impractical for the TES application.

Selecting a suitable additive for CaH_2 and predicting the optimal reaction pathways for the destabilisation reactions is challenging due to the variable thermodynamic predictions or the release of unexpected gases rather than H_2. Therefore, Chapter 7 demonstrates, theoretically and experimentally, the effect of several metal oxides and compares the properties (ZnO, Fe_2O_3, ZrO_2, MnO, SiO_2, TiO_2, CuO, NiO, Y_2O_3 and CeO_2) on the destabilisation of CaH_2.

The addition of ZnO, Fe_2O_3, CuO and NiO reduce the operating temperature of CaH_2 to below 500 °C. Moreover, the CaH_2 - SiO_2 and CaH_2 - ZrO_2 oxide systems were determined as the most promising materials with a reaction temperature above 600 °C. Furthermore, all these selected additives proved that the thermodynamic destabilisation of CaH_2 is achievable, and the best candidates (such as $2CaH_2$ - Al_2O_3, CaH_2 - Zn, CaH_2 - SiO_2 and CaH_2 - ZrO_2) require cycling measurements to verify their suitability as TES systems.

List of Publications

S. Balakrishnan, M.V. Sofianos, M. Paskevicius, M.R. Rowles and C.E. Buckley, Destabilised Calcium Hydride as a Promising High-Temperature Thermal Battery, *J. Phys. Chem. C*, 2020, **124**, 17512-17519. https://doi.org/10.1021/acs.jpcc.0c04754

S. Balakrishnan, M.V. Sofianos, T.D Humphries, M. Paskevicius, and C.E. Buckley, Thermochemical energy storage performance of zinc destabilised calcium hydride at high temperatures, *J.* Phys. Chem. Chem. Phys.**,** **22,** 2020, 25780-25788 https://doi.org/10.1039/D0CP04431H

Table of Contents

List of figures

List of tables

Chapter 1

Introduction

1.1 Need for renewable energy

Energy is considered a vital parameter for a country's growth, and the choice for future energy growth must be carefully considered. There has been a constantly increasing trend of energy consumption across the world. According to the International Energy Agency (IEA), the global energy demand rose by 4.6% in 2021.[1-2] This is the largest increase this decade. Electricity plays a central role and has become the primary energy source everyone relies on for their everyday needs. Electricity's share of the world's final energy consumption has risen steadily and needs a parallel increase in its share of energy-related investment.[2] However, given the limited nature of our fossil fuels, there is an urgent requirement to manage the energy crisis and global warming due to the carbon dioxide emissions from burning these fossil fuels. According to the prediction of the World Coal Institute, at the current consumption rate, the remaining years of availability of non-renewable energy sources such as coal, natural gas and oil are 130, 60 and 42 years, respectively.[3-4]

In addition, the IEA report published in October 2020 claims that the Covid -19 pandemic has caused significant disruption to the energy sector.[5] The report shows that global energy demand and related CO_2 emissions have dropped by 5% and 7%, respectively. In addition, as a part of the Net Zero Emissions (NZE) scenario by 2050, there has been a rapid increase in the number of countries targeting net-zero CO_2 emissions, as shown in Figure 1.1.[2, 5]

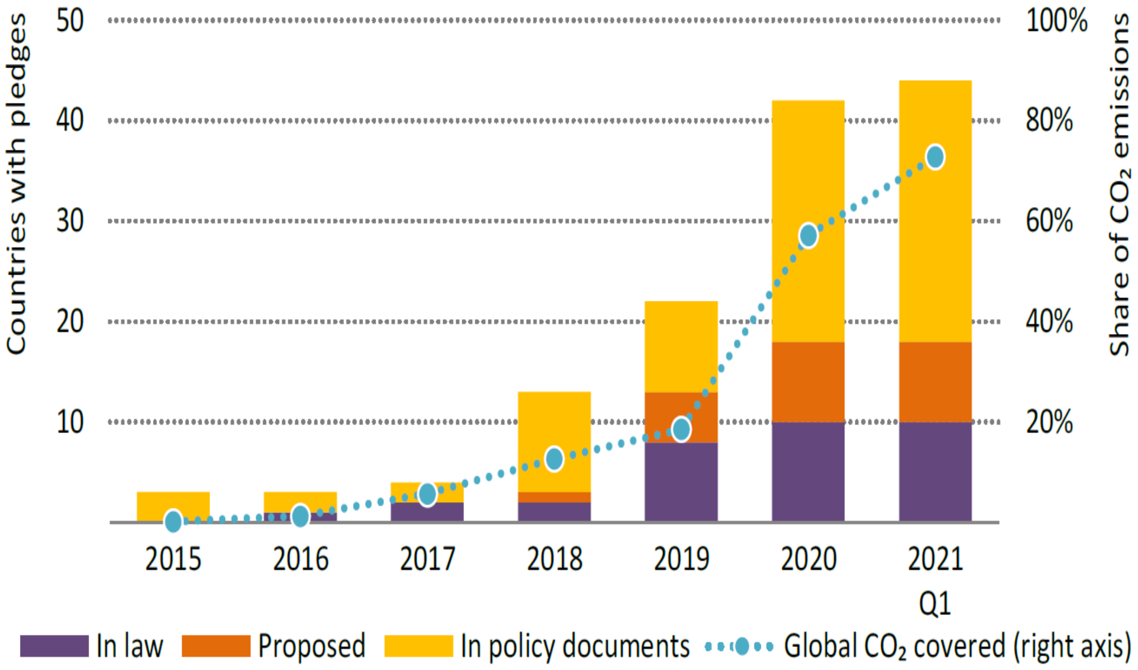

Figure 1.1 A rapid increase in announced net-zero CO_2 emmissions.[2, 5]

Hence, the long-term solution for these problems is using renewable, carbon-neutral energy sources such as solar, wind, hydro, geothermal and biomass. In 2020, even under the Covid 19 lockdowns, the use of renewable energy sources such as wind and solar grew faster than it had in two decades, and electric vehicle sales set a new record.[2] The option of utilising solar energy has been identified as one of the most promising unconventional renewable energy sources because it is environmentally friendly, inexhaustible, free and available in almost all parts of the world where people live. According to the US Department of Energy, the sun delivers more energy to the Earth in one hour than humanity consumes over a year, making solar the only renewable energy source that can keep up with global demands.[6-7] However, there are many problems associated with its use mainly it is a dilute form of energy, and its availability varies widely with time. Consequently, large collecting areas are required as well as energy storage methods.

1.2 Solar energy

Solar energy can be used directly or indirectly. A general classification of the various methods of solar energy utilisation is given in Figure 1.2.[8]

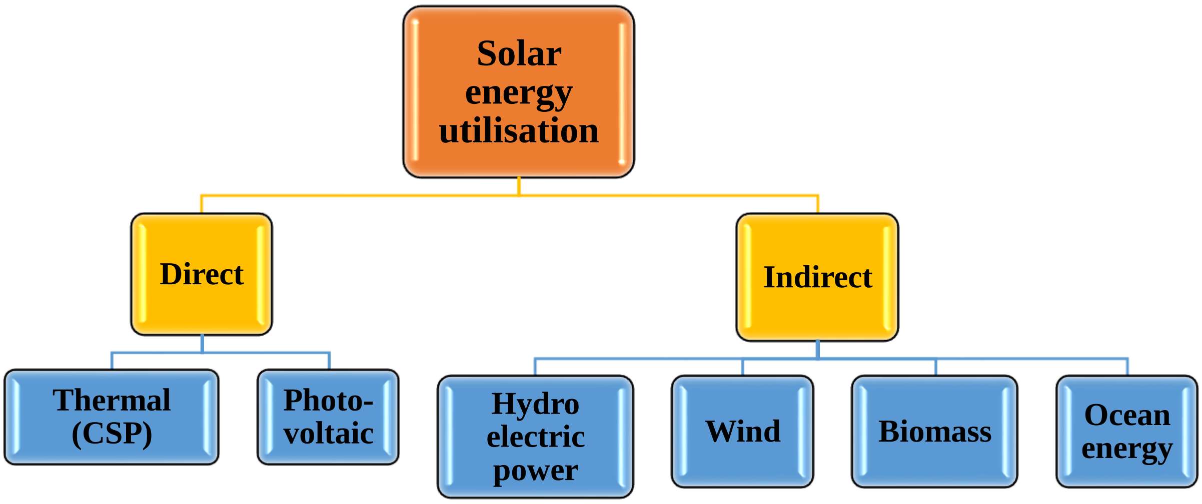

Figure 1.2 Classification of solar energy utilisation.

The International Energy Agency (IEA) announced that solar energy will contribute to approximately 22% of the global electricity production by 2050. Several types of unique solar technologies are available based on different concepts. An overview of these techniques is illustrated in Figure 1.3.[9] Among these, Photovoltaic systems (PV) and Concentrated solar power plants (CSP) are the two most mature technologies and are expected to grow significantly in the future. According to the IEA, PV and CSP can play roughly equal but complementary roles.[10] PV panels can collect direct and diffuse solar irradiations, whereas CSP plants harness direct radiation. Currently, CSP is considered the more attractive solar technology for commercial exploitation based on its higher thermal storage efficiency than solar PV producing direct electrical energy.[11] Power grids usually prefer CSP over PV as it generates AC which can be easily distributed onto the grid. In contrast, PV generates DC, which is then converted to AC (using inverters) for distribution.[9, 11-12] A comparison between PV and CSP systems are listed in Table 3.[9, 13] However, the comparison between these two systems will remain debatable, or in future, they may work together like a hybrid system to increase solar energy production.

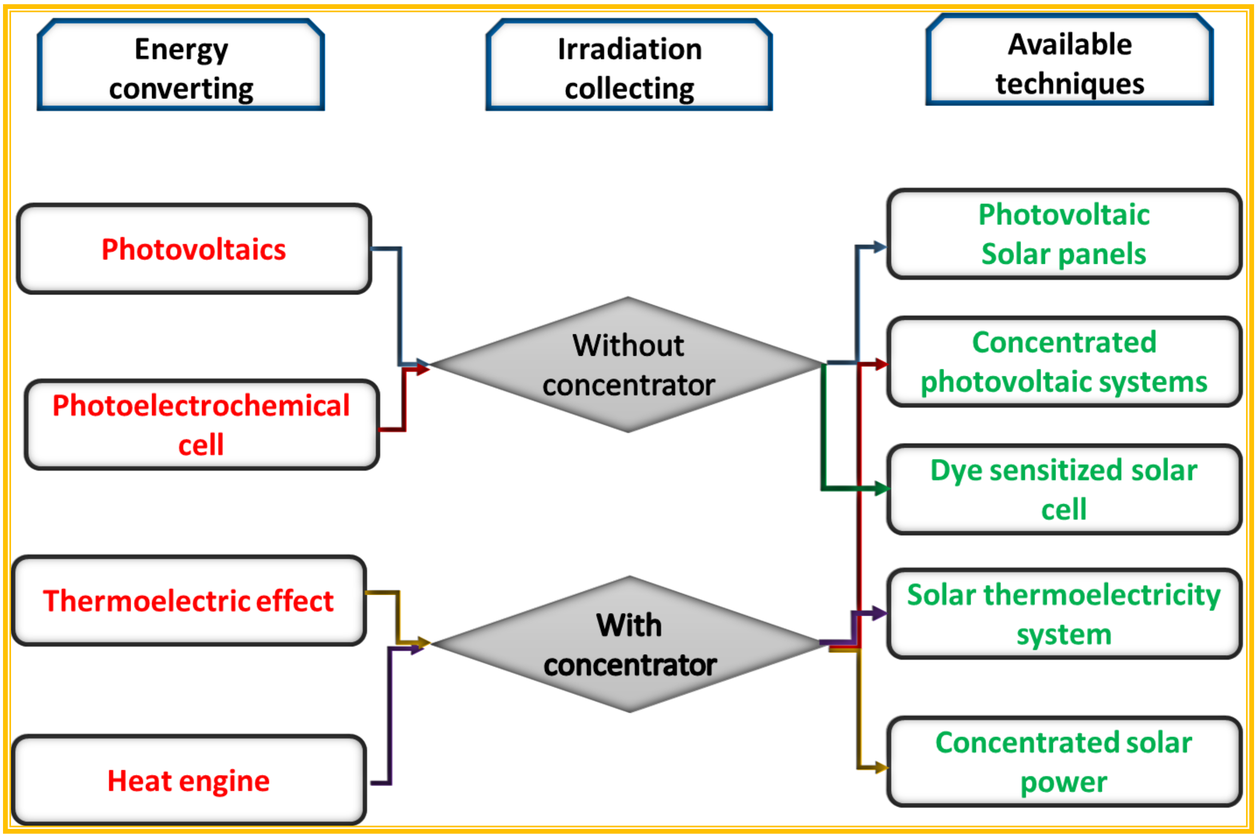

Figure 1.3 Overview of solar technologies.[9]

Table 1.1 Comparison between CSP and PV technologies.*[9, 13-14]

	CSP	**PV**
Principle	Converts the direct sunlight to produce heat. Then heat can be converted to electricity whenever required.	Converts direct and diffuse sunlight directly to electricity.
Type of solar receiver	Uses reflective devices such as mirrors, troughs etc.	Uses PV cells made of semiconductor devices.
Annual electrical energy output	397480.2 MWh/year	264907.3 MWh/year
Capacity utilisation factor	45.4%	30.2%
Solar to electric efficiency	17.12%	16.65%
Simple payback period	17.5 years	4.9 years
Land usage	Unused large flat area	Installed everywhere (roof etc.)
Life span	Higher compared to PV	
Grid options	Power grids usually prefer CSP over PV	PV is preferred more in off-grid applications than CSP

* The values given are based on Tabuk (Saudi Arabia) CSP and PV plant

1.3 Overview of CSP technologies

The easy integration of thermal energy storage systems makes CSP dispatchable and unique among other renewable energy generating alternatives. CSP technologies concentrate the sun's light energy using mirrors and convert it into heat to create steam to drive turbines or engines that produce electricity. The main components of a CSP system are:[15]

- Solar receivers vary depending on the operating temperatures of the CSP systems. There are mainly four types of solar receivers (Figure 1.4)
- A power block to convert heat energy to electricity
- A thermal storage system to account for the continuous supply.

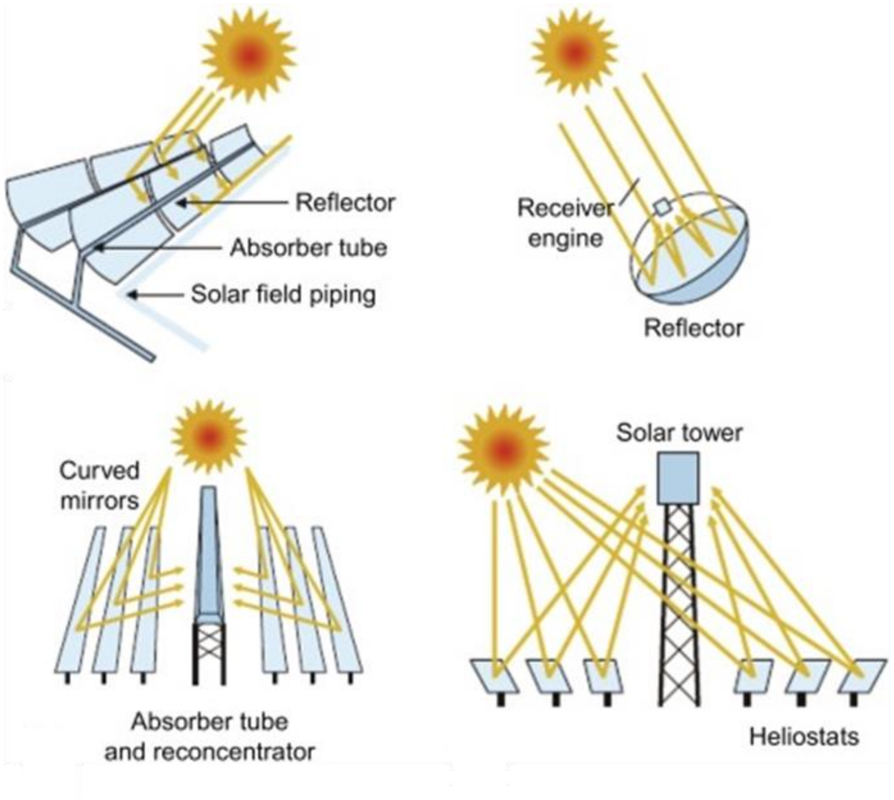

Figure 1.4 Different types of concentrating solar collectors.[16-17]

It has been observed that the number of publications and patents on CSP has grown dramatically over recent years.[13] Apart from electricity production, CSP has a tremendous potential to reduce CO_2 emissions and create many progressive jobs in the industry. The first CSP plant was built between 1984 - 1991 in the Mojave Desert, California, USA, by Luz international Ltd.[13] Nevertheless, the attempt didn't progress due to the drop in oil price, and the venture collapsed. Then, there was no significant progress in the CSP systems for years. However, in 2006, countries like Spain and USA started some initiatives. As a result, in 2014, the California Energy Commission approved licences for 5 CSP plants with a total capacity of 2284 MW.[13, 18] It is noted that in the period between 2010 - 2013, there was a record-breaking number of CSP plants launched (47 plants), whereas between 2013 -2019 only 25 plants were built. In 2018, the growth of totally installed CSP plants increased 4.3 times. The Levelised Cost of electricity reduced to 46% compared to that in 2010.[12, 19] Also, the capacity factor of CSP plants increased from 30% in 2010 to 45% in 2019, since technology improved, deployment occurred in areas with better solar resources and the average number of storage hours increased.[20-21] A list of worldwide CSP installed plants under construction and development is illustrated in Figure 1.5. [22]

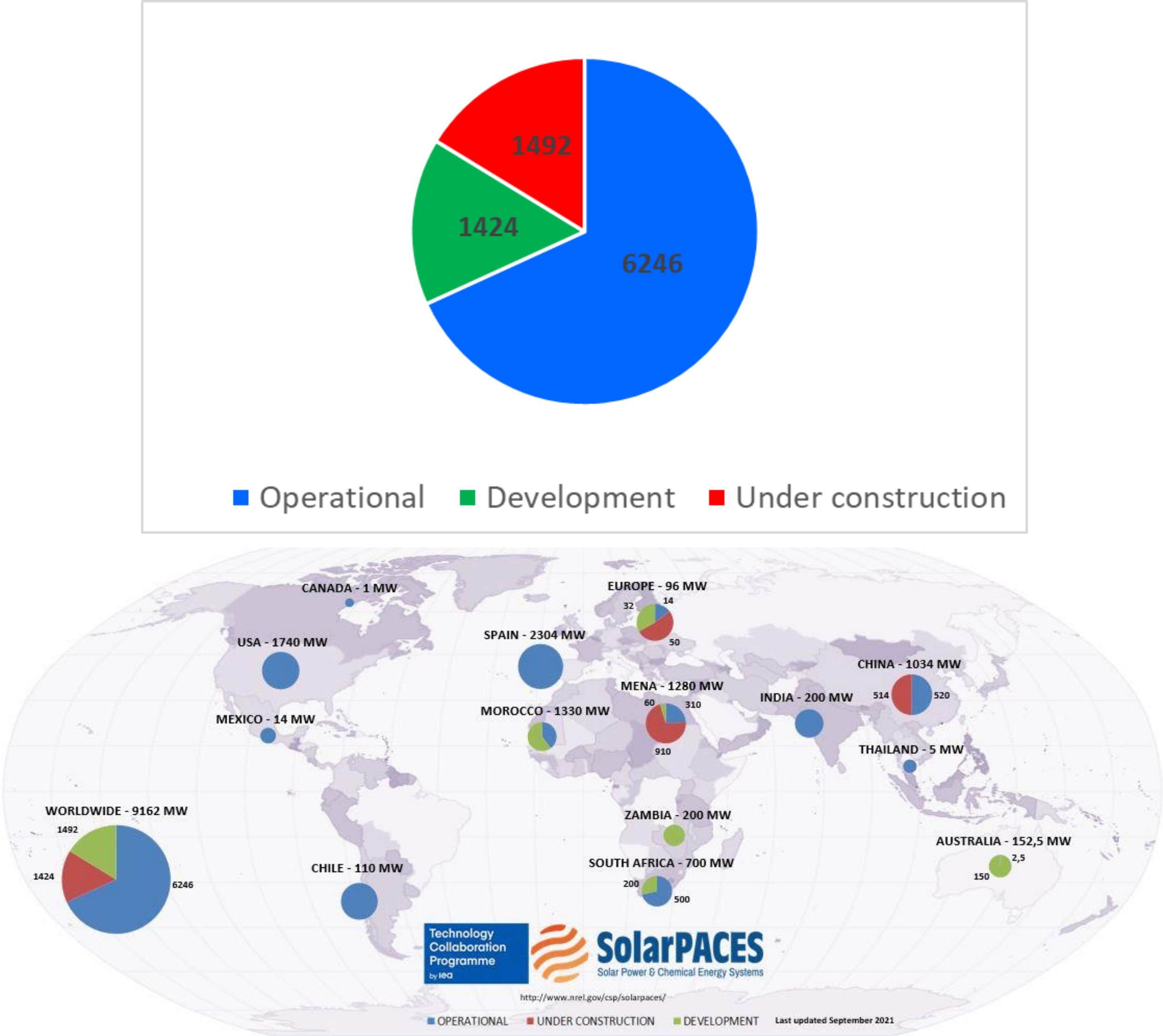

Figure 1.5 CSP projects around the world (based on the reference given).[22]

1.4 Thermal energy storage (TES) techniques

Due to the unreliable nature of solar power, it is required to develop effective storage systems to overcome the instability of the source while also considering grid demands. TES materials can be used to store heat or cold to be used anytime at any temperature, place or power capacity.[23-24] Hence, CSP plants coupled with a TES unit solve the mismatch between energy production and its use, making CSP plants unique compared to other renewable technologies.[25] The selection of a suitable Thermal Energy Storage (TES) material is the main challenge in CSP systems. An ideal TES material should possess a high energy storage density of 0.5 - 1.0 kWh/kg and working temperatures of > 600 °C, required for high-efficiency Stirling engines.

According to the US Department of Energy SunShot vision study, goals were set for future research and listed main three goals by 2030.[26]

1. The main objective is a cost reduction of 40% compared to the CSP plants currently operating. Specifically, to cost less than US \$15/kWh$_{th}$
2. Increase the operating temperature above 600 °C and
3. Increase the efficiency of the Stirling engine to achieve an exergetic efficiency greater or equal to 95%.

Hence, identifying a cost-effective high-temperature TES material that meets these three requirements is essential and challenging.

1.5 Different types of thermal energy storage systems

Several thermal storage systems for medium to high-temperature CSP plants have been developed in recent years. All these TES materials involve three stages: charging, storage and discharging using different states of matter.[24] The three known categorised TES materials so far are:

(1) Sensible heat storage materials
(2) Latent heat storage materials
(3) Thermochemical energy storage (TCES) materials

1.5.1 Sensible heat storage materials

Sensible heat storage materials (for instance, molten salt) are the most mature technology and store/release heat by raising/lowering the temperature of the material.[27-28] The energy stored by sensible heat can be expressed as:

$$Q = m\ C_p\ \Delta T \qquad 1\text{-}1$$

Where m is the mass of the storage material (kg), C_p is the specific heat capacity of the storage material (J.kg^{-1}. K^{-1}), and ΔT is the temperature difference.

The sensible storage method usually consists of a storage medium, containers (two / one tanks) and inlet/outlet devices. An inexpensive solid (rock, sand, or concrete) or liquid (molten salts, mineral or synthetic oils) can be used as sensible storage. A gas medium, air storage, is also used, but they are much bulkier compared to the other two.[29-30]

1.5.2 Latent heat storage materials

In latent heat storage, solar heat energy changes the phase of the material (also known as Phase Change Materials, PCMs). The amount of energy stored depends upon the mass and latent heat of the fusion of the material.[24, 31-32] The heat energy stored can be expressed as:

$$Q = m\,L \qquad 1\text{-}2$$

Where m is the mass of the material (kg) and L is the latent heat of the material (kJ.kg^{-1}).

A solid to liquid (heat of fusion) or liquid to vapour (heat of vapourisation) phase transition can be employed. For instance, during melting, a large amount of heat is stored in the material isothermally and is released while the material solidifies. Water, water-salt solutions, paraffin, nitrates, chlorides, etc., are typical materials used for latent heat storage.

1.5.3 Thermochemical energy storage materials (TCES)

Thermochemical energy storage uses heat to induce an endothermic chemical reaction and store the products separately. When energy is needed, these products are brought together, which undergo a reversible exothermic reaction.[33] The heat energy stored is linked to the reaction enthalpy and can be expressed as:

$$Q = n\,\Delta H_r \qquad 1\text{-}3$$

Where n is the number of moles of the reactant and ΔH_r is the reaction enthalpy.

At the moment, there are six categories of materials that are tested as thermochemical TES systems. They are 1. metal hydrides 2. carbonates 3. hydroxides 4. redox system 5. ammonia and 6. organic systems. Solar heat energy can be stored without much heat loss for a long-term period in the thermochemical method.[24, 34] Moreover, the TCES systems have a wide range of applications such as waste heat recovery, transportation, and solid oxide fuel cells, as shown in Figure 1.6. This thesis is mainly focused on the metal hydride TCES for CSP applications. The most crucial challenge is the high energy storage density and reversibility of metal hydrides.

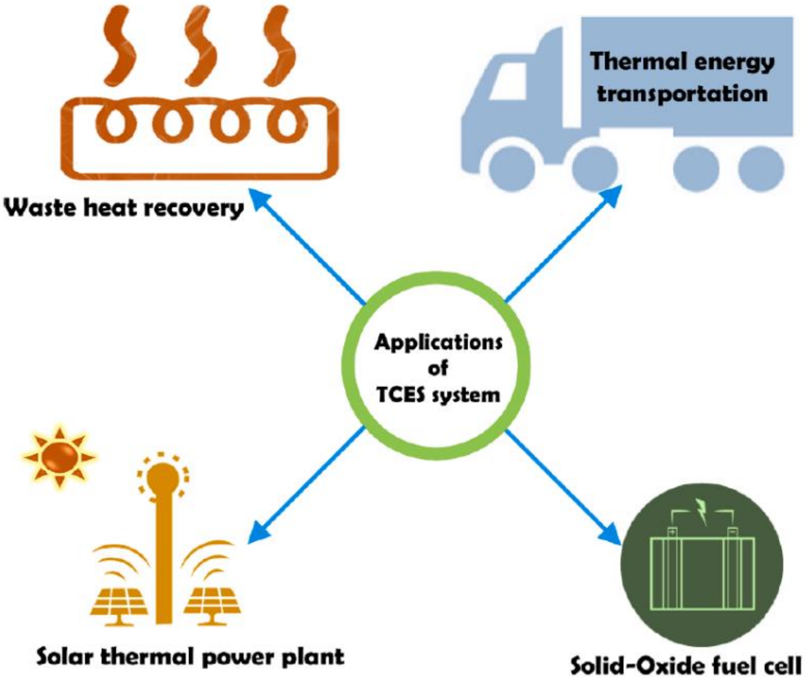

Figure 1.6 Different applications of TCES system.[35]

1.6 Comparison of TES systems

A comparison of three different TES systems is provided in Table 1.2. In addition to the CSP applications, all three TES technologies possess various applications such as solar space heating, hot water production, building constructions, etc.[23] However, thermochemical storage systems possess high volumetric and gravimetric energy densities and high operating temperatures compared to sensible and latent heat storage materials for CSP applications. Moreover, thermochemical systems are the most promising for long term storage due to negligible thermal loss during storage as products can be stored at ambient temperature.

Table 1.2 Comparison of three different TES systems.[23-24, 35-37]

Features	Sensible heat storage (molten salt)	Latent heat	Thermochemical
Principle	Energy is stored as sensible heat by changing the temperature of the material.	Energy is stored by the phase change of material at a constant temperature.	Energy stored using reversible chemical reactions

Energy stored/released	$Q = m\, C_p\, \Delta T$	$Q = m\, L$	$Q = n\, \Delta H_r$
Characteristics affecting storage	Thermal conductivity, Density, Diffusivity, Specific heat capacity, Vapour pressure etc.	Thermal conductivity, Phase separation, Subcooling, Corrosion, Melting enthalpy etc.	Thermal conductivity, Storage density, Supply pressure of the reactant gas, Kinetics, Catalyst activity etc.
Materials	Solids (rock, sand, concrete etc.) or liquid (molten salts, minerals, synthetic oils etc.)	Organic, inorganic, Eutectic	Metal Hydrides Carbonates Hydroxides Redox System Ammonia and Organic system
Theoretical volumetric Energy density ($kWh_{th}\, m^{-3}$)	small ≈ 50	Medium ≈ 100	High ≈ 500
Theoretical gravimetric energy density($kWh_{th}\, kg^{-1}$)	small ≈ 0.02- 0.03	Medium ≈ 0.05 - 0.1[*]	High ≈ 0.5 - 1 $kWh\, kg^{-1}$
Storage temperature	Charging step temperature	Charging step temperature	Ambient temperature
Storage period	Limited	Limited	Theoretically unlimited
Maximum operating temperature in the CSP application	Molten salt - 560 °C	NaCl - 800 °C	CaH_2 - >1000 °C
Transport	Small distance	Small distance	Theoretically unlimited
Maturity	Industrial-scale	Laboratory and Pilot scale	Laboratory and pilot-scale
Technology	Simple	Medium	Complex

[*] The miscibility gap alloys which fall under latent heat category have gravimetric energy densities of > 0.15 $kWh_{th}\, kg^{-1}$

1.7 Hydrogen systems: Metal hydrides for thermochemical storage

Metal hydrides as thermochemical storage systems were first studied by Libowitz *et.al.* in 1974.[38] The presence of reversible hydrogen bonds makes them suitable for various applications such as hydrogen storage, thermal energy storage, electrochemical applications etc. Generally, metal hydrides were studied as solid storage materials due to their increased hydrogen storage density compared to hydrogen gas or liquid hydrogen. For instance, MgH_2 has a hydrogen density of 6.5 H atoms/cm^3 compared with that of H_2 gas (0.99 H atoms/cm^3) or liquid hydrogen (4.2 H atoms/cm^3).[10, 39]

Many metals react with hydrogen to form metal hydrides, as shown below:

$$M + X\,\mathrm{H}_2 \xrightleftharpoons[\Delta H > 0,\ \text{Endothermic}]{\Delta H < 0,\ \text{Exothermic}} M\,H_X + Q$$

Here, M is a metal and $M\,H_X$ is the respective hydride, X is the ratio of hydrogen to metal and Q is the heat energy released during the reaction. At ambient and high temperatures, the formation energy of the hydride is exothermic, the change in enthalpy (ΔH) will be negative, and the reverse reaction is endothermic; therefore, ΔH will be positive.

A vast collection of metals, metal alloys and compounds can reversibly react with hydrogen over a wide range of temperatures (as low −100 °C, $TiCr_{1.9}H_{3.5}$ and as high >1100 °C, LaH_x[40-43]) and have theoretical heat storage potentials that are higher than other thermochemical materials (Table 1.3). For example, CaH_2 has a very high heat storage capacity of almost 4939 $kJ.kg^{-1}$.[44] Moreover, the unique characteristic of metal hydrides that make them potential heat storage materials for CSP plants is that they can absorb or desorb hydrogen at constant pressure. A metal hydride can absorb or release heat by changing the applied hydrogen pressure or temperature.[32] However, the main challenge with metal hydrides is identifying cost-effective materials that are reversible and identifying engineering solutions.

Table 1.3 Comparison of heat storage capacities of metal hydrides with other TES materials.[45-46]

Type of thermal energy storage (TES)	Example of TES material	Total heat storage capacity (kJ.kg^{-1})
Sensible heat	Molten salt mixtures	153 per 100 °C
Latent heat/phase change materials	$NaNO_3$	282
Thermochemical	Oxidation of Co_3O_4	1055
	$MgH_2 \rightleftharpoons Mg + H_2$	2814
	$CaH_2 \rightleftharpoons Ca + H_2$	4939 (theoretical)

Metal hydrides can be categorised into three operating temperature ranges for CSP applications.

1. High operating metal hydrides (600 °C - 1200 °C)
   CaH_2, SrH_2, LiH_2, $YH_{1.8}$
2. Medium operating metal hydrides (400 °C - 600 °C)
   Mg_2FeH_6, NaH
3. Low operating metal hydrides (250 °C - 400 °C)
   $NaMgH_3$, MgH_2 + 2 wt% Ni, MgH_2, Mg_2NiH_4

According to the US Department of Energy SunShot Initiative, to reduce the cost of solar electricity, there has been a new focus on the potential high-temperature metal hydrides (that can operate above 600 °C) to be the next-generation energy storage material for CSP application. The SunShot Initiative research aims to identify cost-effective promising high-temperature metal hydrides, find the thermodynamics, test their H_2 desorption absorption properties, model and design suitable tanks and test beds, and build up a prototype and test it under dynamic conditions.

1.8 High-temperature metal hydride (HTMH, > 600 °C) as a TES in CSP plants

In the past years, metal hydrides with working temperatures of less than 500 °C were the research focus. However, the new generation CSP systems must be replaced with a TES system that will operate > 600 °C. This will increase the efficiency of the power plant by 40% of the currently used ones. The current molten salt systems degrade above 565 °C, limiting the upper operational temperature. The use of the most explored MgH_2 and its alloys (Mg_2FeH_6) is also limited to < 550 °C as Mg metal evaporates at higher temperatures. Therefore, calcium hydride systems, alkali earth metal hydrides of Ba and Sr and Ti hydrides are some of the few systems which can operate in the high-temperature range (> 600 °C). [47]

A schematic of the CSP system coupled with a high-temperature metal hydride (HTMH) thermochemical energy storage system is shown in Figure 1.7. During daytime (Figure 1.7), the received solar radiation by the concentrator is provided to the heat engine and converted to electricity. Any excess heat energy is used to desorb hydrogen from the metal hydride, followed by an endothermic reaction, of which this hydrogen will be stored separately. At night (Figure 1.7), the reverse exothermic reaction occurs. The high-temperature metal hydride is allowed to cool and absorb hydrogen, releasing heat provided to a heat engine to produce electricity. Therefore, this system enables a continuous supply of electricity even in the absence of a solar source. The released hydrogen can be stored either in a volumetric gas tank or another low-temperature metal hydride. Low-temperature metal hydrides have a high volumetric capacity for hydrogen. They can operate over a limited pressure range, but associated issues include selecting suitable material and handling costs, synthesis, and engineering problems.[32] A compressed tank storage has a low capital cost but have the disadvantages of requiring large volume vessel and operating pressure. However, the released H_2 storage via a low-temperature metal hydride will provide the flexibility to choose the operating temperature of the high temperature metal hydride.

Even though metal hydrides are the potential candidates, there are many technical challenges, from material selection (sintering, vaporisation etc.) to engineering issues (gas containment, material compatibility) that need to be overcome to operate at temperatures greater than 600 °C.[47] For the HTMH, the enthalpy, entropy, and operating temperatures determine the hydrogen capacity and heat storage density. The main drawbacks of HTMH are cycling stability and the overall cost of the system. Moreover, to account for a 30-year lifetime CSP plant, a metal hydride must undergo more than 10000 cycles of hydrogen absorption and desorption without altering its essential characteristics.[34] Unfortunately, no candidate has been identified with this stability to date. It is also necessary to enhance the thermal conductivity of metal hydrides so that the heat enters and leaves the system as quickly as possible.

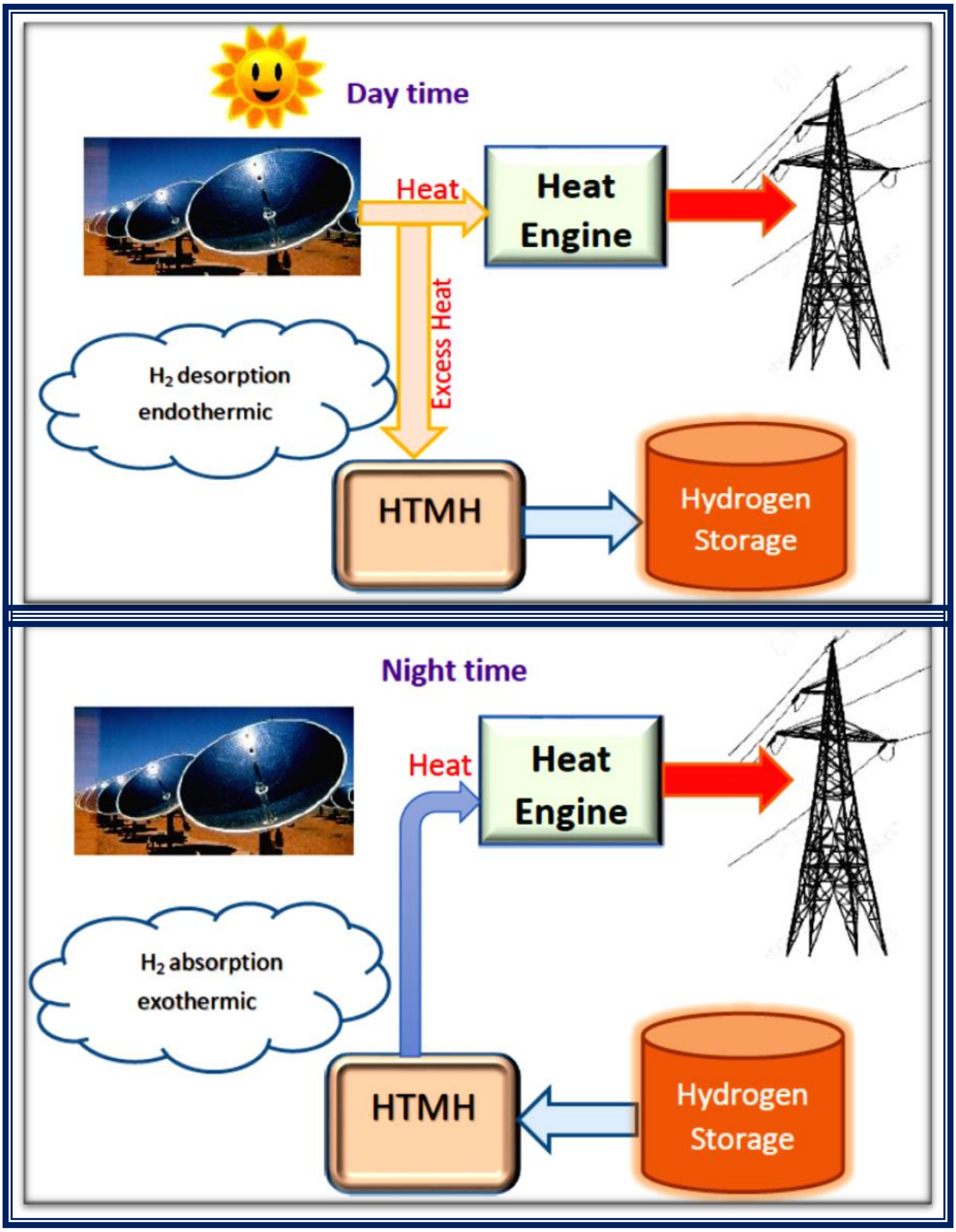

Figure 1.7 Schematic diagram showing the working of HTMH in CSP plants.

1.9 Candidates hydrides for high-temperature thermal energy storage

There are no perfect practical choices for HTMH for CSP applications available so far. Sodium hydride decomposes at 426 °C at 1 bar of H_2 pressure and could operate up to 659 °C at 150 bar of H_2 pressure.[48] The poor reversibility and high vapour pressure of Na limit its use as a TES material. However, modified NaH (fluorine substitution, $NaMgH_2F$, $NaMgH_3$ etc.) can enhance the operating conditions but has the disadvantage of H_2 high pressures above 150 bar.[49-51] Similar issues also happen for the most commonly used MgH_2 and its alloys, and the operating temperatures are limited to below 550 °C. Therefore, HTMH heat storage will need to shift away from traditionally examined Na, Mg-based materials. The potential HTMH for heat storage can be classified into overlapping groups such as 1. simple saline or ionic hydrides 2. metallic or intermetallic 3. complex metal hydrides. The Current HTMH research mainly focuses on CaH_2, TiH_2, SrH_2 and LiH_2 systems.[52-54] Even though Y, Zr, La and Ce hydrides show high operating temperature and enthalpy, they are less investigated.[55] This may be due to the high cost of these transition metals.[44] It can be noted that along with cost-effective CaH_2 systems and attractive Ti, Ba and Sr metal hydrides, complex transition metal hydrides also show promising properties as high-temperature TES materials. Some other potentially identified complex hydrides are Eu_2RuH_6 (1212 °C), Ca_2OsH_6 (1077 °C) and Li_4RhH_4 (912 °C).[55-56] Moreover, a few examples that can operate ≥ 600 °C are listed in Table 1.4.

Table 1.4 Examples of HTMH (≥ 600 °C) for CSP applications.

	Hydride materials	**Theoretical H_2 capacity**	**ΔH (kJ.mol^{-1}. H_2)**	**ΔS (J.K^{-1} mol^{-1}. H_2)**	**T* (°C)**	**P* (bar)**	**Ref.**
Simple Saline or Ionic hydrides	$CaH_2 \rightleftharpoons Ca + H_2(g)$	4.8	207.9	-	950 - 1100	1 - 10	10, 55
	$NaH \rightleftharpoons Na(l) + 1/2H_2(g)$	4.2	130	165	400 - 600	0.5 - 70	57-59
	$LiH \rightleftharpoons Li + 1/2H_2$ (g)	12.6	190	135	950 - 1150	0.1 - 1.5	57, 59-60
	$SrH_2 \rightleftharpoons Sr + H_2(g)$	2.2	183	138	1050 - 1150	1 - 3	61-62

Metallic and intermetallic hydrides of transition metals	$TiH_{1.0} + 0.3H_2 \rightleftharpoons TiH_{1.6}$	1.22	165.5	-	645 - 921		40
	$TiH_{1.72} \rightleftharpoons Ti + 0.86H_2(g)$	3.5	154	161	680 - 750	1 - 4	61
	$TiH_2 \rightleftharpoons Ti + H_2(g)$	4.04	147	140	775 - 850	1 - 3	61
	$ZrH_2 \rightleftharpoons Zr + H_2(g)$	2.16	175	146	925 - 1050	1 - 3	61
	$YH_2 \rightleftharpoons Y + H_2(g)$	2.21	234	157	1217 - 1310	1 - 3	61
	$CeH_2 \rightleftharpoons Ce + H_2(g)$	1.41	214	174	955 - 1025	1 - 3	61
	$LaH_2 \rightleftharpoons La + H_2(g)$	1.43	221	159	1115 - 1200	1 - 3	61
Complex transition metal hydrides	$NaK_2AlH_6 \rightleftharpoons 2KH + NaH + Al + 3/2H_2(g)$	2.25	98	150	380 - 600[a]		40, 63
	$Ca_2NH + H_2(g) \rightleftharpoons CaNH + CaH_2$	2.07	88.7	-	590 - 780	1 - 10	40, 64
	$LiBH_4(l) \rightleftharpoons LiH + B + 3/2H_2(g)$	13.88	57.3	-	460 - 688[b]	-	65
	$LiBH_4(l) \rightleftharpoons LiH_{(l)} + B + 3/2H_2(g)$	13.88	71.7	-	688 - 1000	-	40, 65
	$Ca_4Mg_4Fe_3H_{22} \rightleftharpoons 2Ca_2FeH_6 + 4\,Mg + MgNi_2 + 2H_2(g)$	2.25	113.4	-	800	31	55, 66
	$2CaMgNiH_4 \rightleftharpoons 2CaH_2 + Mg + MgNi_2 + 2H_2(g)$	1.58	129	-	600	136	55, 67

*T - temperature, P- pressure

[a] The upper temperature is limited by the melting point of NaH ≈ 638 °C and KH ≈ 619 °C.

[b] The melting point of LiH is ≈ 688 °C. The enthalpy of melting is 21.8 kJ.mol^{-1}.[40]

1.10 Calcium hydride for high-temperature energy storage

There has been interest in using CaH_2 as thermochemical energy storage since the 1970s. Kuznetsov *et.al.*[68] in 1977 at the conference of energy conversion in the USA explained a particular interest in the energy contained in CaH_2 and that could apply to various fields such as aviation, generation and storage of energy (in homes), agriculture (in fertiliser production), industry and transport.[68] It also mentioned the importance of converting solar energy into heat and electricity and proposed a CSP model with a concentrator on top of 275 m tower with a capacity of 100 MW electric output. A sodium loop will carry the heat from the concentrator to the generator. The heat of formation of CaH_2 is $-$ 4312 $kJ.kg^{-1}$ at 25 °C, and the energy released during hydrogen absorption at 950 °C is 4494 $kJ.kg^{-1}$. This provides the ability to store 1.25 kWh of solar energy per kilogram of CaH_2.[69] The main advantages of the Ca-CaH_2 system are:

1. Its high gravimetric/volumetric energy density (Figure 1.8) compared to molten salts' current state of the art (over 20 times higher than molten salts)[46]
2. High operating temperature
3. Relatively low hydrogen pressure (1 - 10 bar between 950 °C - 1100 °C)[60]
4. Comparatively low cost and abundant
5. High enthalpy of dehydrogenation
6. High melting point
7. High exergetic efficiencies.

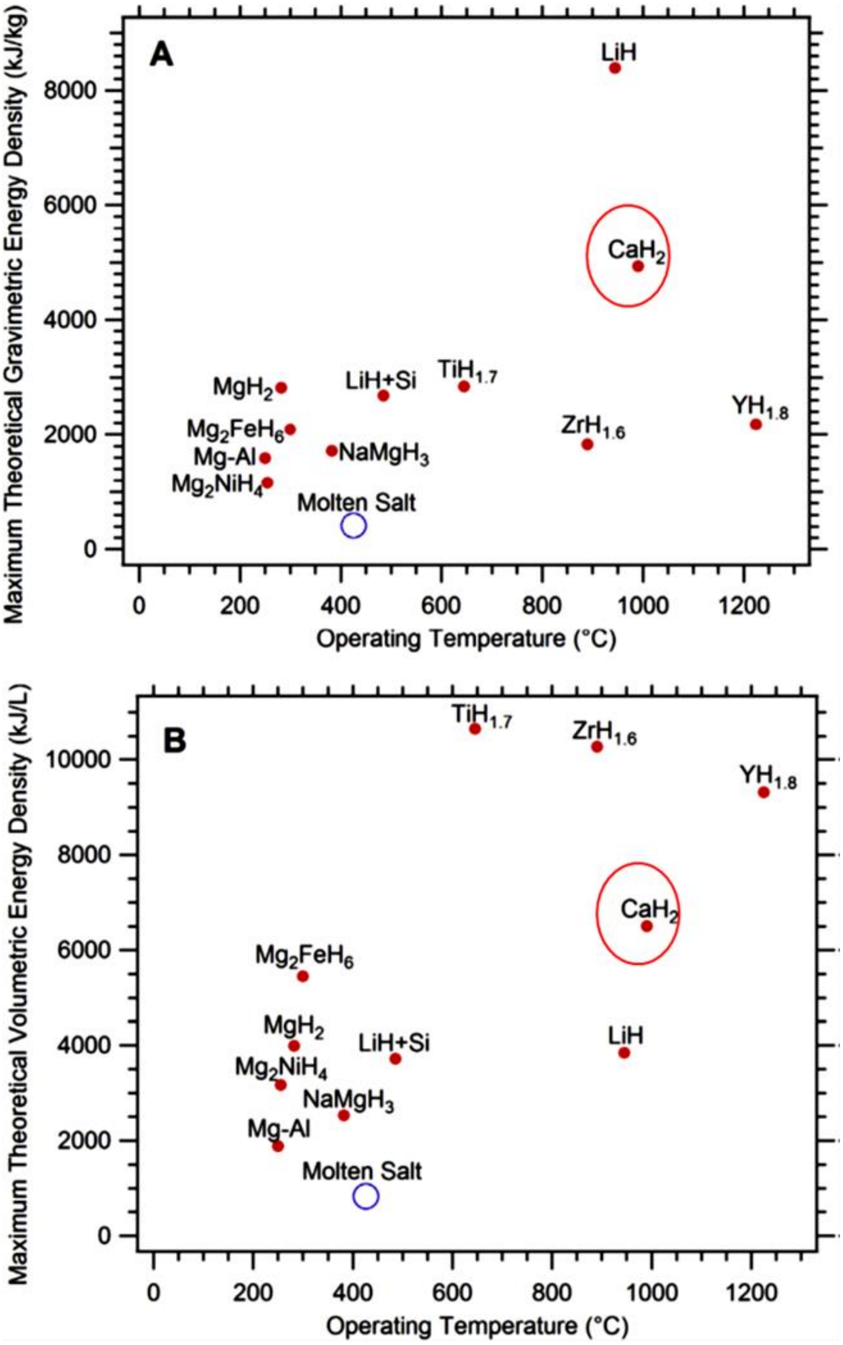

Figure 1.8 comparison of energy densities of CaH_2 with molten salt.[70]

Due to these attractive properties, the use of CaH_2 as a solar thermal energy storage material was patented in 2010.[71] Bliesner *et.al.* and an Australian company EMC Solar proposed a concept of using the Ca/CaH_2 system for a CSP plant with a continuous electric output of 100 kW using a Stirling engine with a 50% conversion efficiency.[32, 71-72] The model employed low temperature (20 °C) Ti-Fe hydride to store H_2 and used boron oxide and nitrate salt tanks as high temperature and low-temperature heat exchangers, respectively. An 18 h storage capacity

(3600 kWh thermal energy) requires 4690 and 234 kg mass of Ca and H_2, respectively. The proposal can test 50 kg of CaH_2. A conceptual design of this CaH_2 reactor is illustrated along with its operation, as shown in Figure 1.9.

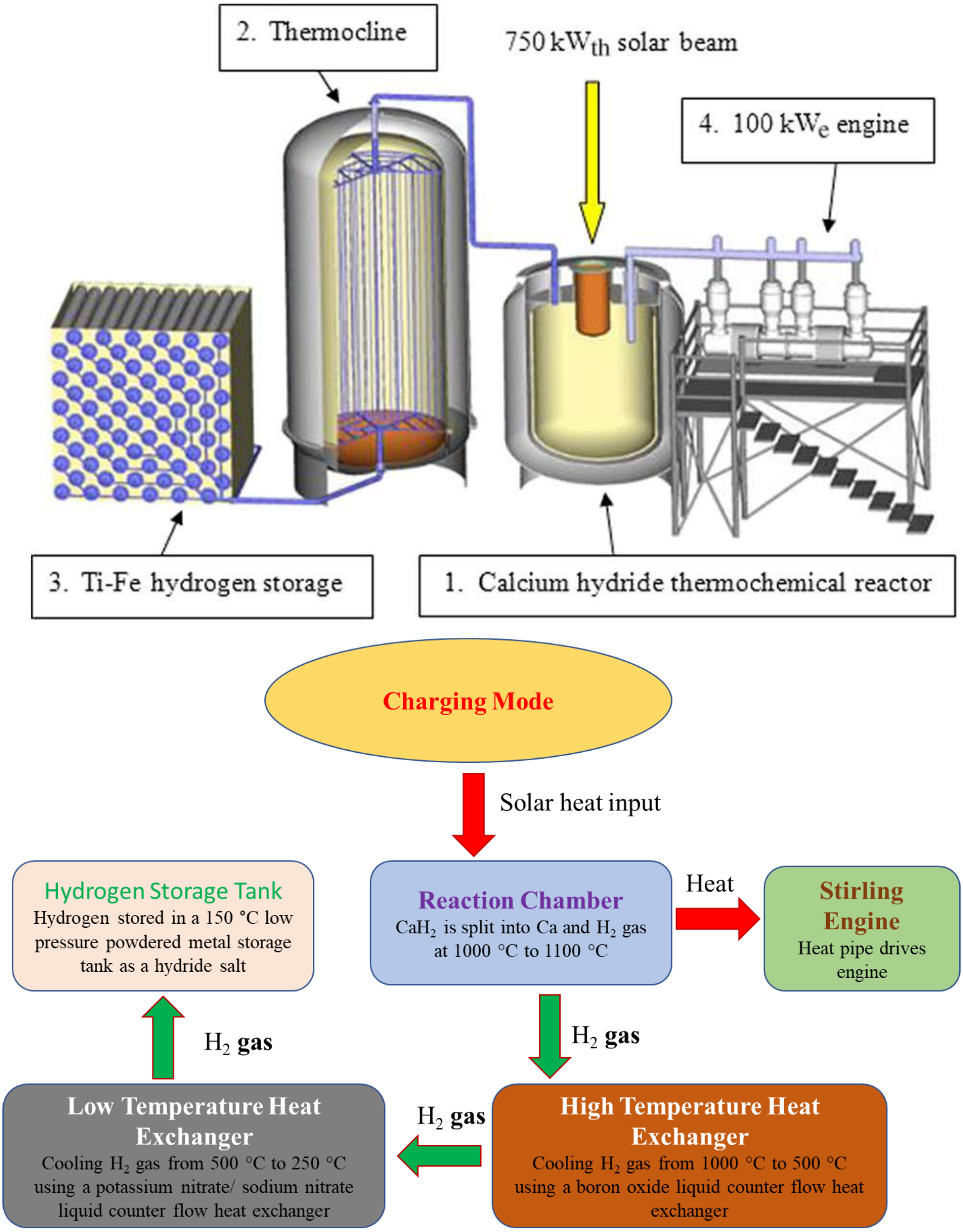

Figure 1.9 A conceptual CaH_2 reactor and its work proposed by EMC solar company.[32, 72]

Unfortunately, the desorption temperature of CaH_2 is too high for the current and proposed next-generation CSP plants. Therefore, the decomposition temperature of CaH_2 can be reduced by the thermodynamic destabilisation process, which is explained in detail in the next section.

1.10.1 Thermodynamic destabilisation of HTMH (CaH_2)

The metal hydrides that operate at temperatures > 600 °C present many challenges, such as material problems and technical difficulties. The CaH_2 is highly corrosive at its operating temperature, 1000 °C, and the melting point of both Ca metal and CaH_2 are 842 and 816 °C. Therefore, an expensive storage tank material requirement and other engineering issues are the main factors that limit the use of pure CaH_2 as a thermochemical TES material. Thermodynamic destabilisation of metal hydrides is one of the best approaches to reducing pure metal hydrides' decomposition temperature. This can be achieved by adding suitable additives to the pure metal hydride and reducing the decomposition temperature and corresponding enthalpies. This is illustrated in Figure 1.10.

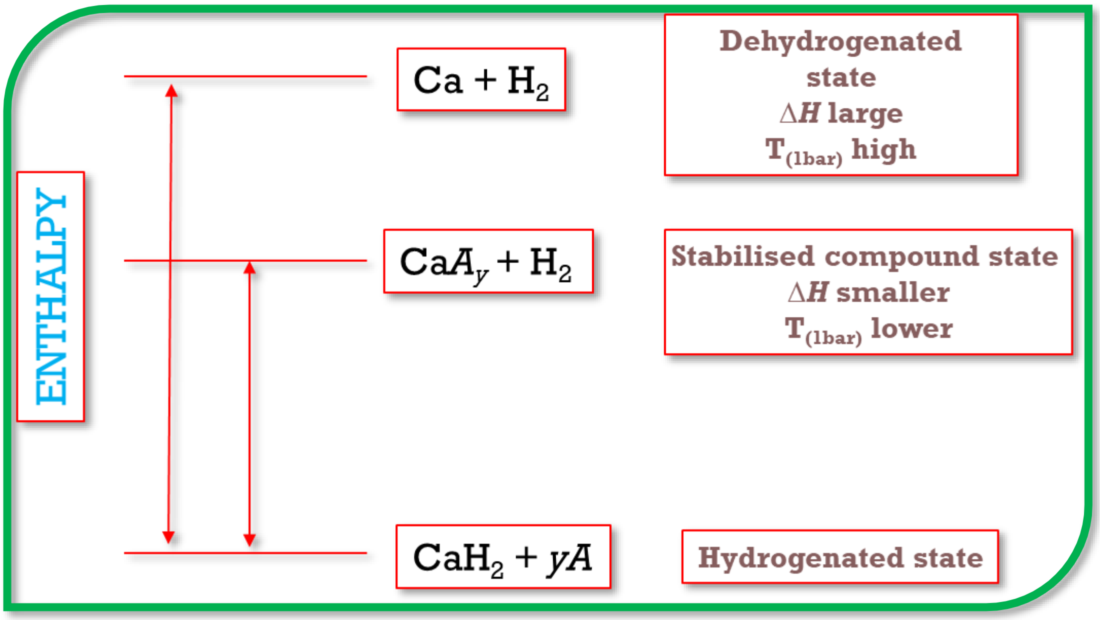

Figure 1.10 General enthalpy diagram showing destabilisation of CaH_2 by adding suitable additives (*A* = Zn, C etc.)

A few examples of the thermodynamic destabilisation of CaH_2 as a TES material for CSP application are discussed below:

1.10.1.1 CaH_2 - Al system

Veleckis successfully showed this method of thermodynamic destabilisation of metal hydride in 1981 using CaH_2 by adding Al to it.[73] The reaction occurred in multiple steps

$CaH_2 + 4Al \rightleftharpoons Al_4Ca + H_2$ 1-4

$CaH_2 + Al_4Ca \rightleftharpoons 2Al_2Ca + H_2$ 1-5

The enthalpy of the reaction 1- 4 and 1-5 found as $\Delta H_{des} \approx 83$ kJ.mol^{-1}.H_2 at $T_{1bar} \approx 414$ °C, and $\Delta H_{des} \approx 90$ kJ.mol^{-1}.H_2 at $T_{1bar} \approx 481$ °C, respectively.[73-74] Ward *et.al.*[75] extended this method (for reaction 1-6) and demonstrated the feasibility of the $CaAl_2$ system as a potential high-temperature thermal battery for CSP applications. However, this requires 62 bar of H_2 pressure at ≈ 700 °C.[55, 73, 75]

$CaH_2 + 2Al \rightleftharpoons CaAl_2 + H_2$ 1-6

1.10.1.2 CaH_2 - $LiBH_4$ system

Yang Li *et.al* showed $CaH_2/LiBH_4$; the complex metal hydride composite can be a potential solar thermal storage material.[76] The destabilisation reaction occurs via the following pathway:

$CaH_2 + 6LiBH_4 \rightleftharpoons 6LiH + CaB_6 + 10H_2$ 1-7

The enthalpy of the reaction $\Delta H_{des} \approx 60$ kJ.mol^{-1}.H_2, and the equilibrium pressure is 0.482 MPa at 450 °C.[76] Additives such as $TiCl_3$, V_2O_5, TiF_3, TiO_2, $LiNH_2$, NbF_5, and $NbCl_5$ were investigated with the $CaH_2/LiBH_4$ system to enhance the kinetic and cycling properties. It was found that $TiCl_3$ was the most effective additive that increased the hydrogen reversibility of the $CaH_2/LiBH_4$ by 9%.[76] However, the high price of $LiBH_4$ will limit the use of this material for CSP applications.

1.10.1.3 CaH_2 - Si system

Griffond *et.al.* showed the thermodynamic destabilistaion of CaH_2 by adding Si.[77] The reaction occurred in 5 steps:

$CaH_2 + 2Si \rightleftharpoons CaSi_2 + H_2$ 1-8

$CaH_2 + 2CaSi_2 \rightleftharpoons Ca_3Si_4 + H_2$ 1-9

$CaH_2 + Ca_3Si_4 \rightleftharpoons 4CaSi + H_2$ 1-10

$CaH_2 + 3CaSi \rightleftharpoons Ca_5Si_3 + H_2$ 1-11

$CaH_2 + Ca_5Si_3 \rightleftharpoons Ca2Si + H_2$ 1-12

The enthalpy and entropy of the reaction 1-11 was calculated by Griffond *et.al.* as ΔH_{des}= 154 ± 4 kJ.mol^{-1}.H_2, ΔS_{des}= 151 ± 3 J.K^{-1}.mol.H_2, at T_{1bar} = 747 ± 33 °C.[77]

1.10.1.4 CaH_2 - MgO system

It was also proved by Griffond *et.al.* that MgO can destabilise CaH_2:[74]

$CaH_2 + MgO \rightleftharpoons CaO + Mg + H_2$ 1-13

The thermodynamic properties calculated were ΔH_{des} = 170.7 ± 25 kJ.mol^{-1}.H_2, ΔS_{des}= 158.4 ± 12 kJ.mol^{-1}.H_2 with an operating temperature of 805 ± 61 °C at 1 bar of H_2 pressure.[74] The loss of Mg at this temperature was one of the issues that need to be addressed for the use of this system.

1.11 Thesis Outline

This study mainly focused on destabilised calcium hydride systems. The importance and the reasons to choose calcium hydride and the materials selected for destabilisation are explained in detail in the following chapters. Moreover, the systems are determined based on the following criteria; cost, availability, operating temperature, and thermodynamic prediction. The thesis consists of 8 chapters. The first chapter is the introduction which includes a brief review of the background information. The second chapter summarises the materials, methods and experimental procedures used in this study. The following six chapters are the main research work, including two peer-reviewed published papers (chapter 4 and 5). The entire process carried out in the thesis can be illustrated in the flow chart (Figure 1.11). Besides, a small outline of each chapter is also provided below:

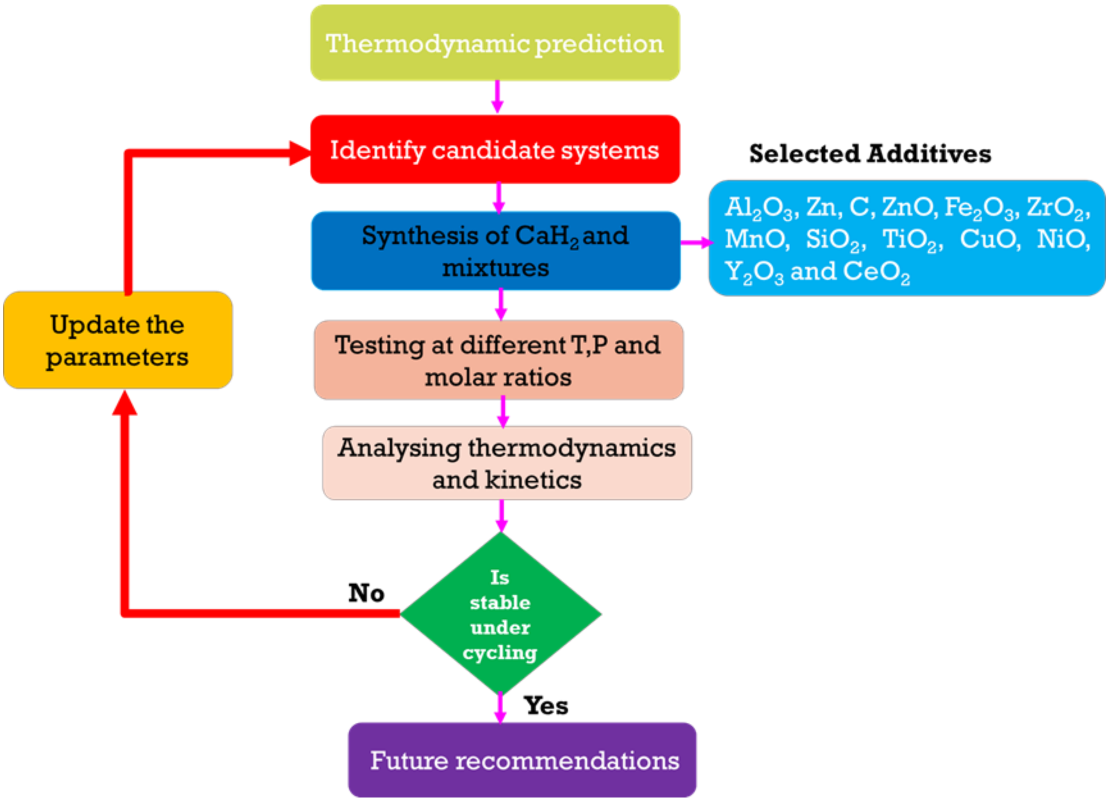

Figure 1.11 A summary of the studies performed in this project.

CHAPTER 2- Experimental methods

The materials and all the theoretical and experimental investigation techniques and procedures used during this project are discussed in detail in Chapter 2.

CHAPTER 3 - Thermodynamic and kinetic properties of CaH_2

Due to the complexity of the Ca - CaH_2 system, little research was carried out after the 1960s, especially on thermodynamics. Moreover, the thermodynamic properties provided by different investigators were conflicting. Hence, this chapter presents an experimental investigation of the thermodynamic and kinetic properties of CaH_2 and compares it with the literature review. The chapter also compares the thermodynamic properties of solid and molten CaH_2.

CHAPTER 4 - Destabilised CaH_2 as a promising thermal battery

Chapter 4 is a peer-reviewed published paper in the Journal Physical Chemistry C in July 2020. The chapter demonstrated that adding Al_2O_3 to CaH_2 altered the reaction pathway reduced the operating temperature at 1 bar of hydrogen equilibrium pressure from ≈ 1000 °C to 636 °C.

Moreover, the chapter provides an overview of calcium hydride's thermodynamic destabilisation, including synthesis, characterisation, thermodynamic and thermal analysis. The cost calculation and cycling capacity were also investigated to test its feasibility as a TES material for CSP application.

CHAPTER 5 - Thermochemical energy storage performance of zinc destabilised calcium hydride at high temperatures

Chapter 5, CaH_2- 3Zn system, is also peer-reviewed and published in the Journal of Physical Chemistry Chemical Physics in October 2020. The high enthalpy of desorption, operating temperature close to 600 °C and cycling stabilities makes this system a potential candidate. However, the low vapour pressure of Zn and the evolution of Zn from the calcium zinc alloys need to be addressed for the practical use of this material.

CHAPTER 6 - Performance of calcium hydride graphite system at high temperatures

This chapter comprises the theoretical and experimental investigation of the CaH_2 - 2C system that exploits the feasibility as a high-temperature thermochemical TES material for third-generation CSP plants. This system has the highest gravimetric heat storage. Unfortunately, due to the formation of methane gas, the CaH_2-2C system shows poor reversibility, which indicates a barrier to the application of the CaH_2-2C system as a TES material for CSP application.

CHAPTER 7 - Metal oxides for the thermodynamic destabilisation of CaH_2: A comparison of several metal oxide systems.

Chapter 7 is a complete study of pure CaH_2 with all possible metal oxides (ZnO, ZrO_2, SiO_2, MnO, Fe_2O_3, NiO, CuO, Y_2O_3 and CeO_2). It investigates and compares the effect of these oxides on the thermodynamic destabilisation of pure CaH_2. Also, it identifies the reaction pathway with each oxide and reports the feasibility of each system as a TES for CSP application.

CHAPTER 8 - Conclusions and future perspectives

The last chapter summarises the significant outcomes of the thesis work and future recommendations.

1.12 References

1. IEA, World Energy Outlook, **2018** https://Www.Iea.Org/Efficiency2018/.
2. IEA, World Energy Outlook, **2021** https://www.iea.org/reports/world-energy-outlook-2021.
3. Abbott, D., Keeping the Energy Debate Clean: How Do We Supply the World's Energy Needs? *Proc. IEEE*, **2009,** *98*, 42-66.
4. Institute, W. C. World Coal Institute https://www.worldcoal.org/coal-facts/what-is-coal-where-is-it-found/ (accessed July **2021**).
5. IEA,World Energy Outlook, **2020** https://Www.Iea.Org/Reports/World-Energy-Outlook-2020.
6. Solar Power Will Make a Difference- Eventually. https://www.technologyreview.com/s/414792/solar-power-will-make-a-difference-eventually/ (accessed July **2021**).
7. How Does Solar Work? https://www.energy.gov/eere/solar/how-does-solar-work. (accessed July **2021**).
8. Sukhatme, S. P.; Nayak, J. K., Solar Energy: Principles of Thermal Collection and Storage; *Tata McGraw-Hill Education*, **1996**.
9. Chu, Y.; Meisen, P., Review and Comparison of Different Solar Energy Technologies. *Global Energy Network Institute (GENI), San Diego, CA* **2011**, *6*, 1-56.
10. Qu, X.; Li, Y.; Li, P.; Wan, Q.; Zhai, F., The Development of Metal Hydrides Using as Concentrating Solar Thermal Storage Materials. *Frontiers of Materials Science* **2015**, *9*, 317-331.
11. Helioscsp, Concentrated Solar Power (CSP) Vs Photovoltaic (Pv). https://helioscsp.com/concentrated-solar-power-csp-vs-photovoltaic-pv/ (accessed September **2021**).
12. Achkari, O.; El Fadar, A., Latest Developments on Tes and CSP Technologies-Energy and Environmental Issues, Applications and Research Trends. *Appl. Therm. Eng.* **2020**, *167*, 114806.
13. Islam, M. T.; Huda, N.; Abdullah, A.; Saidur, R., A Comprehensive Review of State-of-the-Art Concentrating Solar Power (CSP) Technologies: Current Status and Research Trends. Renewable Sustainable Energy Rev. **2018**, *91*, 987-1018.
14. Awan, A. B.; Zubair, M.; Praveen, R.; Bhatti, A. R., Design and Comparative Analysis of Photovoltaic and Parabolic Trough Based CSP Plants. *Sol. Energy* **2019**, *183*, 551-565.
15. Antil Martini, K., On the Feasibility of Thermochemical Energy Storage for CSP Plants: Technology Evaluation and Conceptual Design. **2018**.

16. Fuqiang, W.; Ziming, C.; Jianyu, T.; Yuan, Y.; Yong, S.; Linhua, L., Progress in Concentrated Solar Power Technology with Parabolic Trough Collector System: A Comprehensive Review. *Renewable Sustainable Energy Rev.*, **2017**, *79*, 1314-1328.
17. Ballestrín, J.; Cumpston, J.; Burgess, G., Heat Flux and High Temperature Measurement Technologies for Concentrating Solar Power. In Concentrating Solar Power Technology, *Woodhead Publ. Ser. Energy*, **2021**; pp 633-657.
18. Sharma, A., A Comprehensive Study of Solar Power in India and World. *Renewable Sustainable Energy Rev.*, **2011**, *15*, 1767-1776.
19. IRENA, Renewable Power Generation Costs in 2018. https://www.irena.org/publications/2019/May/Renewable-power-generation-costs-in-2018 (accessed November **2021**).
20. Kuravi, S.; Trahan, J.; Goswami, D. Y.; Rahman, M. M.; Stefanakos, E. K., Thermal Energy Storage Technologies and Systems for Concentrating Solar Power Plants. *Prog. Energy Combust. Sci,.* **2013**, *39*, 285-319.
21. González-Roubaud, E.; Pérez-Osorio, D.; Prieto, C., Review of Commercial Thermal Energy Storage in Concentrated Solar Power Plants: Steam Vs. Molten Salts. *Renewable sustainable energy rev.*, **2017**, *80*, 133-148.
22. Solarpaces, CSP Projects around the World. https://www.solarpaces.org/csp-technologies/csp-projects-around-the-world/ (accessed November 2021)
23. Cabeza, L. F., Advances in Thermal Energy Storage Systems: Methods and Applications. *Woodhead Publ. Ser. Energy*, **2021**; pp 37-54.
24. Pardo, P.; Deydier, A.; Anxionnaz-Minvielle, Z.; Rougé, S.; Cabassud, M.; Cognet, P., A Review on High Temperature Thermochemical Heat Energy Storage. *Renewable Sustainable Energy Rev.*, **2014**, *32*, 591-610.
25. Liu, M.; Tay, N. S.; Bell, S.; Belusko, M.; Jacob, R.; Will, G.; Saman, W.; Bruno, F., Review on Concentrating Solar Power Plants and New Developments in High-Temperature Thermal Energy Storage Technologies. *Renewable Sustainable Energy Rev.*, **2016**, *53*, 1411-1432.
26. US Department of Energy, D.O.E. Sunshot Vision Study. https://www.energy.gov/eere/solar/sunshot-initiative (accessed November **2021**).
27. Ho, C. K., A Review of High-Temperature Particle Receivers for Concentrating Solar Power. *Appl. Therm. Eng.*, **2016**, *109*, 958-969.
28. Valverde, J. M.; Barea-Lopez, M.; Perejon, A.; Sanchez-Jimenez, P. E.; Perez-Maqueda, L. A., Effect of Thermal Pretreatment and Nanosilica Addition on Limestone Performance

at Calcium-Looping Conditions for Thermochemical Energy Storage of Concentrated Solar Power. *Energy Fuels*, **2017**, *31*, 4226-4236.

29. Gil, A.; Medrano, M.; Martorell, I.; Lázaro, A.; Dolado, P.; Zalba, B.; Cabeza, L. F., State of the Art on High Temperature Thermal Energy Storage for Power Generation. Part 1—Concepts, Materials and Modellization. *Renewable Sustainable Energy rev.*, **2010**, *14*, 31-55.
30. Medrano, M.; Gil, A.; Martorell, I.; Potau, X.; Cabeza, L. F., State of the Art on High-Temperature Thermal Energy Storage for Power Generation. Part 2—Case Studies. *Renewable Sustainable Energy Rev.*, **2010**, *14*, 56-72.
31. Chen, X.; Zhang, Z.; Qi, C.; Ling, X.; Peng, H., State of the Art on the High-Temperature Thermochemical Energy Storage Systems. *Energy convers. manage.* **2018**, *177*, 792-815.
32. Harries, D. N.; Paskevicius, M.; Sheppard, D. A.; Price, T. E. C.; Buckley, C. E., Concentrating Solar Thermal Heat Storage Using Metal Hydrides. *Proc. IEEE* **2011**, *100*, 539-549.
33. Wentworth, W.; Chen, E., Simple Thermal Decomposition Reactions for Storage of Solar Thermal Energy. *Sol. Energy*, **1976**, *18*, 205-214.
34. Fellet, M.; Buckley, C. E.; Paskevicius, M.; Sheppard, D. A., Research on Metal Hydrides Revived for Next-Generation Solutions to Renewable Energy Storage. *MRS Bull.*, **2013**, *38*, 1012-1013.
35. Prasad, J. S.; Muthukumar, P.; Desai, F.; Basu, D. N.; Rahman, M. M., A Critical Review of High-Temperature Reversible Thermochemical Energy Storage Systems. *Applied Energy* **2019**, *254*, 113733.
36. Zalba, B.; Marın, J. M.; Cabeza, L. F.; Mehling, H., Review on Thermal Energy Storage with Phase Change: Materials, Heat Transfer Analysis and Applications. *Appl. Therm. Eng.*, **2003**, *23*, 251-283.
37. Zhang, H.; Baeyens, J.; Cáceres, G.; Degreve, J.; Lv, Y., Thermal Energy Storage: Recent Developments and Practical Aspects. *Prog. Energy Combust. Sci.*, **2016**, *53*, 1-40.
38. Libowitz, G. In Metal Hydrides for Thermal Energy Storage, *9th Intersociety Energy Conversion Engineering Conference*, **1974**; pp 322-325.
39. Haynes, W. M., *CRC Handbook of Chemistry and Physics*; CRC press, **2014**.
40. Møller, K. T.; Sheppard, D.; Ravnsbæk, D. B.; Buckley, C. E.; Akiba, E.; Li, H.-W.; Jensen, T. R., Complex Metal Hydrides for Hydrogen, Thermal and Electrochemical Energy Storage. *Energies* **2017**, *10*, 1645.

41. Sandrock, G.; Thomas, G., The Iea/Doe/Snl on-Line Hydride Databases. *Applied Physics A* **2001**, *72*, 153-155.
42. Johnson, J. R., Reaction of Hydrogen with the High Temperature (C14) Form of Ticr2. *Journal of the Less-Common Metals* **1980**, *73*, 345-354.
43. Manchester, F. D., Phase Diagrams of Binary Hydrogen Alloys. *ASM International, Member/Customer Service Center, Materials Park, OH 44073-0002, USA, 2000. 322* **2000**.
44. Rönnebro, E. C.; Whyatt, G.; Powell, M.; Westman, M.; Zheng, F. R.; Fang, Z. Z., Metal Hydrides for High-Temperature Power Generation. *Energies* **2015**, *8*, 8406-8430.
45. Buckley, C. E. High-Temperature Metal Hydrides for Concentrated Solar Thermal Energy Storage. https://lngfutures.edu.au/wp-content/uploads/2018/12/10-Buckley-Talk-for-UWA-Hydrogen-Workshop-Nov_29_2018-V1.pdf.
46. Sheppard, D.; Paskevicius, M.; Humphries, T.; Felderhoff, M.; Capurso, G.; von Colbe, J. B.; Dornheim, M.; Klassen, T.; Ward, P.; Teprovich, J., Metal Hydrides for Concentrating Solar Thermal Power Energy Storage. *Applied Physics A* **2016**, *122*, 395.
47. Ward, P. A.; Corgnale, C.; Teprovich, J. A.; Motyka, T.; Hardy, B.; Sheppard, D.; Buckley, C. E; Zidan, R., Technical Challenges and Future Directions for High-Efficiency Metal Hydride Thermal Energy Storage Systems. *Applied Physics A* **2016**, *122*, 462.
48. Sheppard, D.; Humphries, T.; Buckley, C. E, Sodium-Based Hydrides for Thermal Energy Applications. *Applied Physics A* **2016**, *122*, 406.
49. Sheppard, D. A.; Paskevicius, M.; Buckley, C. E., Thermodynamics of Hydrogen Desorption from Namgh3 and Its Application as a Solar Heat Storage Medium. *Chemistry of Materials* **2011**, *23*, 4298-4300.
50. Humphries, T. D.; Sheppard, D. A.; Rowles, M. R.; Sofianos, M. V.; Buckley, C. E, Fluoride Substitution in Sodium Hydride for Thermal Energy Storage Applications. *Journal of Materials Chemistry A* **2016**, *4*, 12170-12178.
51. Ward, P. A.; Corgnale, C.; Teprovich Jr, J. A.; Motyka, T.; Hardy, B.; Peters, B.; Zidan, R., High-Performance Metal Hydride Based Thermal Energy Storage Systems for Concentrating Solar Power Applications. *Journal of Alloys and Compounds* **2015**, *645*, S374-S378.
52. Peterson, D.; Nelson, S., Equilibrium Hydrogen Pressures in the Strontium-Hydrogen System. *Journal of the Less-Common Metals* **1980**, *72*, 251-256.
53. Wang, K.; Kong, X.; Du, J.; Li, C.; Li, Z.; Wu, Z., Thermodynamic Description of the Ti-H System. *Calphad* **2010**, *34*, 317-323.

54. Vajo, J. J.; Mertens, F.; Ahn, C. C.; Bowman Jr, R. C.; Fultz, B., Altering Hydrogen Storage Properties by Hydride Destabilization through Alloy Formation: LiH and MgH_2 Destabilised with Si. *J. Phys. Chem. B,* **2004**, *108*, 13977-13983.
55. Manickam, K.; Mistry, P.; Walker, G.; Grant, D.; Buckley, C. E.; Humphries, T. D.; Paskevicius, M.; Jensen, T.; Albert, R.; Peinecke, K., Future Perspectives of Thermal Energy Storage with Metal Hydrides. *Int. J. Hydrogen Energy,* **2019**, *44*, 7738-7745.
56. Nicholson, K. M.; Sholl, D. S., First-Principles Screening of Complex Transition Metal Hydrides for High-Temperature Applications. *Inorg. chem.*, **2014**, *53*, 11833-11848.
57. Corgnale, C.; Hardy, B.; Motyka, T.; Zidan, R.; Teprovich, J.; Peters, B., Screening Analysis of Metal Hydride Based Thermal Energy Storage Systems for Concentrating Solar Power Plants. *Renewable Sustainable Energy Rev.*, **2014**, *38*, 821-833.
58. Skolnik, E., Analysis of the Sodium Hydride-Based Hydrogen Storage System Being Developed by Powerball Technologies Llc, Energetics, Incorporated. *Proc. DOE,* **2000**.
59. Mueller, W. M.; Blackledge, J. P.; Libowitz, G. G., *Met. Hydrides*, **2013**.
60. Harries, D. N.; Paskevicius, M.; Sheppard, D. A.; Price, T. E. C.; Buckley, C. E., Concentrating Solar Thermal Heat Storage Using Metal Hydrides. *Proc. of the IEEE,* **2012**, *100*, 539-549.
61. Roine, A. *Hsc Ver.9.0.0* Https://Www.Outotec.Com/Products/Digital-Solutions/Hsc-Chemistry/.
62. Humphries, T. D.; Paskevicius, M.; Alamri, A.; Buckley, C. E., Thermodynamic Destabilisation of SrH_2 Using Al for the Next Generation of High-Temperature Thermal Batteries. *J. Alloys Compd.,* **2022**, *894*, 162404.
63. Sørby, M.; Brinks, H.; Fossdal, A.; Thorshaug, K.; Hauback, B., The Crystal Structure and Stability of K_2NaAlH_6. *J. Alloys Compd.,* **2006**, *415*, 284-287.
64. Chen, P.; Xiong, Z.; Luo, J.; Lin, J.; Tan, K. L., Interaction of Hydrogen with Metal Nitrides and Imides. *Nature,* **2002**, *420*, 302-304.
65. El Kharbachi, A.; Pinatel, E.; Nuta, I.; Baricco, M., A Thermodynamic Assessment of $LiBH_4$. *CALPHAD: Comput. Coupling Phase Diagrams Thermochem.* **2012**, *39*, 80-90.
66. Huang, B.; Yvon, K.; Fischer, P., Synthesis, Structure and Thermal Stability of $Yb_4Mg_4Fe_3H_{22}$. *J. Alloys Compd.,***1993**, *197*, 65-68.
67. Huang, B.; Yvon, K.; Fischer, P., New Quaternary Metal Hydrides with $CaMgNiH_4$-Type Structure. *J. Alloys Compd.,* **1994**, *204*, L5-L8.
68. Kuznetsov, V., Eleventh Conference on Energy Conversion and Research on Thermoelectronic Emission in the USA. *Springer*: 1977.

69. Felderhoff, M.; Urbanczyk, R.; Peil, S., Thermochemical Heat Storage for High-Temperature Applications-a Review. *Green* **2013**, *3*, 113-123.
70. Paskevicius, M.; Sheppard, D.; Williamson, K.; Buckley, C. E, Metal Hydride Thermal Heat Storage Prototype for Concentrating Solar Thermal Power. *Energy* **2015**, *88*, 469-477.
71. Bliesner, W. T., Reversible Hydride Thermal Energy Storage Cell Optimised for Solar Applications. US Patents: **2011**.
72. Emc Solar. EMC Solar Calcium Hydride Thermal Energy Storage System 2010. https://www.nextbigfuture.com/2010/01/emc-solar-claims-calcium-hydridehas. (accessed November **2021**).
73. Veleckis, E., Application of the Hydrogen Titration Method to a Thermodynamic Investigation of Solid Al-Ca Alloys. *J. Less-Common Met.*, **1981**, *80*, 241-255.
74. Griffond, A. C. M. Concentrating Solar Thermal Storage Using Metal Hydride: Study of Destabilised Calcium Hydrides. Curtin University, **2019**.
75. Ward, P. A.; Teprovich Jr, J. A.; Liu, Y.; He, J.; Zidan, R., High-Temperature Thermal Energy Storage in the Caal2 System. *J. Alloys Compd.* **2018**, *735*, 2611-2615.
76. Li, Y.; Li, P.; Qu, X., Investigation on Libh 4-Cah 2 Composite and Its Potential for Thermal Energy Storage. *Sci. Rep.* **2017**, *7*, 41754.
77. Griffond, A. C.; Sofianos, M. V.; Sheppard, D. A.; Humphries, T. D.; Sargent, A.-L.; Dornheim, M.; Aguey-Zinsou, K.-F.; Buckley, C. E., High-Temperature Thermochemical Energy Storage Using Metal Hydrides: Destabilisation of Calcium Hydride with Silicon. *J. Alloys Compd.* **2021**, *858*, 158229.

Chapter 2

Experimental methods

2.1 Introduction

All the experiments with hydrogen were conducted in the Hydrogen lab of the Hydrogen Storage Research Group (HSRG) within the Discipline of Physics and Astronomy at Curtin University. The research required high-temperature conditions high-pressure hydrogen gas pressure, and the laboratory is equipped with all the required equipment and safety systems for hydrogen research. All materials required risk assessments and safety data sheets (SDS) before any research was undertaken. The laboratory is equipped with two glove boxes filled with inert Argon gas, which enables the manipulation of air-sensitive materials. It also contains eight Sievert's gas rigs, four manual and four computer-controlled rigs, several programmable high-temperature furnaces, temperature-programmed mass spectrometer (TPD - MS), Differential Scanning Calorimetry (DSC) instrument and a suite of ball mills, including a planetary ball milling machine, shaker mill and high-pressure ball mill. In this chapter, all the research methods (theoretical and experimental) used during this study are discussed in detail.

The material investigation used during the research can be divided into two parts:

1. Theoretical thermodynamic predictions
2. Experimental techniques

2.2 Theoretical thermodynamic predictions

This thesis focussed on the destabilisation of the HTMH, CaH_2, to convert into an effective TES (working between 600 °C - 800 °C) for next-generation CSP plants. The selection of suitable additives for this purpose was challenging, and therefore, some theoretical predictions were required before practical synthesis and characterisation. The theoretical calculations were performed using HSC Chemistry software.[1] The standard thermodynamic data of the pure elements were taken from the database of Scientific Thermodata Europe (SGTE) by Dinsdale *et.al.*[2] HSC Chemistry software, as the name suggests H - enthalpy, S - entropy and C - heat capacity, provides whether the proposed reaction is thermodynamically favourable or not.[1] It calculates thermodynamic properties of materials such as enthalpy, entropy, Gibb's free energy and heat capacity without considering the reaction kinetics. Moreover, the software aids to identify the thermodynamically favourable reactions between two materials, the pathway of the reaction, reaction products and the temperature at which the reaction occurs. An example of the thermodynamic graphical simulation of pure CaH_2 at 1bar of pressure using HSC Chemistry software is given in Figure 2.1.

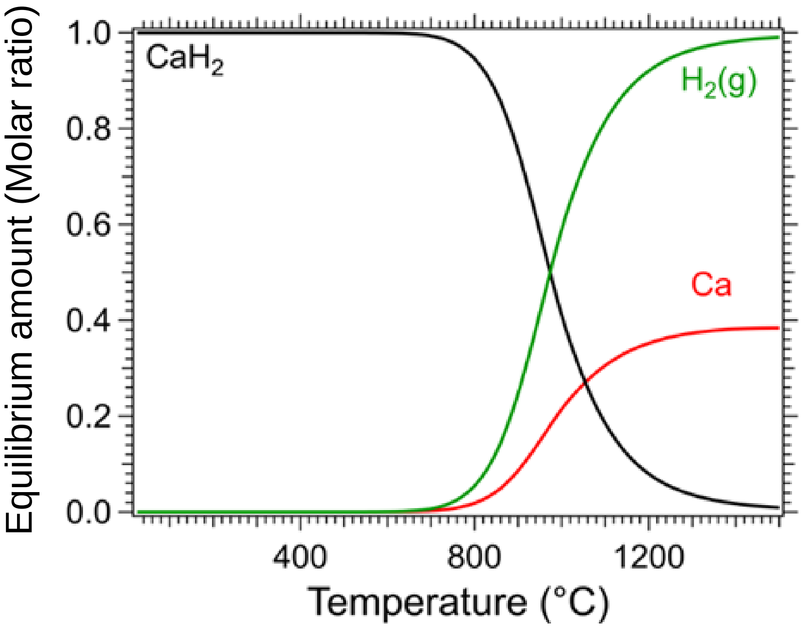

Figure 2.1 Graphical simulation of pure CaH_2 at 1bar of pressure.

2.2.1 Background of *H*, *S* and *G*

Enthalpy (*H*): The thermodynamic quantity defines the total heat energy of a system. It is equal to the sum of the internal energy of the system and the product of its pressure and volume. The sign of the change in enthalpy in a reaction explains whether the reaction is endothermic or exothermic. The absolute value of enthalpy cannot be measured, but the enthalpy difference between two temperatures can be measured using a calorimeter. For the convenience of enthalpy calculations at a higher temperature, it is chosen that the enthalpy of pure elements is zero at its most stable state (reference state) at 25 °C and 1 bar. The heat capacity at constant pressure can be calculated from enthalpy at a temperature T as shown in equation 2-1, and that allows the calculation of enthalpy at any temperature as expressed in equation 2-2.

$$C_p = \left(\frac{\mathrm{d}H}{\mathrm{d}T}\right)_{P,n} \qquad 2\text{-}1$$

$$H(T) = H_f(298.15) + \int_{298.15}^{T} C_P\,\mathrm{d}T + \sum H_{tr} \qquad 2\text{-}2$$

Where $H_f(298.15)$ is the enthalpy of formation at 298.15 K, n is the number of moles and H_{tr} is the enthalpy of transformation that includes the energy absorbed/released during phase transformations.

Entropy (S): Is a measure of the molecular disorder of a system or the system's thermal energy per unit temperature. Entropy has three sources: configurational, electronic, and vibrational, which increases with increasing temperature. Vibrational (or calorimetric) entropy can be calculated from the heat capacity as given in equation 2-3

$$S(T) = S\,(298.15) + \int_{298.15}^{T} \frac{C_P}{T}\,\mathrm{d}T + \sum \frac{H_{tr}}{T_{tr}} \tag{2-3}$$

Where $S\,(298.15) = \int_{0}^{289.15} \frac{C_P}{T}\,\mathrm{d}T$ and H_{tr} is the enthalpy of phase transformation at a temperature T_{tr}.

Heat Capacity (C_P): The amount of heat required to raise the temperature of one unit of material by 1 kelvin. The absolute heat capacity can be calculated using equation 2-1. The heat capacity at higher temperatures cannot be predicted using theoretical thermodynamics. It requires an entirely mathematical model/fitting to fit experimental heat capacities. For instance

$$C_p = A + B\,10^{-3}\,T + C\,10^{-5}\,T^{-2} + D\,10^{-6}\,T^{2} \tag{2-4}$$

Where A, B, C and D are coefficients estimated from experiments.

Gibb's Free energy (G): Gibb's free energy value determines whether a reaction is spontaneous or not. The higher the negative value of Gibb's free energy, the more spontaneous reaction at that temperature will be. The general relation between G, H and S at a temperature T can be written as shown in 2-5:

$$G = H - T\,S \tag{2-5}$$

G can be expressed in terms of temperature as a power series in the form as given in equation 2-6:

$$G = a + b\,T + c\,T\ln(T) + \sum \mathrm{d}T^{\mathrm{n}} \tag{2-6}$$

Where a, b, c, and d are coefficients and n represent a set of integers.

And S, H and Cp can be calculated using equations 2-7, 2-8 and 2-9, respectively.

$$S = -\frac{dG}{dT} = -\,b - c - c\,\ln(T) - \sum n\mathrm{d}T^{n-1} \tag{2-7}$$

$$H = G + T.\,S = a - c\,T - \sum(n-1)\mathrm{d}T^{n} \tag{2-8}$$

$$Cp = -T\,\left(\frac{d^2G}{\mathrm{d}T}\right) = -\,c - \sum n(n-1)\mathrm{d}T^{n-1} \tag{2-9}$$

In some cases, additional contributions from pressure or magnetism can be added to the Gibbs free energy. The pressure contribution for condensed phases can be expressed as shown in 2-10, where A is the constant for a particular element and phase and P is the pressure.

$G_{pres} = A.P\ (a_0\ T + a_1 \frac{T^2}{2} + a_2\ \frac{T^3}{2} + a_3\ T^{-1})$ 2-10

Gibb's free energy of compounds is a function of the Gibbs free energy of formation and a fraction of the Gibbs free energy for each element. For instance, the Gibbs free energy of the compound $CaZn_{11}$ can be calculated using equation 2-11:

$^0G_{CaZn_{11}} = \Delta G_{f\ CaZn_{11}} + G_{Ca}^{bcc} + 11G_{Zn}^{hcp}$ 2-11

Where $\Delta G_{f\ CaZn_{11}} = a + b\ T$, where a and b are constants calculated using mathematical/ computational models.

The G_{Ca}^{bcc} and $11G_{Zn}^{hcp}$ were taken from the review article published by Dinsdale *et.al.*[2] review and they take the form as shown below:

The G for Ca- bcc in the different temperature range in $J.mol^{-1}$ is:

- (298.15 K < T < 716 K)

$-7020.852 + 142.970155\ T - 28.2541\ T \ln(T) + 7.2326 \times 10^{-3}\ T^2 - 4.500217 \times 10^{-6}\ T^3 + 60578\ T^{-1}$ 2-12

- (716 K < T < 1115 K)

$1640.475 + 1.999694\ T - 6.276\ T \ln(T) - 16.1921 \times 10^{-3}\ T^2 - 523000\ T^{-1}$ 2-13

- (1115 K < T < 3000 K)

$-142331.096 + 1023.549046\ T - 143.8726979\ T \ln(T) + 32.543127 \times 10^{-3}\ T^2 - 1.704079 \times 10^{-6}\ T^3 + 25353771.\ T^{-1}$ 2-14

The G for Zn - hcp in the different temperature range in $J.mol^{-1}$ is:

- (298.15 K < T < 1234.93 K)

$-6809.512 + 118.502013\ T - 23.8463314\ T \ln(T) - 1.790585 \times 10^{-3}\ T^2 - 0.398587 \times 10^{-6}\ T^3 - 12011\ T^{-1}$ 2-15

- (1234.93 K < T < 3000 K)

$-14695.252 + 190.566404\ T - 33.472\ T \ln(T) + 1411.773 \times 10^{26}\ T^{-9}$ 2-16

The models and the data for the pure elements/compounds changes according to the state and phase (solid, liquid, α, β,Y phases) of the elements.

2.3 Experimental techniques and general procedures

2.3.1 Sample preparation

Metal hydrides are air sensitive materials; therefore, all the chemical storage and handling were conducted inside the argon-filled glovebox (Unilab Glovebox, MBraun, Germany) to reduce the contamination with moisture and oxygen. The H_2O/O_2 levels inside the glovebox were maintained below one ppm using an automatic argon gas purifier that constantly removes oxygen and water. Table 2.1 lists all the materials used during this research and purchased details with purity.

Table 2.1 List of chemicals used in the project.

Chemicals	State	Purchased from	Purity (%)
CaH_2	Granules	Sigma Aldrich	> 95
Al_2O_3	Powder	Sigma Aldrich	> 98
Zn	Powder	Chem supply	> 98
C (graphite)	Powder	Sigma Aldrich	≤ 100
ZnO	Powder	Sigma Aldrich	99
Fe_2O_3	Powder	Aldrich	≤ 100
SiO_2	Powder, <10-20 nm	Aldrich	99.5
ZrO_2	Powder, < 100 nm	Aldrich	99
MnO	Powder	Chem Supply	> 94
TiO_2	Powder	Aldrich	99
CuO	Powder	Aldrich	99
NiO	Powder	Sigma Aldrich	99.9
Y_2O_3	Powder	Aldrich	99.9
CeO_2	Powder, < 25nm	Aldrich	99
H_2	Gas	Core gas	99.999
Ar	Gas	Core gas	99.997

2.3.1.1 Ball milling

All the materials were synthesised under an argon atmosphere at room temperature using an Across International planetary ball mill (PQ-N04). The ball milling canisters (100 ml) and the balls were made from 316 stainless steel and sealed by an O-ring. The powder mixture was placed inside the canister along with balls in a fixed powder to ball ratio. The majority of materials were synthesised in 40:1 ball (equal number of 10 mm and 6 mm diameter balls) to powder ratio and milled for 3 h. An example of a typical program is bi-directional mode programming by rotation with/without pause. The samples were ball milled for varying hours (depending on each sample) at a rotational speed of 400 rpm, and the direction of the vial was altered every 30 minutes. Figure 2.2 shows a picture of the PQ-N04 planetary ball mill, canister and balls used for the synthesis.

Figure 2.2 Picture of PQ-N04 planetary ball mill, canister and balls used for the synthesis.[3]

2.3.2 X-ray powder diffraction studies

The initial sample characterisation to identify the crystalline phases was performed using *ex-situ* diffraction studies and quantified using the Rietveld method in the TOPAS software package. The X-ray diffraction (XRD) laboratory is equipped with two different diffractometers. The Bruker D8 Advance diffractometer that uses a Cu K_α wavelength radiation (λ = 1.5418 Å, 40 kV, 40 mA) and the Bruker D8 Advance diffractometer with a Co K_α radiation (λ = 1.789 Å, 35 kV, 30 mA).

The basic use of X-ray diffraction is to identify the crystalline peaks and phases in the samples. An X-ray diffractometer mainly consists of three parts: X-ray source, sample holder, and detector, as shown in Figure 2.3. The X-ray source provides X-ray radiation that hits the powder samples, with the atoms in the sample scattering the X-ray beams in a specific direction. The detector receives the scattered waves with a relative phase shift and measures the intensity related to an angle of incidence. The obtained diffraction pattern represents a sample diffraction intensity as a function of the angle between the beam source and detector, denoted as 2θ. Bragg's law (2-17) details the relationship between the distances between atomic layers in the crystal structure d_{hkl}, wavelength and the angle of incidence between the incident ray and scattering planes.[4-5]

$n\lambda = 2\ d_{hkl}$ Sin θ 2-17

Where n is an integer, λ is the wavelength of the incident X-ray beam, d_{hkl} is the distance between atomic layers, 2θ is the angle of incidence between the incident ray and scattering planes. h, k and l, known as Miller indices, represent the lattice planes and determine the peak positions on the diffraction pattern. Every crystal possesses a unique set of Bragg peaks that appear at specific positions and can be identified through XRD. By preliminary qualitative analysis, the different phases in the sample are identified. Then, with the Rietveld refinement method (section 2.3.2.2), quantitative analysis of each phase's proportion and crystal properties can be determined by fitting the profile intensity of the measured data against database references phases using the least-squares method.[6-7]

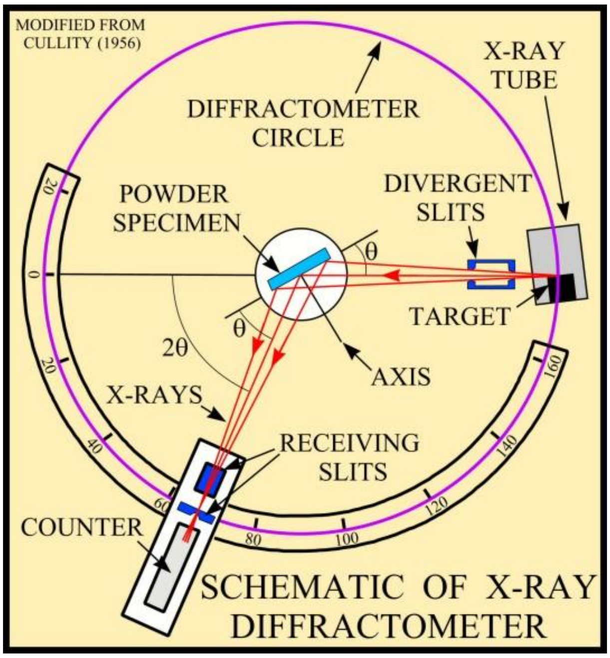

Figure 2.3 The schematic diagram of an X-ray diffractometer.[5, 8]

The samples were loaded and sealed into the XRD sample holders with a bubble cap (Bruker polymethyl methacrylate, PMMA) inside the glove box, as seen in Figure 2.4(a), to avoid oxygen/moisture contamination during data collection. The bubble cap always results in a broad hump centred at 2θ ° in the XRD pattern, as shown in Figure 2.4(b). The Bragg Brentano Bruker D8 Advance X-ray diffractometer was used to perform the XRD experiments of all the samples in this thesis, except samples containing iron, within a 2θ range of 10 - 80° using 0.02°

steps with 0.9 s of count time per steps. A Cu K_α tube produces the unpolarised radiation beam that targets the sample. A linear PSD (Lynx Eye) detector acquires the scattered rays. A Bragg Brentano Bruker, Advanced X-ray diffractometer with Co K_α radiation, was also used to determine the samples' XRD patterns containing fluorescent materials (iron-containing samples). Table 2.2 shows the instrumental parameters of the two XRD instruments and *in-situ* XRD instruments.

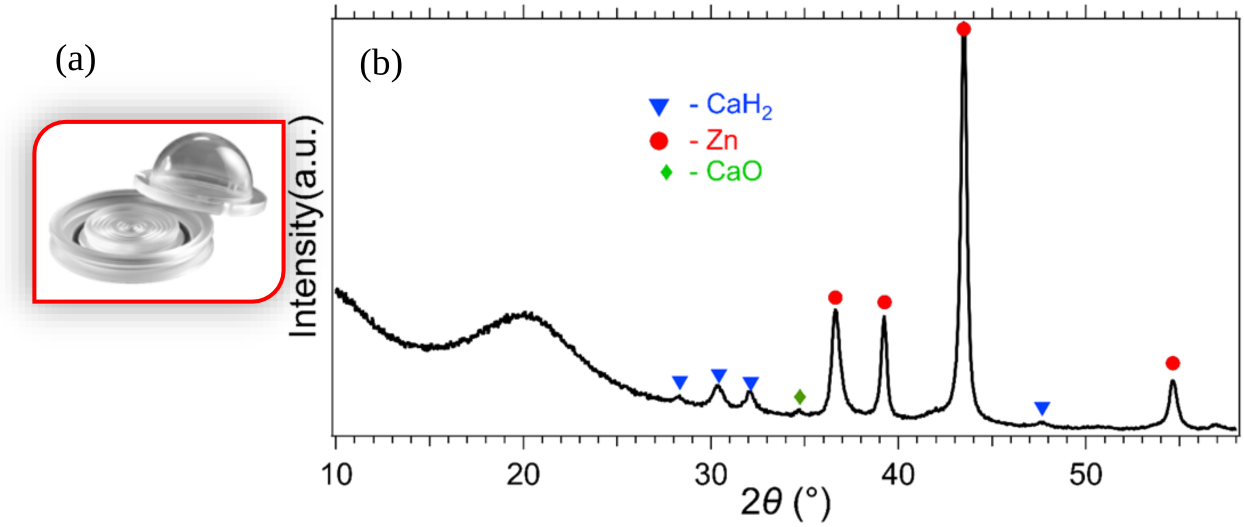

Figure 2.4 (a) Image of XRD sample bubble holder and (b) example of XRD pattern using this for CaH_2- 3Zn system after ball milling.[18]

Table 2.2 X-ray diffraction (XRD) instrumental parameters.

Parameter	D8 Advance XRD	D8 Discover XRD	Thermo Fisher ARL Equinox 5000 *in-situ* diffractometer
Radiation wavelength (Å)	Cu (1.5418)	Co (1.789)	Mo (0.7093)
Operating Voltage (kV)	40	35	50
Operating current (mA)	40	30	30
Detector	Linear PSD (2.94°- 2θ)	Linear PSD (3.4° - 2θ)	CPS - 120, 120° curved detector, 8192 channels
Filter	Ni	Fe	-

Lorentz- Polarisation factor	0	0	0
Goniometer radii	250	217	250
Source length (mm)	12	12	12
Sample length (mm)	25	25	5
Fixed divergence slit angle	0.3	0.3	Parallel mirror, Beam height 0.7 mm
Primary soller slit angle (°)	2.5	2.5	-
Secondary Soller slit angle (°)	2.5	2.5	-

The crystalline peaks obtained from the powder diffraction were identified by comparing them with standard patterns. The two primary databases used for this matching process are the International Centre for Diffraction Data (ICDD) - Powder Diffraction File Database (PDF4+) and Crystallography Open Database (COD). The computer software package called Bruker DIFFRAC EVA 3.0 is used to gain access to these databases. EVA has both automated and manual search-match options. The manual options use filters and ranges to reduce the number of matches and quickly select the correct choice.

2.3.2.1 Quantitative phase analysis using Rietveld refinement method

Quantitative analysis of all samples' X-ray diffraction patterns was performed by me with TOPAS V-5 (Bruker AXS) software using the Rietveld refinement method. The Rietveld method is a refinement technique that uses the non-linear least-squares method to fit a model to the entire XRD profile. Figure 2.5 shows an example refinement using the Rietveld method for the ball-milled CaH_2-2C system. The cif or structure files for each compound or element present in the sample were downloaded from ICCD/PDF4 and used for the fit. The blue line in Figure 2.5 shows the original XRD pattern obtained. The red line and the grey line in Figure 2.5 show the calculated fit model and difference plot. The short vertical lines (blue and red) indicate the compounds' Bragg reflections (CaH_2 and C). The software determines the intrinsic parameters of the phases present in the sample, such as wt% of each compound, crystal size, the lattice parameters, preferred orientation, densities, errors etc. A good fit will have a relative error of < 2 wt%.

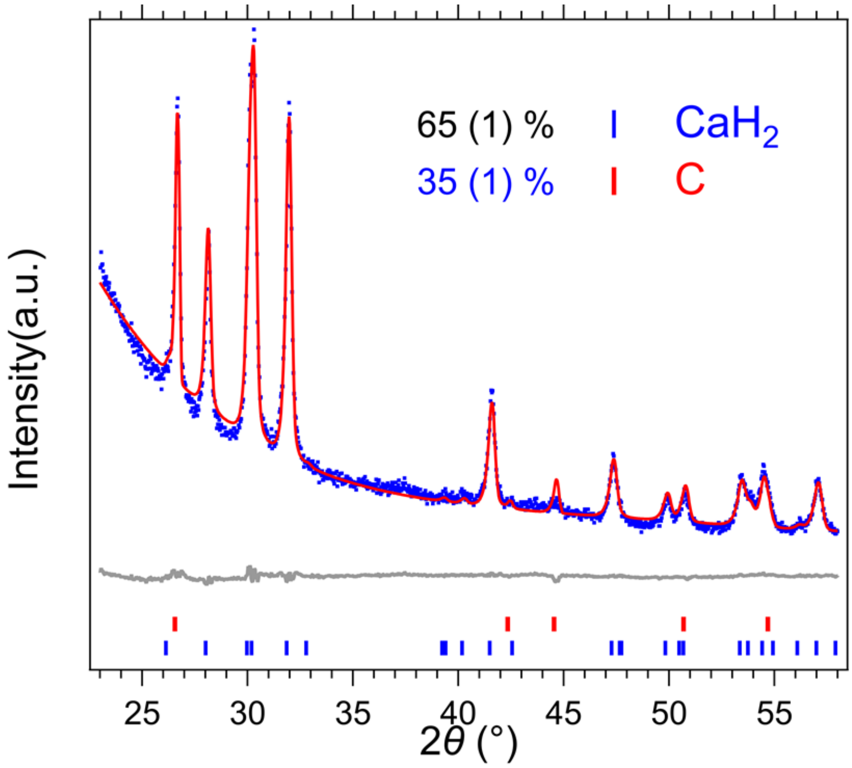

Figure 2.5 Rietveld refinement of the diffraction pattern for CaH_2-2C system, blue line - raw data, red line - fitted data, grey line - difference plot (Cu K_α, λ = 1.5418 Å).

2.3.2.2 *In-situ* X-ray diffraction

An *in-situ* X-ray diffraction experiment was carried out on samples using a Thermo Fisher ARL Equinox 5000 diffractometer. It is helpful to determine the reaction paths, which also allows one to see phase transition at each temperature. The parameters are given in Table 2.2. The X-ray source was molybdenum radiation with a wavelength of 0.7093 Å. The powder samples were loaded inside a quartz capillary tube (0.7 mm outer diameter, 0.01 mm wall thickness), sealed under argon atmosphere, and mounted onto a goniometer head. The samples were heated using a hot air blower at a heating rate range of 2 - 5 °C/min. Data were collected for 60 s exposures while heating. The maximum temperature was limited to 750 °C. The temperature of the hot air blower was calibrated against the known thermal expansion coefficient of both NaCl and Ag. The NaCl and Ag mixture was loaded into the quartz tube heated using the same conditions as the samples. The calibration was repeated every time when the initial setup and conditions were changed.

2.3.3 Differential scanning calorimetry (DSC) analysis

2.3.3.1 Basic theory and experimental set-up

Differential scanning Calorimetry (DSC) initially measures the material's heat capacity by monitoring the heat flow required to raise a sample temperature at a constant rate. It is typically used to investigate the physical transformations such as glass transitions, melting etc. The DSC peaks help to identify whether the reaction is endothermic or exothermic, the compound's polymorphic nature, and thermo kinetics.

The HSRG has a simultaneous thermal analyser NETZSCH STA 449 F3 Jupiter®, equipped with a Platinum furnace to measure the mass changes and thermal events from room temperature to 1300°C. The sample crucibles available for use on the DSC in the lab are Al_2O_3, Al or Pt pans. The choice of pan depends on material compatibility and the maximum temperature used. The operating temperature of the Al pans is limited to 600 °C, and the alumina pans are capable of high temperatures up to 1700 °C. The thermal conductivity and mass of the crucible can affect the DSC peak shape; for instance, Al_2O_3 crucibles can have right-shifted peaks compared to a more thermally conductive and lighter material such as in Al crucibles. In this study, the samples were loaded into the Al_2O_3 crucible inside the glovebox and sealed with lids having a pin-hole to allow gas release. The mass of the samples was between 5 - 20 mg. However, the mass of the sample used can be varied depending on the purpose, as shown in Table 2.3.

Table 2.3 Recommended sample mass for different thermal effects.

Thermal effect	**Sample mass**
Glass transition	10 to 20 mg
Melting/Crystallisation	1 to 5 (10) mg
Chemical reactions	10 to 20 mg
Specific heat	20 to 40 mg
STA/DSC high temp. Metals, glasses, ceramics	Approx. 50 mg

The loaded samples were placed on the sample carrier near the reference crucible made of the same material. The sample environment was then closed and then evacuated and filled with Ar. The analysis can be carried out under heating rates 2, 5, 10, 20 and 25 °C/min by heating from 40 °C to 1000 °C. The temperature and sensitivity calibrations were carried out using In, Zn, Al, Ag and Au reference materials for each heating rate and Ar flow rate to ensure the accuracy of the data. This provides a temperature accuracy of ± 0.2 °C, while the balance has an accuracy of ± 20 μg. Before entering the DSC, the Ar (40 mL/min) was passed through a Zr filter to reduce impurities in the gas stream. The Zr filter was preheated to 200 °C and connected externally to the DSC instrument. The metallic Zirconium (Zr) has a great affinity for oxygen, and by heating, it can easily absorb oxygen from the atmosphere.[9-10] The DSC instrument set up and Ar gas purification unit (Zr filter) is shown in Figure 2.6. The acquired data, temperature, or time vs DSC signal, from the DSC system is analysed using the software NETZSCH Proteus thermal analysis V. 8.0.

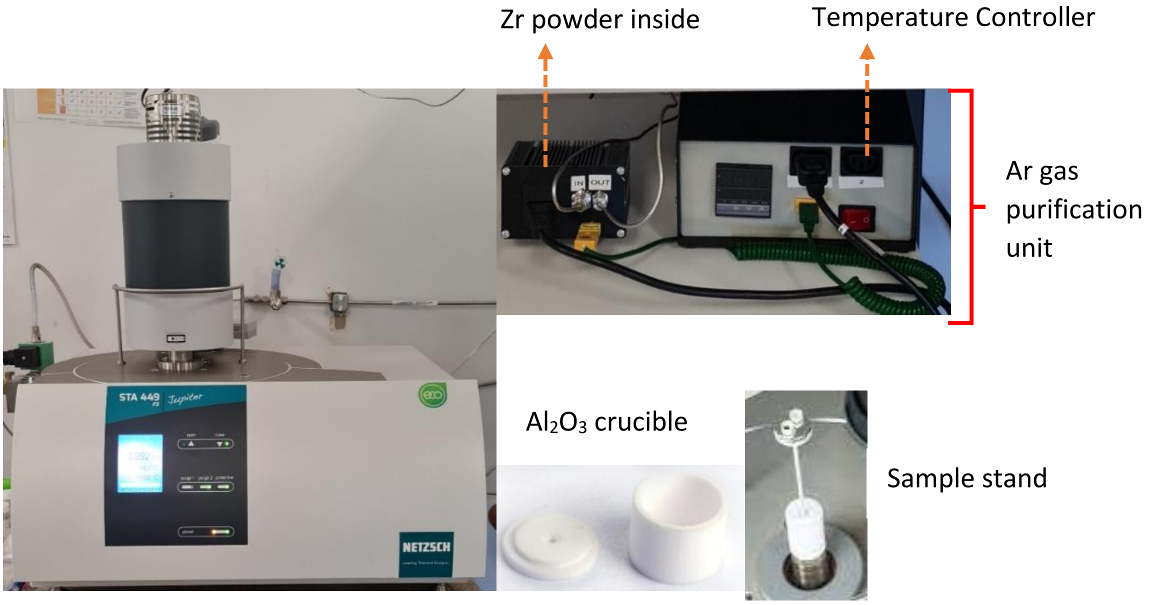

Figure 2.6 Differential scanning calorimetry instrument with Ar purification unit, Al_2O_3 crucible and the sample carrier.

2.3.3.2 Activation energy - The Kissinger method

When a reaction takes place inside a DSC instrument, the change in heat flow or thermal properties of the sample is shown by a deflection or peak. If the reaction occurs at a rate of temperature, it possesses activation energy (E_a), the minimum energy required for a reaction to proceed. Generally, Gibb's energy state of a reaction is always at a higher level for reactants than products; as shown in Figure 2.7.[11] The activation energy will always have a positive value independent of whether the reaction is endo or exothermic. The Kissinger method is the most popular method used to determine the kinetics from DSC measurements and is applicable to very small sample sizes.[12-13] The reactions of the type; solid converting into solid and gas, can be described by the equation:

$$\frac{dx}{dt} = A.\,(1-x)^r.\,e^{\frac{-E_a}{RT}} \qquad 2\text{-}18$$

Where $\frac{dx}{dt}$ = rate of the reaction

x = the reacted fraction

A = constant

r = the empirical order of reaction

E_a = activation energy (kJ.mol^{-1})

T = temperature in K

R = the gas constant (kJ.mol^{-1}.K^{-1})

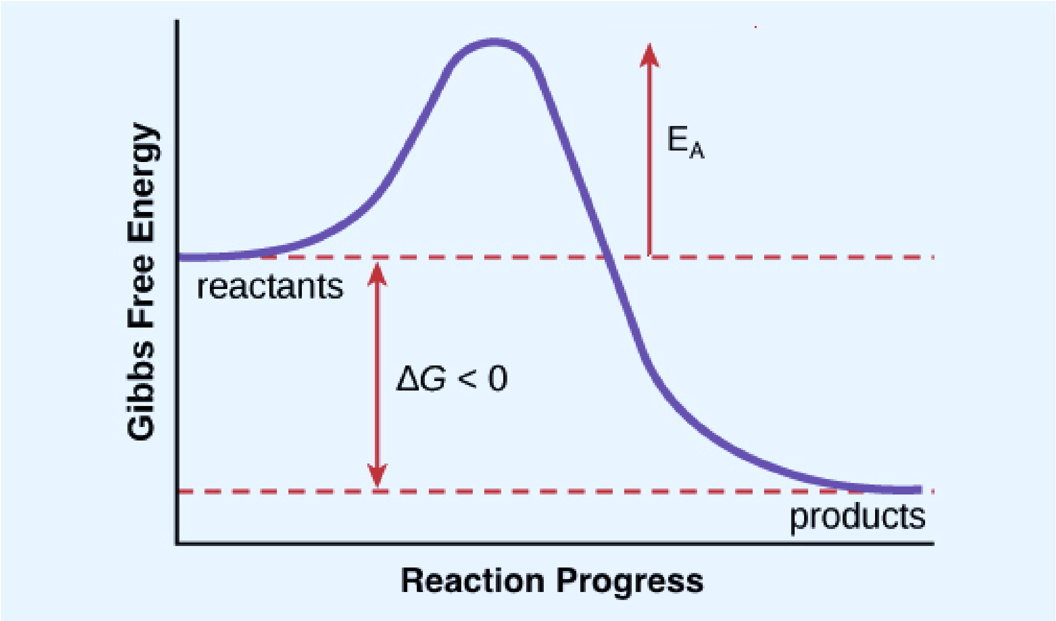

Figure 2.7 Illustration of activation energy for a forward reaction.[11]

Generally, the 'r' in the equation 2-18 varies from 0 to 1, and the effect of the order of the reaction on DSC curves can be illustrated as shown in Figure 2.8.[13]

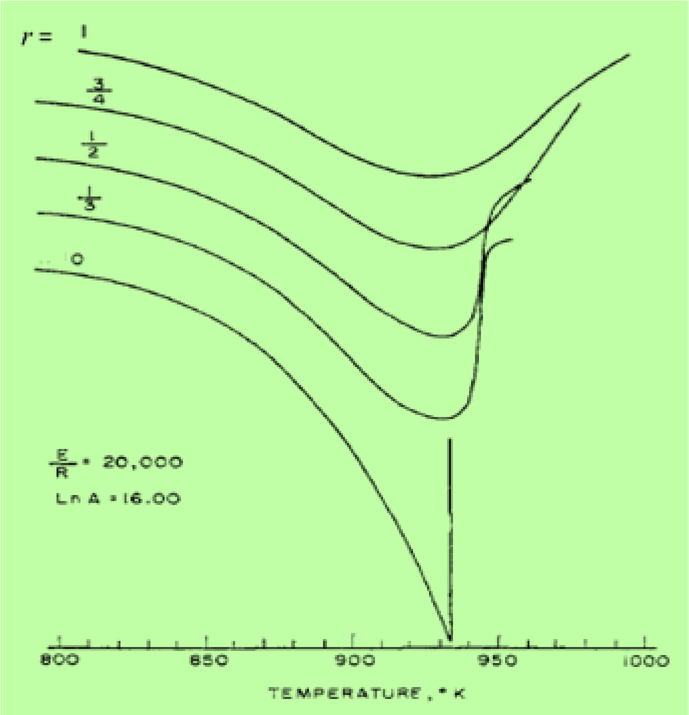

Figure 2.8 Effect of order of the reaction on the shape of the DSC curves.[13]

The temperature rises at a constant rate $\beta = \frac{dT}{dt}$, then differentiation of equation 2-18 gives:

$$\frac{d}{dt}\left(\frac{dx}{dt}\right) = \frac{dx}{dt}\left(\frac{E_a\beta}{T^2} - A\,r\,(1-x)^{r-1}\ e^{\frac{-E_a}{RT}}\right) \qquad 2\text{-}19$$

The maximum rate at a peak temperature, T_m, is $\frac{d}{dt}(\frac{dx}{dt}) = 0$, then equation 2-19 becomes,

$$\frac{E_a\beta}{RT_m{}^2} = A\,r\,(1-x)_m{}^{r-1}\ e^{\frac{-E_a}{RT_m}} \qquad 2\text{-}20$$

The product $r\ (1-x)_m{}^{r-1}$ is independent of β and is nearly equal to one. Substituting and taking logarithmic on equation 2-20:

$$\ln\left(\frac{\beta}{T_m{}^2}\right) = \ln\left(\frac{AR}{E_a}\right) - \frac{E_a}{RT_m} \qquad 2\text{-}21$$

The equation 2-21 is known as the Kissinger equation regardless of reaction order. The Kissinger plot is made by plotting $\ln(\frac{\beta}{T_m{}^2})$ vs $\frac{1}{T_m}$ and taking the line of best fit for the data. The slope of the line equals $-\frac{E_a}{R}$ and the intercept gives $\ln(\frac{AR}{E_a})$ and hence E_a, the activation energy, can be determined.

2.3.4 Temperature programmed mass spectrometry (TPD-MS)

Temperature Programmed desorption mass spectrometry (TPD-MS) was undertaken using a Stanford Research Systems (SRS) residual gas analyser (RGA-300) to detect the gases released from the samples as a function of temperature. The SRS RGA is a mass spectrometer comprising a quadrupole probe, and an Electronics Control Unit (ECU), which mounts directly on the probe's flange and contains all the electronics necessary to operate the instrument (Figure 2.9). The principle of operation is the same for all RGA instruments: a small fraction of the gas molecules are ionised (positive ions), and the resulting ions are separated, detected, and measured according to their molecular masses. RGA's are widely used to identify the different molecules present in a residual gas environment. They can be used to determine the concentrations or absolute partial pressures of the components of a gas mixture.

Less than 5 mg sample was placed in a stainless-steel sample holder inside a silicon carbide reactor that was connected to the RGA mass spectrometer. The corresponding analogue scan (partial pressure vs mass to charge ratio) was acquired and saved using the RGA software. In this thesis, the samples were heated from room temperature to a maximum temperature of 900 °C, with a ramp rate of 5 °C/min. Temperature data were collected using a K-type thermocouple connected internally to the silicon carbide reactor.

Figure 2.9 Temperature programmed mass spectrometer - RGA300 instrument and probe.

2.3.5 Scanning electron microscopy

A scanning electron microscope (SEM) uses an energetic and highly focussed electron beam over a sample surface, and signals from each point of the sample are used to create an image. The morphological analysis of the samples in this thesis was studied by field emission scanning electron microscopy (FE-SEM) using a Neon 40EsB (Zesis, Germany) and Tescan Mira3. These are integrated with electron backscattered diffraction/energy-dispersive X-ray spectroscopy (EBSD/EDS) oxford instrument detectors controlled by the Aztec software at Curtin University using secondary and backscattered electron detectors. The specimens were prepared by placing a small amount of the sample powder onto carbon tape mounted on an aluminium stub (without coating) inside the argon-filled glovebox. To reduce exposure to air, the samples were transferred to the vacuum chamber of the SEM using a custom-made holder. SEM secondary electron (SE) images were collected at an accelerating voltage of 5 kV, an aperture size of 30 µm, and a working distance of ≈ 10 mm. In comparison, backscattered electron (BSE) images were collected at an accelerating voltage of 10 kV, an aperture size of 60 µm, and a working distance of ≈ 7.5 mm.

2.3.5.1 Energy-dispersive X-ray spectroscopy (EDS)

Energy-dispersive X-ray spectroscopy is an analytical technique used for the elemental analysis or chemical characterisation. It allows qualitative and quantitative chemical composition analysis, and the EDS spectra of each sample were acquired along with SEM (Neon 40EsB, Zesis, Germany) and processed using Aztec software. The SEM images were edited using the software program ImageJ.

2.3.6 Sieverts apparatus

The investigation to find energy storage properties can be broken down into three basic categories: material development, fundamental science, and engineering development/storage system-level performance measurements. As this research aims to find a suitable TES for CSP application, the measurements are done for the material developments. There are mainly two types of equipment that can be used to determine a sample's hydrogen absorption/desorption: (1) The thermogravimetric apparatus: where the sample mass loss is measured. (2) The volumetric apparatus (also called manometric and Sievert’s): where the hydrogen pressure changes, due to hydrogen sorption in the reactor, against a known volume at measured temperature and pressure and the number of moles of hydrogen present can be measured.

This study investigated hydrogen sorption measurements using a custom-made volumetric apparatus (Sieverts) in the Hydrogen Storage Research Group (HSRG) laboratory at Curtin University. Three custom-made apparatus have been previously built within the group, but during my studies, I was part of a team that built an apparatus aptly named ‘Pink panther’. Figure 2.10 shows a complete picture of the Sieverts apparatus that we built. The rig can be divided into main two parts. 1. Volumetric section 2. Electronic unit. The first section consists of several volumes separated by valves and connected to a hydrogen gas cylinder, a pressure gauge, and the thermocouples. The electronic unit controls all the automatic valves, pneumatic valve island, power supply to the entire unit, a universal relay module, thermocouple signal conditioner, RTD signal conditioner, the voltage to temperature converter etc.

The volumetric section of the rig (Figure 2.10) consists of 6 valves. The function of each valve is listed below:

Valve 1 - the reference volume, which is directly connected to the hydrogen cylinder

Valve 2 - hydrogen pressure is exposed to all other parts via valve 2

Valve 3 - connected on the sample side

Valve 4 - to drop the pressure to atmospheric value

Valve 5 - connected to the vacuum

Valve 6 - calibration volume

All the valves, connectors and tube fittings are made from 316 stainless steel purchased from Swagelok. The interconnections made airtight using Swagelok VCR gasket fittings and tube connections.

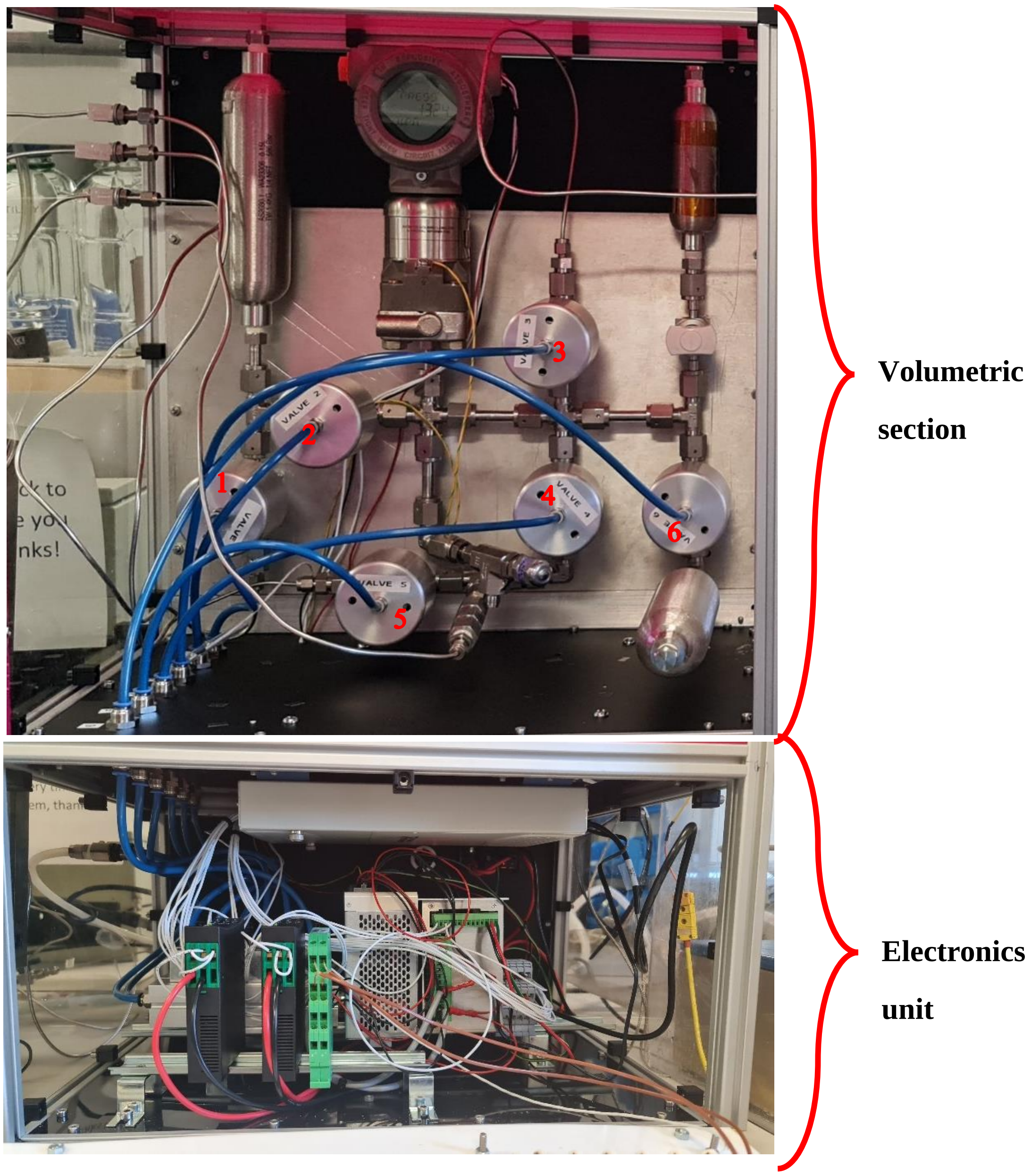

Figure 2.10 The picture of the custom-built Sievert's apparatus; the valves are numbered 1 to 6 in red.

Samples were loaded inside the SiC sample cell reactor using a stainless-steel sample holder (insert in Figure 2.11) that was connected to valve 3 using an external manual valve with Swagelok tubing. Silicon carbide (α-SiC) tubes, sealed at one end, with a length of 450 mm, an outer diameter of ≈ 16.2 mm, a wall thickness of ≈ 2.9 mm and an inner diameter of ≈ 10.4 mm were manufactured by Saint-Gobain, France. The SiC tubes were connected to Swagelok fittings using Teflon ferrules, as shown in Figure 2.11. The heat sink was used to protect the Teflon ferrules from melting at elevated temperatures. The H_2 permeation through these tubes is negligible at high temperatures but limited in pressure (< 25 bar) due to the brittleness of the ceramic SiC.[14-16] The data was collected using Labview software (National Instruments, USA). The software provides live pressure, temperature readings, automated volume calibrations, and automatic hydrogen sorption studies.

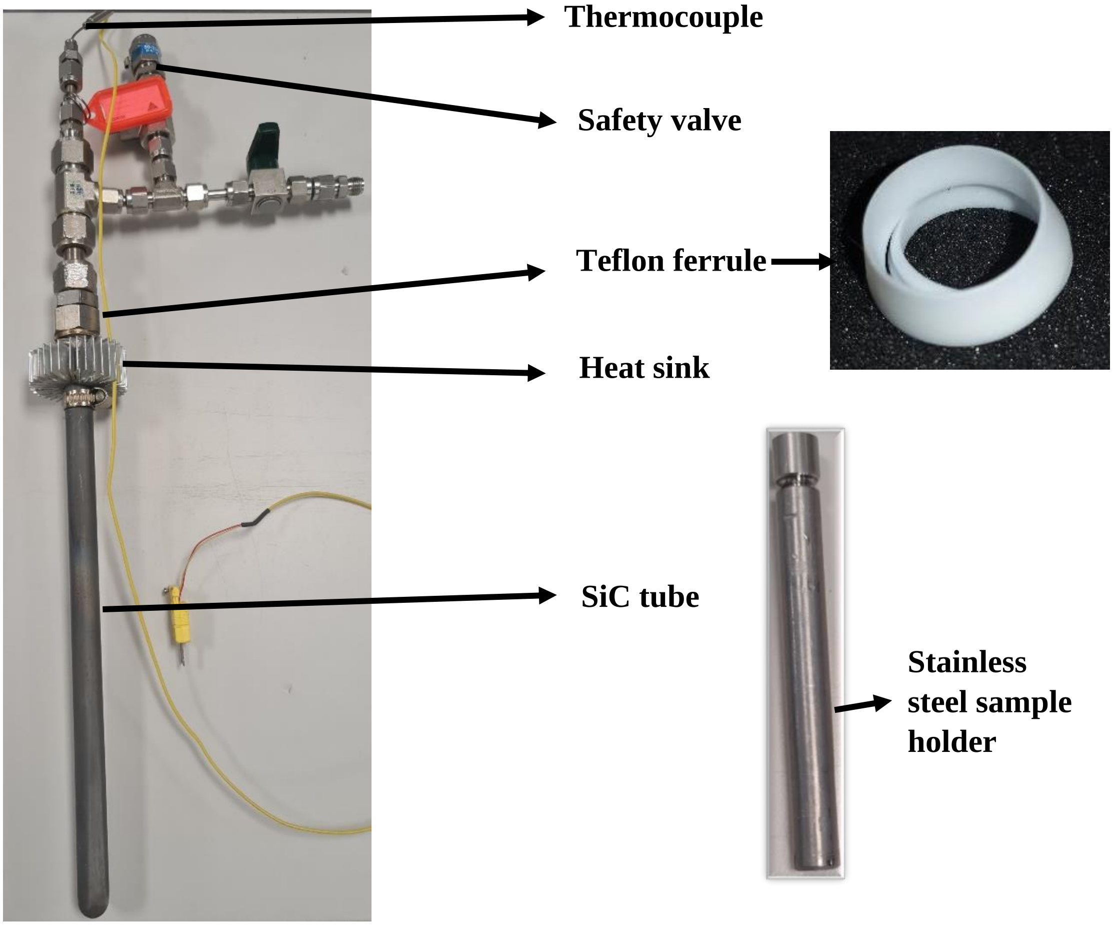

Figure 2.11 The SiC reactor with Swagelok tube fittings and thermocouple used to load the sample and heat under pressure.

2.3.6.1 Pressure transducer and thermocouple

The temperature of the sample was measured using a standard K-type thermocouple (marked in Figure 2.11) associated with an uncertainty of ± 1.5 °C. A Rosemount pressure transducer (model 3051S) was used as a pressure gauge to collect data with accuracy and precision of 0.02% and 0.01%, respectively. The pressure transducers display the pressure as a percentage of the pressure range. To convert the per cent value to a pressure value in units of bar, the following equation was used:

$P_{bar} = \left(\frac{\%*FS-(AtmP-100)}{100}\right)$ 2-22

Where

% = the percentage reading from the pressure gauge.

FS = the full-scale pressure range of the pressure transducer in bar units.

AtmP = the atmospheric pressure reading in kPa.

2.3.6.2 Determining volumes

2.3.6.2.1 Theory

As all the hydrogen sorption measurements were performed using a volumetric apparatus, it was essential to calculate the volumes of each part of the rig. Hence, to calculate the number of moles of hydrogen in each volume. The pressure, temperature and volume were measured in units of bar, kelvin and cm^3, respectively. The behaviour of hydrogen gas at high temperatures and high pressures cannot be considered as an ideal gas. Therefore, we must modify the basic ideal gas equation by considering hydrogen's compressibility factor (*Z*).

The ideal gas equation:

$P\ V = n\ R\ T$ 2-23

Where n = the number of moles of gas

P = the pressure of the gas

V = the volume that the gas occupies

T = the temperature of the gas (in Kelvin)

R = the universal gas constant (8.3145 J. K^{-1}.mol^{-1})

Hence the modified ideal gas equation including Z is:

$P\ V = n\ Z\ R\ T$ 2-24

Where the compressibility factor, $Z = \frac{V_m}{V_m^i}$, V_m is the molar volume = $\frac{V}{n}$ and V_m^i is the molar volume as determined from the ideal gas law.

Real gases differ from ideal gases and they follow the non-ideal gas equation. Hemmes has given a modified van der Waals equation (non-ideal gas equation) as:[17]

$\left[P + \frac{a(P)}{{V_m}^{\alpha(T)}}\right]\left(V_m - b(P)\right) = R\ T$ 2-25

where V_m = molar volume

$a(P)$ = gas constant a

$b(P)$ = gas constant b

V_m is then determined via numerical means followed by the calculation for Z at any given pressure and temperature using the free energy equation.

2.3.6.2.2 The reference side volume, sample side volume and non-ambient sample side volume

The reference volume (V_{ref}, equation 2-26) was volumetrically calibrated using an ethanol filled calibration volume. The sample side volume is divided into two sections; ambient sample side volume (V_s, equation 2-27) and non-ambient sample side volume (V_{na}, equation 2-28). The ambient sample side volume was determined using the following procedure (albeit automatically by the software), according to Figure 2.10:

1. Evacuate the whole system using valves 4 and 5 and then close.
2. Fill the reference volume (V_r) with hydrogen and allow for equilibrium. Measure the pressure (P_r) and temperature (T_r).
3. Open valve 3 and allow for equilibrium, after reaching equilibrium, close valve 3 and measure the equilibrium pressure (P_e) and temperature (T_e).
4. Repeat steps 1 to 3 at least 5 times to determine the average. A wide range of hydrogen pressures should be used to reduce systematic errors. Hence sample side volume can be calculated using equation 2-27

The non-ambient sample side volume is determined after heating the reactor inside a furnace to the required temperature (typically 800 °C) and follow the same procedure for the ambient sample volume measurement. The non-ambient sample side volume is then calculated using 2-28.

$$V_{ref} = \frac{\frac{P_2 V_{cal}}{Z_2 T_2}}{\left(\frac{P_1}{Z_1 T_1} - \frac{P_2}{Z_2 T_2}\right)} \qquad 2\text{-}26$$

$$V_s = V_r \left(\frac{\frac{P_r}{Z_r T_r} - \frac{P_e}{Z_e T_e}}{\frac{P_e}{Z_e T_e}} \right) \qquad 2\text{-}27$$

$$V_{na} = \frac{V_r\left(\frac{P_r}{Z_r T_r} - \frac{P_e}{Z_e T_e}\right) - Vs\left(\frac{P_e}{Z_e T_e}\right)}{\left(\frac{-P_e}{Z_e T_e} + \frac{P_e}{Z_{ena} T_{na}}\right)} \qquad 2\text{-}28$$

where P_1 = the initial pressure in the reference volume

T_1 = the initial temperature in the reference volume

Z_1 = the initial compressibility of hydrogen gas in the reference volume

P_2 = the pressure at equilibrium

T_2 = the temperature at equilibrium

Z_2 = the compressibility of hydrogen gas at equilibrium

V_{cal} = the volume of the calibration volume.

P_r = the initial pressure in the reference side

T_r = the initial temperature of the reference side (K)

Z_r = the compressibility associated with P_r and T_r

P_e = the equilibrium pressure of the system

T_e = the temperature at equilibrium (K)

Z_e = the compressibility associated with P_e and T_e

V_r = the reference side volume

V_s = the sample side volume

T_{na} = the temperature of the non-ambient region (K)

Z_{ena} = the compressibility associated with P_e and T_{na}

V_{na} = the sample side volume at non-ambient temperature

2.3.7 Hydrogen sorption measurements

2.3.7.1 Temperature programmed desorption (TPD) studies

Metal hydrides desorb/absorb hydrogen under specific temperature and pressure conditions, and the rate of H_2 desorption/absorption is a function of temperature. TPD studies are extremely useful to determine these conditions, in which the rate of reaction is monitored as a function of temperature. The samples are heated in the vacuum from room temperature to 800 °C and kept isothermal for a few hours at the highest temperature to ensure complete desorption. TPD provides information about the onset temperature of the reaction, number of steps involved over the temperature range, reaction kinetics, total desorbed H_2 pressure and H_2 capacity. For instance, the differential TPD profile of a CaH_2-3Zn system is given in Figure 2.12, which shows three hydrogen desorbed peaks indicating three different reactions between CaH_2 and Zn (detail in Chapter 5).

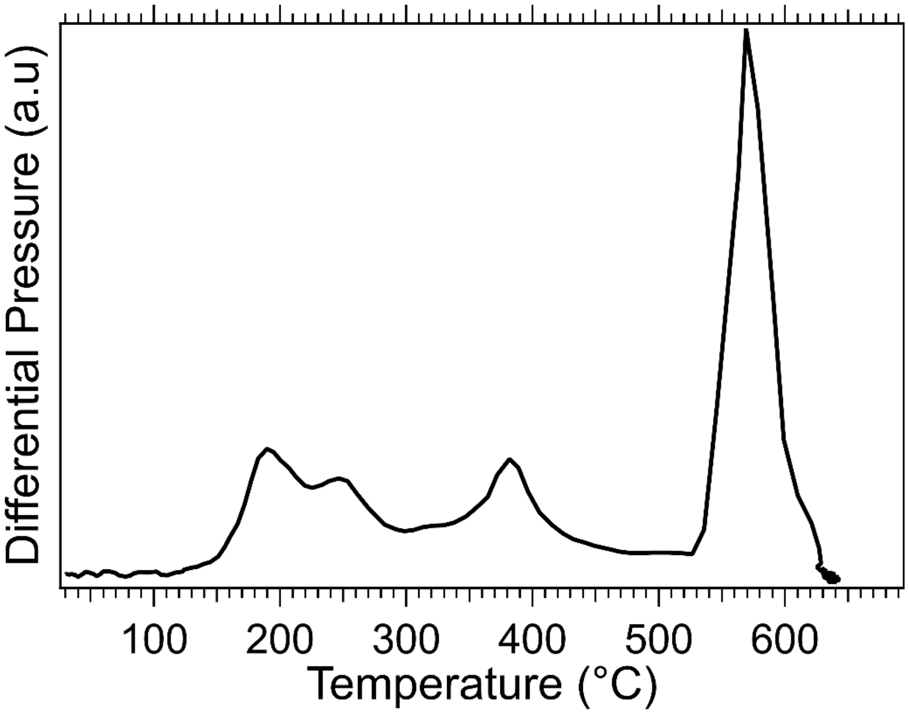

Figure 2.12 The differential TPD profile of a CaH_2-3Zn system.[18]

If the sample is weighed precisely, the desorbed (or absorbed) H_2 wt% can be calculated using the equation:

$$H_2\text{ wt\%} = \frac{n_{des} \cdot M_{H_2}}{m_{sample}} \qquad \text{2-29}$$

Where n_{des} is the number of moles of hydrogen desorbed by the sample and is given by:

$$n_{des} = n_r + n_s - n_e \qquad \text{2-30}$$

$$n_r = \frac{P_r V_r}{Z_r R T_r} \qquad \text{2-31}$$

$$n_s = \frac{P_s (V_s - V_{na})}{Z_s R T_s} + \frac{P_s (V_{na} - V_{sample})}{Z_{na} R T_{na}} \qquad \text{2-32}$$

$$n_e = \frac{P_e V_r}{Z_e R T_e} + \frac{P_e (V_s - V_{na})}{Z_e R T_e} + \frac{P_e (V_{na} - V_{sample})}{Z_{ena} R T_{na}} \qquad \text{2-33}$$

where:

n_r = the initial number of moles in the reference side volume

n_s = the initial number of moles in the sample side volume

n_e = the number of moles at equilibrium

R = the universal gas constant

P_r = the initial reference side volume pressure

P_s = the initial sample side volume pressure

P_e = the final equilibrium volume pressure

V_r = the reference side volume

V_s = the sample side volume

V_{sample} = the solid volume of sample based on sample mass and density

T_r = the initial reference side volume temperature (K)

T_s = the initial sample side volume temperature (K)

T_e = the equilibrium temperature (K)

Z_r = the compressibility value associated with P_r and T_r

Z_s = the compressibility value associated with P_s and T_s

Z_e = the compressibility value associated with P_e and T_e

V_{na} = the sample side volume at non-ambient temperature

T_{na} = the non-ambient temperature (K)

Z_{na} = the compressibility value associated with P_s and T_{na}

Z_{ena} = the compressibility value associated with P_e and T_{na}

2.3.7.2 Pressure composition isotherms (PCI or PCT)

The reaction between hydrogen (H) and a typical metal (M) occurs through various stages. If H/M < 0.1, the hydrogen dissolves exothermically in the metal, expanding the lattice. This is called the α phase (solid solution) of the metal hydride. At H/M > 0.1, strong hydrogen - hydrogen interaction occurs due to the lattice expansion.[19] The hydride phase grows, with α + β-phase, and reaches complete β phase when the ratio of H/M = 1. The thermodynamic properties of the hydride formation are defined by Pressure Composition Isotherms (PCI) which represents hydrogen dissociation pressure as a function of hydrogen concentration (Figure 2.13). When α+β phases co-exist, there is a plateau (equilibrium pressure region) in the isotherms. The length of the plateau region determines the amount of hydrogen stored. The two-phase areas end in a critical temperature beyond which transition from α to β is continuous.

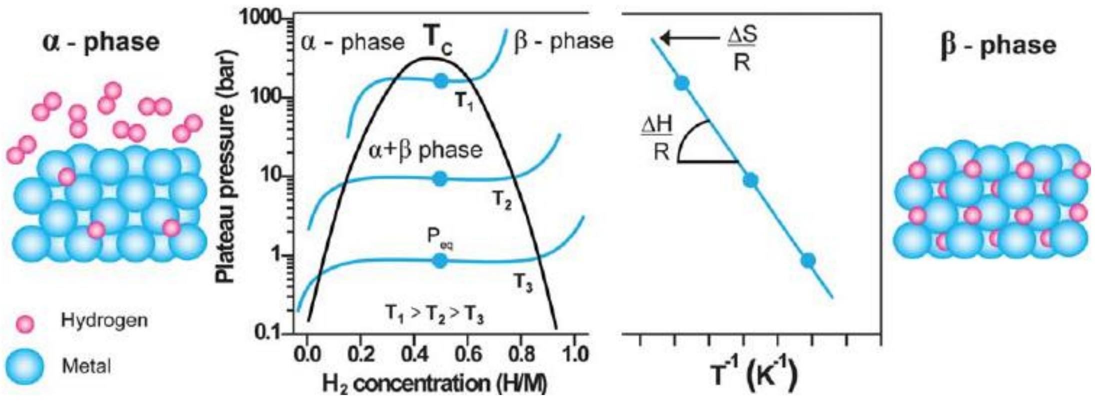

Figure 2.13 Typical pressure composition isotherms for hydrogen absorption (left) and corresponding Van't Hoff plot (right) show hydride formation's enthalpy and entropy. Schematic representation of α phase and β phase of the metal hydride is also shown.[19-20]

Hence, PC isotherm (PCI) is a stepwise method to determine thermodynamic values of H_2 desorption or absorption using a Sievert's apparatus. For desorption of the metal hydride, the sample is heated under a predefined pressure (pressure above the equilibrium pressure of decomposition). Once the sample reaches the required isothermal temperature, a stepwise decrease of the sample pressure is carried out, where the sample is kept at each pressure for a predetermined time (step size). When the pressure reaches the equilibrium point, the sample starts to desorb the gas, revealing an increase in the system's pressure. At each step, the number of moles of H_2 desorbed and wt% can be calculated using the equations 2-30 and 2-29, respectively. Several PCI measurements are performed on the sample at different isotherm temperatures, and corresponding equilibrium pressures are measured. Using the equilibrium pressure and temperature, a Van't Hoff plot can be constructed (Figure 2.13).[19, 21] The enthalpy and entropy of the reaction can be calculated using the Van't Hoff plot, the plot of $1/T$ vs ln (P/P_0). The Van't Hoff equation for a hydrogen desorption reaction can be written as:

$$\ln\left(\frac{P_{eq}}{P_0}\right) = -\frac{\Delta H_{reaction}(P,T)}{R.T} + \frac{\Delta S_{reaction}(P,T)}{R} \qquad 2\text{-}34$$

The Van't Hoff equation, developed from the definitions of Gibbs free energy of a reaction and for an isotherm, is given in 2-35 and 2-36. Combining these two equations will lead to 2-34, Van't Hoff equation.

$$\Delta G = \Delta H - T\,\Delta S \qquad 2\text{-}35$$

$$\Delta G = -\mathrm{R}\,T\,\ln\left(\frac{P_{eq}}{P_0}\right) \qquad 2\text{-}36$$

From the Van’t Hoff plot, the slope and intercept of the graph will be:

$$\text{Slope} = -\frac{\Delta H_{reaction(P,T)}}{R} \qquad 2\text{-}37$$

$$\text{Intercept} = \frac{\Delta S_{reaction(P,T)}}{R} \qquad 2\text{-}38$$

Hence, the enthalpy and entropy of the reaction can be calculated as ;

$$\Delta H = -\text{Slope/R} \qquad 2\text{-}39$$

$$\Delta S = \text{Intercept/R} \qquad 2\text{-}40$$

2.3.8 Uncertainty calculations

In experimental science, it is impossible to obtain a true value of any quantity and is always associated with a degree of uncertainty. However, the determination of uncertainties and displaying error bars on the calculated ΔH and ΔS quantities from a Van’t Hoff plot is often ignored in the literature or not reported in their method of determination or reported wrongly. In addition, it is important to include the error bars on figures and error ranges on the values when reporting material for hydrogen storage properties to compare the performance of materials and precision of testing methods.

Random and systematic errors are the two types of measurement errors that lead to uncertainty. Random errors are unpredictable and arise from uncontrollable factors such as environmental conditions that vary from one measurement to another. This affects the precision of the measurements cannot be eliminated, although it can be reduced by repeating the measurements several times. Systematic errors are predictable and often come from faulty instrumentation or imperfect calibration, affecting the measurement's accuracy. The value of systematic error will be constant and can be reduced by recalibrating the instruments and the correct use of experimental techniques. The significant factors in determining the uncertainties in this thesis are associated with the temperature and pressure measurements. The mean value and standard error are based on the standard deviation of the collection. The standard error can be calculated by dividing the standard deviation by the square root of several measurements. The standard deviation of a quantity in arithmetic calculation can be calculated as shown in Table 2.4.[22-25]

Table 2.4 Formulas for calculating the standard deviation with basic arithmetic operations.[22-25]

Arithmetic operation	Example*	Standard deviation
Addition or subtraction	$x = a + b + c$	$S_x = \sqrt{a^2 + b^2 + c^2}$
Multiplication or division	$x = \frac{a\,b}{c}$	$S_x = x\sqrt{(\frac{S_a}{a})^2 + (\frac{S_b}{b})^2 + (\frac{S_c}{c})^2}$
Exponentiation	$x = a^y$	$S_x = y\,x\,\frac{S_a}{a}$
Logarithm	$x = \log_{10} a$	$S_x = 0.434\,(\frac{S_a}{a})$
Natural logarithm	$x = \ln a$	$S_x = \frac{S_a}{a}$
Antilogarithm	$x = \text{antilog}_{10}\, a$	$S_x = 2.303\, x\, S_a$
Natural Antilogarithm	$x = e^a$	$S_x = x\, S_p$

**a, b,* and *c* are experimental variables whose standard deviations are S_a, S_b, and S_c, respectively. y is a constant

2.3.8.1 Least-squares fitting

The error of a linear fit can be calculated from a set of data values using the following equations:

Let us assume a line equation : (*x* and *y* are the data points; *N* is the number of data points and *Δ* is the symbol for the denominator)

$y = m.x + c$ 2-41

$\Delta = N.\sum x^2 - (\sum x)^2$ 2-42

The *y* intercept, $c = \sum x^2 . \sum y - \sum x . \sum x\, y$ 2-43

The slope, $m = \frac{N.\sum xy - \sum x . \sum xy}{\Delta}$ 2-44

The standard deviation of the *y*, $\sigma_y = \sqrt{\frac{1}{N-2}\sum_{i=1}^{N} y_i - b - mx_i)^2}$ 2-45

The standard deviation of the *y*-intercept, $\sigma_c = \sigma_y \sqrt{\frac{\sum x^2}{\Delta}}$ 2-46

The standard deviation of the slope, $\sigma_m = \sigma_y \sqrt{\frac{N}{\Delta}}$ 2-47

Therefore, the line equation with error can be expressed as:

$y = (m \pm \sigma_m)\, x + c \pm \sigma_c$ 2-48

2.3.8.2 Total least squares: Orthogonal distance regression

When you fit a model to a data, it is usually assumed that *x* is perfectly known, and *y* is measured with error (i.e., all the errors are in the dependent variable and no errors for the independent variable). This is often true if the errors in the y are much higher than errors in x, and it will not cause much difference to the curve fit. For instance, in the Van't Hoff plot $\ln(P/P_0)$ vs $1000/T$, the error in x ($1000/T$) is very large compared to *y* ($\ln(P/P_0)$and is the same case for Kissinger plot, $\ln\left(\frac{\beta}{{T_m}^2}\right)$ vs ($1000/T$). The fitting of such data (have an error on both *x* and *y* or higher error on *x* than *y*) using standard or ordinary least squares can lead to bias in the solution. This issue can be solved using the orthogonal distance regression (ODR) method, known as the total least square's method. ODR adjust both model coefficients and independent variables to reduce the orthogonal distance (shortest distance) from the data to the fitted curve instead of minimising the sum of squared errors in the dependent variable. Hence, ODRPACK can give real solutions, and useful statistical information's for linear and non-linear problems than ordinary least squares.[26] The uncertainty analysis in this thesis was carried out by ODRPACK 95 using Igor Pro software. An example of ODR fit with error bars, and solutions of the Kissinger plot for the CaH_2 system is shown in Figure 2.14. The errors in *x* and *y* were calculated using the formulas given in the Table and displayed in the graph with the help of Igor pro software. The slope and y-intercept errors were found by running an ODR fitting command in the Igor pro. Hence the activation energy from Figure 2.14 can be calculated as $E_a = 203 \pm 12$ kJ.mol^{-1}. The error in the enthalpy and entropy can also be calculated using this method.

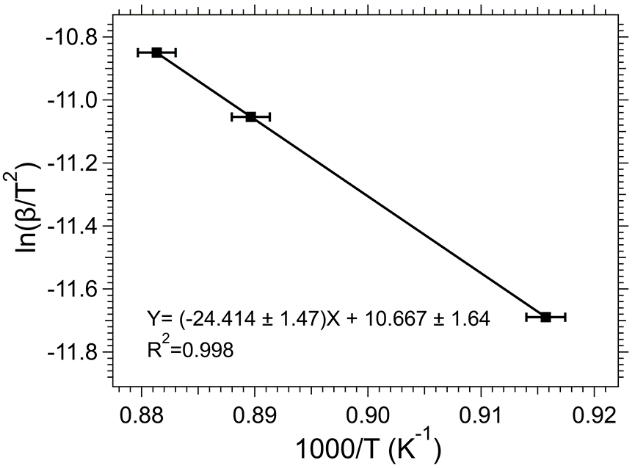

Figure 2.14 Kissinger plot for CaH_2 system and the line fitted with errors using ODR method.

2.4 References

1. Roine, A. *Hsc Ver.9.0.0* *Https://Www.Outotec.Com/Products/Digital-Solutions/Hsc-Chemistry/*.
2. Dinsdale, A. T., SGTE Data for Pure Elements.*CALPHAD: Comput. Coupling Phase Diagrams Thermochem.* **1991**, *15*, 317-425.
3. Planetary Ball Mill Jars. https://cykylabequipment.en.made-in-china.com/product/nKZJNBmxhWpX/China-High-Throughput-Horizontal-Planetary-Ball-Mill-with-16-Channel-Ss-Milling-Jars.html (accessed December **2021**).
4. Pecharsky, V. K.; Zavalij, P. Y., Collecting Quality Powder Diffraction Data. Fundamentals of Powder Diffraction and Structural Characterisation of Materials **2009**, 301-346.
5. Cullity, B. D., Elements of X-Ray Diffraction; Addison-Wesley Publishing, **1956**.
6. Rietveld, H., A Profile Refinement Method for Nuclear and Magnetic Structures. *J. Appl. Crystallogr.*, **1969**, *2*, 65-71.
7. Rietveld, H., The Rietveld Method? A Historical Perspective. *Aust. J. Phys.*, **1988**, *41*, 113-116.
8. Chan, Ngai-yui., Study of Barium Strontium Zirconate Titanate Thin Films and Their Microwave Device Applications. **2010**.
9. Hayes, E.; Roberson, A., Some Effects of Heating Zirconium in Air, Oxygen, and Nitrogen. *J. Electrochem. Soc.*, **1949**, *96*, 142.
10. Lilliendahl, W.; Wroughton, D.; Gregory, E., The Quantitative Evaluation of Oxygen in Zirconium. *J. Electrochem. Soc.*, **1948**, *93*, 235.
11. Khanacademy Activation Energy. https://www.khanacademy.org/science/ap-biology/cellular-energetics/enzyme-structure-and-catalysis/a/activation-energy (accessed December **2021**).
12. Blaine, R. L.; Kissinger, H. E., Homer Kissinger and the Kissinger Equation. *Thermochim. Acta*, **2012**, *540*, 1-6.
13. Kissinger, H. E., Reaction Kinetics in Differential Thermal Analysis. *Anal. chem.*, **1957**, *29*, 1702-1706.
14. Sheppard, D. A.; Paskevicius, M.; Javadian, P.; Davies, I. J.; Buckley, C. E., Methods for Accurate High-Temperature Sieverts-Type Hydrogen Measurements of Metal Hydrides. *J. Alloys Compd.*, **2019**, *787*, 1225-1237.
15. Causey, R.; Fowler, J.; Ravanbakht, C.; Elleman, T.; Verghese, K., Hydrogen Diffusion and Solubility in Silicon Carbide. *J. Am. Ceram. Soc.*, **1978**, *61*, 221-225.

16. Forcey, K.; Ross, D.; Wu, C., The Formation of Hydrogen Permeation Barriers on Steels by Aluminising. *J. Nucl. Mater.,* **1991**, *182*, 36-51.
17. Hemmes, H.; Driessen, A.; Griessen, R., Thermodynamic Properties of Hydrogen at Pressures up to 1 Mbar and Temperatures between 100 and 1000K. *J. Phys. C Solid State Phys.,* **1986**, *19*, 3571.
18. Balakrishnan, S.; Sofianos, M. V.; Humphries, T. D.; Paskevicius, M.; Buckley, C. E, Thermochemical Energy Storage Performance of Zinc Destabilised Calcium Hydride at High-Temperatures. *Phys. Chem. Chem. Phys.,* **2020**.
19. Züttel, A., Materials for Hydrogen Storage. *Mater. Today,* **2003**, *6*, 24-33.
20. Bardhan, R.; Ruminski, A. M.; Brand, A.; Urban, J. J., Magnesium Nanocrystal-Polymer Composites: A New Platform for Designer Hydrogen Storage Materials. *Energy Environ. Sci.,* **2011**, *4*, 4882-4895.
21. Adametz, P.; Müller, K.; Arlt, W., Energetic Evaluation of Hydrogen Storage in Metal Hydrides. *Int. J. Energy Res.,* **2016**, *40*, 1820-1831.
22. Bland, J. M.; Altman, D. G., Statistics Notes: Measurement Error. *Bmj* **1996**, *312*, 1654.
23. Cochran, W. G., Errors of Measurement in Statistics. *Technometrics* **1968**, *10*, 637-666.
24. Dodge, Y.; Cox, D.; Commenges, D., *The Oxford Dictionary of Statistical Terms*; Oxford University Press on Demand, **2006**.
25. Taylor, J., Introduction to Error Analysis, the Study of Uncertainties in Physical Measurements, **1997**.
26. Boggs, P. T.; Rogers, J. E., Orthogonal Distance Regression. *Contemporary Mathematics* **1990**, *112*, 183-194.

Chapter 3

Experimental investigation of thermodynamic and kinetic properties of CaH_2

3.1 Introduction

3.1.1 Discovery and uses

The existence of CaH_2 has been known since 1891 by Clemens A. Winkler.[1] Lime (CaO) and Mg was heated together in an atmosphere of H_2 and reported a new product formulated as CaH. In 1893 Henri Moissan produced CaH_2 from Ca and steam.[1] Later, CaH_2 was produced commercially and used for many practical purposes such as a source of hydrogen, reducing agent, catalyst, purification, condensing and drying agent and even in nuclear reactors.[1-2] Early CaH_2 was called Hydrolith that reacts with water and releases hydrogen.[3] Today, CaH_2 remains an effective source of hydrogen, and its high operating temperature at low pressures (1100 - 1400 °C at 1- 5 bar), storage density (4939 $kJ.kg^{-1}$) and reversible hydrogen storage property makes it attractive as a high-temperature thermal battery.[4-5]

3.1.2 Production

Different methods are available for the production of calcium hydride. The most popular and industrial process is synthesis from its elements Ca and H_2.[3] CaH_2 is prepared by heating Ca metal under 1 bar of H_2 pressure at 300 to 400 °C.[2-3]

$$Ca + H_2 \xrightarrow[H_2\text{ pressure}]{\text{heat}} CaH_2 \qquad 3\text{-}1$$

The reaction 3-1 is strongly exothermic and is controlled by limiting the hydrogen pressure. A typical installation set-up for the synthesis of high purity CaH_2 is shown in Figure 3.1.[6] According to Bulanov *et.al.*, under a high vacuum, the reactor is packed with calcium and heated to 400 °C and then filled with purified H_2 to a pressure of 5 bar. The increase in the absorption rate of H_2 is explained by the high rate of the hydrogenation reaction on the surface of Ca. The flow of H_2 was controlled so that the pressure of H_2 in the reactor is limited, as the increase in H_2 pressure results in a temperature rise. The temperature rise may lead to the melting of CaH_2, which creates difficulties to remove it from the reactor. Higher conversions are possible in the lower temperature ranges because the high melting points of CaH_2 and Ca indicate that there are no liquid phases in the lower ranges. Increasing temperature increases the solubility of metal and hydride in each other and thereby lowers the conversion factor.[1, 6]

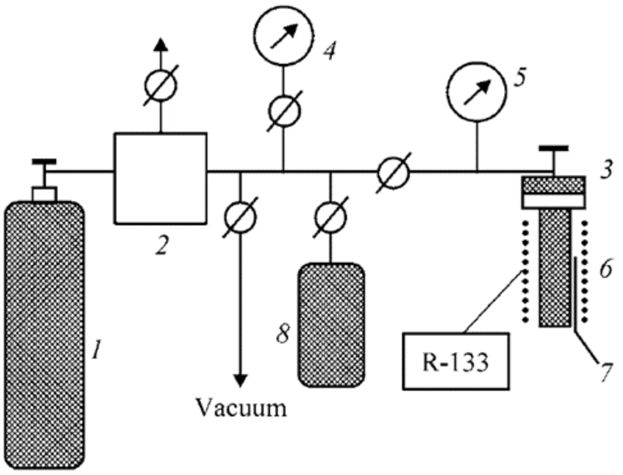

1. H_2 Cylinder
2. H_2 purification unit
3. Reactor
4. Vacuum gauges
5. Vacuum gauges
6. Temperature control unit
7. Thermocouple
8. Temperature data logger (R-133)
9. Receiver

Figure 3.1. Schematic of typical equipment used in the synthesis of high purity CaH_2.[6]

3.1.3 Properties

The general properties of both Ca, and CaH_2 are listed in Table 3.1.

Table 3.1 The general properties Ca and CaH_2 system.[7-9]

Physical Properties			Comments
	Ca	CaH_2	
Appearance	Silvery white	White to grey	White when pure CaH_2
Crystal structure	Face centred cubic	Orthorhombic	
Molar mass (g.mol^{-1})	40.08	42.096	
Melting point (°C)	839 - 852	816 - 1000	depending on the purity of both Ca and CaH_2
Boiling point (°C)	1484	-	
Density (g.cm^{-3} at 25 °C)	1.54	1.7	
Density (g.cm^{-3} at X °C)	1.378 1.319	- -	X = 842 °C X = 1100 °C
Thermal conductivity (W.cm^{-1}.K^{-1} at 27 °C)	2.00	-	
Heat capacity at 25 °C (J.mol^{-1}.K^{-1})	25.94	41.00	

Heat capacity at X °C (J.mol^{-1}.K^{-1})	35.0	75.0	X = 1000 °C
Specific heat capacity at 25 °C (J.kg^{-1}. K^{-1})	647	974	
Specific heat capacity at X °C (J.kg^{-1}. K^{-1})	35.0	75.0	X = 1000 °C
Reaction desorption enthalpy (kJ.mol^{-1} H_2)		~ 207.7	Different values reported by various investigators.[1,12-21]
Theoretical Storage capacity (wt% H_2)		4.79	
Practical storage capacity (wt% H_2)		2.4	
1 bar equilibrium temperature (°C)		~ 990	Varies from 950 - 1100
Possible temperature range (°C)		1000 - 1100	
Theoretical energy to weight (kJ.kg^{-1})		4934	
Practical energy to weight (kJ.kg^{-1})		2472	
Theoretical energy to volume (kJ.L^{-1})		6508	

3.1.4 Phase diagram

Peterson and Fattore first reported the calcium-calcium hydride phase diagram in 1961, as shown in Figure 3.2.[10] The calcium-calcium hydride phase diagram is similar to the barium-barium hydride system except for the additional complexity coming from the allotropy of calcium.[2] The phase diagram helps to understand the allotropic transitions relations between liquid and solid phases of Ca and CaH_2 as a function of hydrogen content and temperature. A crystal structure transition from fcc to bcc (αCa to βCa) was observed in pure Ca metal at 448 ± 2 °C on heating and 442 ± 2 °C on cooling. An intermediate hcp phase of Ca, γCa, may exist in this temperature range depending on the hydrogen impurities present in the calcium. CaH_2 undergoes a polymorphic transition from orthorhombic (*Pnma*) to cubic (*Fm*-3*m*) (αCaH_2 to βCaH_2) at 780 °C.[11] Solid solubility of CaH_2 in Ca is observed and reaches a maximum of 24 mole% at the peritectic temperature of 890 °C. Also, the maximum solubility of H in βCa at this temperature was 32% for liquid + βCaH_2 = βCa. Above 842 °C, beyond the melting point of Ca, liquid Ca exists with CaH_2. Also, no data is available above 980 °C.

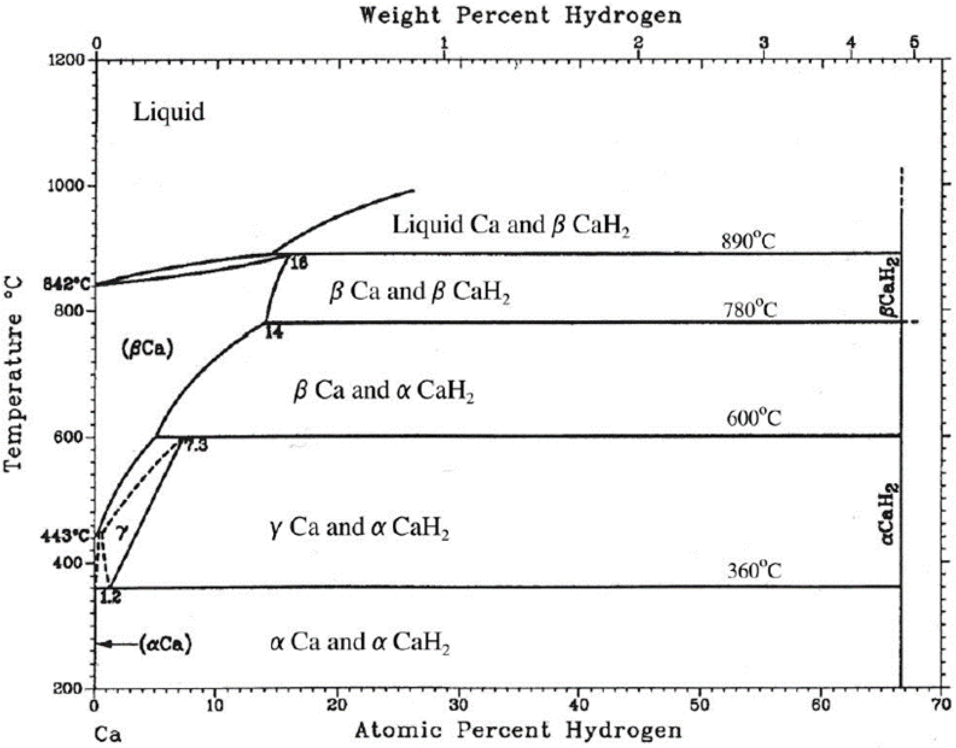

Figure 3.2 Phase diagram for the calcium-calcium hydride system.[10]

3.1.5 Initial thermodynamic studies for the desorption of CaH_2

Several authors have studied the Ca-CaH_2 system by conducting the desorption pressure composition isotherm (PCI) experiments. The equilibrium pressure and corresponding temperature for the desorption of the CaH_2 system from seven studies, reported by Hurd, Moldenhauer, Kassner, Kraus, Treadwell, Bronsted and Johnson were taken, and the corresponding Van 't Hoff plot can be derived and plotted as shown in Figure 3.3.[12-18] In addition, all the significant works on the thermodynamic properties for the desorption of CaH_2 system, so far available in the literature (from 1913 - 1959), are tabulated in Table 3.2.

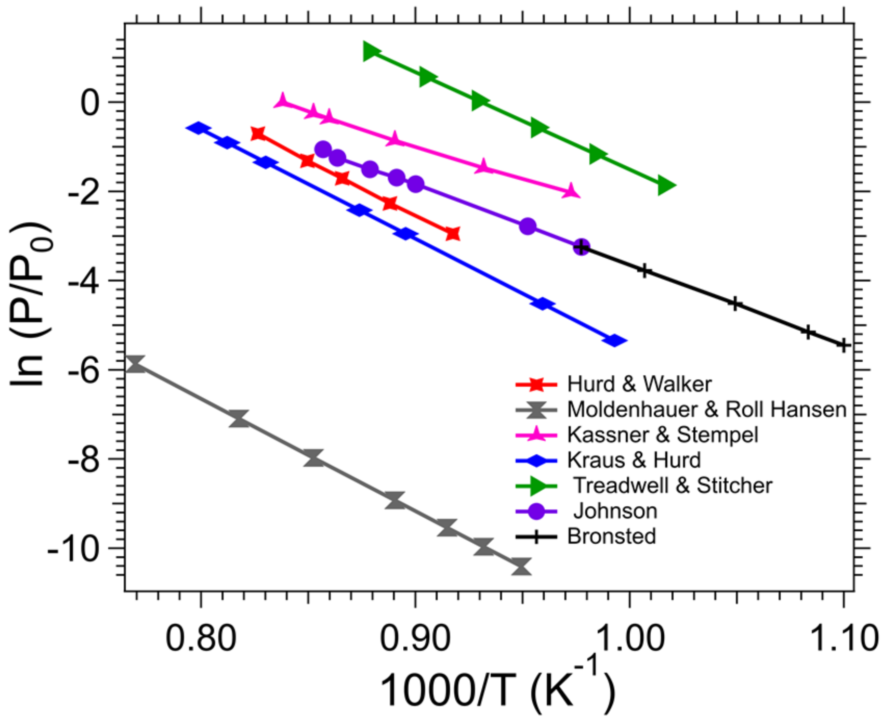

Figure 3.3 Van't Hoff plot for the desorption of CaH_2 system from different investigators.[1, 12-21]

Table 3.2 The thermodynamic properties for the desorption of CaH_2 system from the literature.[1, 12-21]

No.	**Investigator**	**Year**	***T** range (°C)**	**ΔH_{des}^* (kJ.mol^{-1} H_2)**	**ΔS_{des}^* (J.K^{-1}.mol^{-1} H_2)**	***T** in (°C) at 1 bar**	**Comments**
1	Moldenhauer and Roll Hansen	1913	780 - 1027	209	112	1593	Supports the sub hydride theory. Proved the presence of CaH. CaH volatile & CaH_2 non-volatile.

2	Bronsted	1914	641 - 747	197	155	997	Does not support the sub hydride theory. Mentioned the CaH - CaH_2 existence.
3	Ephriam and Michel	1921	N/A	N/A	N/A	N/A	Does not support the sub hydride theory. Supports type 3 equilibrium. Condensed phases have a composition $CaH_2.2Ca$.
4	Kraus and Hurd	1923	734 - 985	204	158	1017	Found a three-phase equilibrium. Unknown third phase formulated as CaH.
5	Huttig and Brodkorb	1926	N/A	N/A	N/A	N/A	Supports the sub hydride theory.
6	Kassner and Stempel	1929	755 - 920	125	104	928	Supports the sub hydride theory.
7	Remy- Cennete	1929	815 - 970	214	N/A	N/A	Does not support the sub hydride theory.
8	Hurd and Walker	1931	816 - 936	205	164	977	Does not support the sub hydride theory.
9	Stubbs	1931	N/A	N/A	N/A	N/A	Does not support the sub hydride theory.

							Supports Type 3 equilibrium. Also, states that equilibrium does not exist.
10	Johnson	1939	636 - 894	150	119	987	Does not support the sub hydride theory. Supports type 4 equilibrium.
11	Treadwell and stitcher	1953	711 - 941	181	169	797	Supports type 4 equilibrium. Mentioned a solution of calcium in calcium hydride (nCa.CaH$_2$ +$\frac{n}{2}$ H$_2$).

$^*T$ -Temperature, ΔH_{des} = desorption enthalpy, ΔS_{des} = desorption entropy

3.1.5.1 Types of equilibrium for the desorption of CaH_2 system

The main differences in the results and conclusions of individual investigators may be due to the different types of dissociation equilibrium that exist in the CaH_2 system. The four types of equilibrium explained in the literature are listed below:

(a) Type 1 equilibrium

The 1st type of equilibrium was reported by four investigators, Bronsted, Hurd and Walker, Remy-Cennete and Kraus and Hurd, and they reported the decomposition reaction occurs in one step, as shown in 3-2.[12, 15, 17] The equilibrium exists in equation 3-2 is the equilibrium between CaH_2, Ca and H_2 and the equilibrium hydrogen pressure is independent of the solid phases present. All these four studies tried to confine all materials except hydrogen.

$$CaH_2 \rightleftharpoons Ca + H_2\,(g) \qquad 3\text{-}2$$

(b) Type 2 equilibrium

The 2nd type of equilibrium was reported by other four investigators, Moldenhauer and Roll-Hansen, Kassner and Stempel, Huttig and Brodkorb, Ephriam and Michel, found the dissociation occurs in two steps, as shown in 3-3 and 3-4. The equilibrium contains four phases, CaH_2, CaH, Ca, and H_2, and the equilibrium H_2 pressure is independent of the solid phases present. Huttig reported a steady increase in hydrogen pressure when the system was kept at a constant temperature.[19] Moldenhauer and Roll Hansen believed that they proved the existence of CaH.[13] In the experiments, they used a compound with one half the usual amount of hydrogen present in CaH_2, and the pressure measured reached a value one half the normal magnitude. They also stated CaH_2 is non-volatile and that CaH is very volatile. Even though the opinions of various investigators vary about the reaction for the dissociation of CaH_2, they all agree that molecular hydrogen constitutes the gaseous product.

$$CaH_2 \rightleftharpoons CaH + \frac{1}{2} H_2 (g) \qquad 3\text{-}3$$

$$CaH \rightleftharpoons Ca + \frac{1}{2} H_2 (g) \qquad 3\text{-}4$$

(c) Type 3 equilibrium

Hurd, Huttig, Ephriam and Michel and Stubb also discussed a third type of equilibrium that consists of CaH_2 and metallic Ca forming a series of solid solutions, and dissociation pressure is dependent on the composition of the condensed mixture phase.[12, 19-20] The condensed mixture phase had a composition of $CaH_2.2Ca$ and may vary as a decomposition function.

(d) Type 4 equilibrium

Johnson and Treadwell reported the 4th type of equilibrium similar to the 3rd type, but the dissociation pressure depends on the condensed phase composition below 20 to 25 and above 90 to 95% CaH_2.[16, 18] Between these limits (25 - 90%), the dissociation pressure is independent of the composition of the condensed mixture phase. Treadwell and Stitcher concluded that the condensed mixture contains a solution of calcium in calcium hydride, $n\text{Ca}.CaH_2$.[16] Finally, Stubbs *et al.* reported that there is no true equilibrium that exists in the calcium hydride system.[1, 18]

The disagreement in results from each investigator, as shown in Table 3.2, may be due to differences in the experimental procedure. This includes the purity of both Ca and CaH_2, mode of preparation, apparatus, the form of the reactants, the difference in melting point of Ca and

CaH_2, surface area, allotropic formations of Ca and CaH_2, the solubility of Ca and CaH_2 and vice versa, as explained in the previous section in the phase diagram. Also, the reactions may be further blocked due to the presence of surface films, poor kinetics, different step sizes in PCI's, not reaching the equilibrium plateau and CaH_2 phase compositional variations with the hydrogen pressure. For the investigators who used open sample cells inside the reactors, volatile solid products may have evaporated and deposited in the cooler parts, which could also reabsorb H_2, reducing the equilibrium pressure. Also, the investigators used quartz reactors which may react with calcium hydride at high temperatures and release hydrogen.[8] This affects the measured equilibrium pressure. The sample cell should be closed to Ca and CaH_2 but be permeable to hydrogen for better results.

Little research has been conducted on the Ca-H system since 1960, especially on thermodynamics and kinetics. This may be due to the high-temperature requirement to achieve reasonable pressures to perform these experiments. Therefore, in this chapter, the kinetic and thermodynamic properties of pure CaH_2 are experimentally investigated and reported below. The study's novelty lies in finding accurate thermodynamic values of solid and molten CaH_2 by considering the melting points of both Ca and CaH_2.

3.2 Results and discussion

3.2.1 Synthesis and initial phase analysis

Calcium hydride purchased from Sigma Aldrich (>95% purity) was stored and handled inside an Ar filled MBraun Unilab glovebox to reduce oxygen (< 1 ppm) and water (< 1 ppm) contamination. CaH_2 was ball-milled using an Across International Planetary Ball mill (PQ-N04) under argon atmosphere at room temperature. The samples were sealed inside a stainless-steel vial with a 40:1 ball (equal number of 10 mm and 6 mm diameter balls) to powder ratio and milled for 3 h at a rotational speed of 400 rpm. The XRD pattern of ball-milled CaH_2 is displayed in Figure 3.4. It shows that the sample contains minor CaO impurities. The sample includes both CaO and $Ca(OH)_2$ as impurities, but they are not crystalline enough to produce a peak at room temperature. However, it is clear from the *in-situ* SXRD data (Figure 3.7) that at temperatures of ≈ 100 °C, these peaks can be seen as the material expands, resulting in more crystallinity than at room temperature.

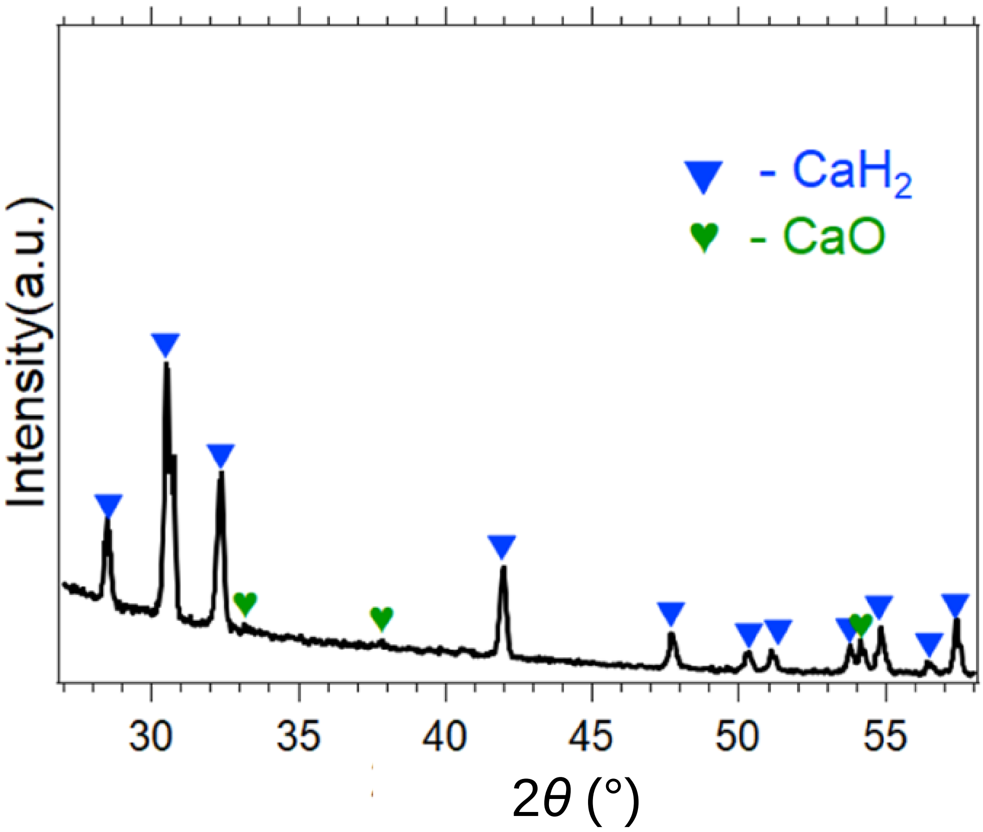

Figure 3.4 *Ex-situ* XRD patterns of ball-milled CaH_2 using Cu K_α radiation (λ = 1.5418 Å).

3.2.2 Mass spectrometry

To determine the release of H_2 gas or other gases, temperature-programmed desorption mass spectrometry (TPD-MS) studies were performed on ball-milled CaH_2 using an SRS RGA-300 mass spectrometer.[22] A 3 mg of sample was placed in a stainless-steel sample holder inside a silicon carbide reactor, connected to the RGA mass spectrometer separately, and heated from room temperature to 900 °C with a ramp rate of 5 °C/min. As a high vacuum ($< 7 \times 10^{-4}$ mbar) is employed in this technique, CaH_2 begins to release hydrogen at 500 °C and reaches its highest intensity of desorption at 600 °C, as seen in Figure 3.5. The smaller peaks at a lower temperature are due to the impurities in the CaH_2 sample.

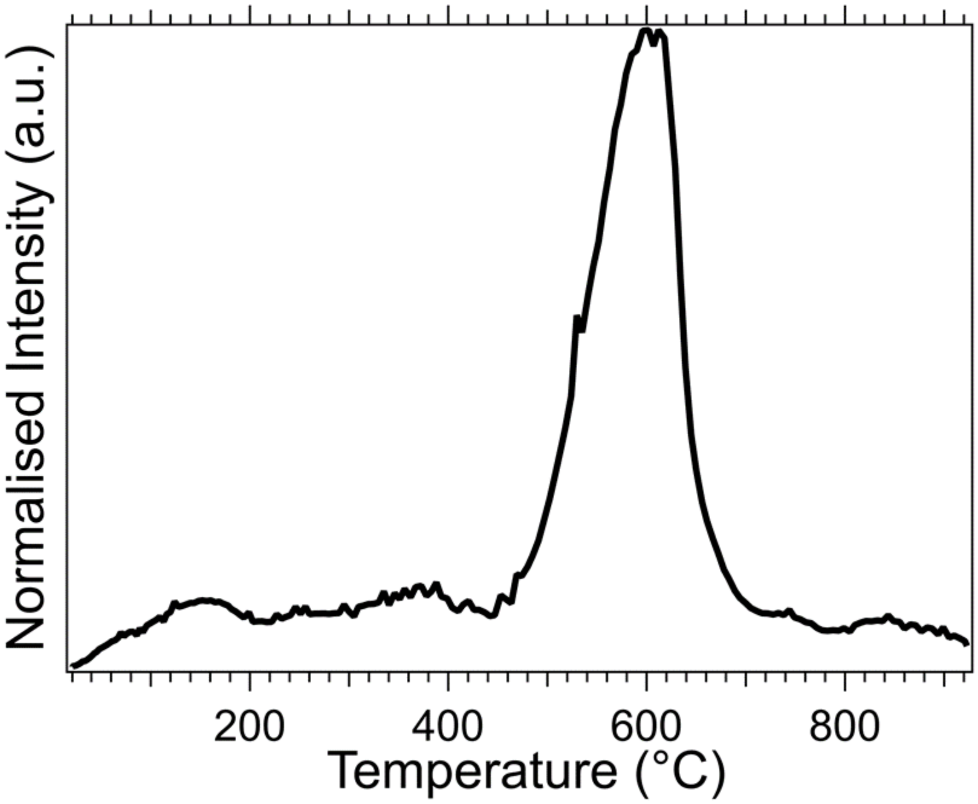

Figure 3.5 Hydrogen desorption profiles as observed by TPD-MS measurements of CaH_2 at a heating rate of 5 °C/min under a high vacuum ($< 7 \times 10^{-4}$ mbar).

3.2.3 Determination of melting point

Several investigators reported varying melting points for the CaH_2 system (800 to ≥ 1000 °C), and no actual experimental data is available in the literature.[1] Hence, the melting point of ball-milled CaH_2 was measured during thermal ramps while maintaining a hydrogen pressure of 6 bar to minimise the possibility of sample decomposition. The ball-milled CaH_2 was heated initially from room temperature to 1000 °C and then cooled to 700 °C with a ramp rate of 10 °C/min. The heating and cooling profile were repeated three times between 1000 °C and 700 °C. A sharp thermal signal and discontinuity in the temperature derivative with respect to time was observed at the solidus-liquidus phase transition temperature of 816 ± 2 °C, as shown in Figure 3.6.

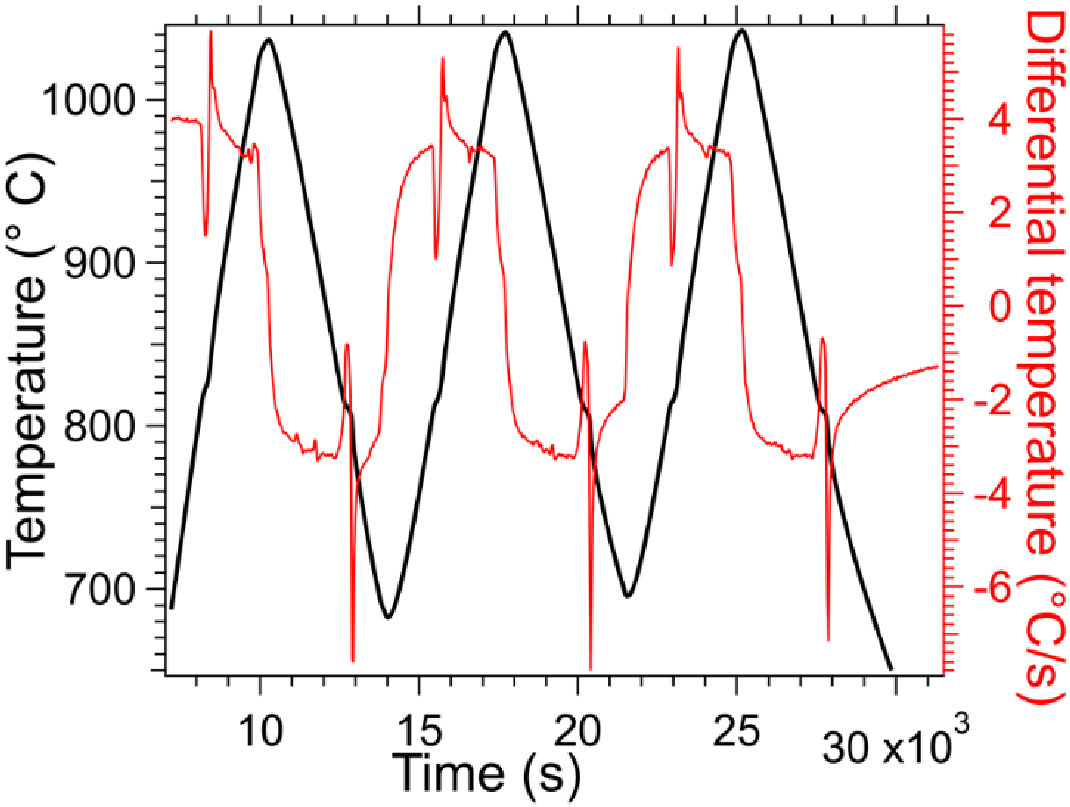

Figure 3.6. Melting point analysis of pure CaH_2 indicating sample temperature (black line) and its differential (red line).

3.2.4 *In-situ* synchrotron XRD studies

In-situ synchrotron radiation X-ray powder diffraction (SR-XRD) was performed on pure CaH_2 and is presented in Figure 3.7. The sample was loaded in a quartz capillary and heated using a hot air blower from room temperature to 900 °C with a 10 °C/min heating rate under a dynamic vacuum. The temperature of the hot air blower was calibrated against the known thermal expansion coefficient of NaCl and Ag.[23-25] According to figure 3.7, the impurities CaO and $Ca(OH)_2$ are more visible at high temperatures than at room temperature. The $Ca(OH)_2$ peaks disappear after 300 °C, decomposing below that temperature. The first phase transformation is observed at 600 °C. In addition, the presence of CaH_x ($0 < x < 2$) in temperatures below 800 °C may support the two-step decomposition of the CaH_2 system (sub hydride theory) as explained in works of literature shown in section 3.1.5. Griffond *et.al.* identified CaH_x possessing a pseudo cubic centred structure ($Fd\bar{3}m$ space group).[26] It can represent one peak and a series of peaks with a similar structure but different stoichiometry of CaH_x solid solution. All the peaks of CaH_2 and CaH_x phases have disappeared after 880 °C.

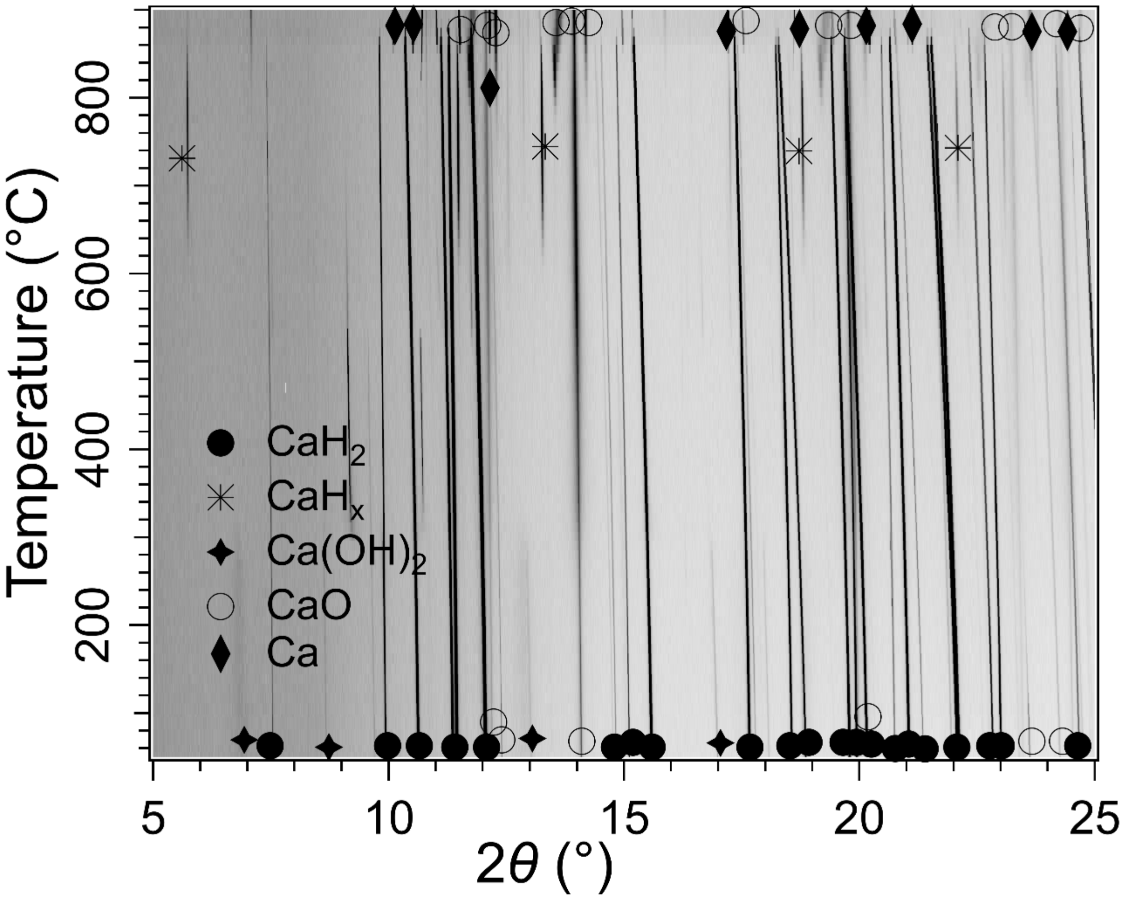

Figure 3.7 *In-situ* SR-XRD pattern of pure CaH_2 with a heating rate of 10 °C/min (λ= 0.58974 Å).

3.2.5 Thermodynamic properties of CaH_2

As explained in section 3.1.5, the initial thermodynamic studies from several authors show disagreement in results with no further experimental thermodynamic data measured in recent years. None of the investigators presented the results of the thermodynamics of the CaH_2 system in liquid and solid states. The temperature ranges for PCI experiments were selected without considering the melting points of both Ca and CaH_2 that may affect the thermodynamic values of the decomposition reaction. In this study, the solid to the liquid phase transition of CaH_2 was found experimentally at 816 °C, as shown in section 3.2.3; therefore, the thermodynamic measurements were carried out in two sets: (1) Above the melting point where CaH_2 is in a liquid state (2) below the melting point, that of solid CaH_2.

Determining the thermodynamics of CaH_2 was a difficult task due to the extremely slow kinetics hence obtaining a complete PCI curve took several weeks. The low equilibrium pressures at the utilised temperatures caused slow kinetics, especially at temperatures below the melting point. In addition, the volatility of Ca after formation from CaH_2 and the formation of solid solutions also caused serious experimental difficulties. The volatile calcium evaporated and deposited on the cooler parts of the reactor, which may cause reabsorption of H_2 that can reduce the observed weight per cent of hydrogen desorbed from the material. The formation of molten surface films on the CaH_2 powder may also inhibit hydrogen desorption. The kinetics of the experiments improved at higher temperatures, although this was constrained by the maximum operating temperature of the furnace (≈ 1000 °C). In addition, intermittent power outages also prevented measurements from lasting longer than required to complete a single PCI curve over 2 to 3 months, while obtaining three full PCI curves for a Van’t Hoff plot was near impossible. One other factor that has been observed while studying CaH_2 desorption is a steady increase of pressure at a constant temperature, as mentioned by Huttig *et.al* and Johnson *et.al*.[18-19] Overall, 14 PCI’s were performed to determine the thermodynamics of solid and molten CaH_2, with the best three being plotted in Figure 3.8 and 3.9.

3.2.5.1 Thermodynamic properties of molten CaH_2

Figure 3.8 shows the PCI's above the melting points of both Ca (842 °C) and CaH_2 (816 °C) and corresponding Van't Hoff plot. The measurements were conducted at 902, 912 and 932 °C. The step size varied from one day to over 3 days to ensure complete desorption, although, as mentioned previously, this was often impossible (Figure 3.8(c)). The corresponding enthalpy and entropy from the Van't Hoff plot were calculated as $\Delta H_{des} = 216 \pm 10$ kJ.mol^{-1} H_2, $\Delta S_{des} = 177 \pm 9$ J.K^{-1}.mol^{-1} H_2. Therefore, the equilibrium desorption temperature is T_{des} at 1 bar = 947 ± 48 °C.

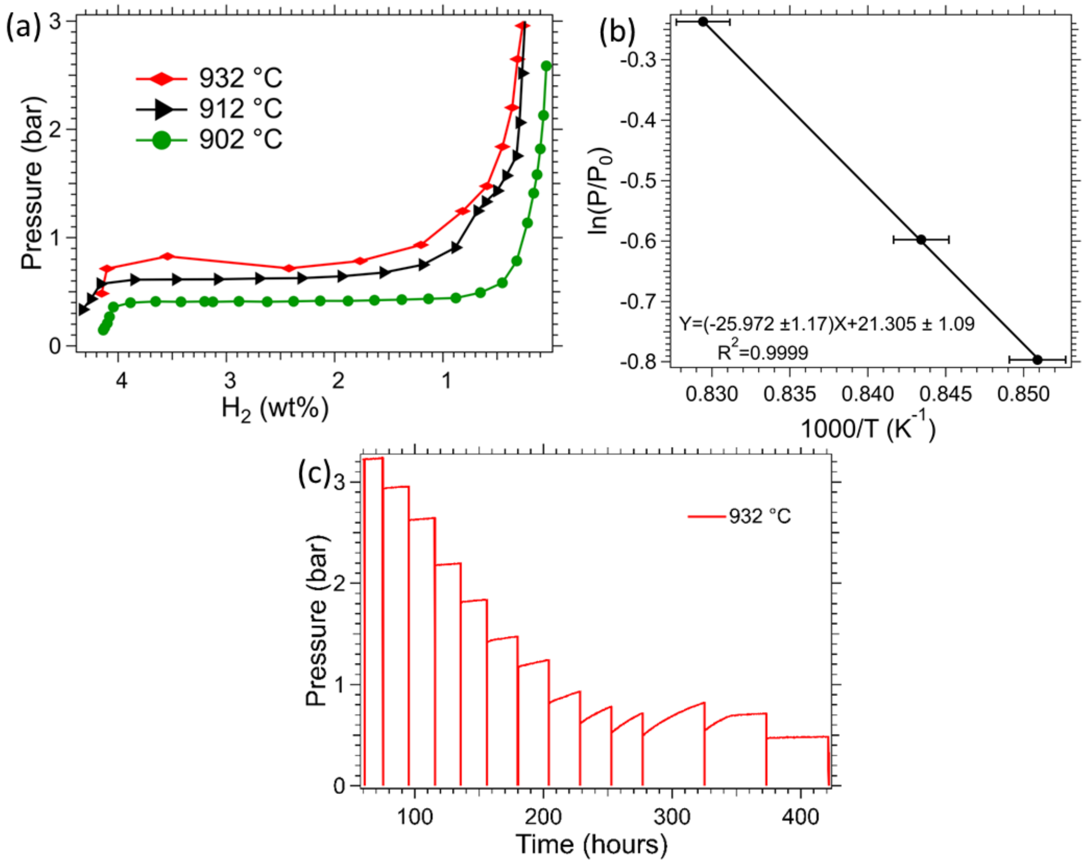

Figure 3.8 (a) PCI’s at 902, 912, 932 °C, and corresponding (b) Van’t Hoff plot of molten CaH_2 (c) equilibrium pressure curves for 932 °C.

3.2.5.2 Thermodynamic properties of solid CaH_2

As mentioned in the previous section, thermodynamic investigations were repeated for temperatures below the melting points of both Ca and CaH_2. Figure 3.9(a) shows the PCI's at three different temperatures of 788, 800 and 807 °C. The PCI curves clearly show that the decomposition of the CaH_2 system occurs in two steps at temperatures below the melting point that may support the type 2 equilibrium explained in section 3.1.5. Unfortunately, despite several attempts, it was not possible to finish measuring the PCI curves. This is due to the extremely slow reaction kinetics; the waiting time for each step varied from 3 days to 3 weeks and was still not enough to complete the hydrogen desorption (as shown in Figure 3.9 (c)). The Van’t Hoff plot for the second plateau region of the PCI curves was constructed (Figure 3.9(b)), and corresponding enthalpy and entropy were calculated as $\Delta H_{\mathrm{des}} = 172 \pm 12$ kJ.mol^{-1} H_2, $\Delta S_{\mathrm{des}} = 144 \pm 10$ J.K^{-1}.mol^{-1} H_2 and hence, the equilibrium desorption temperature is T_{des} at 1 bar = 921 ± 63 °C.

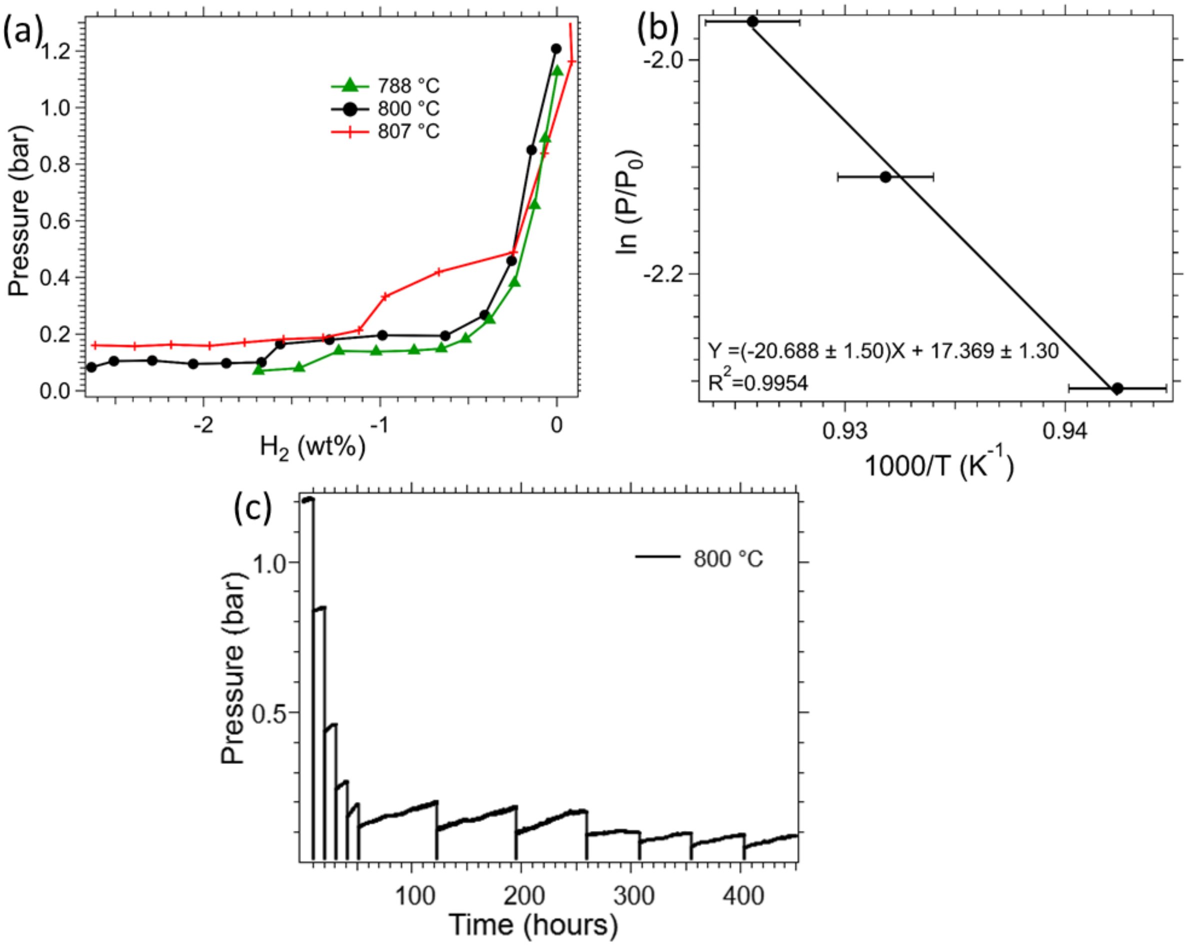

Figure 3.9 (a) PCI's at 788, 800, 807 °C, and corresponding (b) Van't Hoff plot of solid CaH_2 (c) equilibrium pressure curves for 800 °C.

3.2.6 Comparison thermodynamic properties with literature works

A comparison of the present thermodynamic studies of molten and solid CaH_2 with literature work is presented in Figure 3.10. The grey line in figure 3.10 represents the melting point of CaH_2. It is clear from figure 3.10, all the previous studies were performed across the melting point. If the lowest temperature values for the thermodynamics of Hurd and walker [12] (214 $kJ.mol^{-1}$. H_2 and 171 $J.mol^{-1}.K^{-1}.H_2$) are excluded the temperature range above the melting point of CaH_2 match with molten CaH_2 values calculated in this study, within the uncertainty limit. Moreover, the uncertainty in these numbers may be underestimated as the desorption steps may not have been complete. The values in the literature may also be underestimated, although this is difficult to ascertain as no kinetic curves have been published. For example, Curtis *et. al.* mention that 12 to 16-hour steps were used during the experiment for temperatures above 880 °C.[8] The majority of investigators discussed the presence of CaH_x and condensed phase with a composition of $nCa.CaH_2$ or $nCaH_2.Ca$. The current investigation also supports the formation of CaH_x as shown in the *in- situ* SR-XRD studies and found that the dissociation of CaH_2 occurs in two steps at lower temperatures (below 816 °C) and one single step at higher temperatures (above 816 °C). The studies which don't support the formation of sub hydride (CaH) interpreted the two-step dissociation as shown in Equations 3-5 and 3-6.[18] Moreover, the present studies also agree with Stubbs opinion that there is no true equilibrium in the CaH_2 system, since it may change depending on the physical and chemical conditions.[18]

$CaH_2 \rightleftharpoons$ solution rich in $CaH_2 + H_2$ (g) 3-5

Solution rich in $CaH_2 \rightleftharpoons$ solution poor in $CaH_2 + H_2$ (g) 3- 6

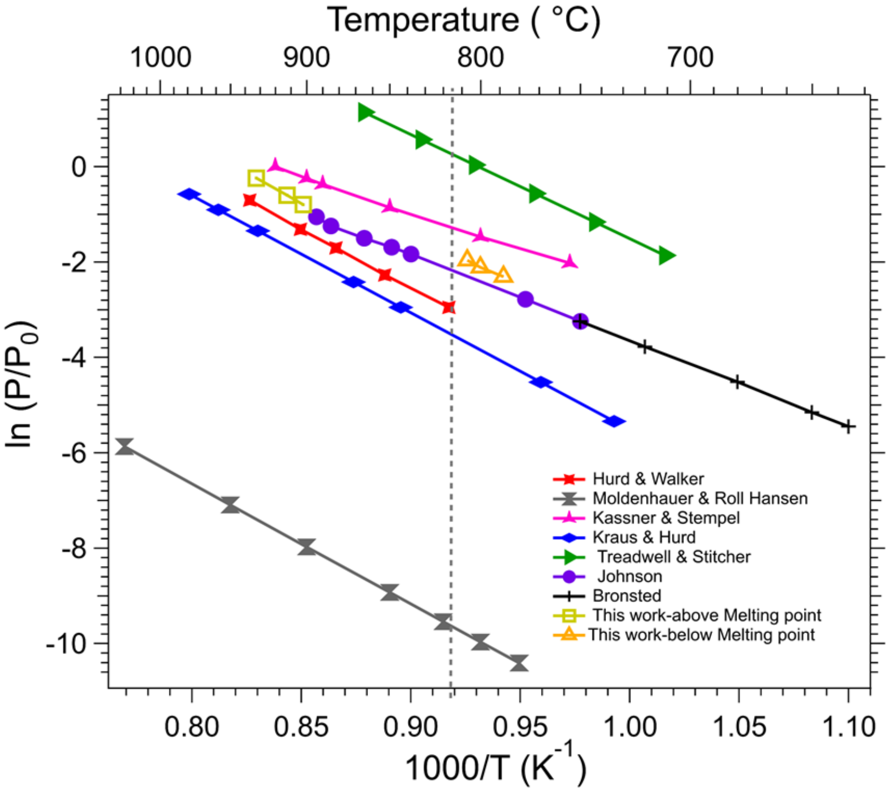

Figure 3.10. Comparison of thermodynamic properties of the present studies with literature works.[1, 12-21] The grey hashed line illustrates the melting point of CaH_2.

3.2.7 Kinetic studies

All the initial studies on the CaH_2 system have focused on determining thermodynamics, while no studies have determined the activation energy for the desorption of H_2 from the CaH_2 system. Therefore, Differential scanning Calorimetry (DSC) analysis was performed on the ball-milled CaH_2 using a Netzsch (STA 449 F3 Jupiter) under Ar flow of 40 mL/min using an Al_2O_3 crucible. Before entering the DSC, the Ar was passed through a Zr filter (heated to 200 °C) to reduce impurities in the gas stream. Figure 3.11(a) shows the DSC data measured at three different heating rates of 10, 20 and 25 °C/min. Each DSC curve shows two peaks. The first peak temperature was identical at all heating rates, indicating the solid-liquid phase transition of $CaH_{2,}$ while the second peak was attributed to the decomposition of CaH_2. The melting peak determined by DSC is 802 °C, which is lower than the value of 816 °C obtained from the melting point analysis (section 3.2.3). Sample contamination often causes a reduction in melting point.[27] In this instance may be caused by residual impurities in the Ar flow or by slight oxidation of the sample that occurred while transferring the crucible from the glovebox to the DSC instrument.

The Kissinger method was employed to calculate the activation energy of the CaH_2 system.[28-29] The three different heating rates and the corresponding peak temperature of decomposition were used to graph the Kissinger plot, as shown in Figure 3.11(b). The activation energy of the CaH_2 system was calculated as 203 ± 12 kJ.mol^{-1}. This is a relatively high value compared to other metal hydrides such as MgH_2 of 124 kJ.mol^{-1}.[30] The increased activation energy explains the low reaction rates during the PCI step size to complete from 3 days to weeks.

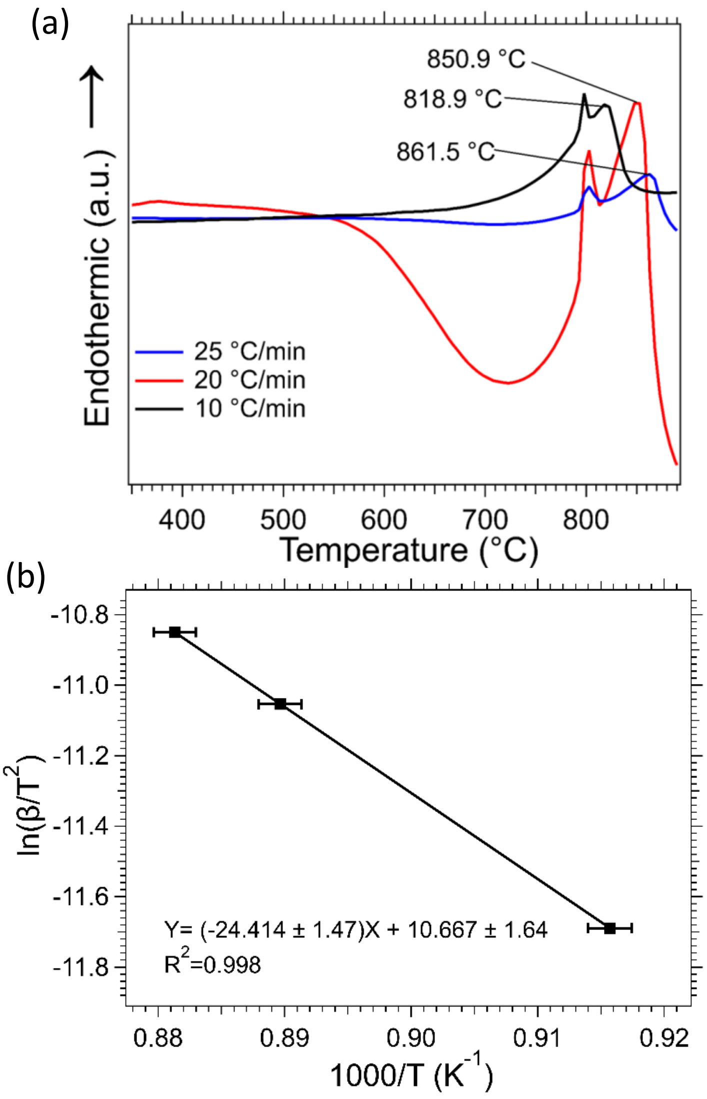

Figure 3.11 (a) Differential scanning calorimetry pattern of CaH_2 system (b) corresponding Kissinger plot for CaH_2 system.

3.3 Summary

A critical assessment has been made on the previous studies of the CaH_2 system. A complete literature review of the thermodynamic studies of CaH_2 has been detailed. As such, very little research has been carried out on the CaH_2 system since the 1960s. Several investigators reported different results and conclusions about the thermodynamic properties of the system. All the thermodynamic studies were completed without considering the melting point of Ca and CaH_2. Hence, the primary purpose of this study is to determine the thermodynamics of both liquid and solid CaH_2.

A complete experimental investigation was performed on the system. The melting point of CaH_2 is determined as 816 ± 2 °C using a thermal ramp experiment inside a Sievert's apparatus. The thermodynamics of CaH_2 above and below this point has been determined. The molten CaH_2 has high enthalpy and entropy values compared to solid CaH_2. The PCI curves below 816 °C show a two-step decomposition that may support the sub hydride theory for CaH presence. *In-situ* SXRD studies also indicate the presence of the compound CaH_x below 810 °C. The activation energy of the system is calculated from the Kissinger plot as 203 ± 12 $kJ.mol^{-1}$, which is a high value compared to other metal hydrides. This explains the long waiting times for desorption during the PCI, especially at low temperatures. The slow reaction kinetics, the solubility of Ca in CaH_2 and vice versa (formation of condensed mixture phase), allotropic transformations of both Ca and CaH_2, volatile nature of Ca, corrosiveness nature of CaH_2 and the high-temperature requirement for a reasonable pressure makes the Ca-CaH_2 system complicated and challenging to investigate.

3.4 References

1. Kilb, E. P. Literature Survey on Calcium Hydride. University of Arizona, **1959**.
2. Brauer, G., Handbook of Preparative Inorganic Chemistry V2; Elsevier, **2012**; Vol. 2.
3. Rittmeyer, P.; Wietelmann, U., Hydrides. *Ullmann's Encycl. Ind. Chem.,* **2000**.
4. Manickam, K.; Mistry, P.; Walker, G.; Grant, D.; Buckley, C. E.; Humphries, T. D.; Paskevicius, M.; Jensen, T.; Albert, R.; Peinecke, K., Future Perspectives of Thermal Energy Storage with Metal Hydrides. *Int. J. Hydrogen Energy,* **2019**, *44*, 7738-7745.
5. Balakrishnan, S.; Sofianos, M. V.; Humphries, T. D.; Paskevicius, M.; Buckley, C. E, Thermochemical Energy Storage Performance of Zinc Destabilised Calcium Hydride at High-Temperatures. *Phys. Chem. Chem. Phys.,* **2020**.
6. Bulanov, A.; Troshin, O. Y.; Balabanov, V., Synthesis of High-Purity Calcium Hydride. *Russ. J. Appl. Chem.,* **2004**, *77*, 875-877.
7. Harries, D. N.; Paskevicius, M.; Sheppard, D. A.; Price, T. E. C.; Buckley, C. E., Concentrating Solar Thermal Heat Storage Using Metal Hydrides. *Proceedings of the IEEE* **2011**, *100*, 539-549.
8. Curtis, R.; Chiotti, P., Thermodynamic Properties of Calcium Hydride1. *J. Phys. Chem.* **1963**, *67*, 1061-1065.

9. Lide, D. R., *CRC* Handbook of Chemistry and Physics; *CRC press*, 2004; Vol. 85.
10. Peterson, D.; Fattore, V., Calcium-Calcium Hydride Phase System1. *J. Phys. Chem.* **1961**, *65*, 2062-2064.
11. Wang, K.; Du, J.; Kong, X.; Zeng, X.; Zou, J.; Li, Z.; Wu, Z., Ab Initio and Thermodynamic Investigation on the Ca-H System. *Int. J. Hydrogen Energy*, **2011**, *36*, 13632-13639.
12. Hurd, C. B.; Walker, K. E., The Thermal Dissociation of Calcium Hydride. *J. Am. Ceram. Soc.*, **1931**, *53*, 1681-1689.
13. Moldenhauer, W.; Roll-Hansen, C., Über Calciumwasserstoff. *Zeitschrift für anorganische Chemie*, **1913**, *82*, 130-140.
14. Kaßner, G.; Stempel, B., Über Die Aufnahme Von Wasserstoff Durch Calcium Und Seine Legierungen. *Zeitschrift für anorganische und allgemeine Chemie*, **1929**, *181*, 83-94.
15. Kraus, C. A.; Hurd, C. B., Equilibria in Systems Involving Calcium, Hydrogen and Nitrogen. *J. Am. Ceram. Soc.*, **1923**, *45*, 2559-2574.
16. Treadwell, W.; Sticher, J., Über Den Wasserstoffdruck Von Calciumhydrid. *Helvetica Chimica Acta*, **1953**, *36*, 1820-1832.
17. Bronsted, J., Thermodynamics of Calcium Hydride Formation. *Z. Elektrochem. Angew. Phys. Chem*, **1914**, *20*, 81-83.
18. Johnson, W. C.; Stubbs, M. F.; Sidwell, A. E.; Pechukas, A., The Rate of Formation and the Dissociation of Calcium Hydride. *J. Am. Ceram. Soc.*, **1939**, *61*, 318-329.
19. Hüttig, G. F.; Brodkorb, F., Studien Zur Chemie Des Wasserstoffes. Iv. Zur Kenntnis Des Kupferhydrids. *Zeitschrift für anorganische und allgemeine Chemie*, **1926**, *153*, 235-245.
20. Ephraim, F.; Michel, E., Über Metallhydride Ii. Hydride Der Erdalkalimetalle Und Des Lithiums. *Helvetica Chimica Acta*, **1921**, *4*, 900-924.
21. Wang, M.; Sun, W.; Sha, C.; Hu, B.; Du, Y.; Sun, L.; Xu, H.; Wang, J.; Liu, S., Thermodynamic Modeling of the Li-H and Ca-H Systems. *J. Phase Equilib. Diffus.*, **2012**, *33*, 89-96.
22. Stanford Research Systems. https://www.thinksrs.com/products/vac.html (accessed October 2021).
23. Pathak, P.; Vasavada, N., Thermal Expansion of Nacl, KCl and CsBr by X-Ray Diffraction and the Law of Corresponding States. *Acta Crystallogr., Sect. A: Cryst. Phys., Diffr., Theor. Gen. Crystallogr.*, **1970**, *26*, 655-658.

24. Suh, I.-K.; Ohta, H.; Waseda, Y., High-Temperature Thermal Expansion of Six Metallic Elements Measured by Dilatation Method and X-Ray Diffraction. *J. Mater. Sci.* **1988**, *23*, 757-760.
25. Hansen, B. R.; Møller, K. T.; Paskevicius, M.; Dippel, A.-C.; Walter, P.; Webb, C. J.; Pistidda, C.; Bergemann, N.; Dornheim, M.; Klassen, T., *In-Situ* X-Ray Diffraction Environments for High-Pressure Reactions. *J. Appl. Crystallogr.* **2015**, *48*, 1234-1241.
26. Griffond, A. C. M. Concentrating Solar Thermal Storage Using Metal Hydride: Study of Destabilised Calcium Hydrides. Curtin University, **2019**.
27. Brittain, C. Using Melting Point to Determine Purity of Crystalline Solids. https://www.chm.uri.edu/mmcgregor/chm228/use_of_melting_point_apparatus.pdf (accessed July **2021**).
28. Kissinger, H. E., Reaction Kinetics in Differential Thermal Analysis. *Anal. Chem.*, **1957**, *29*, 1702-1706.
29. Blaine, R. L.; Kissinger, H. E., Homer Kissinger and the Kissinger Equation. *Thermochim. Acta*, **2012**, *540*, 1-6.
30. Perejón, A.; Sánchez-Jiménez, P. E.; Criado, J. M.; Pérez-Maqueda, L. A., Magnesium Hydride for Energy Storage Applications: The Kinetics of Dehydrogenation under Different Working Conditions. *J. Alloys Compd.*, **2016**, *681*, 571-579.

Chapter 4

Destabilised calcium hydride as a promising high-temperature thermal battery

S. Balakrishnan, M.V. Sofianos, M. Paskevicius, M.R. Rowles and C.E. Buckley, Destabilised Calcium Hydride as a Promising High-Temperature Thermal Battery, *J. Phys. Chem. C*, 2020, **124**, 17512-17519. **https://doi.org/10.1021/acs.jpcc.0c04754**

Abstract

Calcium hydride (CaH_2) is considered an ideal candidate for thermochemical energy storage (thermal battery) due to its high energy density and low cost. Its very high operating temperature, and poor cycling stability are the main factors that hinder its development and implementation as a thermal battery for concentrated solar power (CSP) plants. In this work, CaH_2 was thermodynamically destabilised with aluminium oxide (Al_2O_3) at a 1:1 molar ratio to release hydrogen at a lower temperature than the hydride alone. Temperature programmed desorption measurements showed that the addition of Al_2O_3 destabilised the reaction thermodynamics of hydrogen release from CaH_2 by reducing the decomposition temperature to ≈ 600 °C in comparison to 1000 °C for pure CaH_2 at 1 bar H_2 pressure. The experimental enthalpy and entropy of this system were determined by pressure composition isotherm measurements between 612 and 636 °C. The enthalpy was measured to be $\Delta H_{\mathrm{des}} = 100 \pm 2$ kJ.mol^{-1} H_2 and entropy $\Delta S_{\mathrm{des}} = 110 \pm 2$ J.K^{-1}mol^{-1} H_2. The XRD after TPD and *in-situ* XRD data confirmed the main product as $Ca_{12}Al_{14}O_{33}$. The system exhibited a loss of capacity during hydrogen cycling at 636 °C, which was found to be due to the sintering of excess Al_2O_3, as confirmed by X-ray diffraction and scanning electron microscopy. The hydrogen cycling capacity was significantly improved by reducing the initial amount of Al_2O_3 to a 2:1 molar ratio of CaH_2 to Al_2O_3, deeming it as a highly promising high-temperature thermal battery for the next generation of CSP plants.

4.1 Introduction

There is an increasing trend of energy consumption across the world, and according to the International Energy Agency, the global energy demand rose by 2% in 2017.[1] This has been the fastest rise during the decade, and an urgent requirement for managing the emerging energy crisis, as well as global warming, has been deemed essential. Renewable energy such as solar, wind, geothermal and biomass are encouraged in every country. Among these, solar energy is by far the most prominent solution for addressing present and emerging problems such as climate change, pollution and energy insecurity since it is unlimited, clean, and available in almost all parts of the world.[2-5] However, there are many problems associated with its use mainly it is a dilute form of energy, and its availability varies widely over time. Consequently, large collection areas and storage are required.[5-6]

Solar photovoltaic cells (PV) and concentrated solar power (CSP) are the two most mature technologies that utilise sunlight directly to produce electricity. From the 1990s, PV played a

central role, while CSP gained attention in recent years and is growing at a 40% annual rate.[7] Compared with PV systems, CSP has a higher life span, and on a large scale, storing heat energy is cheaper than storing electrical energy.[8, 9] The integration of a thermal energy storage system makes CSP dispatchable and unique among all other renewable energy-generating alternatives. The aim of CSP technologies is to concentrate the sun's light using solar receivers and convert it into heat, to create steam, to drive turbines or engines, which generate electricity.[8, 9] Due to the intermittent nature of solar power, a reliable energy storage system is required to overcome this instability in power generation and to meet grid demand.[10] The selection of a suitable thermal energy storage (TES) system is the focus of CSP technology. An ideal TES system should possess high energy storage density of 0.5 - 1.0 kWh/kg, and working temperatures above 600 °C, as required for a heat engine to operate at a higher efficiency than the currently operating ones (up to 565 °C) for electricity production.[11]
Sensible, latent and thermochemical energy storage are the three developed thermal energy storage systems for CSP plants. Half of the current CSP plants use mature molten salt storage technology.[7] Molten salts store heat depending on their temperature change, with their maximum operating temperature limited to below ≈ 565 °C.[7, 13-16]

Thermochemical energy storage uses heat from the sun to induce an endothermic chemical reaction. Metal hydrides are one of the most promising next-generation high-temperature thermochemical storage materials. Libowitz *et al.* first studied metal hydrides as thermochemical energy storage systems in 1974.[16.] A large collection of metals can reversibly react with hydrogen over a wide range of temperatures and have theoretical heat storage capacities higher than other thermal energy storage systems (sensible and latent). Even though metal hydrides are potential candidates for the next-generation storage systems for CSP plants, there are many technical challenges, from material selection to engineering issues, that need to be overcome and operate at temperatures > 600 °C. For instance, calcium, barium, strontium and titanium hydrides are some of the systems that can operate in the high-temperature range (> 600 °C) for operation in higher efficiency CSP plants.[17, 18] Calcium hydride has interesting properties, including a high heat of formation 4312 kJ/kg at 25 °C, high thermal gravimetric heat storage capacity 4494 kJ/kg at 950 °C and a low cost compared with other metal hydrides, for instance, cost of pure LiH is 50 US $\$kWh_{th}^{-1}$, and that of CaH_2 is 2.84 US $\$kWh_{th}^{-1}$.[11, 12]

Due to the high energy density and operating temperature, CaH_2 was identified in 2010 as a solar thermochemical storage material.[19] Ward *et al.* showed that CaH_2 could operate as a high-temperature material with $TiFeH_2$ as a hydrogen storage tank while being economically suitable for solar thermochemical energy storage.[17] Unfortunately, its operating temperature is too high (> 1000 °C), and needs to be reduced to below 1000 °C. The melting point of both CaH_2 and Ca metal are 983 °C and 842 °C respectively, and are highly corrosive which could lead to expensive containment vessels.[20-22] The decomposition temperature of CaH_2 can be reduced by adding suitable additives to it, and this process is called thermodynamic destabilisation.[23] Veleckis [24] successfully showed this method in 1981 by adding Al to calcium hydride, where a multistep reaction was detected:

$CaH_2 + 4Al \rightleftharpoons Al_4Ca + H_2$ 4-1

$CaH_2 + Al_4Ca \rightleftharpoons 2Al_2Ca + H_2$ 4-2

The enthalpy of reaction 4-1 was found to be $\Delta H_{des} \approx 74$ kJ.mol^{-1} H_2 at 1 bar of H_2 pressure and 414 °C.[23] In 2017, Ward *et al.*[25] extended this method and demonstrated the feasibility of the Al_2Ca system as a potential high-temperature thermal battery for CSP applications.

This work is the first ever to demonstrate the destabilisation of CaH_2 by adding Al_2O_3, and its contribution to developing novel low-cost and highly-efficient thermal batteries that can operate at the required conditions for the next generation of CSP plants. Aluminium oxide or alumina is the most common naturally occurring thermally stable oxide of aluminium, which is also known as mineral corundum or α-Al_2O_3. Properties such as high melting point, catalytic activity, low cost and abundance in nature make it attractive all over the world for different industrial applications.[26-28] The aim of this study was to focus on the thermal analysis, thermodynamic characterisation and cycling stability of the CaH_2-Al_2O_3 mixture by applying temperature-programmed desorption (TPD), pressure composition isotherms (PCI), *ex-situ* and *in-situ* XRD analysis. The cycling stability of the CaH_2-Al_2O_3 mixture was significantly improved when a 2:1 molar ratio of CaH_2 to Al_2O_3 was achieved. The morphological differences of the sample before and after cycling were studied by field emission scanning electron microscopy (FE-SEM). The experimental enthalpy and entropy for the CaH_2-Al_2O_3 mixture between 612 and 636 °C were calculated, and so was the raw material cost, deeming this system as a highly promising thermal battery for the next generation of CSP plants.

4.2 Experimental methods

4.2.1 Theoretical thermodynamic calculations

HSC Chemistry software[29] was used to initially identify whether the chemical reaction between CaH_2-Al_2O_3 is thermodynamically favourable, without taking into consideration reaction kinetics. The enthalpy, entropy, Gibbs free energy and heat capacity for the different chemical reactions between CaH_2 and Al_2O_3 were calculated. Thermodynamic data for pure elements (Ca, Al) and compounds (CaH_2, Al_2O_3) were collected from Dinsdale *et al.* and Binnewise et al.[30, 31] The phase diagram of CaO-Al_2O_3[32] provided the necessary information regarding the formation of various calcium aluminium oxide compounds at a particular molar ratio at the temperature of interest.

4.2.2 Sample preparation

Metal hydrides are sensitive to moisture and oxygen; therefore, all chemical storage and handling were completed inside an argon-filled glove box (MBraun, Germany), where the H_2O/O_2 levels were less than 1 ppm. The CaH_2-Al_2O_3 mixture was synthesised by ball-milling calcium hydride and aluminium oxide (both purchased from Sigma Aldrich with purity > 95% and > 98 % respectively) in 1:1 and 2:1 molar ratios, under an argon atmosphere at room temperature using an Across International Planetary Ball Mill (PQ-N04) and employing stainless steel vials. An equal number of 10 mm and 6 mm diameter stainless steel balls were used with a 40:1 ball to powder mass ratio. The samples were ball milled for 3 hours at a rotational speed of 400 rpm. The direction of the vial rotation was altered every 30 min without pausing between each rotation.

4.2.3 Sample characterisation

Crystalline phase analysis of the starting materials and the thermally analysed samples was done by *ex-situ* powder X-ray diffraction, using a Bruker D8 Advance diffractometer that uses Cu K_α wavelength radiation (λ = 1.5418 Å, 40 kV, 40 mA). An airtight sample holder covered with a polymethyl methacrylate dome was used for all air and moisture sensitive samples to prevent contamination. Data were collected over a 10° - 80° 2θ range using 0.3° divergence slits and 0.3° antiscattering slits with a 0.03° step size. The counting time was 1.6 s/step associated with a rotational speed of 30 rpm. Bruker EVA and the International Centre for Diffraction Data (ICCD) PDF4 database were used to identify the phases. Quantitative analysis of peaks present in the X-ray diffraction patterns of all samples used was completed with TOPAS software[33] using the Rietveld method.[34] Both ICDD PDF4 and the Crystallography Open Database (COD) were used for structural information.[35]

In-situ X-ray diffraction (λ = 0.7093 Å, Mo-K_α) was conducted on the CaH_2-Al_2O_3 mixture using a Thermo Fisher ARL Equinox 5000 diffractometer by heating from room temperature to 750 °C using a hot air blower with a 2 °C/min heating rate; the sample was cooled at the maximum rate. Data were collected for 60 s exposures while heating and cooling. The powder sample was loaded inside a quartz capillary (0.7 mm outer diameter, 0.01 mm wall thickness), sealed under argon pressure and mounted onto a sample holder. The temperature of the hot air blower was calibrated against the known thermal expansion coefficient of both NaCl and Ag.[36-38]

Temperature programmed desorption-mass spectrometry (TPD-MS) using a Stanford Research Systems (SRS) residual gas analyser (RGA-300) consisting of a quadrupole mass spectrometer was used to detect the gases released from the CaH_2 and CaH_2-Al_2O_3 mixture under high vacuum ($< 7 \times 10^{-4}$ mbar) while heating samples to 900 °C at 5 °C/min. The RGA separates the ionised gas molecules according to their respective masses and measures the ion currents at each mass. A 3 mg sample of pure CaH_2 and CaH_2-Al_2O_3 mixture (1:1 molar ratio) as prepared was taken in the silicon carbide reactor and connected to the RGA mass spectrometer separately and the corresponding analogue scan (partial pressure vs mass to charge ratio) was obtained. Temperature data was collected using a K-type temperature sensor that connected internally to the reactor. The data was collected every 5 s.

Thermal analysis of the CaH_2-Al_2O_3 mixture was also studied by TPD, PCI, and cycling measurements by using a computer-controlled Sieverts apparatus described elsewhere.[39] TPD measurements were conducted from vacuum to an H_2 pressure of 2 bar. PCI measurements were performed between 612 °C and 636 °C with pressure increments of 3 bar after 3 h for 636 °C and 5 h for the rest of the temperatures as waiting time. As the melting point of aluminium is 660 °C[40], the PCI measurements were constrained to < 660 °C to provide consistent thermodynamics. The CaH_2-Al_2O_3 mixtures (1:1 and 2:1 molar ratios) were pressure cycled at 636 °C at a ramping rate 5 °C/min for 10 h steps. The hydrogen pressure increment during charging and discharging was 10 and 3 bar respectively. For the gas measurements, a silicon carbide (SiC) sample cell was used. The hydrogen permeation through SiC cells at high temperature is negligible.[39, 41] All samples were loaded into a stainless-steel sample holder within the SiC sample cell.

The morphological changes of the CaH_2-Al_2O_3 mixtures before and after hydrogen cycling were studied by field emission scanning electron microscopy (FE-SEM) using a Zeiss Neon (40EsB). The specimens were placed onto carbon tape mounted on an aluminium stub inside the argon-filled glove box. To reduce exposure to air, the samples were transferred to the vacuum chamber of the SEM using a custom-made holder.

4.3 Results and discussion

4.3.1 Thermodynamic predictions

Thermodynamic predictions of the CaH_2 destabilisation reaction with Al_2O_3 at different molar ratios were calculated as presented in Table 4.1. The predicted reaction pathways demonstrate favourable reaction enthalpies that might meet the US DOE Sunshot's target for the next-generation TES systems.[42] It is clear that reaction 1 and 2 from Table 1 is the most favourable reaction, according to HSC. These two reactions are favourable in the high-temperature region, and both significantly starts from 400 °C and 500 °C, respectively (Figure 4.1). However, these are thermodynamically favourable according to prediction but have not been tested, and the kinetics are unknown.

Table 4.1 Thermodynamic predictions of the reaction between CaH_2 and Al_2O_3 at 1 bar of H_2 pressure.

No.	Predicted Reaction	Theoretical operating temperature °C	Theoretical H_2 wt%	Enthalpy kJ/kg	Enthalpy ΔH_{des} kJ.mol^{-1} H_2
1	$3CaH_2 + Al_2O_3 \rightleftharpoons 3CaO + 2Al + 3H_2(g)$	510	2.65	1446	110
2	$12CaH_2 + 11Al_2O_3 \rightleftharpoons Ca_{12}Al_{14}O_{33} + 8Al + 12H_2(g)$	375	1.48	760	103
3	$1.5CaH_2 + 2\,Al_2O_3 \rightleftharpoons Ca_{1.5}Al_3O_6 + Al + 1.5H_2(g)$	340	1.13	528	94
4	$1.5CaH_2 + 3.5\,Al_2O_3 \rightleftharpoons Ca_{1.5}Al_6O_{10.5} + Al + 1.5H_2(g)$	240	0.7	307	86
5	$1.5CaH_2 + 9.5Al_2O_3 \rightleftharpoons Ca_{1.5}Al_{18}O_{28.5} + Al + 1.5H_2(g)$	175	0.2	77	79

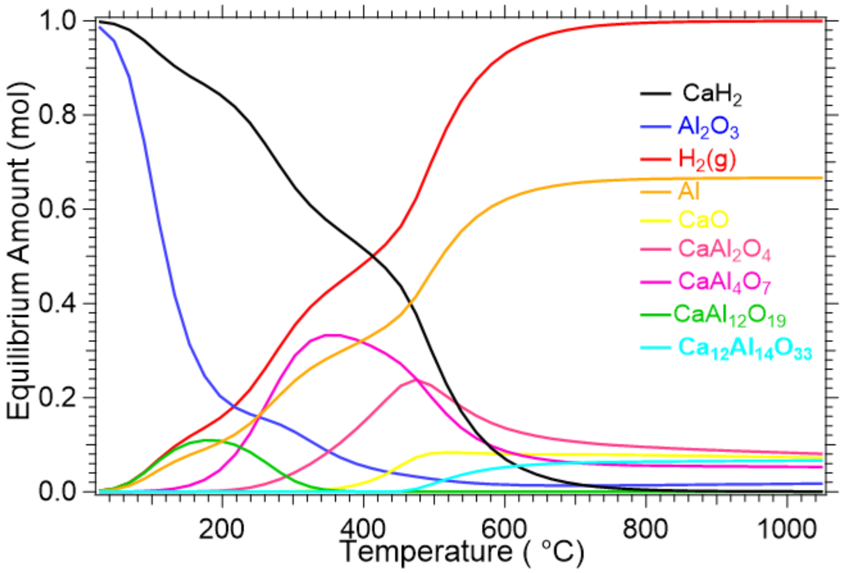

Figure 4.1 Graphical simulation of the CaH_2-Al_2O_3 mixture at 1bar of pressure.

4.3.2 Initial phase analysis

E*x-situ* X-ray diffraction patterns of the starting material (CaH_2 and Al_2O_3), together with the CaH_2-Al_2O_3 mixture (1:1 molar ratio) are presented in Figure 4.2 (a), (b) and (c) respectively. Diffraction patterns were refined by the Rietveld method to determine their purity. It was found that the CaH_2 sample comprised of 91.0 ± 1.5% CaH_2 with 9.0 ± 1.5% CaO as an impurity (Figure 4.3). The diffraction pattern of CaH_2-Al_2O_3 mixture as prepared consisted of only peaks that were assigned to CaH_2 (27.88 ± 0.50 wt%), CaO (0.54 ± 0.20 wt%) and Al_2O_3 (71.58 ± 0.50 wt%) (Figure 4.4), indicating that CaH_2 and Al_2O_3 did not react with each other during ball milling to form a calcium aluminium oxide. The CaO weight percentage in the CaH_2-Al_2O_3 mixture is lower than expected; this may be due to the ball milling process were CaO particles have become smaller and hence their diffraction peaks broaden and are lost in the background. It can be seen that the intensity associated with the diffraction peaks of Al_2O_3 is much higher and narrower than the CaH_2 peaks. This is due to Al_2O_3 being more crystalline than CaH_2.

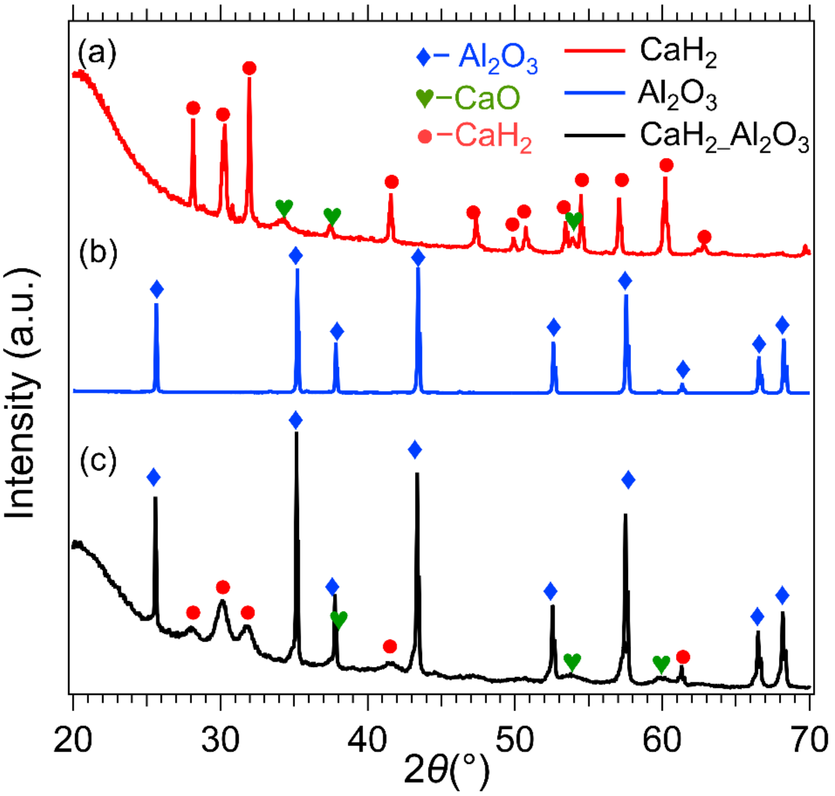

Figure 4.2 *Ex-situ* powder diffraction patterns of (a) CaH_2, (b) Al_2O_3 and (c) CaH_2-Al_2O_3 mixture as prepared using Cu K_α radiation (λ = 1.5418 Å).

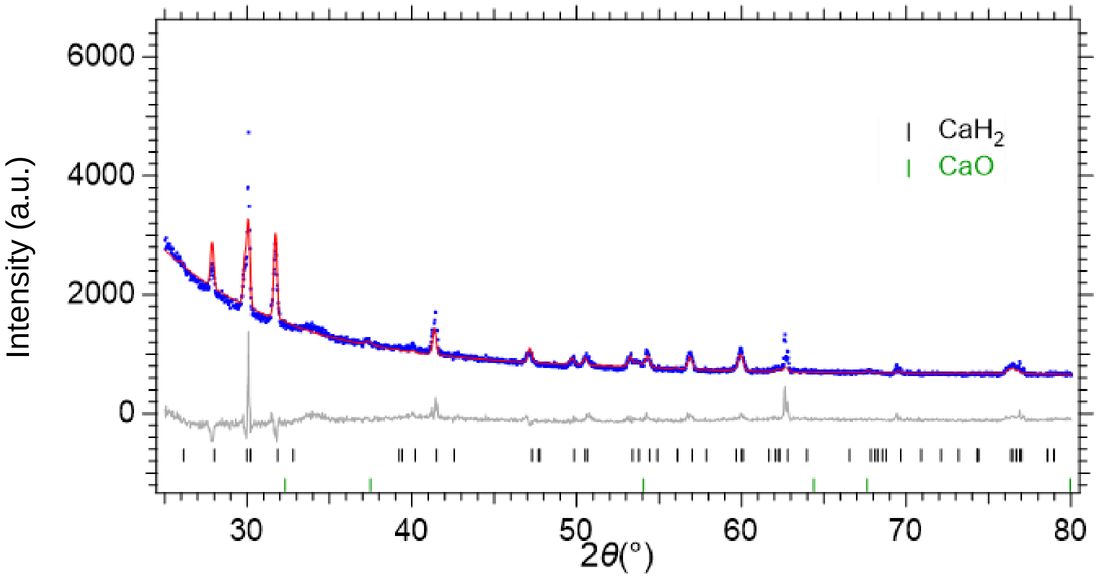

Figure 4.3 Rietveld refinement of the diffraction pattern for pure CaH_2.

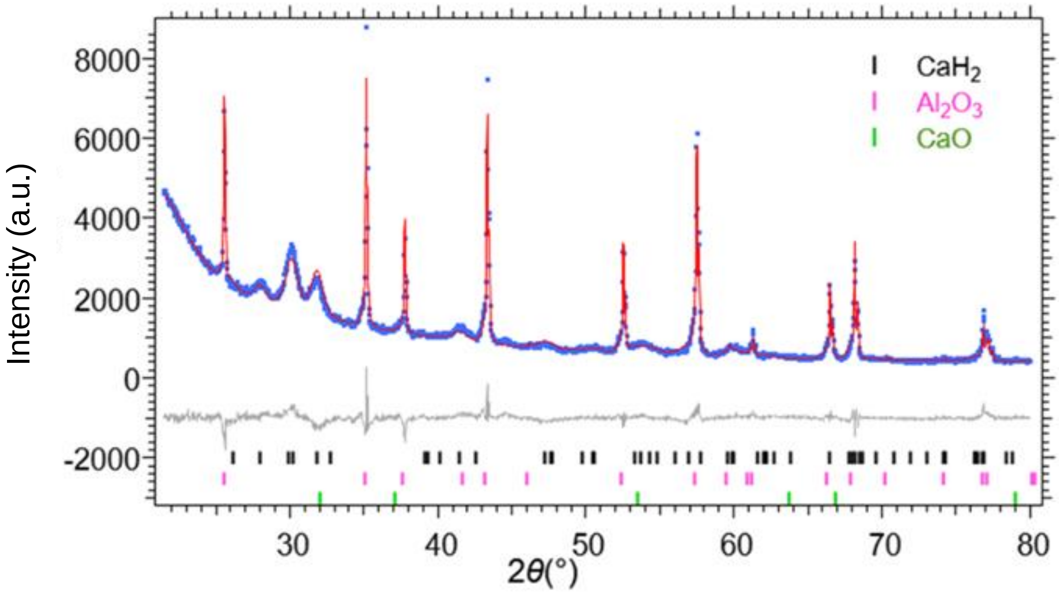

Figure 4.4 Rietveld refinement of the diffraction pattern for the CaH_2-Al_2O_3 mixture after ball milling.

4.3.3 Thermal analysis

TPD-MS measurements were performed on CaH_2 and the CaH_2-Al_2O_3 mixture to both determine and compare their hydrogen desorption profiles. As vacuum was used, CaH_2 started to release hydrogen at 500 °C and reached its highest intensity of desorption at 600 °C (Figure 4.5 (a)). Figure 4.5 (b) shows the hydrogen desorption profile of the CaH_2-Al_2O_3 mixture, with the main peak lowered by ≈ 400 °C in comparison to pure CaH_2. This clearly indicates that the addition of Al_2O_3 to CaH_2 reduces the decomposition temperature. No other gasses were detected by the mass spectrometer in the mass range 1 - 150 amu.

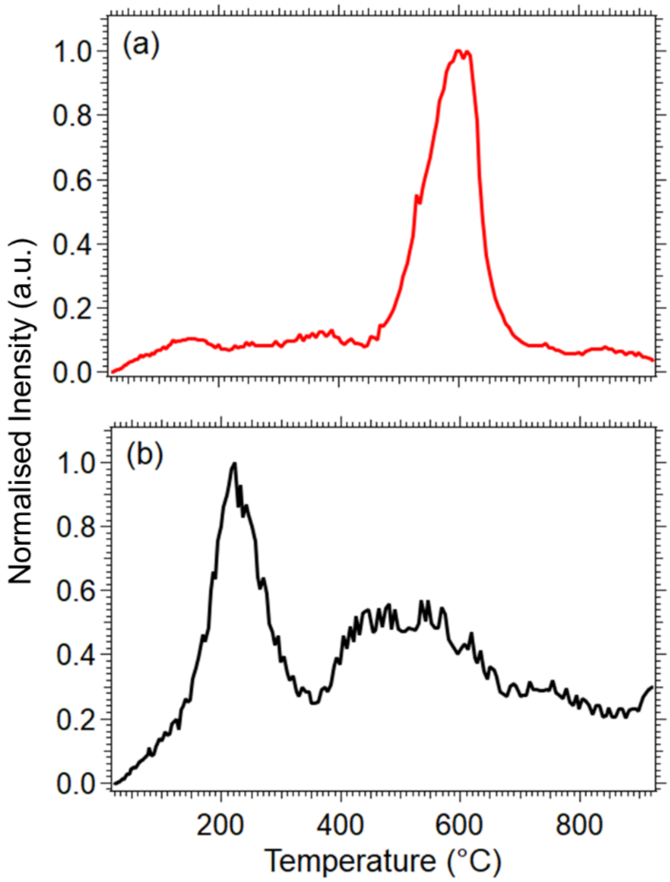

Figure 4.5 Hydrogen desorption profiles as observed by TPD-MS measurements of (a) CaH_2 and (b) the CaH_2-Al_2O_3 mixture in 1:1 molar ratio at a heating rate of 5 °C/min under vacuum.

Temperature programmed desorption was performed from room temperature to 800 °C on the CaH_2-Al_2O_3 mixture. According to Figure 4.6 (b), a small amount of gas is released at lower temperatures (200 - 550 °C) than expected, and it may be due to the presence of impurities. The reaction between CaH_2 and Al_2O_3 becomes significant from ≈ 560 °C reaching maximum hydrogen desorption of 1.2 wt% at ≈ 700 °C (equivalent to 2 bar of H_2 pressure). The measurement started at vacuum and reached its maximum hydrogen desorption value in less than the 7 hours required for the system to reach 800 °C from room temperature, as observed in Figure 4.7 Specifically, the desorption reaction was completed as soon as the required temperature was reached with no further increase in the H_2 wt% was observed after the 6h (Figure 4.7), indicating fast hydrogen desorption kinetics. The mixture was kept at 800 °C for almost 5h with no significant change in the wt% of desorbed hydrogen.

The *in-situ* X-ray diffraction data of CaH_2-Al_2O_3 mixture is presented in Figure 4.6 (a) and compared with the TPD curve (collected separately). From Figure 4.6 (a) it is evident that the reaction between CaH_2 and Al_2O_3 is significant above 500 °C, which is in agreement with the TPD curve in Figure 4.6 (b). In addition, the CaH_2 completely reacts by 500 °C and commences to form a new compound $Ca_{12}Al_{14}O_{33}$.

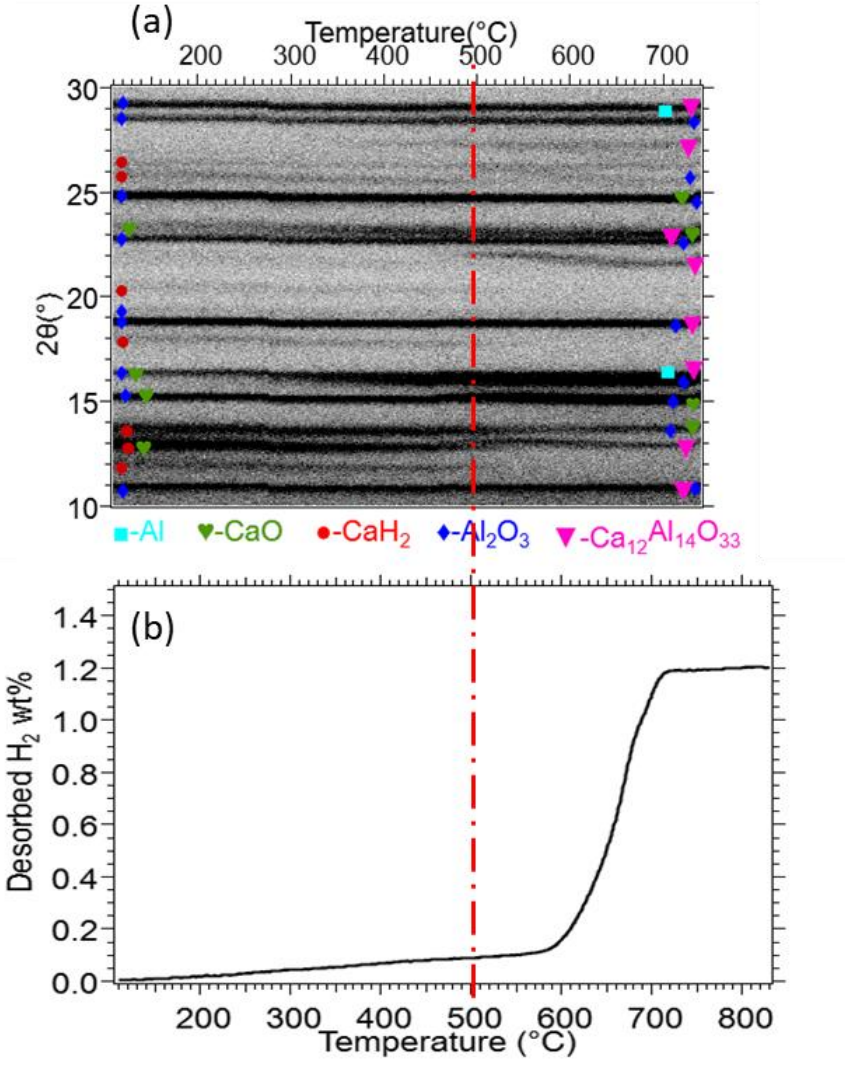

Figure 4.6 (a) *In-situ* X-ray diffraction patterns using Mo K_α of $\lambda = 0.7093$ Å and (b) TPD profiles of the CaH_2-Al_2O_3 mixture from vacuum to a maximum H_2 pressure of 2 bar.

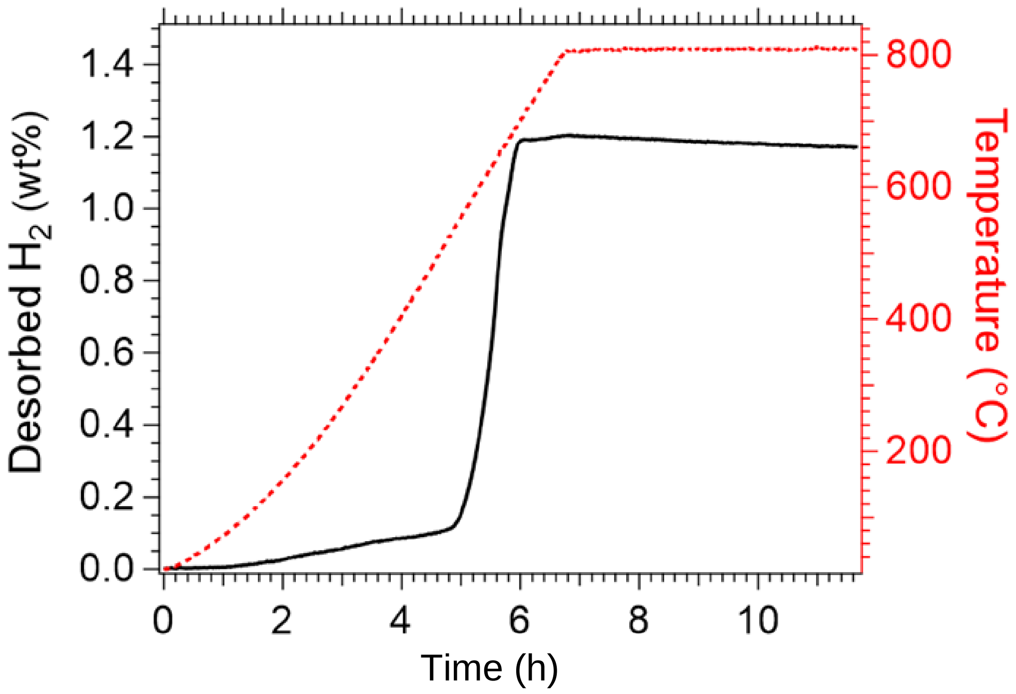

Figure 4.7 TPD profiles of the CaH_2-Al_2O_3 mixture from room temperature to 800 °C at a heating rate of 5 °C/min.

The decomposition products after the TPD measurement for the CaH_2-Al_2O_3 mixture were determined by *ex-situ* X-ray powder diffraction (Figure 4.8) and quantified by the Rietveld refinement method. $Ca_{12}Al_{14}O_{33}$ was the main decomposition product (48.78 ± 0.70 wt%), along with 7.35 ± 0.30 wt% of CaO, 7.93 ± 0.40 wt% of Al and 35.90 ± 0.70 wt% of unreacted Al_2O_3 (Figure 4.9). These experimentally determined decomposition products are the same as predicted in reactions (1) and (2), when combined, as seen in Table 4.1. Hence, the actual destabilisation reaction of CaH_2 with Al_2O_3 is different from the predicted reactions from HSC. Table 4.2 shows the comparison between the predicted and experimental destabilisation reactions for CaH_2 with the addition of Al_2O_3.

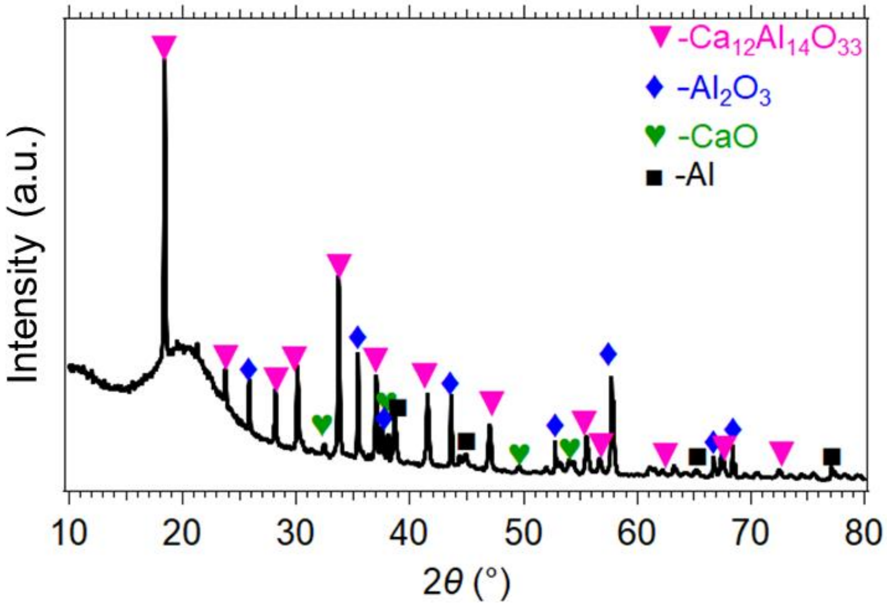

Figure 4.8 *Ex-situ* X-ray diffraction pattern of the CaH_2-Al_2O_3 mixture as prepared after the TPD experiment (Cu Kα, $\lambda = 1.5418$ Å).

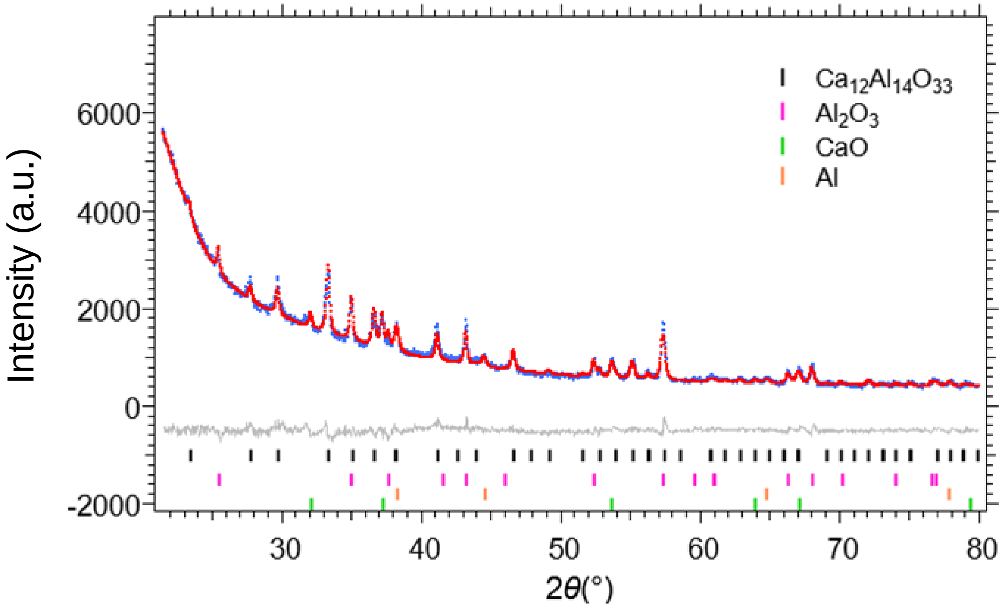

Figure 4.9 Rietveld refinement of the diffraction pattern for the CaH_2-Al_2O_3 mixture after TPD.

Table 4.2 Comparison between theoretical (**Table 4.1**) and experimental reactions (XRD Rietveld data)

Theoretical	**Experimental**
1.$12CaH_2 + 11Al_2O_3 \rightleftharpoons Ca_{12}Al_{14}O_{33} + 8Al + 12H_2(g)$ ΔH_{des} = 102.8 kJ.mol^{-1} H_2, ΔS_{des} = 159.1 J.K^{-1}mol^{-1} H_2	1:1 ratio of CaH_2:Al_2O_3 $CaH_2 + Al_2O_3 \rightleftharpoons \frac{1}{21}Ca_{12}Al_{14}O_{33} + \frac{9}{21}CaO + \frac{2}{3}Al + \frac{1}{3}Al_2O_3 + H_2(g)$ Optimised 3:2 ratio of CaH_2:Al_2O_3
2. $3CaH_2 + Al_2O_3 \rightleftharpoons 3CaO + 2Al + 3H_2(g)$ ΔH_{des} = 110.2 kJ.mol^{-1} H_2, ΔS_{des} = 140.8 J.K^{-1}mol^{-1} H_2	$3CaH_2 + 2Al_2O_3 \rightleftharpoons \frac{1}{7}Ca_{12}Al_{14}O_{33} + \frac{9}{7}CaO + 2Al + 3H_2(g)$ ΔH_{des} = 100 ± 2 kJ.mol^{-1} H_2, ΔS_{des} = 110 ± 2 J.K^{-1}mol^{-1} H_2

Pressure Composition Isotherm (PCI) measurements were performed at three different temperatures (612, 626 and 636 °C) (Figure 4.10 (a)). The Van't Hoff plot (Figure 4.10 (b)) was constructed by taking the mid-point values of each PCI profile (Figure 4.10(a)) as to determine the thermodynamic values (enthalpy and entropy) of the proposed destabilisation reaction. All three PCI profiles (Figure 4.10 (a)) show a slightly slopping pressure plateau, which may influence the engineering of the container as hydrogen absorption and desorption at a constant pressure and temperature is desired due to the simplicity of the system.[43] The kinetic data for the PCI measurements at 636, 626 and 612 °C (Figure 4.11) show that the equilibrium plateau was almost reached after each desorption step. PCI measurements were also obtained at 645 and 655 °C (Figure 4.12), which profiles exhibited slopping plateaus, and as such thermodynamic data from these measurements could not be trustable. The enthalpy and entropy were determined from the Van't Hoff plot as ΔH_{des} = 100 ± 2 kJ.mol^{-1} H_2 and ΔS_{des} = 110 ± 2 J.K^{-1}.mol^{-1} H_2, respectively. The theoretical enthalpy and entropy were, ΔH_{des} = 103 kJ.mol^{-1} H_2, ΔS_{des} = 160 J.K^{-1}.mol^{-1} H_2. The mismatch between the theoretical and experimental values may be due to the different reaction pathways observed between theoretical and experimental. However, for a more definite answer further investigation is required.

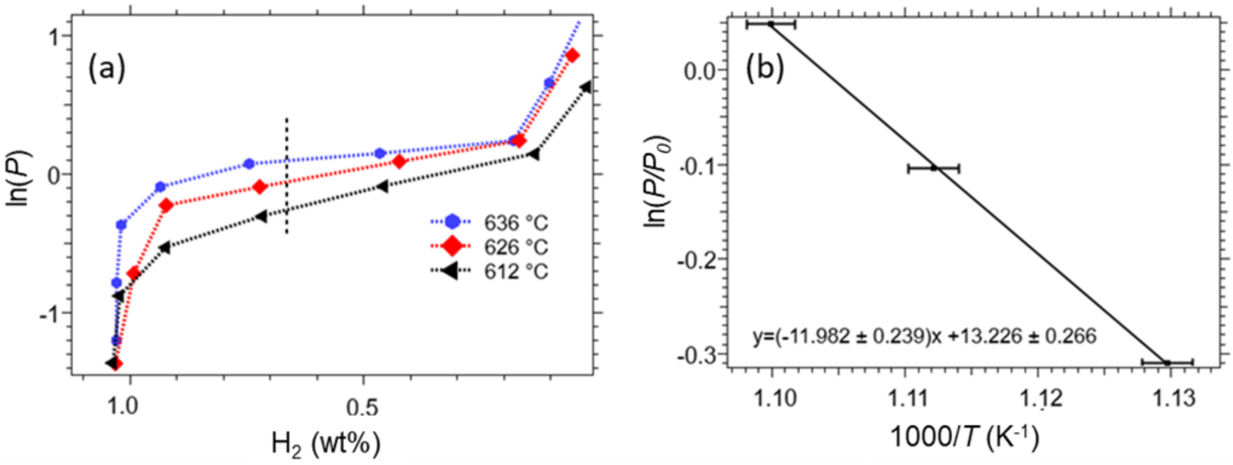

Figure 4.10 (a) Pressure Composition Isotherms of CaH_2-Al_2O_3 mixture at 612 °C (black arrow), 626 °C (red diamond) and 636 °C (blue hexagon) and (b) corresponding Van't Hoff plot.

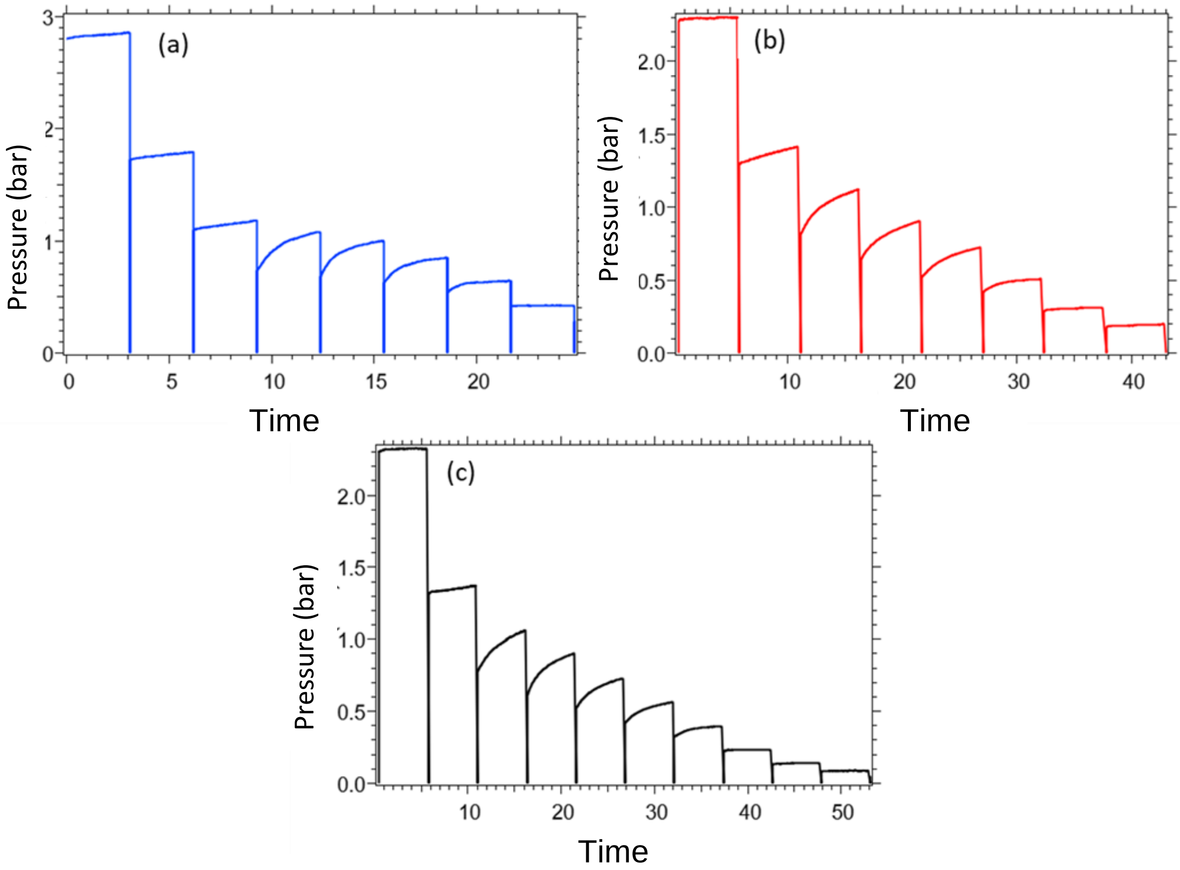

Figure 4.11 Equilibrium pressure curves of PCI performed at (a) 636 °C with a 3 hr, (b) 626 °C with 5 hr and (c) 612 °C with 5 hr desorption step sizes.

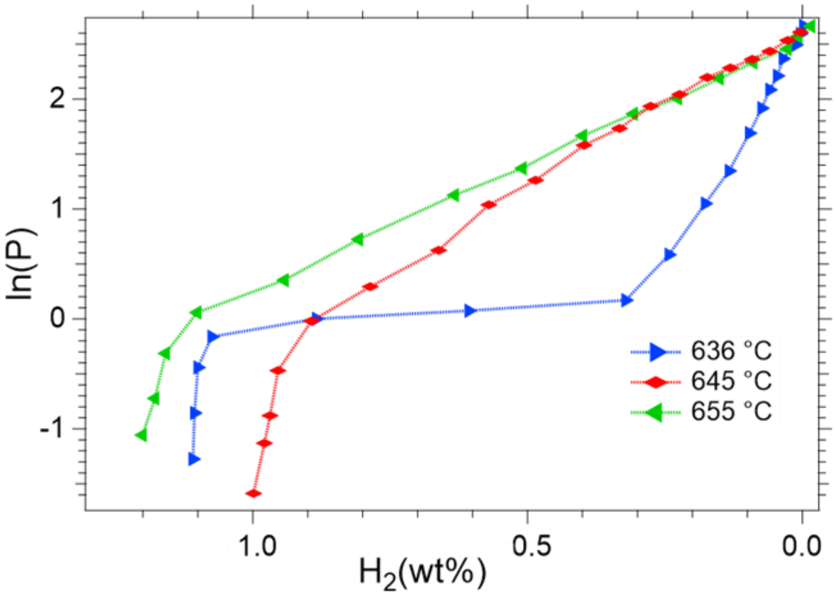

Figure 4.12 Comparison of Pressure Composition Isotherms of the CaH_2-Al_2O_3 mixture between 636, 645 and 655 °C.

In order to check the feasibility of the as prepared CaH_2-Al_2O_3 mixture (1:1 molar ratio) as a high-temperature thermal battery, the mixture was cycled at 636 °C by absorbing and releasing hydrogen. Figure 4.13 shows, four hydrogen desorption/ absorption cycles of the mixture. It is noted that each cycle reaches a plateau, indicating that the kinetics of the desorption and absorption reaction are fast enough to be completed within the 10 h of each step duration. It is evident that after each cycle, the material degrades by 50% in comparison to the previous cycle. After the 3rd cycle, the mixture lost its reversibility with a 90% loss in storage capacity.

The reasons why the hydrogen capacity of the CaH_2-Al_2O_3 mixture degrades may be due to: (i) the presence of excess unreacted alumina (35.6 ± 0.5 wt%) that is present in the cycled mixture (Figure 4.14) that may hinder the reaction kinetics, (ii) the sample may also sinter after heating to high temperature. SEM was utilised to investigate these possibilities. The sintering effect can be seen from the SEM micrographs of the CaH_2-Al_2O_3 mixture before (Figure 4.15 (a)) and after (Figure 4.15 (b)) cycling, where the particle sizes of the cycled mixture are evidently bigger than the ones prior to cycling.

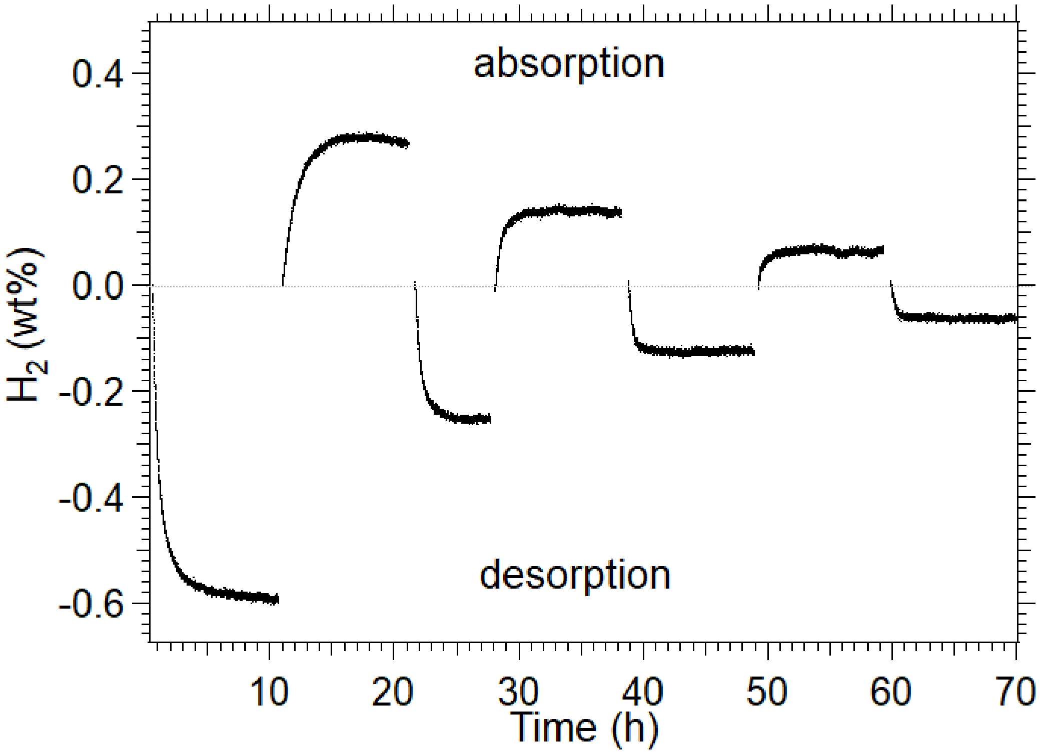

Figure 4.13 H_2 desorption and absorption cycles of the CaH_2-Al_2O_3 mixture at 636 °C.

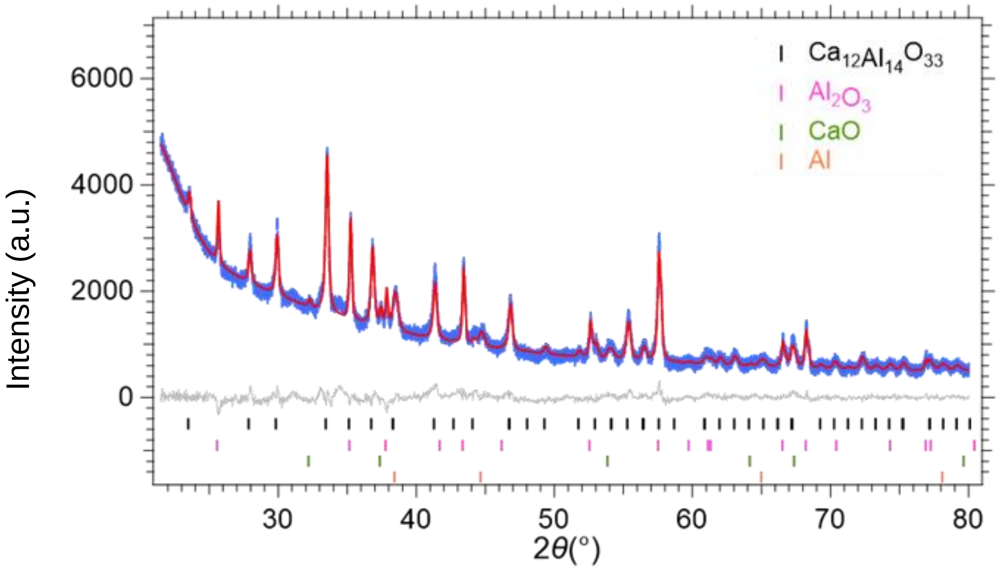

Figure 4.14 Rietveld refinement of the diffraction pattern for the CaH_2-Al_2O_3 mixture after cycling.

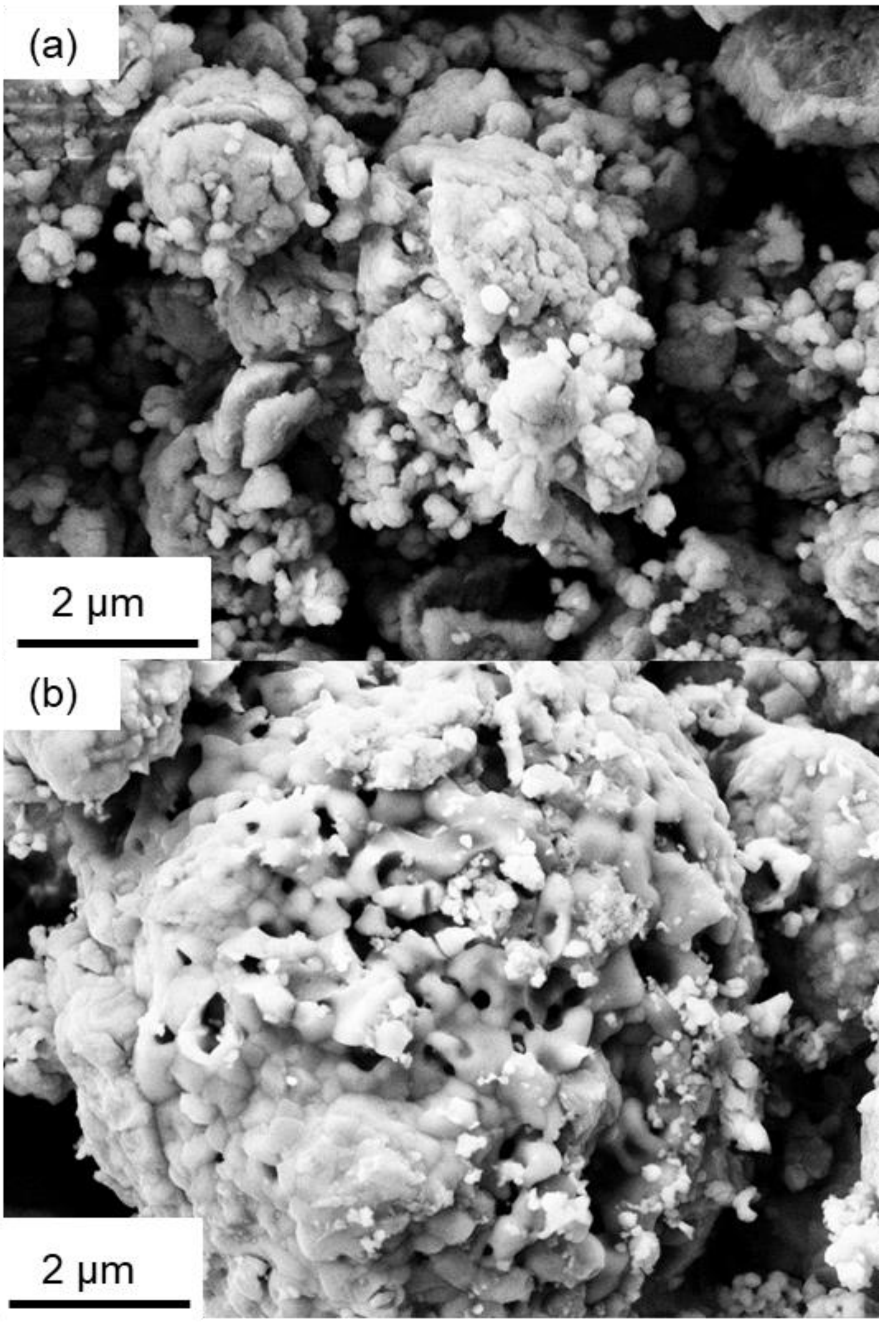

Figure 4.15 Scanning electron micrographs of the CaH_2-Al_2O_3 mixture (1:1 molar ratio) (a) before and (b) after 4 cycles at 636 °C.

In order to improve the reversibility of the CaH_2-Al_2O_3 system a new mixture of CaH_2 and Al_2O_3 was synthesised in a 2:1 molar ratio to minimise the quantity of excess Al_2O_3. The $2CaH_2$-Al_2O_3 mixture showed significant improvement regarding its cyclic hydrogen reversibility as seen in both Figure 4.16 and the comparative figure of the two molar ratios (Figure 4.17), without much loss in hydrogen storage capacity, deeming this new mixture promising as a high-temperature thermal battery for CSP applications. It is noted from the same figure that each cycle has not reached a plateau, indicating that the kinetics of the desorption and absorption reaction are not fast enough to be completed within the 10 h of each step duration. This phenomenon could be due to the sample sintering as observed in Figure 4.18. Moreover, the unreacted Al_2O_3 left over after cycling was reduced to 5.5 ± 0.3 wt% (Figure 4.19) compared to 35.6 ± 0.5 wt% in the first mixture.

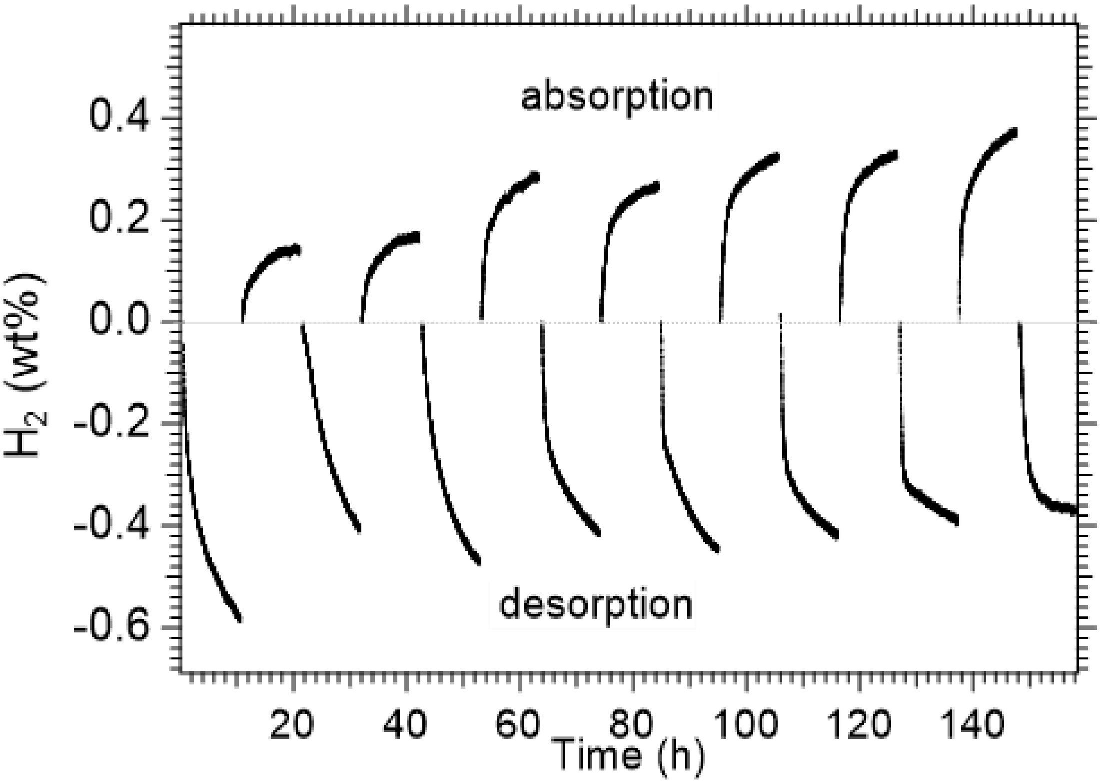

Figure 4.16 H_2 desorption and absorption cycles of the $2CaH_2$-Al_2O_3 mixture at 636 °C.

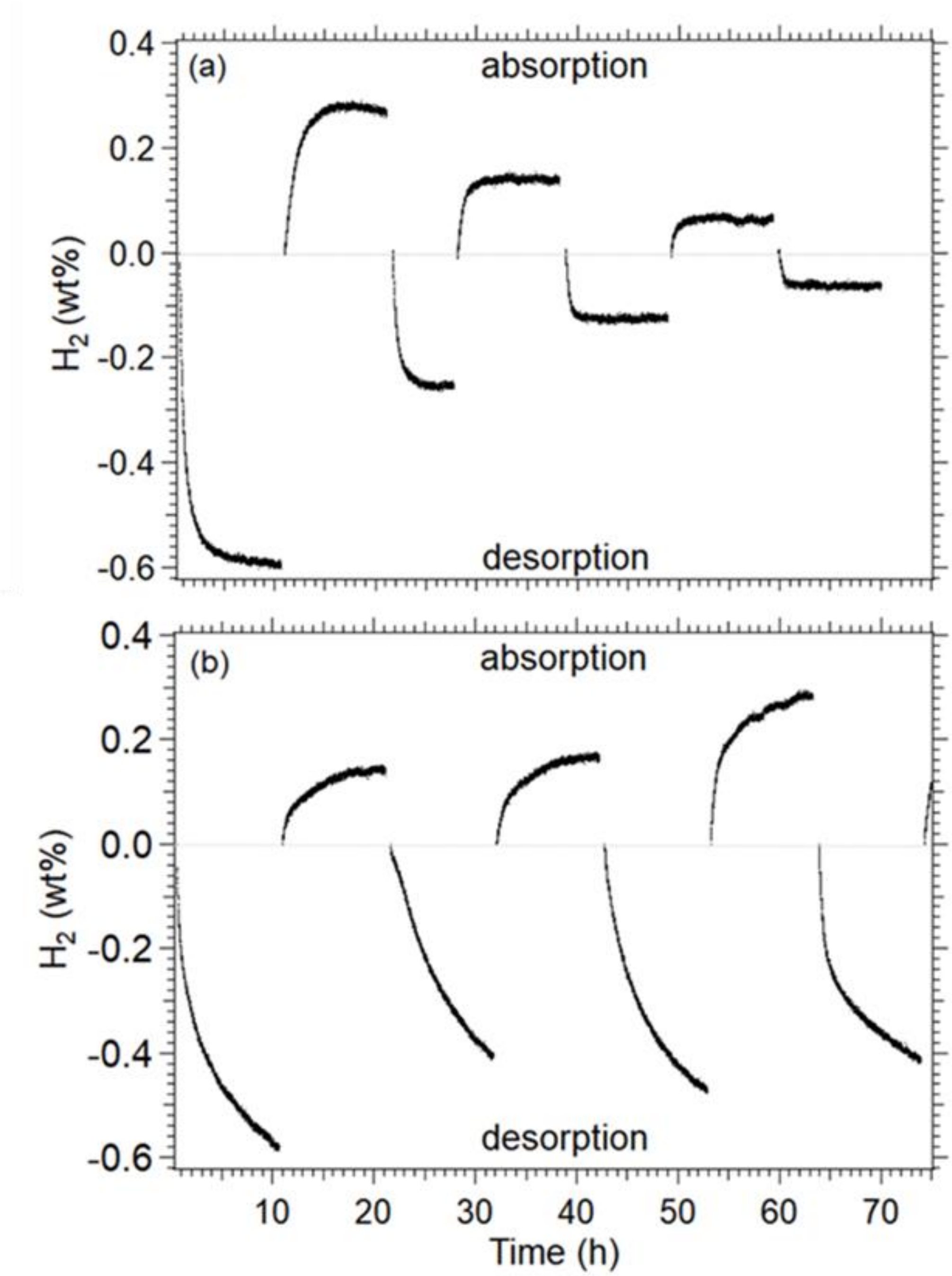

Figure 4.17 Comparison of cycling studies between the (a) 1:1 and (b) 2:1 CaH_2 to Al_2O_3 molar ratios at 636 °C.

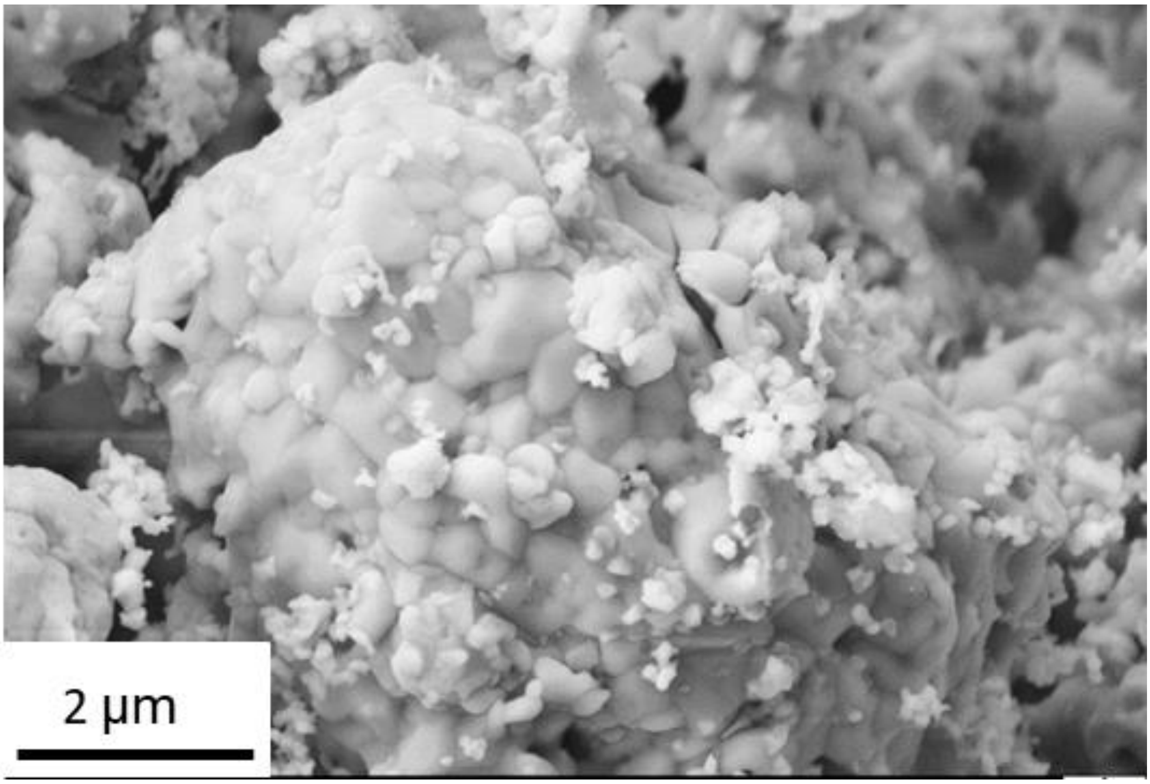

Figure 4.18 Scanning electron micrographs of the $2CaH_2$-Al_2O_3 mixture after cycling at 636 °C.

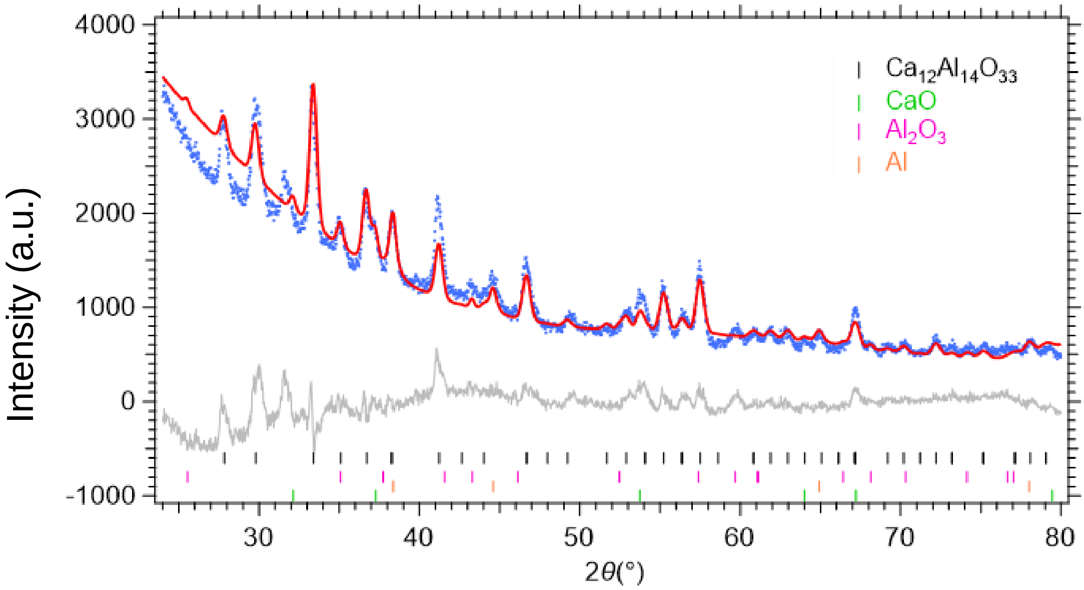

Figure 4.19 Rietveld refinement of the diffraction pattern for the $2CaH_2$-Al_2O_3 mixture after cycling.

Table 4.3 shows a comparison of the CaH_2-Al_2O_3 mixture with pure CaH_2 and the CaH_2-2Al system in terms of cost and operating conditions. It can be seen that the CaH_2-Al_2O_3 mixture operates at a high temperature and low pressure (636 °C at 1 bar) and is a low-cost material making it a promising high-temperature thermal battery for the next generation of CSP applications.

Table 4.3 A comparison of three systems in terms of cost and operating conditions.

	Δ*H* (kJ.mol^{-1} H_2)	**Δ*H* (kJ. kg^{-1})**	**US $ (tonne)**	**US $ (kWh$_{th}$)**	**Operating conditions**
$3CaH_2 + 2Al_2O_3$ [44]	100	908	2460	9.7	636 °C 1 bar
CaH_2 +2Al [12, 23, 24, 45]	84	875	3631	14.9	700 °C 62 bar
CaH_2 [46]	162	3857	6000	5.6	1000 °C 1.2 bar

4.4 Conclusions

The feasibility of CaH_2 destabilised with Al_2O_3 and used as a high-temperature thermal battery for the next-generation of CSP applications was investigated. Thermal desorption studies showed that the decomposition temperature of the CaH_2-Al_2O_3 mixture was ≈ 600 °C and obtained a maximum gravimetric H_2 wt% of 1.2 when heated to 850 °C. *Ex-situ* and *in-situ* X-ray diffraction studies showed that the main product of the destabilisation reaction was $Ca_{12}Al_{14}O_{33}$. The high enthalpy of reaction, the high operating temperature at low pressure (636 °C at 1 bar) and low materials cost of this system, makes it a promising high-temperature thermal battery for the next generation of CSP applications. Though, due to the presence of excess unreacted alumina and sintering effects demonstrated a poor performance upon cycling initially, however, the hydrogen cycling capacity was significantly improved by reducing the initial amount of Al_2O_3 by half. Further investigation into the reaction kinetics, heat transfer, thermal conductivity and hydrogen cycling stability over 100 cycles are required to prove its overall efficiency as a TES material.

4.5 References

1. International Energy Agency https://www.iea.org/efficiency2018/ (accessed January 2019).
2. Jacobson, M.Z.; Delucchi, M.A. Providing all global energy with wind, water, and solar power, Part I: Technologies, energy resources, quantities and areas of infrastructure, and materials. *Energy policy*, **2011**, *39*, 1154-1169.
3. Sukhatme, S. P.; Nayak, J. K., Solar Energy: Principles of Thermal Collection and Storage; *Tata McGraw-Hill Education*, **1996**.
4. Abbott D. Keeping the energy debate clean: How do we supply the world's energy needs? *Proc. IEEE***, 2009**, *98*, 42-66.
5. Pardo, P.; Deydier, A.; Anxionnaz-Minvielle, Z.; Rougé, S.; Cabassud, M.; Cognet, P. A review on high temperature thermochemical heat energy storage. *Renewable Sustainable Energy Rev.,* **2014**, *32*, 591-610
6. Spencer, LC. A review on high temperature thermochemical heat energy storage. *Sol Energy*, **1989**, *43*, 191-196.
7. Prasad, J.S.; Muthukumar, P.; Desai, F.; Basu, D.N.; Rahman, M.M. A critical review of high-temperature reversible thermochemical energy storage systems. *Appl. Energy*, **2019**, *254*, 113733.
8. Chu, Y; Meisen, P. Global Energy Network Institute (GENI). San Diego,CA; 2011.
9. Desideri, U.; Zepparelli, F.; Morettini, V.; Garroni, E. Comparative analysis of concentrating solar power and photovoltaic technologies: Technical and environmental evaluations. *Appl. Energy*, **2013**, *102*, 765-784.
10. Kuravi, S.; Trahan, J.; Goswami, D.Y.; Rahman, M.M.; Stefanakos, E.K. Thermal energy storage technologies and systems for concentrating solar power plants. *Prog. Energy Combust. Sci.*, **2013**, *39*, 285-319.
11. Manickam, K.; Mistry P.; Walker G.; Grant D.; Buckley C.E.; Humphries T.D.; Paskevicius M.; Jensen T.; Albert R.; Peinecke K.; et al. Future perspectives of thermal energy storage with metal hydrides. *Int. J. Hydrogen Energy*, **2019**, *44*, 7738-7745.
12. Sofianos, M.V.; Randal, S.; Paskevicius, M.; Aguey-Zinsou, K.-F.; Rowles, M.R.; Humphries, T.D.; Buckley, C.E. Exploring halide destabilised calcium hydride as a high-temperature thermal battery. *J. Alloys Compd.*, **2020**, *819*, 153340.
13. Sheppard, D.A.; Humphries, T.D.; Buckley, C.E. What is old is new again. *Mater. Today*, **2015,** *18*, 4174-415.

14. Carrillo, A.J.; González-Aguilar J.; Romero, M.; Coronado, J.M. Solar energy on demand: A review on high temperature thermochemical heat storage systems and materials. *Chem Rev* **2019**, *119*, 4777-4816.
15. Harries, D.N.; Paskevicius, M.; Sheppard, D.A.; Price, T.E.C.; Buckley, C.E. Concentrating solar thermal heat storage using metal hydrides. *Proc. IEEE* **2012**, *100,* 539-549.
16. Libowitz, G. In Metal Hydrides for Thermal Energy Storage, *9th Intersociety Energy Conversion Engineering Conference*, **1974**; pp 322-325.
17. Ward, P.A.; Corgnale, C.; Teprovich, J.A.; Motyka, T.; Hardy, B.; Sheppard, D.A.; Buckley, C.E.; Zidan, R. Technical challenges and future direction for high-efficiency metal hydride thermal energy storage systems. *Appl Phys A* **2016** *122*, 462.
18. Rönnebro, E.C.; Whyatt, G.; Powell, M.; Westman, M.; Zheng, F.R.; Fang, Z.Z. Metal hydrides for high-temperature power generation. *Energies*, **2015**, *8*, 8406-8430.
19. Bliesner, W.T. Reversible hydride thermal energy storage cell optimised for solar applications US Pat., 20110100356A1, **2010**.
20. Curtis, R.; Chiotti, P. Thermodynamic properties of calcium hydride. *J. Phys. Chem.*, **1963**, *67*, 1061-1065.
21. Peterson, D.; Fattore, V. Calcium-calcium hydride phase system. *J. Phys. Chem.*, **1961**, *65*, 2062-2064.
22. Wang, M.; Sun, W.; Sha, C.; Hu, B.; Du, Y.; Sun, L.; Xu, H.; Wang, J.; Liu, S. Thermodynamic Modelling of the Li-H and Ca-H Systems. *J. Phase Equilibria Diff.*, **2012**, *33*, 89-96.
23. Vajo, J.J.; Olson, G.L. Hydrogen storage in destabilised chemical systems. *Scr. Mater.*, **2007**, *56*, 829-834.
24. Veleckis, E. Application of the hydrogen titration method to a thermodynamic investigation of solid Al-Ca alloys. *J. Less-Common Met.*, **1981**, *80*, 241-255.
25. Ward, P.A; Teprovich, Jr. J.A; Liu, Y.; He, J.; Zidan, R. High temperature thermal energy storage in the $CaAl_2$ system. *J. Alloys Compd.*, **2018,** *735*, 2611-2615.
26. Levin, I.; Brandon, D. Metastable alumina polymorphs: crystal structures and transition sequences. *J. Am. Ceram. Soc.*, **1998**, *81*, 1995-2012.
27. Elam, J.; Londergan, A.; van der Straten, O.; Roozeboom, F.; De Gendt, S.; Bent, S.; Delabie, A. Atomic layer deposition applications 6; Electrochemical Society; Pennington, N.J, **2010**.

28. Auerkari, P. Mechanical and physical properties of engineering alumina ceramics; Technical Research Centre of Finland Espoo; Finland,**1996**.
29. Outotec, R.O. *HSC,* version 6.12, Rauhalanpuisto 9, 02230 Espoo, Finland, 1974 - 2007.
30. Dinsdale, A.T. SGTE data for pure elements. *CALPHAD: Comput. Coupling Phase Diagrams Thermochem.,* **1991**, *15,* 317-425.
31. Binnewies, M.; Milke, E. *Thermochemical data of elements and compounds*; Wiley-VCH; Bridgewater, NJ, **1999**.
32. Hallstedl, B. Assessment of the CaO-Al_2O_3 System. *J. Am. Ceram. Soc.,* **1990**, *73,* 15-23.
33. Coelho, A.A. TOPAS and TOPAS-Academic: an optimization program integrating computer algebra and crystallographic objects written in C^{++}. *J. Appl. Crystallogr.,* **2018**, *51*, 210-218.
34. Rietveld, H. A profile refinement method for nuclear and magnetic structures. *J. Appl. Crystallogr.,* **1969**, *2*, 65-71.
35. Gražulis, S.; Daškevič, A.; Merkys, A.; Chateigner, D.; Lutterotti, L.; Quiros, M.; Serebryanaya, N.R.; Moeck, P.; Downs, R.T.; Le Bail, A. Crystallography open database (COD): an open-access collection of crystal structures and platform for world-wide collaboration. *Nucleic Acids Res.,* **2011**, *40*, D420-D427.
36. Pathak, P.; Vasavada, N. Thermal expansion of NaCl, KCl and CsBr by X-ray diffraction and the law of corresponding states. *Acta Crystallogr. A* **1970**, *26*, 655-658.
37. Hu, J.; Cai, W.; Li, C.; Gan, Y.; Chen, L. *In-situ* X-ray diffraction study of the thermal expansion of silver nanoparticles in ambient air and vacuum. *Appl. Phys. Lett.,* **2005**, *86*, 151915.
38. Hansen, B.R.; Møller, K.T.; Paskevicius, M.; Dippel, A.-C.; Walter, P.; Webb, C.J.; Pistidda, C.; Bergemann, N.; Dornheim, M.; Klassen, T.; et al. *In-situ* X-ray diffraction environments for high-pressure reactions. *J. Appl. Crystallogr.,* **2015**, *48,* 1234-1241.
39. Sheppard, D.A; Paskevicius, M.; Javadian, P.; Davies, I.J.; Buckley, C.E. Methods for accurate high-temperature Sieverts-type hydrogen measurements of metal hydrides. *J. Alloys Compd.,* **2019**, *787,* 1225-1237.
40. Itkin, V.; Alcock, C.; Van Ekeren, P.; Oonk, H.A. The Al - Ca (Aluminum-Calcium) system. *J. Phase Equilib. Diff.,* **1988**, *9,* 652-657.

41. Alonso, J.A.; Retuerto, M.; Sanchez-Benitez, J.; Fernández-Díaz, M.T. Crystal structure and bond valence of CaH_2 from neutron powder diffraction data. *Z Krist-Cryst Mater.*, **2010**, *225*, 225-229.
42. US Department of Energy. SunShot Vision Study. https://www.energy.gov/eere/solar/sunshot-vision-study (accessed November 2019)
43. Sheppard, D.A.; Corgnale, C.; Hardy, B.; Motyka, T.; Zidan, R.; Paskevicius, M.; Buckley, C.E. Hydriding characteristics of $NaMgH_2F$ with preliminary technical and cost evaluation of magnesium-based metal hydride materials for concentrating solar power thermal storage. *RSC Adv.*, **2014**, *4*, 26552-26562.
44. Alumina prices, https://investors.alcoa.com/financial-reports/quarterly-earnings/2019 (accessed January 2020)
45. Aluminium prices, https://www.focus-economics.com/commodities/base-metals/aluminium (accessed November 2019)
46. Humphries, T.D.; Møller, K.T.; Rickard, W.D.; Sofianos, M.V.; Liu, S.; Buckley, C.E.; Paskevicius M. Dolomite: a low-cost thermochemical energy storage material. *J. Mater. Chem. A*, **2019**, *7*, 1206-1215.

Chapter 5

Thermochemical energy storage performance of zinc destabilised calcium hydride at high-temperatures

S. Balakrishnan, M.V. Sofianos, T.D Humphries, M. Paskevicius,and C.E. Buckley, Thermochemical energy storage performance of zinc destabilised calcium hydride at high temperatures, ***J.*** Phys. Chem. Chem. Phys., **22,** 2020, 25780-25788. https://doi.org/10.1039/D0CP04431H

Abstract

CaH_2 has 20 times the energy density of molten salts and was patented in 2010 as a potential solar thermal energy storage material. Unfortunately, its high operating temperature (> 1000 °C) and corrosivity at that temperature make it challenging to use as thermal energy storage (TES) material in concentrating solar power (CSP) plants. To overcome these practical limitations, here we propose, the thermodynamic destabilisation of CaH_2 with Zn metal. It is a unique approach that reduces the decomposition temperature of pure CaH_2 (1100 °C at 1 bar of H_2 pressure) to 597 °C at 1 bar of H_2 pressure. Its new decomposition temperature is closer to the required target temperature range for TES materials used in proposed third-generation high-temperature CSP plants. A three-step dehydrogenation reaction between CaH_2 and Zn (1: 3 molar ratio) was identified from mass spectrometry, temperature-programmed desorption, and *in-situ* X-ray diffraction studies. Three reaction products, $CaZn_{13}$, $CaZn_{11}$ and $CaZn_5$, were confirmed from *in-situ* X-ray diffraction studies at 190 °C, 390 °C and 590 °C, respectively. The experimental enthalpy and entropy of the second hydrogen release reaction were determined by pressure composition isotherm measurements, conducted between 565 and 614 °C, as $\Delta H_{des} = 131 \pm 4$ kJ.mol^{-1} H_2 and $\Delta S_{des} = 151 \pm 4$ J.K^{-1}.mol^{-1} H_2. Hydrogen cycling studies of $CaZn_{11}$ at 580 °C showed sufficient cycling capacity with no significant sintering occurring during heating, as confirmed by scanning electron microscopy, demonstrating its great potential as a TES material for CSP applications. Finally, a cost comparison study of known destabilised CaH_2 systems was carried out to assess the commercial potential.

5.1 Introduction

The primary objective of the next-generation concentrating solar power plants (CSP) is to provide continuous electrical power supply at a 40% cost reduction in comparison to the plants currently operating.[1] This cost reduction can be met due to the higher power cycle efficiency achieved in a 600 - 800 °C temperature range by replacing a conventional steam power engine with a Stirling engine.[2] Specifically, the US Department of Energy released the Sun Shot research programme with a target to develop thermal energy storage (TES) materials that operate above 600 °C, have ≥ 95% exergetic efficiency and cost less than \$15/kWh$_{th}$ by 2030. Hence, the identification of a cost-effective high-temperature TES material that meets these requirements is both essential and challenging.[3-7]

There are a plethora of known TES materials that can be categorised depending on their heat storage mechanism, storage density and operating temperature. Sensible heat storage materials, such as molten salts, are the most commonly used TES materials in the industry.[3] Nevertheless, molten salts suffer from several drawbacks such as low energy density (0.02 - 0.03 kWh/kg), corrosion and limited operating temperature (< 565 °C).[8-9] Latent heat storage materials have a higher energy density (0.05 - 0.1 kWh/kg) than the sensible heat storage materials, but most of the materials presently studied have issues such as low thermal conductivity, and high thermal losses.[4, 10-11] To overcome these drawbacks, a third category of TES materials known as thermochemical energy storage is gaining increasing popularity due the high energy density (0.5 - 1 kWh/kg) that these materials possess despite their increased complexity. The superior energy storage properties are based on reversible chemical reactions that take place at high temperatures.[12-13] At present, six systems, namely hydrides, carbonates, hydroxides, oxides, ammonia and organic are identified as thermochemical TES materials.[11] The unique property of metal hydrides to absorb and release hydrogen at a specific pressure at high temperatures, makes them the most promising thermochemical system amongst the rest, and thereby meeting the requirements of the next generation CSP plants.[10, 14-16] Calcium hydride is a promising high-temperature metal hydride due to its: (i) low cost ($6000/tonne) and abundance, (ii) low operating hydrogen pressure at high temperature (1 - 5 bar at 1100 - 1400 °C), (iii) high enthalpy of dehydrogenation (207.9 $kJ.mol^{-1}H_2$), and (iv) high gravimetric (4939 $kJ.kg^{-1}$) and volumetric energy densities (8396 $MJ.m^{-3}$).[2 , 17-18] Its high operating temperature (1100 °C), melting point of both CaH_2 and Ca metal are 816 °C and 842 °C, and expensive tank material requirements to store the corrosive CaH_2, are the main factors that limit the use of pure CaH_2 as a thermochemical TES material.[17, 20-21] Thermodynamic destabilisation of CaH_2 using suitable additives, is one approach for reducing the decomposition temperature of CaH_2, and transforming it as a suitable TES material for the third generation CSP plants.[22]

The main novelty of this study lies in the selection of a relatively inexpensive and abundant metal such as zinc ($1.93/kg), to be used as an additive in order to reduce the decomposition temperature of CaH_2 as illustrated in Figure 5.1. This method successfully showed by adding Al_2O_3 to CaH_2, where the enthalpy of the reaction was found to be $\Delta H = 100$ $kJ.mol^{-1}$ H_2 at 636 °C and 1 bar of H_2 pressure.[23] CaH_2-3Zn is an alternate system that exploits the feasibility of Zn as a high-temperature thermochemical TES material for the third generation CSP plants. The aim of this study focused on thermal analysis, and thermodynamic characterization of the CaH_2-3Zn system using mass spectrometry, temperature programmed desorption and *in-situ* X-ray diffraction studies. Its cycling capacity, sample morphology before and after cycling using field emission scanning electron microscopy (FE-SEM) and cost analysis were also investigated and reported.

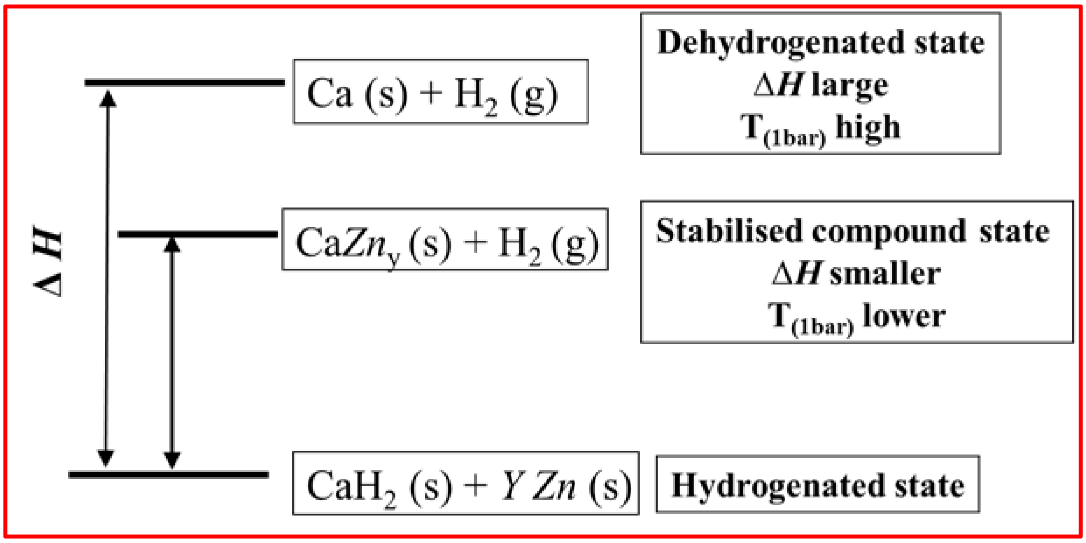

Figure 5.1 General enthalpy diagram showing destabilisation of CaH_2 by adding Zn through the formation of calcium zinc alloys.[24]

5.2 Experimental methods

5.2.1 Sample preparation

All chemicals were stored and handled inside an Ar filled MBraun unilab glovebox to reduce oxygen (< 1 ppm) and water (< 1 ppm) contamination. CaH_2 (Sigma Aldrich, > 95% purity powder) and Zn (Chem supply, > 98% purity powder) were mixed in a 1:3 molar ratio and milled under an Ar atmosphere using an Across International Planetary Ball Mill (PQ-N04), employing stainless steel vials and balls. The mixture was ball milled for 3 hours with a 40:1 ball (equal number of 10mm and 6mm diameter balls) to powder ratio. The rotational speed was set to 400 rpm with a change of direction every 30 minutes without pausing.

5.2.2 Sample characterization

5.2.2.1 Theoretical predictions

The possible reaction pathways between CaH_2 and Zn were predicted using the phase diagram of the Ca-Zn system.[25-26] The volatility of solid calcium zinc alloys are linked with the vapor pressure of Zn. The vapor pressure of pure Zn metal and Ca was calculated from room temperature to 1000 °C.[27] Vapor pressure data of calcium zinc solid alloys were also derived from Chiotti et al.[37]and Hodge et al.[39] and the vapor pressures of eight calcium zinc alloys

(Ca_3Zn, Ca_5Zn_3, CaZn, $CaZn_2$, $CaZn_3$, $CaZn_5$, $CaZn_{11}$ and $CaZn_{13}$) were plotted along with pure Zn and Ca as a function of temperature in Figure 5.2. Among the eight solid alloys, Zn rich alloys have high vapor pressures and are less volatile than Zn poor alloys at higher temperatures (> 600 °C).

5.2.2.2 Powder X-ray diffraction

Ex-situ powder X-ray diffraction (XRD) was used to identify the crystalline materials in each sample. Airtight polymethyl methacrylate domed sample holders were used to avoid oxygen and moisture contamination during data collection. Data were collected using a Bruker D8 Advance Diffractometer with a copper X-ray tube ($\lambda = 1.5418$ Å, 40 kV, 40 mA) in the 10° - 80° 2θ range with a 0.03° step size and 1.6 s/step count time. The diffraction peaks were quantitatively analysed by the Rietveld method[28] using the Bruker TOPAS Version 5 software.[29] The structural information was extracted from ICDD PDF4 database and the Crystallography Open Database (COD).[30]

In-situ X-ray diffraction was performed using a Thermo Fisher ARL Equinox 5000 diffractometer ($\lambda = 0.7093$ Å, Mo-K_α, 50 kV, 30 mA). The sample was loaded into a quartz capillary tube (0.7 mm outer diameter, 0.01 mm wall thickness), sealed and then mounted onto a sample holder inside an Ar filled glovebox. The sample was heated from room temperature to 692 °C using a hot air blower (5 °C/min) and kept isothermal for 2 hours. Data were acquired on a CPS 120 detector (0 - 60°,2θ) with a 60 s exposure time. The temperature of the hot air blower was calibrated against the known thermal expansion coefficient of both NaCl and Ag.[31-33]

5.2.2.3 Mass spectrometry

Temperature programmed desorption-mass spectrometry (TPD-MS) measurements were obtained using a Stanford Research Systems (SRS, RGA-300) residual gas analyzer consisting of a quadrupole mass spectrometer.[34] A 3 mg sample of pure CaH_2 and CaH_2-3Zn was placed in a stainless steel sample holder inside a silicon carbide reactor that was connected to the spectrometer. The samples were heated to 850 °C at 5 °C/min under high vacuum ($< 7 \times 10^{-4}$ mbar). The corresponding analogue scan of partial pressure vs mass to charge ratio was obtained from the RGA software. A K-type thermocouple with an uncertainty of ± 1.5 °C was connected inside the SiC tube to record the temperature of the sample.

5.2.2.4 Temperature programmed desorption and pressure composition isotherms

H_2 sorption properties were studied by Temperature Programmed Desorption (TPD), using a computer-controlled Sievert's apparatus.[35] CaH_2-3Zn was heated to either 630 °C or 830 °C, with 5 °C/min heating rates. The powder mixture was placed inside a stainless-steel sample holder and then loaded into a silicon carbide (SiC) reactor. H_2 has a negligible hydrogen permeation through SiC at high temperatures (> 450 °C) and therefore was chosen as the most suitable reactor material for such measurements.[35-36] The sample temperature was measured using a K-type thermocouple which is kept inside the SiC reactor and direct contact with the sample. Pressure Composition Isotherms (PCI) measurements of CaH_2-3Zn were conducted on the same apparatus to acquire the thermodynamic properties of the dehydrogenation reaction between 565 °C and 614 °C with a 1 bar pressure step size and a 3 h equilibration time per step. H_2 desorption and absorption cycling studies were performed on CaH_2-3Zn at 580 °C with a ramp rate of 5 °C/min. The H_2 pressure and equilibration time during desorption was ≈ 0.8 bar and 3 h respectively, whereas during absorption it was ≈ 2.8 bar and 5 h.

5.2.2.5 Scanning electron microscopy and energy dispersive X-ray spectroscopy

Field emission scanning electron microscopy (FE-SEM) and energy dispersive X-ray spectroscopy were carried out using a Tescan Mira3 integrated with EBSD/EDS Oxford Instrument detectors controlled by the Aztec software. The SEM images of the CaH_2-3Zn system before and after cycling were collected using both secondary and back-scattered electron detectors. The SEM samples were prepared inside an Ar filled glove box by placing a small amount of powder onto a carbon tape, and then transferred to the SEM chamber with minimum air exposure.

5.3 Results and discussion

5.3.1 Theoretical predictions

The phase diagram of the Ca-Zn system shows eight different alloys (Ca_3Zn, Ca_5Zn_3, CaZn, $CaZn_2$, $CaZn_3$, $CaZn_5$, $CaZn_{11}$ and $CaZn_{13}$) at different molar ratios.[25-26] Table 5.1 indicates theoretically possible reactions between CaH_2 and Zn and the corresponding theoretical H_2 wt%. The vapor pressure of Zn plays a vital role in the formation and volatility of the solid alloy formation.[27, 37-39] Figure 5.2 shows the vapor pressure curve of pure Ca, Zn and solid calcium zinc alloys as a function of temperature. It shows that the vapor pressure of pure Zn is higher than pure Ca until 600 °C, after which the vapor pressure of Zn is less than that of pure Ca. From Figure 5.2 and the Ca-Zn phase diagram it can be seen that Zn rich alloys have higher vapor pressures and hence are less likely to produce vaporised Zn above 600 °C.[25] Moreover, above ≈ 700 °C no calcium zinc solid alloys exist.

Table 5.1 Theoretical predictions of possible reaction between CaH_2 and Zn and corresponding H_2 wt%.

	Predicted reaction	Theoretical H_2 wt%
1	$3CaH_2 + Zn \rightleftharpoons Ca_3Zn + H_2(g)$	3.15
2	$5CaH_2 + 3Zn \rightleftharpoons Ca_5Zn_3 + H_2(g)$	2.47
3	$CaH_2 + Zn \rightleftharpoons CaZn + H_2(g)$	1.87
4	$CaH_2 + 2Zn \rightleftharpoons CaZn_2 + H_2(g)$	1.16
5	$CaH_2 + 3Zn \rightleftharpoons CaZn_3 + H_2(g)$	0.84
6	$CaH_2 + 5Zn \rightleftharpoons CaZn_5 + H_2(g)$	0.54
7	$CaH_2 + 11Zn \rightleftharpoons CaZn_{11} + H_2(g)$	0.26
8	$CaH_2 + 13Zn \rightleftharpoons CaZn_{13} + H_2(g)$	0.22

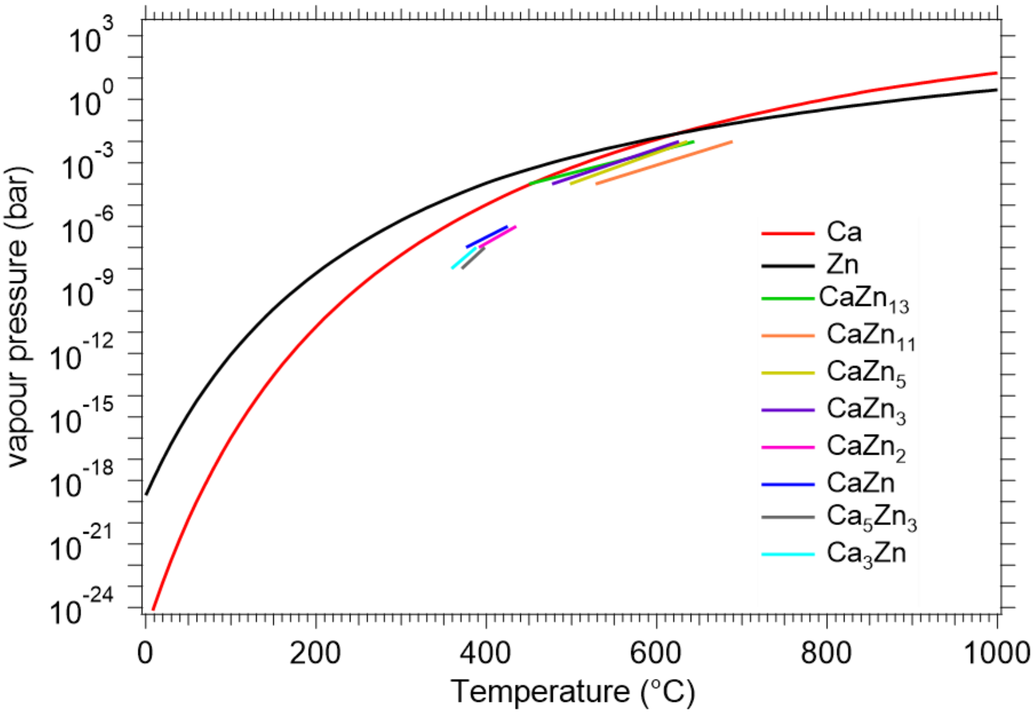

Figure 5.2 Vapour pressure curves for pure Ca and Zn and calcium zinc alloys as a function of temperature.[1-4]

5.3.2 Initial phase analysis

The diffraction patterns of as-supplied CaH_2, Zn and ball-milled CaH_2-3Zn are presented in Figure 5.3 (a), (b) and (c), respectively. Quantitative phase analysis was used to determine the purity of the materials using the Rietveld method. Quantitative phase analysis of the CaH_2 reagent shows CaH_2 with a negligible amount of crystalline CaO, while the XRD and refinement pattern for the ball milled CaH_2-3Zn only shows CaH_2 (16.5 ± 0.8 wt%), and Zn (83 ± 1 wt%) (Figure 5.3 (c) and Figure 5.4). This indicates that no reaction occurred between CaH_2 and Zn during ball milling to form a Ca-Zn product as expected by the high required enthalpy of reaction.

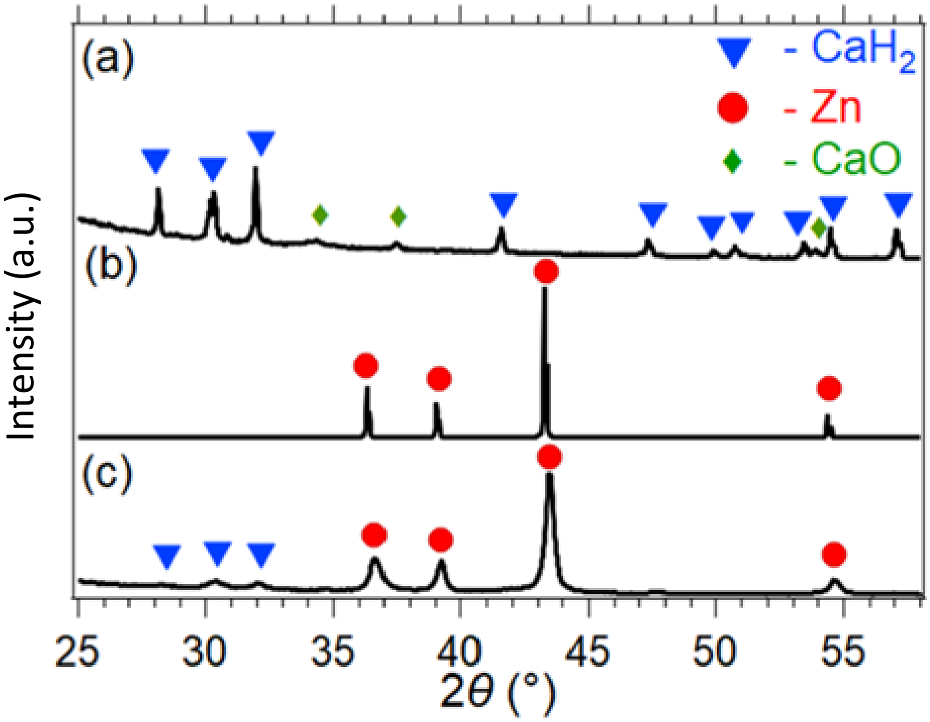

Figure 5.3 *Ex-situ* XRD patterns of (a) CaH_2, (b) Zn and (c) CaH_2-3Zn system after ball milling using Cu K_α radiation (λ = 1.5418 Å).

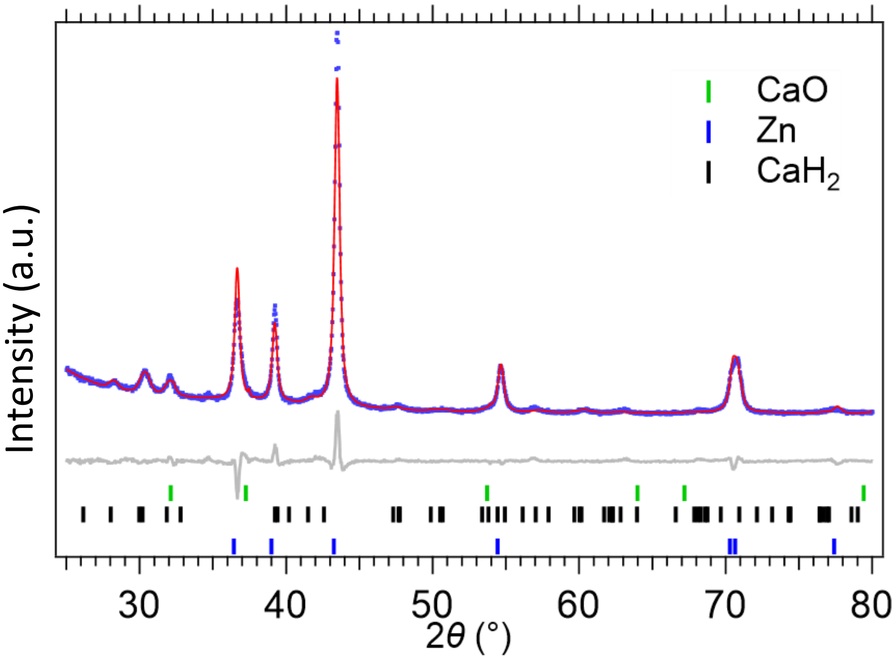

Figure 5.4 Rietveld refinement of the diffraction pattern for CaH_2-3Zn system after ball milling (Cu K_α, λ = 1.5418 Å).

5.3.3 The destabilisation of CaH_2 using Zn

TPD-MS measurements were performed on CaH_2 and CaH_2-3Zn to compare the H_2 gas release profiles as a function of temperature (Figure 5.5(a) and (b) respectively). Due to the high vacuum (< 7 x 10^{-4} mbar) employed in this technique, CaH_2 commenced H_2 release at 500 °C and reached the highest rate of hydrogen release at 600 °C (Figure 5.5(a)), with the single decomposition peak indicative of a one-step decomposition reaction. The H_2 desorption profile of CaH_2-3Zn (Figure 5.5(b)) consisted of three H_2 peaks denoting a three-step decomposition reaction, either due to differing kinetics or thermodynamics of reaction. The first small peak appeared at 200 °C, followed by two high intensity peaks at 300 °C and 420 °C, respectively. H_2 was the only gas detected during heating to 800 °C. The three low-temperature decomposition peaks of the CaH_2-3Zn sample show that the addition of Zn thermodynamically destabilises the CaH_2.

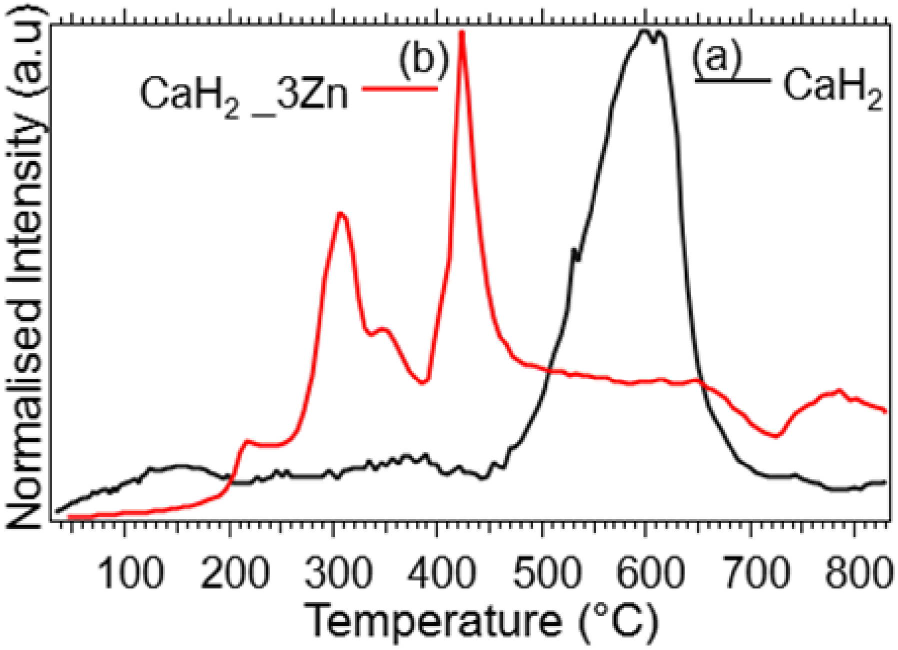

Figure 5.5 H_2 desorption profiles as observed by TPD-MS measurements of (a) CaH_2 and (b) CaH_2-3Zn while heating under vacuum.

5.3.4 Thermal analysis

A TPD measurement was conducted on CaH_2-3Zn by heating the sample from room temperature to 830 °C (5 °C/min), before keeping the temperature isothermal at 830 °C for 10 hours to check the volatility of the alloy formed (Figure 5.6(a)). The measurement was commenced under initial static vacuum and reached a maximum H_2 pressure of 0.9 bar. After 2 hours at 830 °C the hydrogen pressure began to decrease. The reason for this pressure decrease was due to: (i) zinc evaporation from the alloy as evidenced by zinc metal deposition on the cool regions of the sample cell, and (ii) H_2 reabsorption into the zinc-poor calcium metal to reform CaH_2. This was confirmed from the sample's *ex-situ* XRD pattern obtained after the TPD measurement (Figure 5.7(a)), which comprised of CaH_2 and Zn peaks with no calcium zinc alloy peaks being present. The TPD measurement was repeated with a maximum temperature of 630 °C and a subsequent isotherm for 10 h. A maximum H_2 pressure of 0.58 bar was reached starting from vacuum. Figure 5.6(b) illustrates the TPD profile, which exhibits an almost isobaric profile after reaching 630 °C with reduced Zn evaporation observed in comparison to the data obtained at 830 °C. $CaZn_{11}$ and $CaZn_5$ alloys were the main decomposition products at 630 °C as confirmed by the sample's *ex-situ* XRD pattern obtained after the TPD measurement (Figure 5.7(b)).

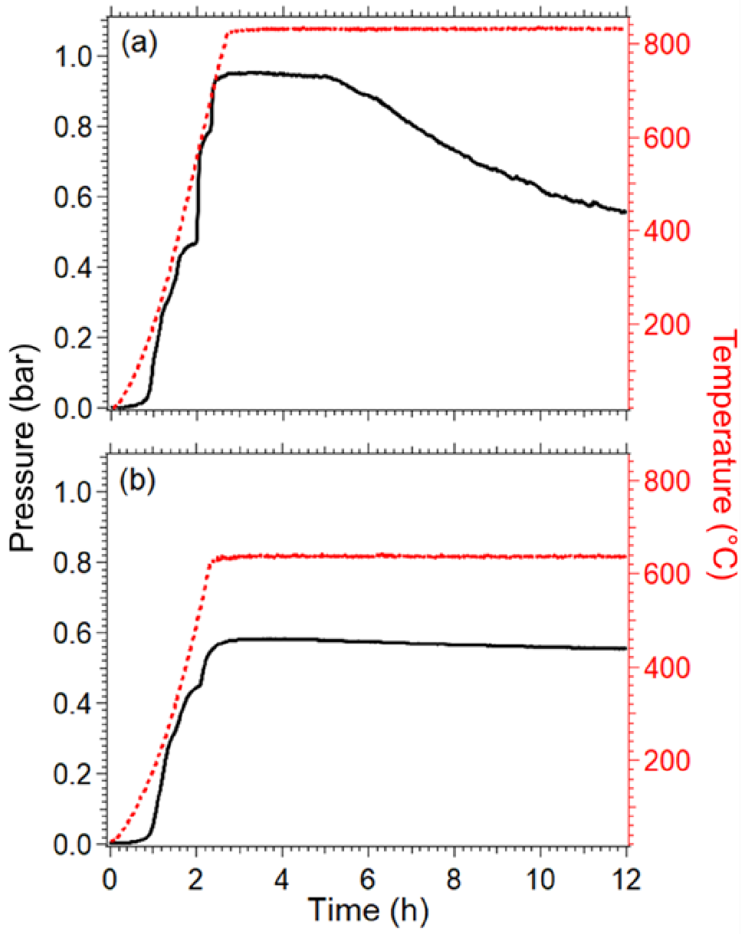

Figure 5.6 TPD profiles of CaH_2-3Zn from room temperature to (a) 830 °C and (b) 630 °C. Black solid line = pressure, red dotted line = temperature.

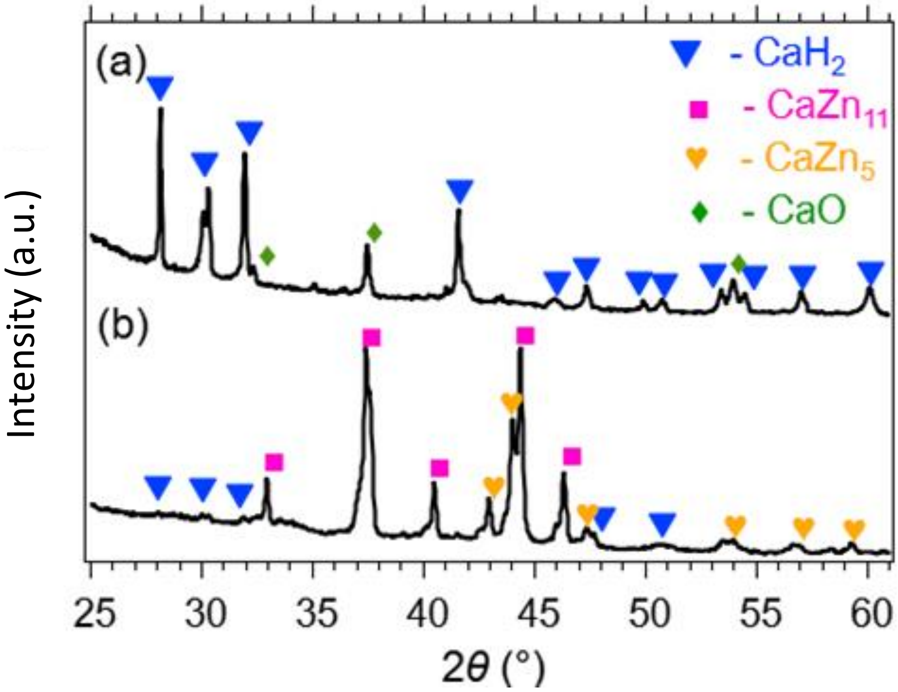

Figure 5.7 *Ex-situ* XRD pattern of CaH_2-3Zn after the TPD measurements at (a) 830 °C and (b) 630 °C (Cu Kα, λ = 1.5418 Å).

5.3.5 Identifying the reaction pathway by *in-situ* X-ray diffraction

In-situ XRD data of CaH_2 -3Zn during thermal ramping under argon is presented in Figure 5.8 (a) is compared with its differential TPD profile (Figure 5.8(b)). It is evident from the *in-situ* XRD patterns that the reaction between CaH_2 and Zn occurs in a three-step reaction between 190 and 590 °C, which is in a good agreement with the TPD profiles. It is clear from Figure 5.8(a) the three different alloys formed are $CaZn_{13}$, $CaZn_{11}$ and $CaZn_5$ at three different temperature ranges of 190 - 390 °C, 390 - 590 °C and > 590 °C, respectively. The experimental reaction can be predicted from the *in-situ* XRD data as follows, which shows the presence of excess CaH_2.

$$CaH_2 + 3Zn \rightarrow \frac{3}{13}CaZn_{13} + \frac{10}{13}CaH_2 + \frac{3}{13}H_2\,(g) \qquad 5\text{-}1$$

$$\frac{3}{13}CaZn_{13} + \frac{10}{13}CaH_2 \rightarrow \frac{3}{11}CaZn_{11} + \frac{8}{11}CaH_2 + \frac{6}{143}H_2\,(g) \qquad 5\text{-}2$$

$$\frac{3}{11}CaZn_{11} + \frac{8}{11}CaH_2 \rightarrow \frac{3}{5}CaZn_5 + \frac{2}{5}CaH_2 + \frac{18}{55}H_2\,(g) \qquad 5\text{-}3$$

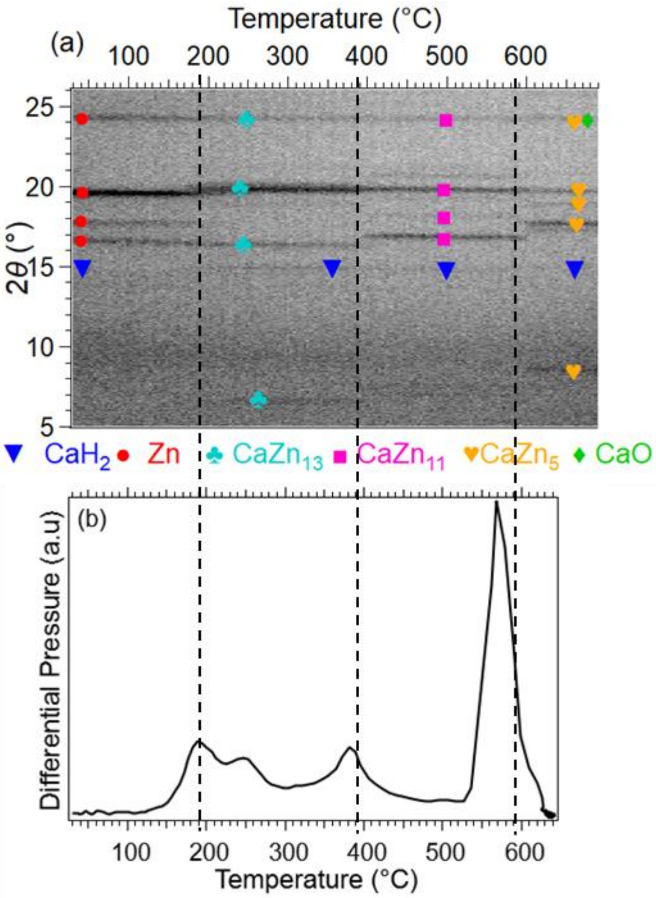

Figure 5.8 (a) *In-situ* XRD patterns of CaH_2-3Zn from room temperature to 690 °C (Mo K_α of $\lambda = 0.7093$ Å) (b) Differential TPD profiles of CaH_2-3Zn from room temperature to 640 °C.

5.3.6 Thermodynamic calculations

As the *ex-situ* XRD pattern of CaH_2-3Zn after the TPD measurement at 830 °C did not exhibit any solid calcium-zinc alloy present in the decomposed sample, PCI measurements were performed at temperatures below 630 °C. The measurements were carried out at 565, 580, 600 and 614 °C (Figure 5.9(a)). The corresponding van 't Hoff plot (Figure 5.9(b)) was constructed by plotting the midpoint values from the first plateau region of each PCI measurement to acquire the enthalpy and entropy of reaction. The optimised form (no excess CaH_2) of the above mentioned three reactions can be written as follows:

$CaH_2 + 13Zn \rightarrow CaZn_{13} + H_2$ (g) 5-4

$CaH_2 + 11Zn \rightarrow CaZn_{11} + H_2$ (g) 5-5

$CaH_2 + \frac{5}{6}CaZn_{11} \rightarrow \frac{11}{6}CaZn_5 + H_2$ (g) 5-6

The corresponding enthalpy and entropy of the optimised reaction 5-5, obtained from first plateau as shown in Figure 5.9(a), were calculated as $\Delta H_{des} = 131.5 \pm 4.0$ kJ.mol^{-1} H_2, ΔS_{des} =

151.1 ± 4.0 J.K^{-1}.mol^{-1} H_2, respectively. Therefore, the equilibrium desorption temperature at 1 bar pressure is $T_{des} = \Delta H/\Delta S$ = 597 ± 35 °C. The pressure curves of each PCI measurement show that thermodynamic equilibrium was reached for each of the 3 h desorption steps, indicating fast reaction kinetics (Figure 5.10). The existence of two plateau regions in the PCI measurements is evident from Figure 5.9(a). The second plateau region is not accurately measured due to (i) zinc evaporation (rate is high at higher temperatures and also depends on time exposed at that temperature) and (ii) limitation of the Sievert's apparatus to achieve very low pressure increments (< 1mbar). The formation of $CaZn_{11}$ from reaction (5) followed by $CaZn_5$ from reaction (6) during the PCI measurements were confirmed using *ex-situ* XRD. Figure 5.11(a) and (b) show the XRD patterns of CaH_2-3Zn measured at the regions marked as (i) and (ii) in Figure 5.9(a) of the PCI measurement conducted at 600 °C, respectively. Figure 5.11(a) confirmed $CaZn_{11}$ to be the main phase with only minor $CaZn_5$ peaks present, whereas Figure 5.11(b) shows that all $CaZn_{11}$ peaks have been replaced with $CaZn_5$ peaks formed during the second equilibrium pressure region. These XRD findings confirm the reactions given above (5-4 to 5-6).

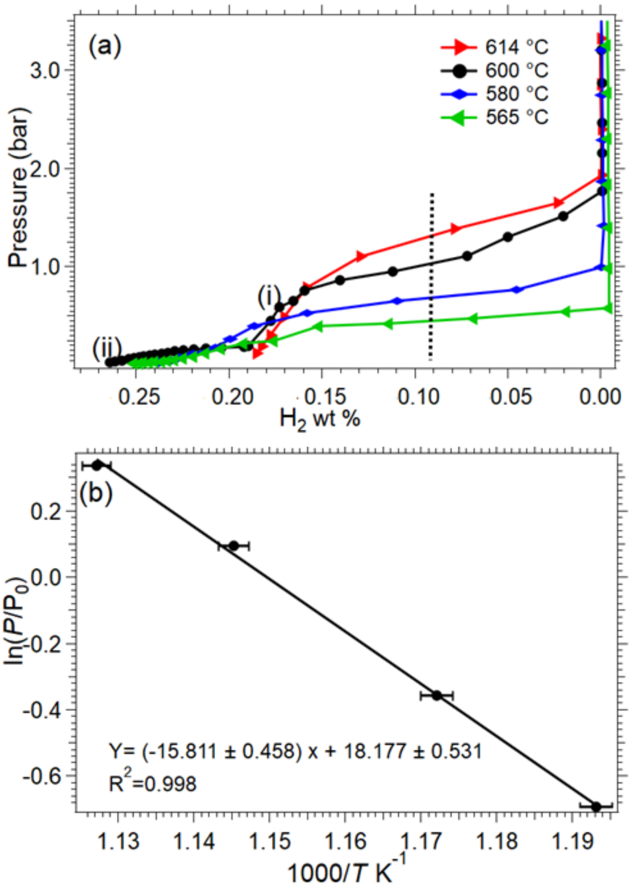

Figure 5.9 (a) Pressure Composition Isotherms of CaH_2-3Zn between 565 °C (green), 580 °C (blue), 600 °C (black) and 614 °C (red) and (b) the corresponding van 't Hoff plot.

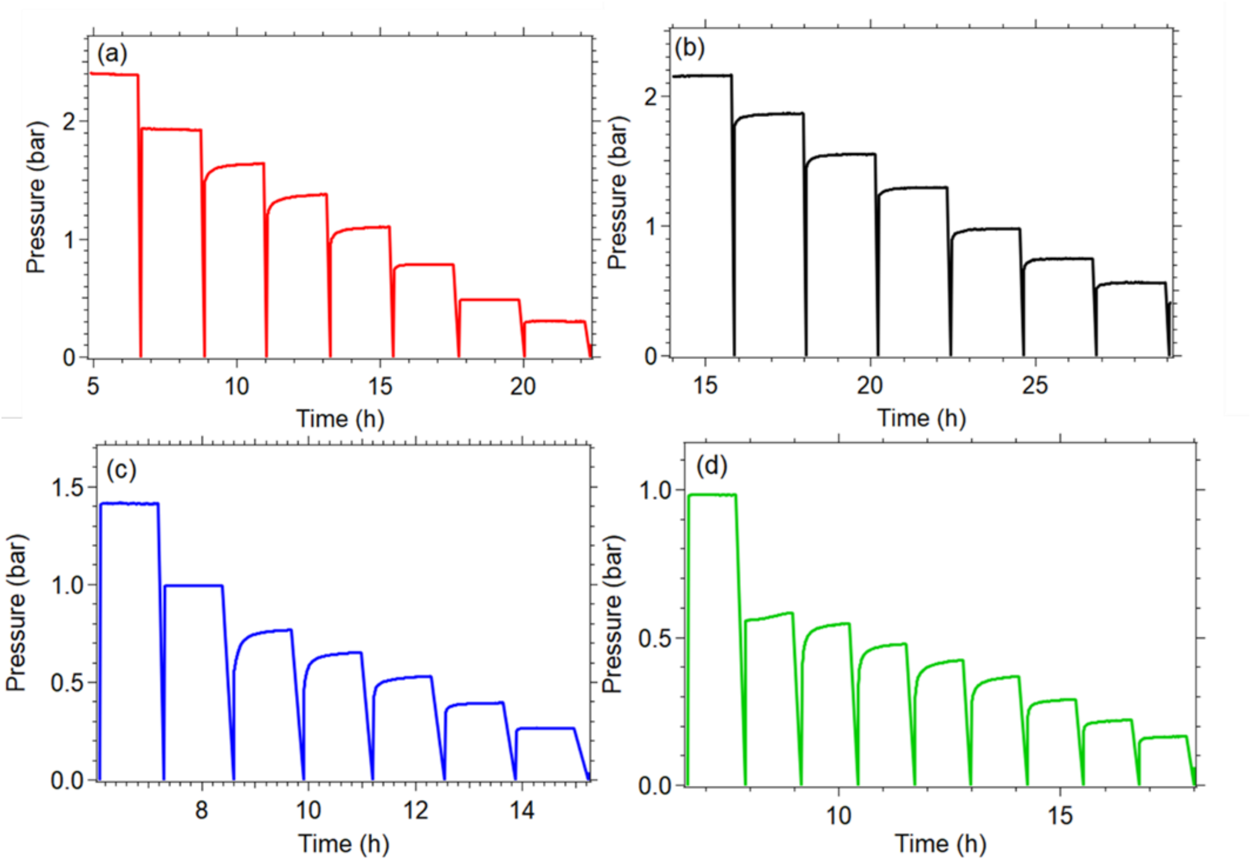

Figure 5.10 Equilibrium pressure curves of PCI performed at (a) 614 °C (b) 600 °C (c) 580 °C and (d) 565 °C with 3 h desorption step sizes.

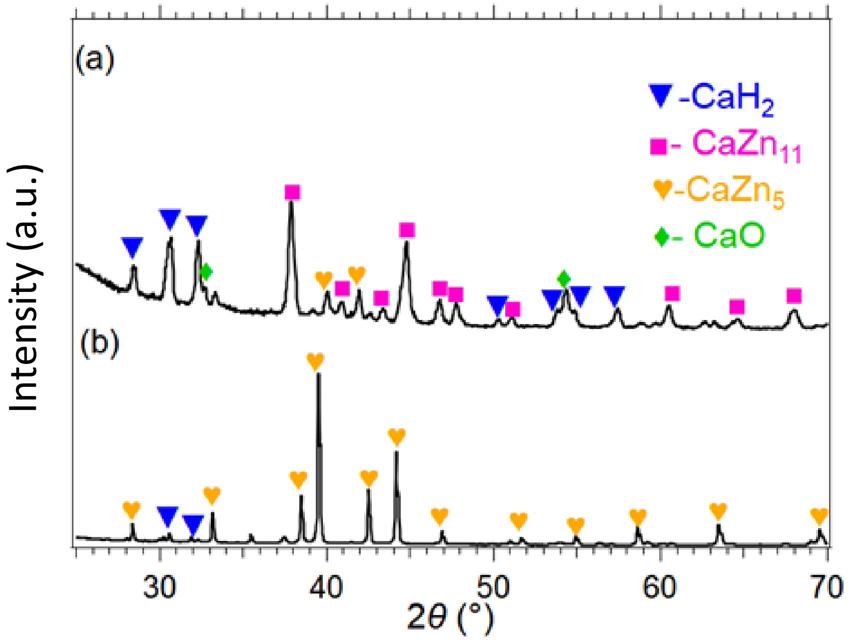

Figure 5.11 *Ex-situ* XRD patterns of CaH_2-3Zn in the marked regions (a) at (i) and (b) at (ii) in the Figure 5.8(a) from the PCI measurement at 600 °C (Cu Kα, λ = 1.5418 Å).

5.3.7 Cycling studies

CaH_2-3Zn was cycled at 580 °C, which follow the proposed optimised expressed in reaction (5-5), to assess its H_2 cycling capacity and thermochemical reversibility. This temperature was chosen in order to reduce the Zn evaporation rate from the sample. Figure 5.12 illustrates the ten H_2 desorption and absorption cycles showing good thermochemical reversibility overall. Each desorption and absorption step was 3 and 5 hrs, respectively. It is evident from Figure 5.12 that the kinetics of the desorption reaction are faster than the absorption. However, none of the reactions were completed within the allocated step time. The evaporation of Zn from the formed calcium zinc alloy during cycling was also confirmed from the presence of Zn metal deposition on the colder regions of the reactor. Therefore, after the completion of the 10th cycle, 80% of its initial capacity was retained. The cycling capacity of CaH_2-3Zn may be enhanced by improving the design of the sample holder so that it can contain the evaporated Zn and also by initially synthesizing with 1:11 molar ratio of CaH_2-Zn. This may result in a complete desorption and absorption reaction upon cycling within the allocated waiting times. Also, it may allow more cycles without degradation as commercial thermochemical storage system requires a cycling reliability of up to 10000 cycles over a 30-year lifespan for CSP plants. An *ex-situ* XRD pattern (Figure 5.13) was obtained after the 10th desorption cycle, confirming that $CaZn_{11}$ was the main crystalline phase present in the decomposed samples, as previously confirmed from TPD, PCT and *in-situ* XRD studies.

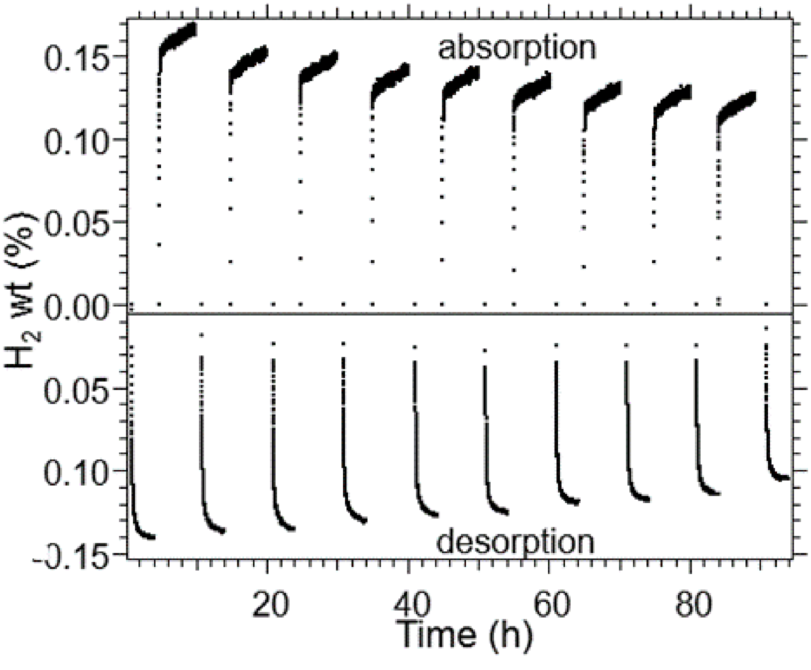

Figure 5.12 H_2 desorption and absorption cycles of the CaH_2-3Zn mixture at 580 °C.

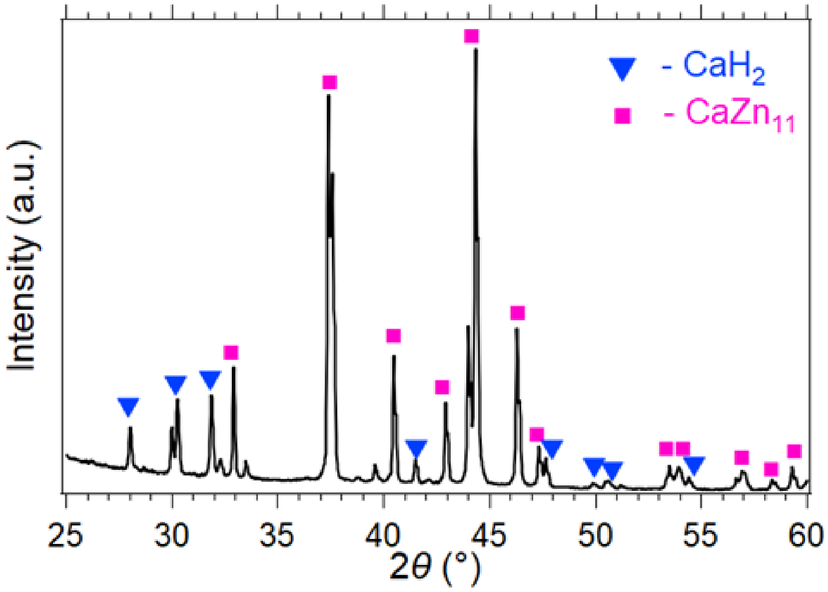

Figure 5.13 *Ex-situ* XRD pattern of the CaH_2-3Zn mixture as prepared after cycling at 580 °C (Cu Kα, λ = 1.5418 Å).

5.3.8 Morphological studies

SEM micrographs of CaH_2-3Zn before and after cycling are presented in Figure 5.14(a) - (c) and (d) - (f), respectively. It is evident from Figure 5.14(a), obtained using backscattered electrons, that CaH_2 and Zn are evenly distributed through the sample creating a homogenous powder after ball-milling. No distinctive bright and dark areas were observed in the micrograph that may have been created due to areas with inhomogeneous distributions of particles with excessively different atomic number, as observed in Figure 5.14(d) after cycling is performed. Specifically, the bright areas in Figure 5.14(d) indicated with yellow dashed circles are areas rich in Zn, whereas the dark areas indicated with red circles are Ca rich, as confirmed by their associated EDS spectra (Figure 5.15). To study the morphological differences before and after cycling, Figures 5.14(b), (c) and (e), (f) were obtained using secondary electrons. It can be seen from Figure 5.14(c) and (f) that the powder particles before and after cycling are relatively the same size and the particles did not sinter or melt upon heating, as often is the case with other metal hydrides at temperatures above 500 °C.[2]

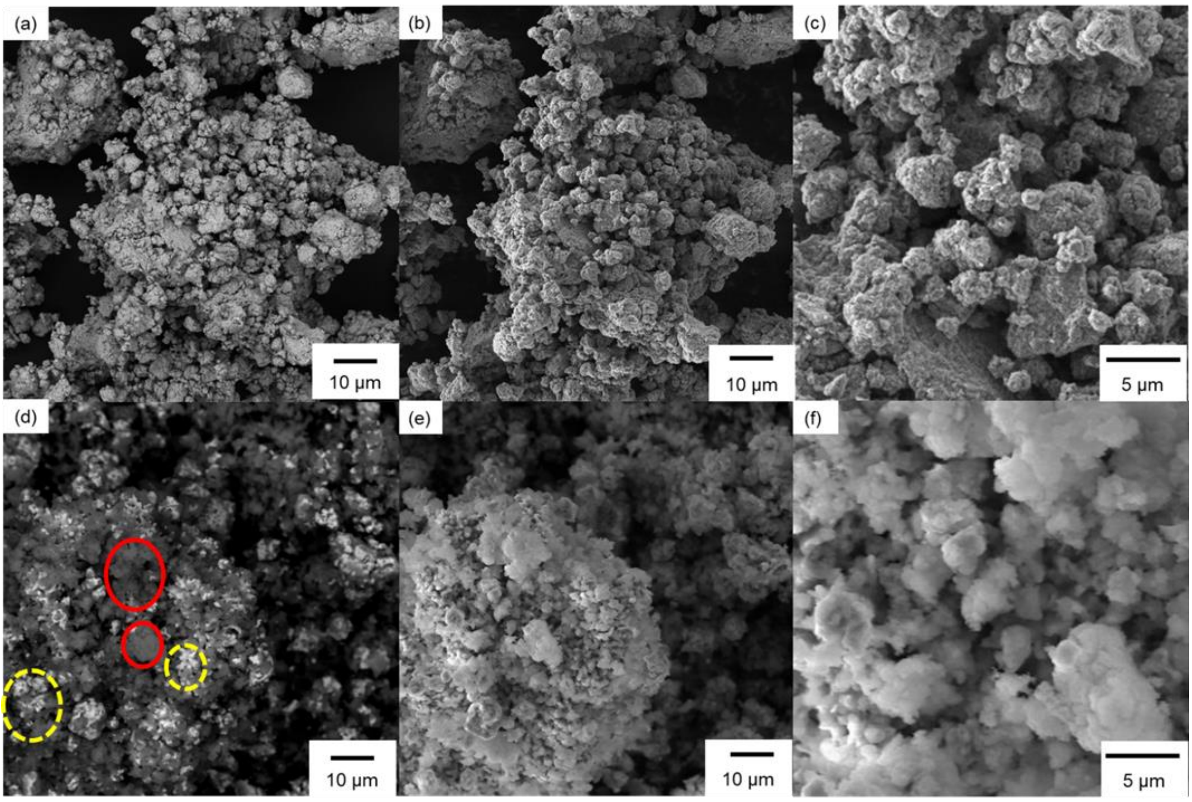

Figure 5.14 SEM micrographs of the CaH_2-3Zn mixture using (a) back scattered electrons, (b, c) secondary electrons before cycling, and (d) back scattered and (e, f) secondary electrons after 10 cycles at 580 °C.

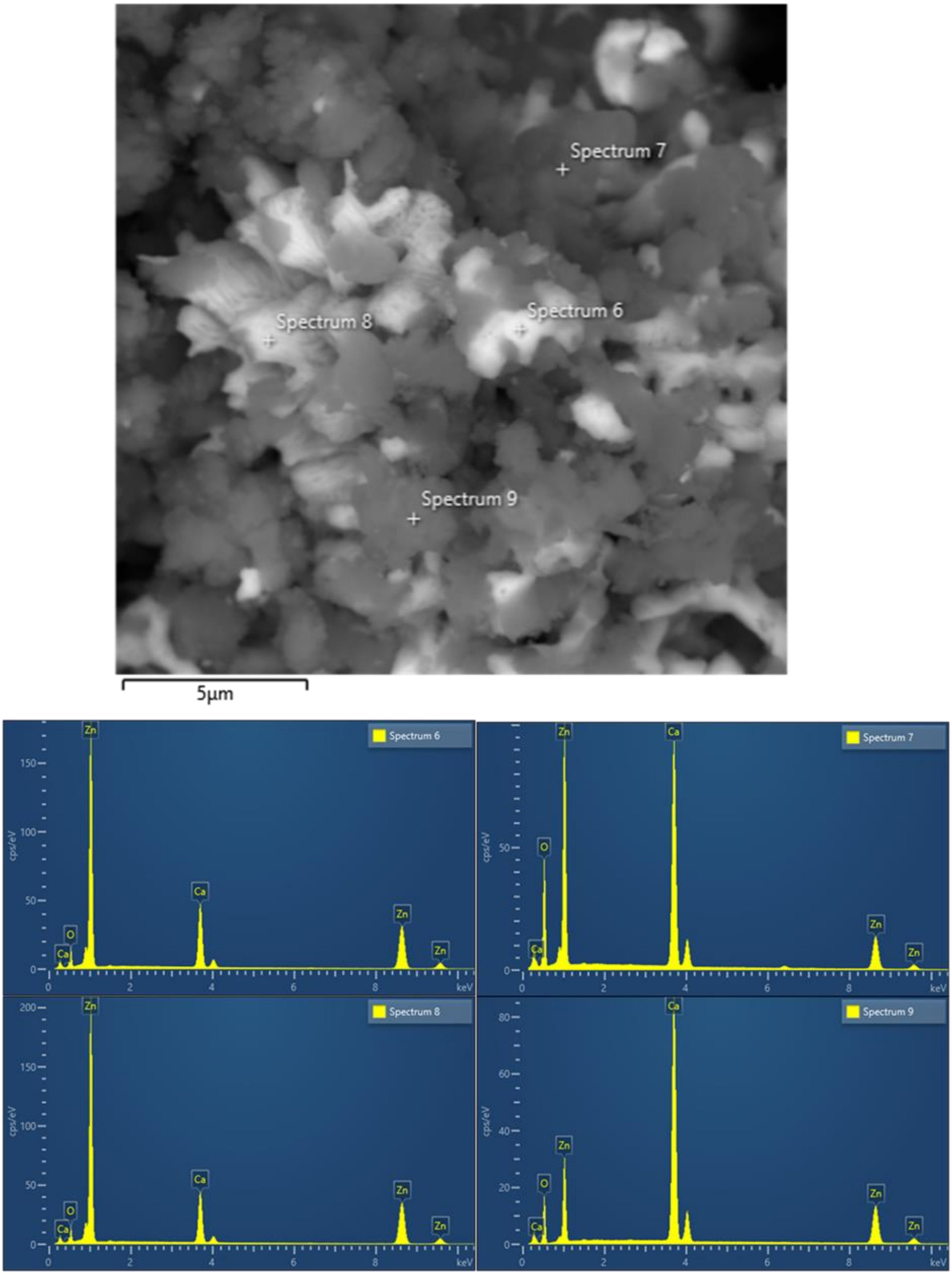

Figure 5.15 SEM images of CaH_2-3Zn after 10 cycles using backscattered electrons and corresponding EDS spectrum.

5.3.9 Cost

A cost comparison of the present system with other destabilised CaH_2 systems and molten salt is listed in Table 5.2. The cost of the raw material (CaH_2-11Zn) is currently estimated as \$55/ kWh_{th},[19, 40] which is higher than molten salts and other destabilised CaH_2 systems, such as Al and Al_2O_3 while significantly less compared with $LiBH_4$ as shown in Table 5.2.[43-44] However, the CaH_2-11Zn system possesses high enthalpy of reaction and relatively low operating pressure at the working temperature (1 bar H_2 pressure at ≈ 600 °C) compared with the CaH_2-Al system (62 bar H_2 pressure at ≈ 700 °C).[2,41] Overall the high cost, multistep reactions and Zn evaporation issues makes the CaH_2-3Zn system challenging to use as a commercial thermochemical storage material.

Table 5.2 Cost comparison study of CaH_2-3Zn system with pure CaH_2, other CaH_2 destabilised systems and molten salt in the CSP scenario[a,b].

TES Material	**Δ*H* (kJ.mol^{-1} H_2)**	**Δ*H* (kJ.kg^{-1})**	**US \$ (tonne)**	**US \$ (kWh_{th})**	**T (°C)**	**P (bar)**	**Mass required tonnes [b]**	**Ref.**
CaH_2	207.9	4939	6000	4.4	1000	1.2	265	[2,19]
CaH_2 + 11Zn	131	172	2649	55.4	597	1	8920	[40]
$3CaH_2$ + $2Al_2O_3$	100	909	2460	9.7	636	1	1650	[23]
CaH_2 + 2Al	84	874	3631	14.9	700	62	1660	[2, 23,41-42]
CaH_2 + $6LiBH_4$	60	347	190500	1976	450	10	4960	[43-44]
Molten salt (40 $NaNO_3$: 60 KNO_3)	39	413	630	5.8	565	-	5250	[19]

[a] Note that values were calculated in an assumption of 100% conversion of reactants.

[b] To generate 1TJ of energy

5.4 Conclusions

This study has developed a novel approach to thermodynamically destabilise CaH_2 by adding low cost Zn metal in a 1:3 molar ratio and investigate its potential as a TES material for third generation CSP plants. *In-situ* XRD diffraction studies showed the formation of three different calcium zinc alloys, $CaZn_{13}$, $CaZn_{11}$ and $CaZn_5$, at 190, 390 and 590 °C, respectively. The enthalpy and entropy of formation of CaH_2-3Zn system was found to be $\Delta H_{des} = 131 \pm 4$ kJ.mol^{-1}.H_2, $\Delta S_{des} = 151 \pm 4$ J.K^{-1}.mol^{-1}.H_2, respectively. The CaH_2-3Zn system's operating condition was found to be 597 ± 35 °C at 1 bar of H_2 pressure. Cycling studies of the material over the first step of the reaction show reasonable thermochemical reversibility over 10 cycles. SEM studies before and after cycling confirmed no significant sintering of the sample upon heating. The cost of the raw material was estimated as \$55/kWh$_{th}$. The destabilisation of CaH_2 with Zn proves that thermodynamic destabilisation can be achieved, but lower cost destabilising agents must be found. It is challenging to predict the optimal reaction pathways for these destabilisation reactions due to unreliable thermodynamic predictions for several reaction products.

5.5 References

1. Murphy, C.; Sun, Y.; Cole, W. J.; Maclaurin, G. J.; Mehos, M. S.; Turchi, C. S. The Potential Role of Concentrating Solar Power within the Context of Doe's 2030 Solar Cost Targets; National Renewable Energy Lab. (NREL), Golden, CO (United States): **2019**. https://doi.org/10.2172/1491726
2. Manickam, K.; Mistry, P.; Walker, G.; Grant, D.; Buckley, C. E.; Humphries, T. D.; Paskevicius, M.; Jensen, T.; Albert, R.; Peinecke, K., Future Perspectives of Thermal Energy Storage with Metal Hydrides. *Int. J. Hydrogen Energy*, **2019**, *44*, 7738-7745.

3. Pelay, U.; Luo, L.; Fan, Y.; Stitou, D.; Rood, M., Thermal Energy Storage Systems for Concentrated Solar Power Plants. *Renewable Sustainable Energy Rev.*, **2017**, *79*, 82-100.
4. Chen, X.; Zhang, Z.; Qi, C.; Ling, X.; Peng, H., State of the Art on the High-Temperature Thermochemical Energy Storage Systems. *Energy convers. manage.*, **2018**, *177*, 792-815.
5. Carrillo, A. J.; González-Aguilar, J.; Romero, M.; Coronado, J. M., Solar Energy on Demand: A Review on High Temperature Thermochemical Heat Storage Systems and Materials. J. *Chem. Rev.*, **2019**, *119*, 4777-4816.
6. US Department of Energy, D.O.E. Sunshot Vision Study. https://www.energy.gov/eere/solar/sunshot-initiative (accessed June 2020)
7. The Potential Role of Concentrating Solar Power within the Context of DOE 's 2030 Solar Cost Targets https://www.nrel.gov/docs/fy19osti/71912.pdf (accessed June 2020)
8. Ho, C. K., A Review of High-Temperature Particle Receivers for Concentrating Solar Power. *Appl. Therm. Eng.*, **2016**, *109*, 958-969.
9. Valverde, J. M.; Barea-Lopez, M.; Perejon, A.; Sanchez-Jimenez, P. E.; Perez-Maqueda, L. A., Effect of Thermal Pretreatment and Nanosilica Addition on Limestone Performance at Calcium-Looping Conditions for Thermochemical Energy Storage of Concentrated Solar Power. *Energy Fuels*, **2017**, *31*, 4226-4236.
10. Harries, D. N.; Paskevicius, M.; Sheppard, D. A.; Price, T. E. C.; Buckley, C. E., Concentrating Solar Thermal Heat Storage Using Metal Hydrides. *Proc. IEEE.*, **2011**, *100*, 539-549.
11. Pardo, P.; Deydier, A.; Anxionnaz-Minvielle, Z.; Rougé, S.; Cabassud, M.; Cognet, P., A Review on High Temperature Thermochemical Heat Energy Storage. *Renewable Sustainable Energy Rev.*, **2014**, *32*, 591-610.
12. Ervin, G., Solar Heat Storage Using Chemical Reactions. *J. Solid state chem.*, **1977**, *22*, 51-61.
13. Gil, A.; Medrano, M.; Martorell, I.; Lázaro, A.; Dolado, P.; Zalba, B.; Cabeza, L. F., State of the Art on High Temperature Thermal Energy Storage for Power Generation. Part 1—Concepts, Materials and Modellization. *Renewable Sustainable Energy Rev.*, **2010**, *14*, 31-55.
14. Lai, Q.; Paskevicius, M.; Sheppard, D. A.; Buckley, C. E.; Thornton, A. W.; Hill, M. R.; Gu, Q.; Mao, J.; Huang, Z.; Liu, H. K., Hydrogen Storage Materials for Mobile and Stationary Applications: Current State of the Art. *ChemSusChem* **2015**, *8*, 2789-2825.
15. Sheppard, D.; Corgnale, C.; Hardy, B.; Motyka, T.; Zidan, R.; Paskevicius, M.; Buckley, C. E, Hydriding Characteristics of $NaMgH_2F$ with Preliminary Technical and Cost Evaluation

of Magnesium-Based Metal Hydride Materials for Concentrating Solar Power Thermal Storage. *RSC Advances* **2014**, *4*, 26552-26562.

16. Ragheb, M., Hydrides Alloys for Hydrogen Storage. Energy Storage and Conveyance-Bridging the Supply-Demand Gap. Urbana-Champaign, USA*: University of Illinois* **2011**.
17. Rönnebro, E. C.; Whyatt, G.; Powell, M.; Westman, M.; Zheng, F. R.; Fang, Z. Z., Metal Hydrides for High-Temperature Power Generation. *Energies* **2015**, *8*, 8406-8430.
18. Sheppard, D.; Paskevicius, M.; Humphries, T.; Felderhoff, M.; Capurso, G.; von Colbe, J. B.; Dornheim, M.; Klassen, T.; Ward, P.; Teprovich, J., Metal Hydrides for Concentrating Solar Thermal Power Energy Storage. *Appl. Phys. A*, **2016**, *122*, 395.
19. Humphries, T. D.; Møller, K. T.; Rickard, W. D.; Sofianos, M. V.; Liu, S.; Buckley, C. E.; Paskevicius, M., Dolomite: A Low Cost Thermochemical Energy Storage Material. *J. Mater. Chem. A*, **2019**, *7*, 1206-1215.
20. Curtis, R.; Chiotti, P., Thermodynamic Properties of Calcium Hydride1. *J. Phys. Chem.* **1963**, *67*, 1061-1065.
21. Peterson, D.; Fattore, V., Calcium-Calcium Hydride Phase System1. *J. Phys. Chem.*, **1961**, *65*, 2062-2064.
22. Sofianos, M. V.; Randall, S.; Paskevicius, M.; Aguey-Zinsou, K.-F.; Rowles, M. R.; Humphries, T. D.; Buckley, C. E., Exploring Halide Destabilised Calcium Hydride as a High-Temperature Thermal Battery. *J. Alloys Compd*, **2020**, *819*, 153340.
23. Balakrishnan, s.; Sofianos, M. V.; Paskevicius, M.; Rowles, M. R.; Buckley, C. E., Destabilised Calcium Hydride as a Promising High-Temperature Thermal Battery. *J. Phys. Chem. C*, **2020**.
24. Vajo, J. J.; Olson, G. L., Hydrogen Storage in Destabilised Chemical Systems. *Scripta Materialia* **2007**, *56*, 829-834.
25. Okamoto, H., Ca-Zn (Calcium-Zinc). *J. Phase Equilib. Diffus.*, **2013**, *34*, 171-171.
26. Messing, A.; Adams, M.; Steunenberg, R. Contribution to the Phase Diagram Calcium-Zinc; Argonne National Lab., Ill.: **1962**.
27. Vapor Pressure Calculator. https://www.iap.tuwien.ac.at/www/surface/vapor_pressure (accessed May 2020)
28. Rietveld, H., A Profile Refinement Method for Nuclear and Magnetic Structures. *J. Appl. Crystallogr.*, **1969**, *2*, 65-71.
29. Coelho, A. A., Topas and Topas-Academic: An Optimization Program Integrating Computer Algebra and Crystallographic Objects Written in C++. *J. Appl. Crystallogr.*, **2018**, *51*, 210-218.

30. Gražulis, S.; Daškevič, A.; Merkys, A.; Chateigner, D.; Lutterotti, L.; Quiros, M.; Serebryanaya, N. R.; Moeck, P.; Downs, R. T.; Le Bail, A., Crystallography Open Database (Cod): An Open-Access Collection of Crystal Structures and Platform for World-Wide Collaboration. *Nucleic Acids Res.,* **2011**, *40*, D420-D427.
31. Pathak, P.; Vasavada, N., Thermal Expansion of NaCl, KCl and CsBr by X-Ray Diffraction and the Law of Corresponding States. *Acta Crystallogr., Sect. A: Cryst. Phys., Diffr., Theor. Gen. Crystallogr.,* **1970**, *26*, 655-658.
32. Hu, J.; Cai, W.; Li, C.; Gan, Y.; Chen, L., *In-Situ* X-Ray Diffraction Study of the Thermal Expansion of Silver Nanoparticles in Ambient Air and Vacuum. *Appl. Phys. Lett.,* **2005**, *86*, 151915.
33. Hansen, B. R.; Møller, K. T.; Paskevicius, M.; Dippel, A.-C.; Walter, P.; Webb, C. J.; Pistidda, C.; Bergemann, N.; Dornheim, M.; Klassen, T., *In-Situ* X-Ray Diffraction Environments for High-Pressure Reactions. *J. Appl. Crystallogr.*, **2015**, *48*, 1234-1241.
34. Systems, S. R., SRS RGA Https://Www.Thinksrs.Com/Products/Vac.Html.
35. Sheppard, D. A.; Paskevicius, M.; Javadian, P.; Davies, I. J.; Buckley, C. E., Methods for Accurate High-Temperature Sieverts-Type Hydrogen Measurements of Metal Hydrides. *J. Alloys Compd.,* **2019**, *787*, 1225-1237.
36. Alonso, J. A.; Retuerto, M.; Sanchez-Benitez, J.; Fernández-Díaz, M. T., Crystal Structure and Bond Valence of CaH_2 from Neutron Powder Diffraction Data. *Zeitschrift für Kristallographie-Crystalline Materials*, **2010**, *225*, 225-229.
37. Chiotti, P.; Hecht, R., Thermodynamic Properties of the Calcium-Zinc System. *AIME MET SOC TRANS* **1967**, *239*, 536-541.
38. Itkin, V.; Alcock, C., The Ca-Zn (Calcium-Zinc) System. *Bull. Alloy Phase Diagrams,* **1990**, *11*, 328-333.
39. Hodge, W.; Jaffe, R.; Gonser, B. Calcium and Calcium-Base Alloys; BATTELLE MEMORIAL INST COLUMBUS OH: **1949**.
40. Zn Metal Prices. https://markets.businessinsider.com/commodities/zinc-price (accessed April 2020)
41. Ward, P. A.; Teprovich Jr, J. A.; Liu, Y.; He, J.; Zidan, R., High Temperature Thermal Energy Storage in the $CaAl_2$ System. *J. Alloys Comp*d., **2018**, *735*, 2611-2615.
42. Veleckis, E., Application of the Hydrogen Titration Method to a Thermodynamic Investigation of Solid Al-Ca Alloys. *J. Less-Common Met.*, **1981**, *80*, 241-255.

43. Li, Y.; Li, P.; Qu, X., Investigation on $LiBH_4$-CaH_2 Composite and Its Potential for Thermal Energy Storage. *Sci. Rep.*, **2017**, *7*, 41754.

44. $LiBH_4$ Prices. https://www.sigmaaldrich.com/catalog/search?term=LiBH4&interface=All&N=0&mode=partialmax&lang=en&region=AU&focus=product (accessed April 2020)

Chapter 6

Performance of calcium hydride graphite system at high temperatures

6.1 Introduction

The reaction between CaH_2 and carbon was first reported in the 1920s, in which Reich *et al.* mentioned that calcium hydride might react with carbon to form calcium carbide and hydrogen.[1] The production of calcium carbide by reacting CaH_2 and graphite in different ratios at high temperatures has also been discussed by Konar *et al.* to study the structural polymorphs of CaC_2.[2] Different polymorphs of CaC_2 were synthesised by reacting CaH_2 and graphite at temperatures of 700 °C to 1400 °C with specific molar ratios between 1:1.8 and 1:2.2. The degassed graphite powder (heat the graphite powder at 900 °C under dynamic vacuum to remove the moisture) and CaH_2 were mixed thoroughly using a mortar and pestle before being pressed into pellets and then sealed in Ta ampoules by welding. The reactions were carried out at temperatures between 700 °C to 1100 °C, and the significant findings were the existence of three different crystal modifications of CaC_2, as shown in Table 6.1. By varying the pressure applied and temperature, both monoclinic forms have the potential to transform into CaC_2 I. A fourth high-temperature cubic face centred CaC_2 IV crystal structure was also discussed.

Table 6.1 Polymorphs of CaC_2.[2-3]

phase	Crystal structure	Phase group	Structural Parameters (Å)	
CaC_2 I	tetragonal	*I4/mmm*	*a*	3.8845(1)
			c	6.3969(2)
CaC_2 II	monoclinic	*C2/c*	*a*	6.6479(1)
			b	4.2007(3)
			c	7.3335(5)
			β	107.2590(3)
CaC_2 III	monoclinic	*C2/m*	*a*	7.2317(4)
			b	3.8540(1)
			c	7.3780(3)
			β	107.3660(2)
CaC_2 IV	Cubic face centred	$Fm\bar{3}m$	*a*	5.8911(6)

In addition, the interaction between solid graphite and molecular gaseous hydrogen was also studied by several investigators. In 1968, Bernal *et al.* discussed the reaction kinetics between graphite and gaseous hydrogen in the temperature range between 180 - 925 °C.[4] The products of the reaction were methane and molecular hydrogen. It was also noted that the reaction rate increases with temperature and the temperature at which the maximum reaction rate occurs vary with the chemical nature of reactants and products and the catalysts used.[4-5]

As explained in Chapter 1, CaH_2 is identified as a promising next-generation thermochemical energy storage material due to its high gravimetric & volumetric energy density. Due to the corrosive nature of CaH_2, the most challenging part is to find a suitable additive that thermodynamically destabilises the CaH_2 and hence reduces the operating temperature. Properties such as low cost ($ 1/kg), the low molar mass of graphite (12.011 $g.mol^{-1}$) and the high theoretical gravimetric heat storage capacity (2072 $kJ.kg^{-1}$ for the predicted equation 6-1) of the CaH_2 and graphite system makes graphite a suitable candidate for thermodynamic destabilisation of calcium hydride.[6] Recently, Griffond *et al.* investigated CaH_2 mixed with expanded natural graphite (ENG) as thermochemical energy storage (TES) material.[7] During thermal decomposition, the release of an acetylene gas at 400 °C, along with CaC_2 and H_2, was reported.[7] However, the reversibility of the CaC_2 was unknown, as these studies were not investigated.

In this chapter, the performance of the CaH_2-graphite system as a TES material for CSP application was investigated both theoretically and experimentally at high temperatures. The study focuses on the thermal analysis, thermodynamic and kinetic characterisation of the CaH_2-graphite system using temperature-programmed desorption (TPD), pressure composition isotherms (PCIs), differential scanning calorimetry (DSC) and thermal gravimetric analysis (TGA). Its cycling capacity and morphological changes of the sample before and after cycling using field emission scanning electron microscopy (FE-SEM) were also investigated.

6.2 Results and discussion

6.2.1 Theoretical thermodynamic predictions

HSC Chemistry was used to initially identify whether the chemical reaction between CaH_2 and 2C (graphite) is thermodynamically favourable without considering reaction kinetics.[8-11] The software was used to plot a graph to show how the equilibrium ratio of materials alters as a function of temperature (Figure 6.1). The initial reactants CaH_2 and C were provided in a 1:2 ratio, and the possible products were predicted. The graph clearly shows that the reaction between CaH_2 and 2C is thermodynamically favourable in the high-temperature region. The reaction between CaH_2 and 2C starts from 500 °C, and the main reaction product was confirmed as CaC_2. It can also be confirmed from Figure 6.1 that there is no release of acetylene gas during the reaction between CaH_2 and 2C as mentioned by Griffond *et.al.*[7] The predicted reaction and the thermodynamic conditions from HSC Chemistry software are

$$CaH_2 + 2C \rightleftharpoons CaC_2 + H_2\,(g) \qquad 6\text{-}1$$

and

ΔH = 137 kJ.mol^{-1}.H_2, ΔS = 177 J.K^{-1} mol^{-1}.H_2, $T_{1\,\text{bar}} = \frac{\Delta H}{\Delta S}$ = 501 °C, and H_2 wt% = 3.05.

According to the HSC predictions, adding graphite to CaH_2 reduces the 1 bar hydrogen equilibrium pressure and enthalpy of pure CaH_2 from 1055 °C to 501 °C and 167 kJ.mol^{-1}.H_2 to 137 kJ.mol^{-1}.H_2, respectively. According to the prediction, this reaction is thermodynamically favourable; however, the kinetics are unknown.

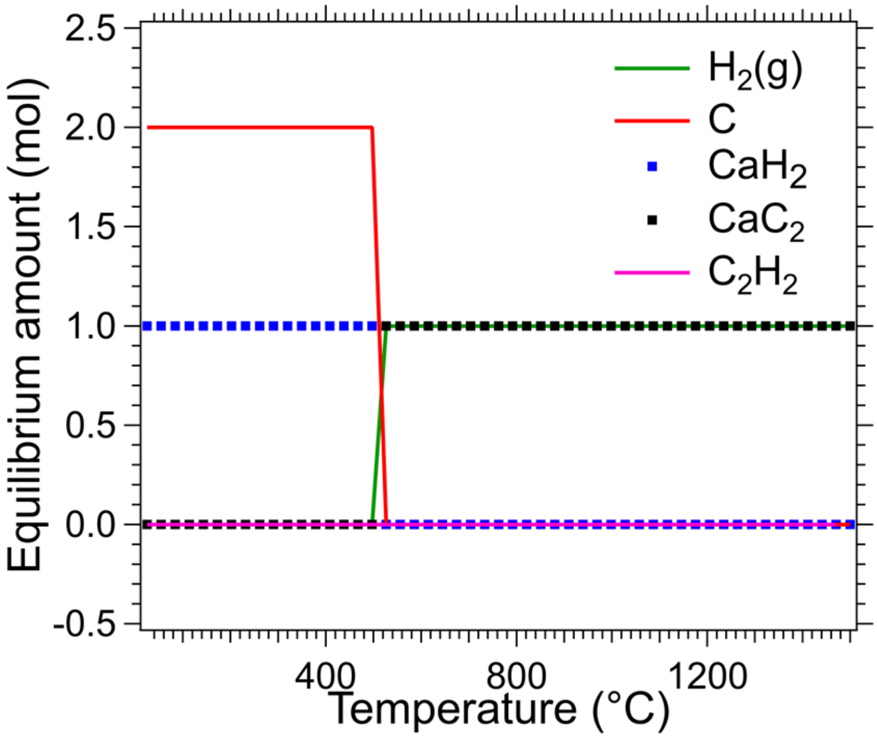

Figure 6.1 HSC graphical simulation of CaH_2-2C system at a pressure of 1 bar.

6.2.2 Synthesis and initial phase analysis

All the samples were handled inside the Ar filled glove box (O_2 and H_2O level < 0.1 ppm). The graphite (Sigma Aldrich, ≤ 100%) was outgassed at 550 °C for 12 hours under a dynamic vacuum to remove any moisture and then mixed with calcium hydride (Sigma Aldrich, > 95%) in a 2:1 molar ratio. Next, the mixture was ball milled for 3 hours under an Ar atmosphere using an Across International Planetary Ball Mill, employing stainless steel vials and balls with a 40: 1 ball to powder ratio.

The diffraction patterns of as-supplied CaH_2, outgassed graphite and ball-milled CaH_2-2C are presented in Figure 6.2 (1)(a), (b), and (c), respectively. Quantitative phase analysis was used to determine the purity of the materials using the Rietveld method.[12] All these analyses were performed by me. Quantitative phase analysis of the CaH_2 reagent shows CaH_2 with a negligible amount of crystalline CaO and $Ca(OH)_2$ (< 1%). The XRD and refinement pattern for the ball-milled CaH_2-2C shows CaH_2 (65 ± 1 wt%), and C (35 ± 1 wt%) (Figure 6.2 (1)(c) and Figure 6.2(2)). This indicates that no reaction has occurred between the CaH_2 and graphite during ball milling to form any crystalline Ca-C products.

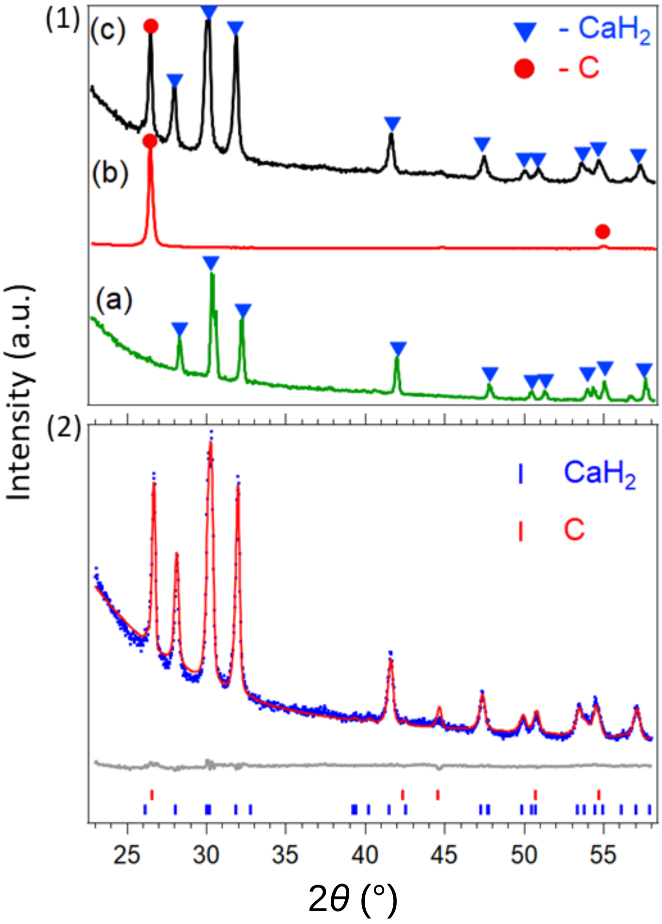

Figure 6.2 (1) *Ex-situ* XRD patterns of (a) CaH_2, (b) outgassed graphite, and (c) Ball milled CaH_2-2C and (2) Rietveld refinement of the diffraction pattern for CaH_2-2C system. Blue line - raw data, red line - fitted data, grey line - difference plot (Cu K_α, $\lambda = 1.5418$ Å).

6.2.3 Thermal analysis

TPD-MS (Temperature Programmed desorption- Mass Spectrometry) measurements were performed on CaH_2 and the CaH_2-2C mixture to compare their hydrogen desorption profiles. As a high vacuum (< 10^{-4} mbar) was employed in this technique, CaH_2 started to release hydrogen at 500 °C and reached its highest intensity of desorption at 600 °C (Figure 6.3(a)). Figure 6.3(b) shows the hydrogen desorption profile of the CaH_2-2C mixture, with a smaller peak at 240 °C and a prominent peak at 550 °C. The smaller peak at a lower temperature may be due to the presence of $Ca(OH)_2$ impurities in the CaH_2 sample, which decomposes below 300 °C.[13] It indicates that adding 2C to CaH_2 reduces the decomposition temperature of CaH_2 slightly with a peak shift of 50 °C. No other gases, including acetylene, were detected.

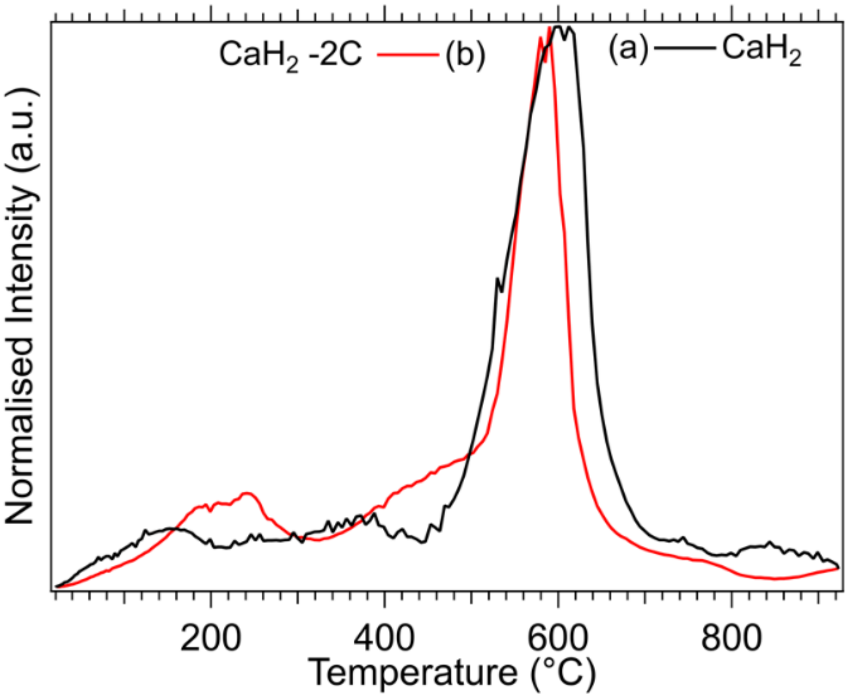

Figure 6.3 Hydrogen desorption profiles as observed by TPD-MS measurements of (a) CaH_2 and (b) the CaH_2-2C mixture at a heating rate of 5 °C/min under a dynamic vacuum.

Temperature programmed desorption (TPD) was performed from room temperature to 800 °C (5 °C/min) on the CaH_2-2C mixture (Figure 6.4). Figure 6.4 (a) shows the plot between time and desorbed H_2 wt%, and Figure 6.4(b) is presented as temperature vs differential pressure. The reaction between CaH_2 and 2C becomes significant from ≈ 500 °C reaching maximum hydrogen desorption of 2.8% H_2 at ≈ 740 °C as shown in Figure 6.4(a). The measurement was initiated under vacuum conditions (less than 0 bar) and reached its maximum hydrogen desorption value (an equivalent pressure of 2.85 bar) in less than the 3 hours required for the system to reach 800 °C from room temperature. The mixture was kept at 800 °C for almost 7 h with no significant change in the wt% of desorbed hydrogen.

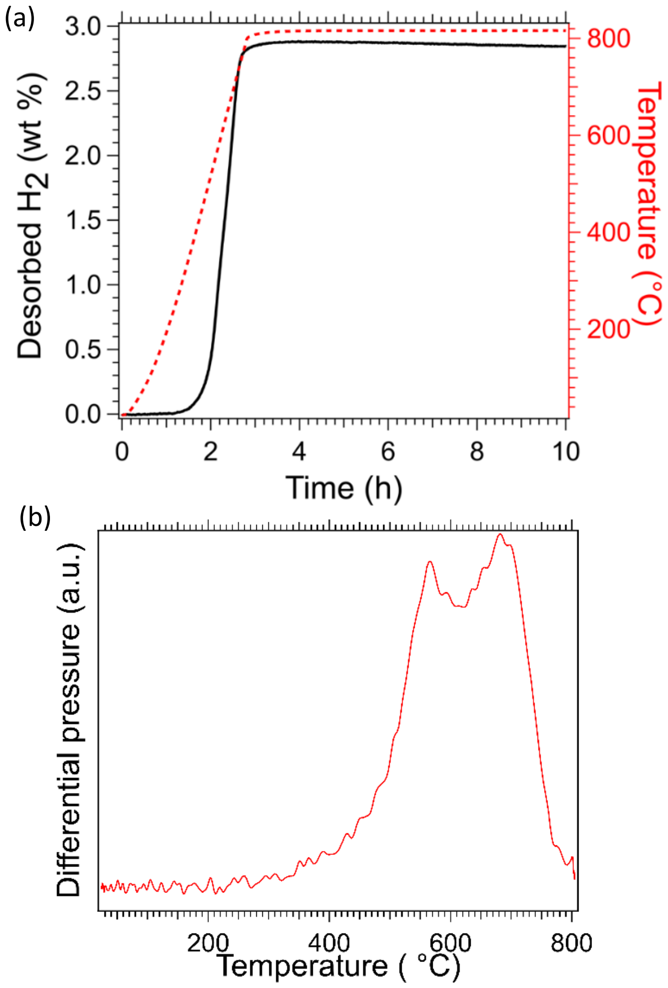

Figure 6.4 TPD profiles of the CaH_2-2C mixture with a ramp rate of 5 °C/min (a) time vs desorbed H_2 wt% and (b) temperature vs differential pressure from room temperature to 800 °C.

The decomposition products for the CaH_2-2C system after the TPD measurement were determined by *ex-situ* X-ray powder diffraction (Figure 6.5 (1)) and quantified by the Rietveld refinement method (Figure 6.5(2). It was confirmed that CaC_2 was the main decomposition product, albeit existing in two different crystallographic polymorphs. Both room temperature polymorphs exist in monoclinic space groups and are identified as CaC_2 II (*C*2/*c*) and CaC_2 III

(*C2*/*m*), with a wt% of 30 ± 2 and 63 ± 2 respectively (Figure 6.5(2)). Also, the wt% of CaO was determined from Figure 6.5(2) as 7.0 ± 0.3.

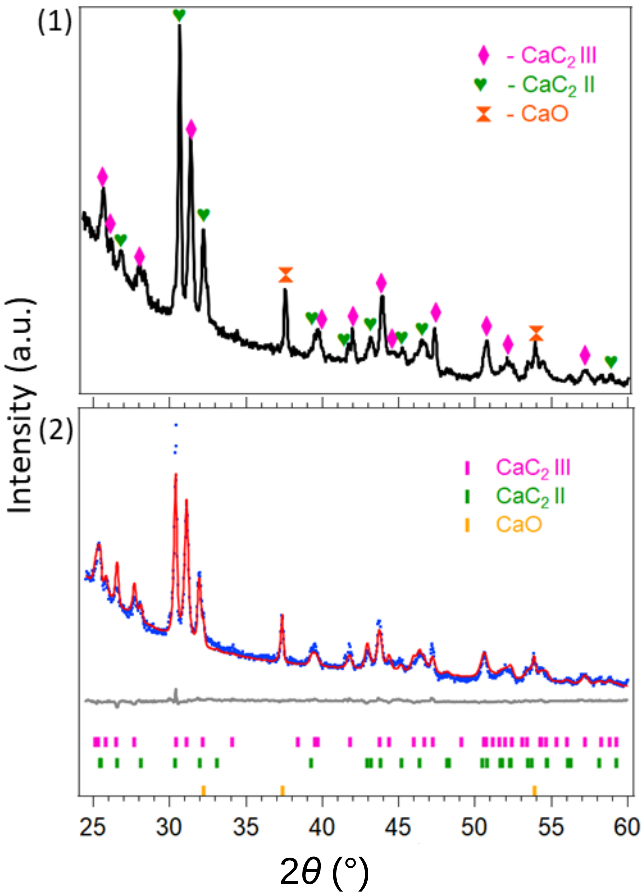

Figure 6.5 (1) *Ex-situ* powder diffraction pattern and corresponding **(2)** Rietveld refinement of CaH_2-2C system after TPD (Cu K_α, $\lambda = 1.5418$ Å).

To confirm the polymorphic transitions of CaC_2 and decomposition pathway of the CaH_2-2C system, the material was heated to varying temperatures of 300, 460, 580, and 700 °C under a dynamic vacuum. The samples were placed in the stainless steel sample cells inside the SiC reactor and heated to each temperature with a heating rate of 5 °C/min and stayed isothermal for 10 hours and then cooled with the same ramp rate of heating. The *ex-situ* XRD patterns of these materials after heating were collected and illustrated in Figure 6.6. The XRD patterns of the room temperature and material heated to 300 °C are identical, indicating that no reaction between CaH_2 and 2C occurred below 300 °C. Figure 6.6(c) shows small Bragg peaks for CaC_2 III, indicating that the reaction between CaH_2 and 2C commences below 460 °C. The material heated to 580 °C and 700 °C (Figure 6.6 (d) and (e)), show that all of the CaH_2 and C peaks have completely disappeared and have been replaced by CaC_2 II and CaC_2 III phases, which is in good agreement with the XRD pattern after TPD measurements.

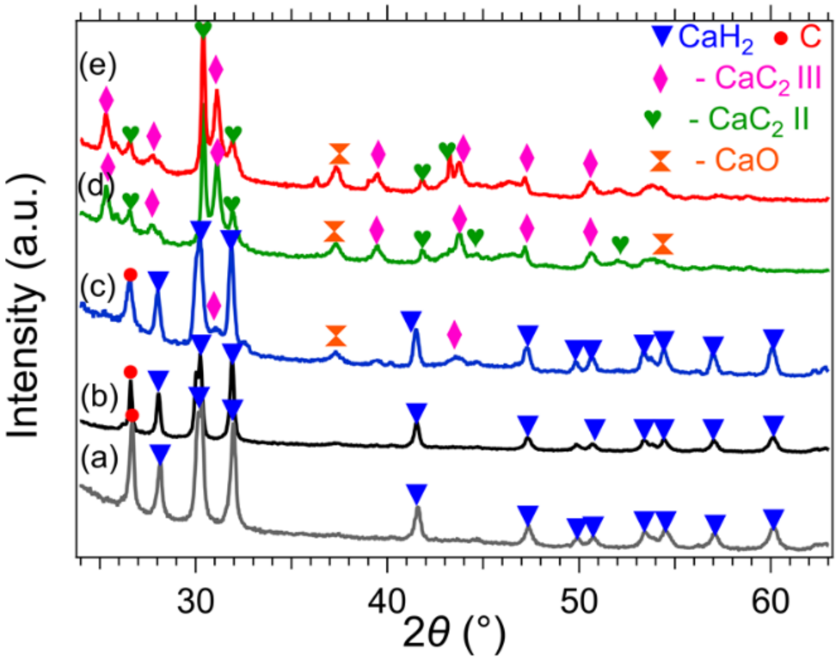

Figure 6.6 *Ex-situ* XRD patterns of CaH_2-2C system at (a) room temperature (b) 300 °C (c) 460 °C (d) 580 °C and (e) 700 °C (Cu K_α, $\lambda = 1.5418$ Å).

6.2.4 *In-situ* X-ray diffraction and differential scanning calorimetry studies

In-situ XRD data of the CaH_2-2C system was collected during heating and cooling with a ramp rate of 5 °C/min under a static argon atmosphere in a sealed quartz capillary tube, with the data being presented in Figure 6.7 (a) and compared with DSC plot as shown in Figure 6.7(b). It is evident from the *in situ* XRD and DSC patterns that the reaction between CaH_2 and 2C is significant above 500 ° C, which is in agreement with the TPD curves in Figure 6-4 (b).

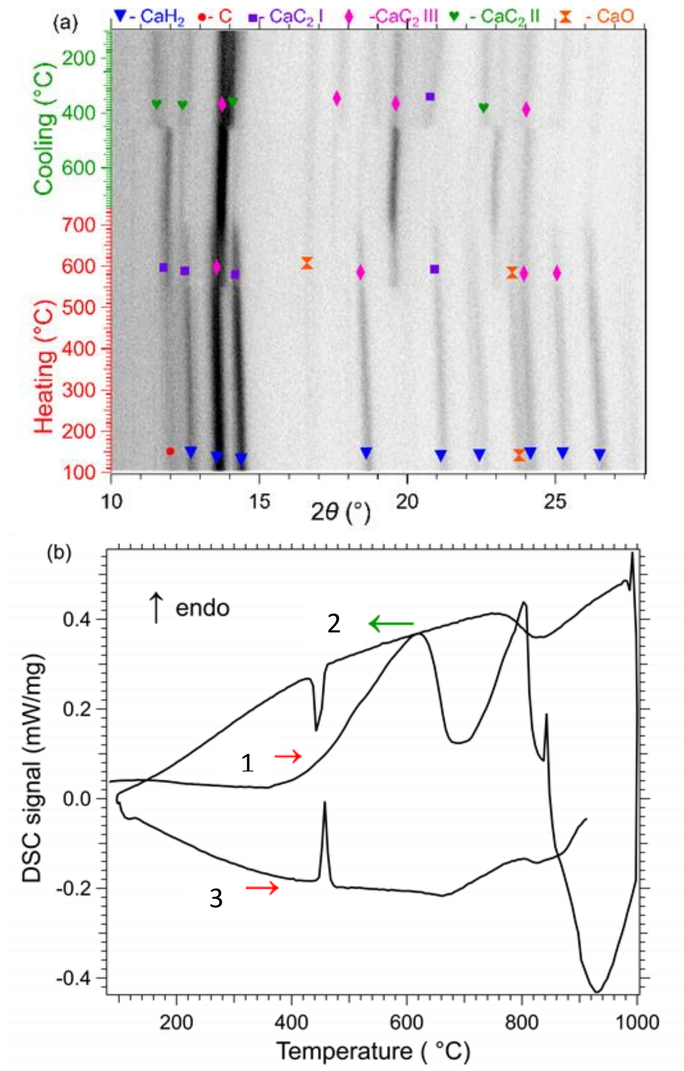

Figure 6.7 (a) *In-situ* XRD patterns using Mo K_α of $\lambda = 0.7093$ Å and (b) DSC plots upon heating and cooling with a ramp rate of 5 °C/min for the CaH_2-2C system.

At temperatures above 550 °C, the two polymorphs of CaC_2, CaC_2 I (*I*4/*mmm*) and CaC_2 III (*C*2/*m*), was observed from the in situ pattern and can be compared to the two endothermic peaks in the DSC scan. Also, the *in situ* data show the structure transition of CaC_2 when cooling from tetragonal CaC_2 I (*I*4/*mmm*) to monoclinic CaC_2 II (*C*2/*c*) at 450 °C that is precisely correlated with the DSC cooling and second heating curve as shown in Figure 6.7(b). The tetragonal structure of CaC_2 (CaC_2 I (*I*4/*mmm*)) is unstable at room temperature but present at high temperature and, hence, cannot be identified by the *ex-situ* XRD measurements.[2-3]

6.2.5 Kinetics of CaH_2-2C system

Kinetics of the CaH_2-2C system were calculated by DSC analysis using a Netzsch (STA 449 F3 Jupiter) under Ar flow of 40 mL/min with an Al_2O_3 crucible to load the sample. The three DSC curves with heating rates of 20, 10 and 5 °C/min and the corresponding first peak temperatures of decomposition are labelled as shown in Figure 6.8 (a). Using these heating rates and peak temperatures, Kissinger graph[14] is plotted to calculate the activation energy of the system, as shown in Figure 6.8 (b). The activation energy E_a for the CaH_2-2C system was calculated as 215 ± 12 $kJ.mol^{-1}$, close to the value 203 ± 12 $kJ.mol^{-1}$ obtained for pure CaH_2 in chapter 3 (section 3.2.8). This comparison indicates adding 2C might not alter or improve the kinetics of decomposition of CaH_2. The higher the activation energy, the lower the reaction kinetics. Therefore, the high value of E_a for the CaH_2-2C system indicates slow kinetics.

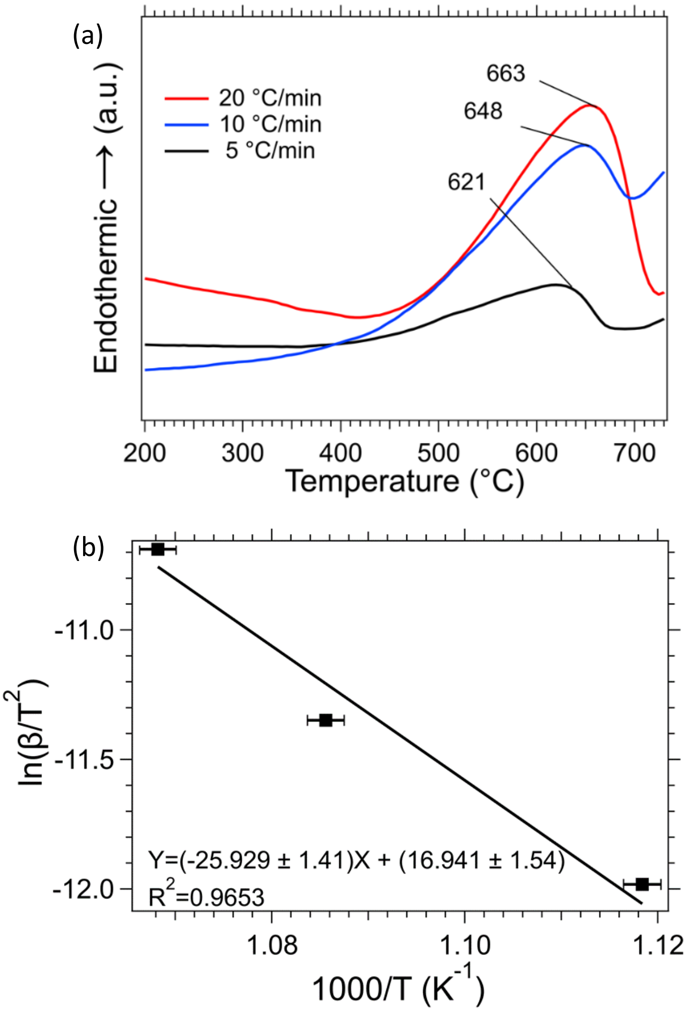

Figure 6.8 (a) Differential scanning calorimetry pattern of CaH_2-2C system and corresponding (b) Kissinger plot for hydrogen release from the CaH_2-2C system.

6.2.6 Thermodynamics of CaH_2-2C system

To determine the thermodynamics of the CaH_2-2C system, eight PCI's were performed in the temperature range of 580 - 670 °C. Generally, as the sample desorbs the gas for the hydrogen desorption PCI analysis, the volumetric gas system will reveal an increase in pressure, as explained in chapter 2, Section 2.3.7.2. However, for the CaH_2-2C system, during each desorption PCI experiment, a steady increase in pressure was not observed. It showed an unexpected decrease in pressure at some temperatures, as shown in Figure 6.9. Moreover, when the PCI's were repeated at the same temperature and initial conditions, it was found that the pattern was not reproducible, as shown in Figure 6.9 (a) and (b). It is clear from Figure 6.9 (a) and (b) even though performed at the same temperature of 625 °C, the pressure curves are different. In the first experiment, a decrease in pressure was initially observed before the system pressure remained constant after further steps. In the second experiment, an increase in pressure during the first step was observed, followed by a gradual decrease in the system pressure in the following steps. Figure 6.9 (c) shows desorption of only 1.3 wt%, while in Figure 6.9 (d), the pressure remained constant throughout the steps, although a small change in pressure at 3 bar was observed. The PCI at 660 °C was repeated (Figure 6.9 (e)), and a different pattern was again obtained with a pressure decrease observed below 1 bar (see insert in Figure 6.9 (e)). This trend was observed in almost all performed PCI's in the temperature range from 580 to 670 °C, and therefore it was not possible to identify an equilibrium plateau on the pressure vs H_2 wt% plots. Hence, it was impossible to determine the thermodynamics of the system. XRD data were collected after PCI to determine the decomposition products after PCI. It was clear from the XRD after PCI measurements and from the quantification (Figure 6.10 (1) & (2)) that there was an excess of CaH_2 present (38 ± 1 wt%) and less carbon (4 ± 1 wt%) being available to react with CaH_2. The wt% of formed CaC_2 II, CaC_2 III and CaO was quantified as 14 ± 1, 40 ± 1 and 4 ± 1, respectively. The presence of CaH_2 remaining after the PCI measurement was due to the loss of carbon in the form of methane gas, which was later confirmed by TPD-MS analysis of the final system gas composition. As explained in the literature, this may be due to the reaction between graphite and gaseous hydrogen, which means fewer moles of H_2 gas and hence a decrease in the system pressure.[4-5] The reaction can be written as shown in equation 6-2.

$$C + 2H_2\,(g) \rightarrow CH_4\,(g) \qquad 6\text{-}2$$

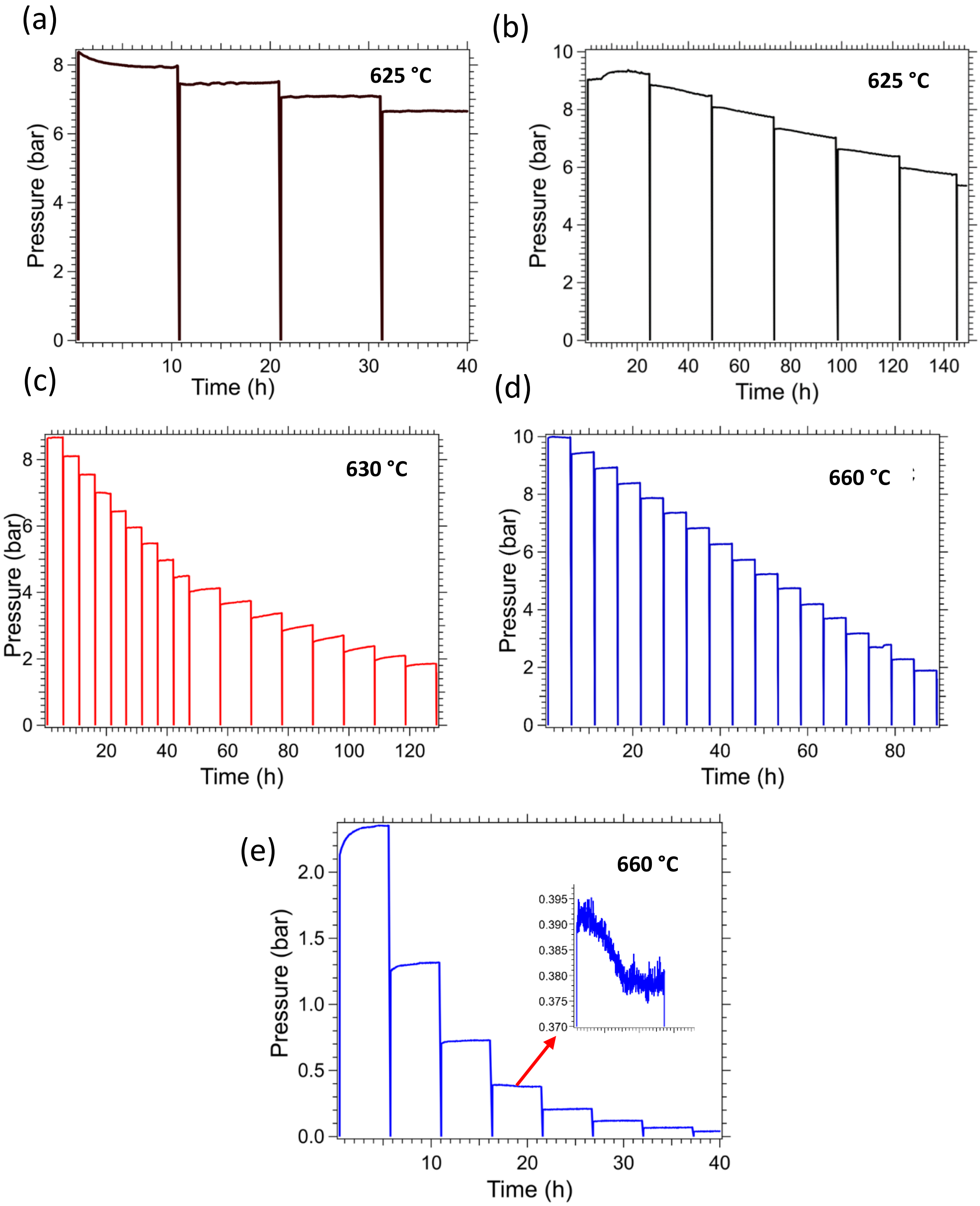

Figure 6.9 Examples of hydrogen pressure curves of CaH_2-2C system at 625 °C, 630 °C and 660 °C while performing PCI's.

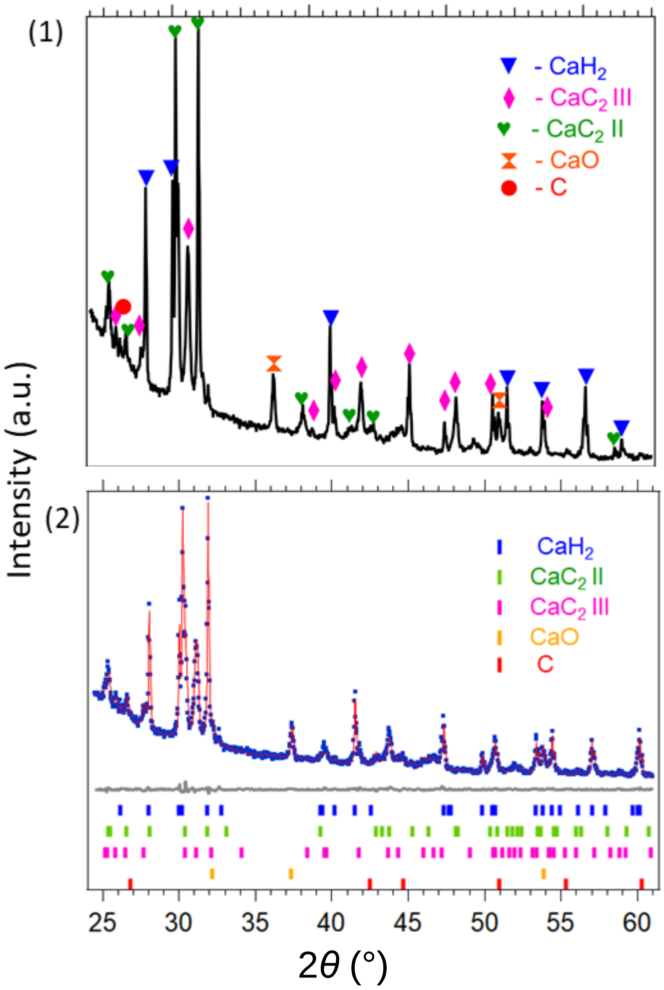

Figure 6.10 (1) *Ex-situ* powder diffraction pattern and corresponding (2) Rietveld refinement of CaH_2-2C system after PCI (Cu K_α radiation, $\lambda = 1.5418$ Å).

6.2.7 Methane production at moderate H_2 pressures

To confirm the loss of carbon during the PCI experiment, the CaH_2-2C material was heated from room temperature to 600 °C (ramp rate of 5 °C/min) under 6 bar of H_2 pressure to avoid the decomposition of the system at elevated temperature based on the thermodynamics calculated in HSC Chemistry. A gas sample was extracted using a stainless-steel double-ended sample cylinder (77 cm^3) and connected to a mass spectrometer for compositional analysis. As shown in Figure 6.11, the TPD-MS analysis revealed the release of methane gas along with hydrogen and therefore explains the unexpected pressure decrease observed during desorption PCI measurements. From the mass spectrometer a partial pressure of methane (3.7×10^{-5} mbar) was observed of which was almost equal to that of H_2 (3.6×10^{-5} mbar) with a composition 51 and 49%, respectively. Methane and hydrogen were the only two species of gas observed with no acetylene release detected, which is contradictory to the findings of Griffond et.al.[7]

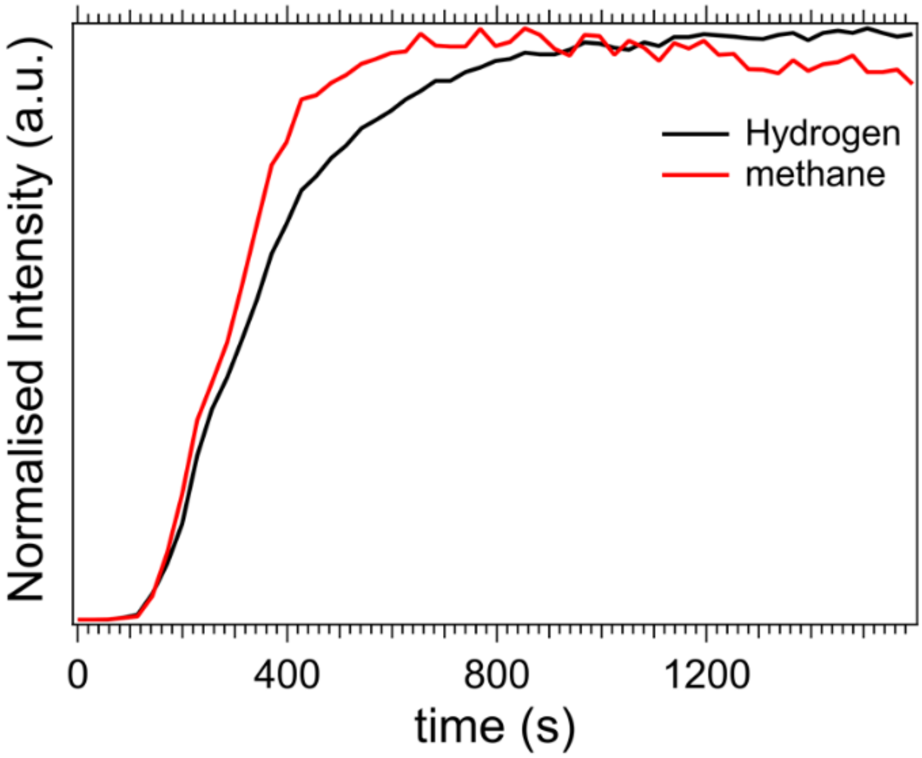

Figure 6.11 Major gases released measured by TPD-MS on the CaH_2-2C system.

As explained in section 6.2.5, the inconsistent and non-equilibrium patterns of the PCI curves make it difficult to find the reaction thermodynamics of the system. However, to test the reversibility of the system, an absorption and desorption was performed after a desorbed PCI (corresponding to one sorption cycle). Figure 6.12 (1) and (2) shows the XRD pattern and corresponding Rietveld refinement of the CaH_2-2C system after second desorption, which shows excess CaH_2 and no more carbon available to react with CaH_2. Almost 56 ± 2 wt% of CaH_2 and 0 wt% C remained to react after 2nd desorption. This explains the degradation of the system after the first cycle. The products formed have a wt% of 30 ± 3, 6 ± 1 and 9 ± 1 CaC_2 III, CaC_2 II and CaO, respectively. The availability of graphite to react with CaH_2 after each cycle will be less as it absorbs H_2 and forms methane gas under H_2 pressure. The reversibility is the crucial parameter determining the potential application of this material as a TES in CSP plants. Therefore, the formation of methane gas may ultimately limit the use of the CaH_2-2C system as a TES material.

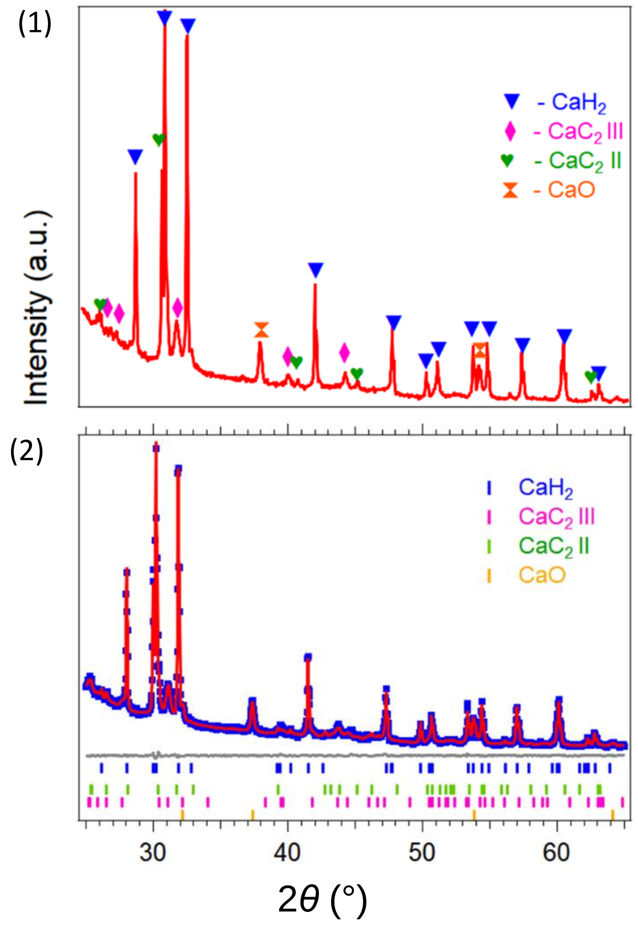

Figure 6.12 (1) *Ex-situ* powder diffraction patterns and corresponding **(2)** Rietveld refinement of CaH_2-2C system after cycling (λ = 1.5418 Å).

As discussed in the previous section (6.2.5), it is difficult to measure the thermodynamics of equation 6-1 experimentally due to the formation of methane gas and slow kinetics. Hence, the theoretical thermodynamic calculations were repeated using HSC Chemistry software to include methane as a product, and the data plotted in Figure 6.13. It is clear from Figure 6.13 that the formation of acetylene (C_2H_2) is not thermodynamically favourable, and only methane gas is found, a prediction that is in good agreement with the TPD-MS observations. As such an alternate theoretical reaction pathway between CaH_2 and C was predicted, as shown in equation 6-3. The Gibbs free energy values of a reaction determine whether the reaction is thermodynamically favourable or not and if $\Delta G \leq 0$, the reaction will occur spontaneously. The ΔG values of equation 6-3 are more negative compared to equation 6-1, as shown in Figure 6.14. Hence, it may also explain the formation of methane during experiments. Therefore, it is hard to explain the exact reaction pathway of the CaH_2-2C system, and it is possible that the three reactions (6-1, 6-2 and 6-3) may occur at the same time.

$$2CaH_2 + 5C \rightarrow CaC_2 + CH_4\,(g) \qquad 6\text{-}3$$

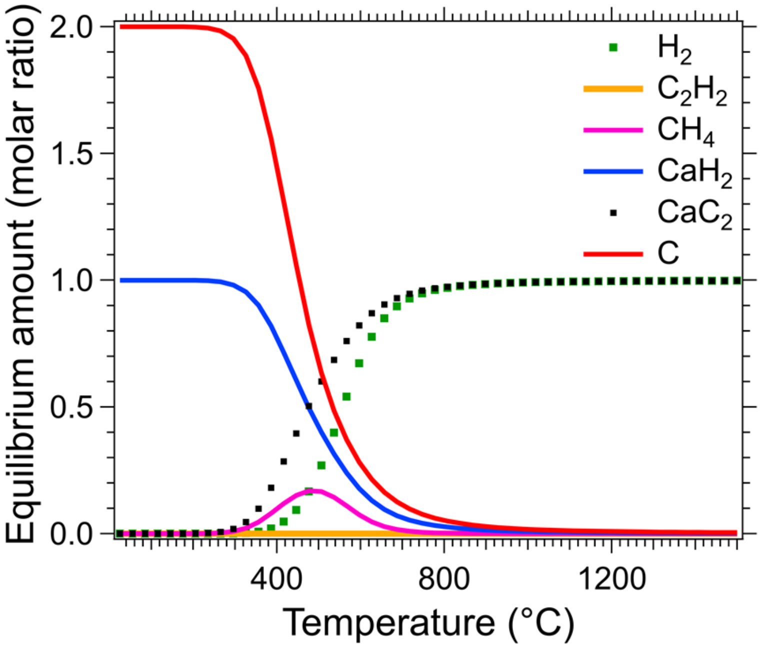

Figure 6.13 Graphical simulation of CaH_2-2C system at 1 bar of pressure including CH_4 as a reaction product.

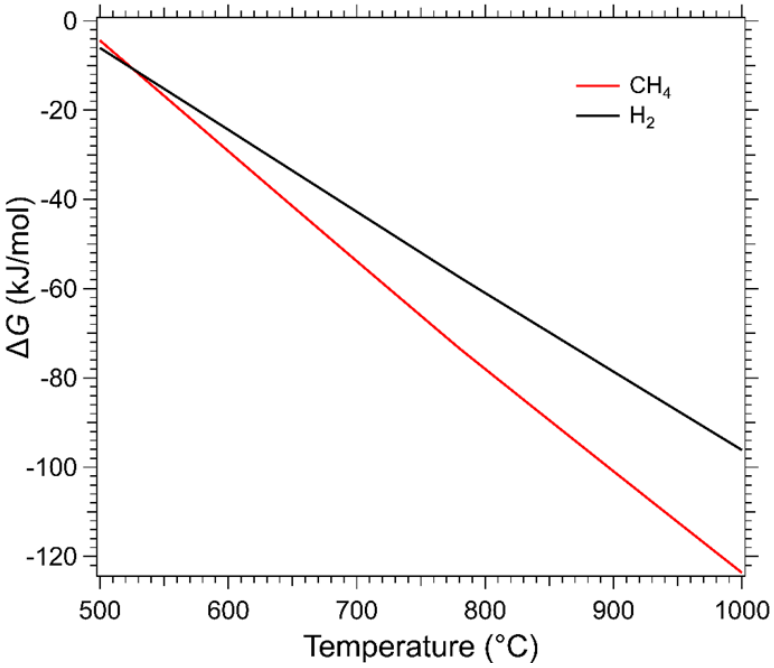

Figure 6.14 Gibbs free energy values for the reactions 6-1(H_2 release-black line) & 6-2 (CH_4 release-red line).

6.2.8 SEM

The morphological changes of the CaH_2-2C system before and after one cycle were studied by field emission scanning electron microscopy (Figure 6.15 (a) & (b)), and the corresponding energy dispersive X-ray Spectroscopy (EDS) spectra also acquired and presented in Figure 6.15 (c) & (d)) respectively. It is evident from Figure 6.15 (a) that after ball milling CaH_2 and C are evenly distributed throughout the sample, having brighter regions representing Ca rich regions. Figure 6.15 (c) shows the EDS spectra of the ball-milled CaH_2-2C system, which confirms the elemental compositions of Ca, C and O only; no other impurities were found as expected. The powder particle size of the cycled mixture is almost 2 μm bigger than the prepared ball-milled ones, which may be due to the thermal expansion or due to the sintering. It can be seen from Figure 6.15 (b) that the particles are sintered or melted after heating.

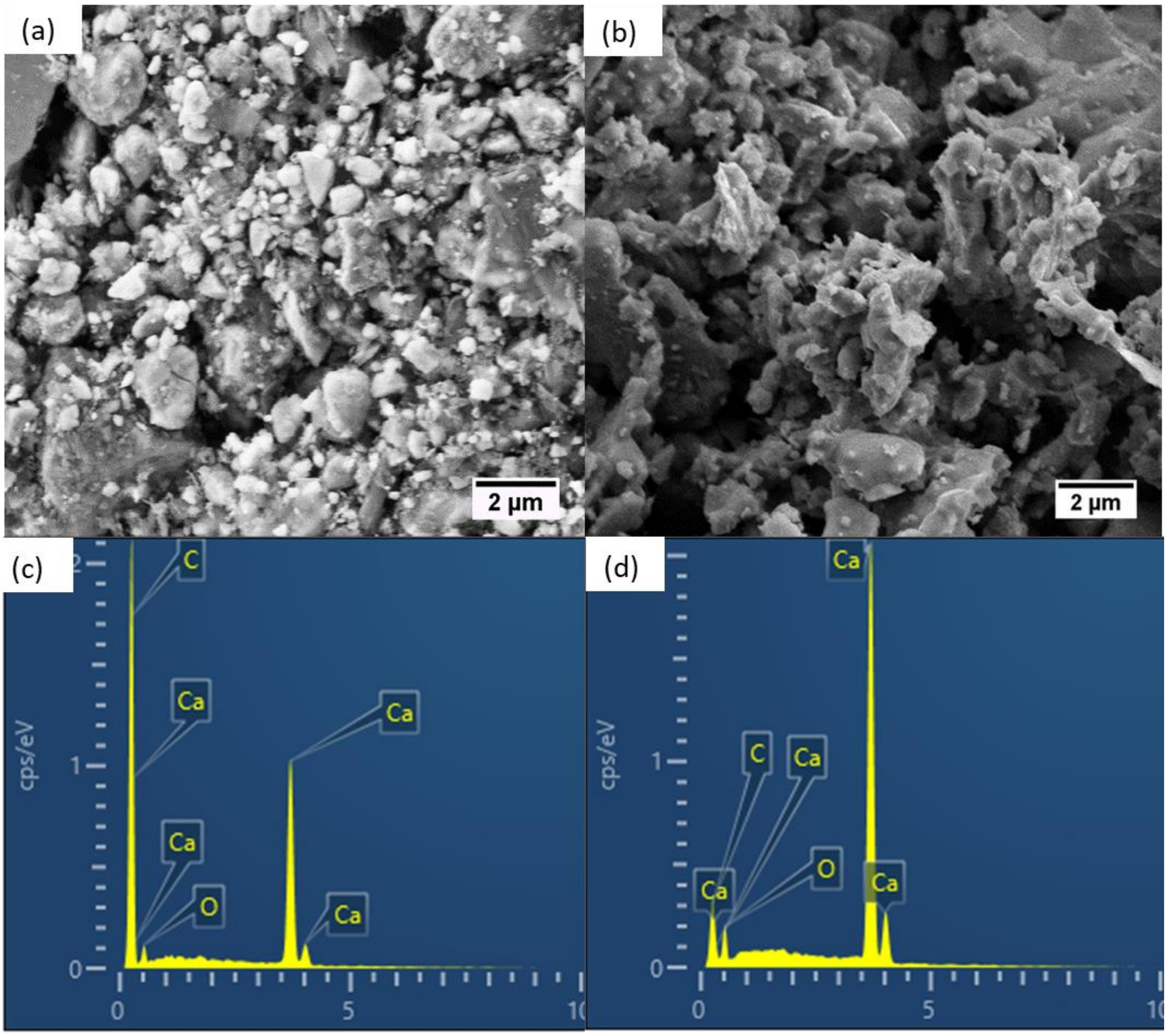

Figure 6.15 SEM micrographs of the CaH_2-2C system and corresponding EDS spectra (a & c) as prepared (b & d) after cycling.

6.3 Summary

The Calcium hydride graphite mixture was synthesised in a 1:2 ratio by ball milling and experimentally investigated and its feasibility as a TES material for CSP applications is reported. Temperature programmed desorption (TPD) and XRD data after 800 °C showed CaC_2 as the main decomposition product. *In situ* XRD studies revealed different polymorphic transformations of CaC_2 as CaC_2 I ($I4/mmm$) and CaC_2 III ($C2/c$), while heating. Also, it confirmed the transformation of CaC_2 I to CaC_2 II ($C2/m$) while cooling. DSC analysis and corresponding Kissinger plot calculated the activation energy of the system as 215 ± 12 $kJ.mol^{-1}$.Thermal analysis and mass spectrometry studies revealed the formation of methane gas in addition to hydrogen under H_2 pressure. The theoretical data from HSC chemistry software shows that the methane formation (6- 3) is more thermodynamically favourable than hydrogen production in reaction (6-1), which is also confirmed experimentally. Unfortunately, the formation of methane gas, the possibility of three different reactions occurring at same time, the slow reaction rate, and the poor reversibility indicates a barrier to applying the CaH_2-2C system as a TES material for CSP application. However, the system may be used for industrial methane and calcium carbide production. Industrial methane production could be less feasible due to the high cost associated with material itself, CaH_2 ($6000/tonne) compared to the other available methods as the current average market price of methane around the world is $0.95 per litre.[15-16]

6.4 References

1. Reich, S.; Serpek, H., Sur Quelques Réactions De L'hydrure De Calcium. *Helvetica Chimica Acta* **1920**, *3*, 138-144.
2. Konar, S.; Nylén, J.; Svensson, G.; Bernin, D.; Edén, M.; Ruschewitz, U.; Häussermann, U., The Many Phases of CaC_2. *J. Solid State Chem.,* **2016**, *239*, 204-213.
3. Knapp, M.; Ruschewitz, U., Structural Phase Transitions in CaC_2. *Chemistry-A European Journal* **2001**, *7*, 874-880.
4. Wood, B. J.; Wise, H., Reaction Kinetics of Gaseous Hydrogen Atoms with Graphite. *J. Phys. Chem.,* **1969**, *73*, 1348-1351.

5. Goethel, P. J.; Yang, R. T., Mechanism of Graphite Hydrogenation Catalysed by Nickel. *J. Catal.* **1987**, *108*, 356-363.
6. Graphite Prices. https://www.alibaba.com/products/graphite/CID9090402.html?IndexArea=product_en. (accessed November **2021**).
7. Griffond, A. C. M. Concentrating Solar Thermal Storage Using Metal Hydride: Study of Destabilised Calcium Hydrides. Curtin University, **2019**.
8. Roine, D. A., Hsc Ver.9.0.0 Https://Www.Outotec.Com/Products/Digital-Solutions/Hsc-Chemistry/.
9. Takahashi, Y.; Westrum Jr, E. F., Glassy Carbon Low-Temperature Thermodynamic Properties. *J. Chem. Thermodyn.*, **1970**, *2*, 847-854.
10. Lutcov, A.; Volga, V.; Dymov, B., Thermal Conductivity, Electric Resistivity and Specific Heat of Dense Graphites. *Carbon* **1970**, *8*, 753-760.
11. Dobrosavljevic, A.; Perovic, N.; Maglic, K., Thermophysical Properties of POCO A× M-5Q1 Graphite in the 300 to 1800 K Range. *High Temperatures. High Pressures (Print)* **1987**, *19*, 303-310.
12. Rietveld, H., A Profile Refinement Method for Nuclear and Magnetic Structures. *J. Appl. Crystallogr.* **1969**, *2*, 65-71.
13. Lin, S.; Wang, Y.; Suzuki, Y., High-Temperature Cao Hydration/Ca (Oh) 2 Decomposition over a Multitude of Cycles. *Energy Fuels* **2009**, *23*, 2855-2861.
14. Kissinger, H. E., Reaction Kinetics in Differential Thermal Analysis. *Anal. Chem.* **1957**, *29*, 1702-1706.
15. Global Petrol Prices. https://www.globalpetrolprices.com/methane_prices/ (accessed November **2021**).
16. Humphries, T. D.; Møller, K. T.; Rickard, W. D.; Sofianos, M. V.; Liu, S.; Buckley, C. E.; Paskevicius, M., Dolomite: A Low Cost Thermochemical Energy Storage Material. *J. Mater. Chem. A* **2019**, *7*, 1206-1215.

Chapter 7

Metal oxides for the thermodynamic destabilisation of CaH_2: A comparison of several metal oxide systems.

7.1 Introduction

Calcium can be used as a reducing agent in metallic or hydride forms. P.P Alexander was the first person who discovered that calcium hydride might be used as a reducing agent for producing pure metals from their metal oxides.[1-2] The reduction process was used in the preparation of chromium, titanium and uranium and was patented in 1934.[3] It was noted that the calcium reduction reaction is more exothermic than the calcium hydride reduction reaction; a portion of the heat of the reaction will be required to break the bonds of hydride.[4] The general reduction reaction between CaH_2 and a *M*O (metal oxide) can be expressed as shown in 7-1.

$$MO + CaH_2 \rightleftharpoons M + CaO + H_2(g) \qquad 7\text{-}1$$

As explained in chapter 2, finding a suitable additive is the most important and demanding one to convert CaH_2 into a suitable TES for the next generation CSP plants. The thermodynamic destabilisation of CaH_2 with Al_2O_3 and Zn was achieved and reduced the operating temperature of pure CaH_2 to 636 and 597 °C, respectively (Chapter 4 & 5). However, adding C to CaH_2 (Chapter 6) did not destabilise as theoretically expected. It is difficult to predict the exact reaction pathway due to variable or unrealistic thermodynamic predictions for various reaction products.

Metal oxides are comparatively cheaper, have high melting and boiling points, are less volatile, more stable, safer to handle in air and more readily available. Therefore, this chapter details the effect of some commonly available oxides (as shown in Table 7.1) on the thermodynamic destabilisation of CaH_2. A brief literature review, theoretical thermodynamic predictions, and these oxides' specific features are given in the next section.

Table 7.1 The selected ten different oxides for the destabilisation of CaH_2 and their physical properties.

	Oxide	**Chemical formula**	**Manufacturer**	**Purity (%)**	**Molar mass (g. mol^{-1})**	**Density (g.cm^{-3})**	**Melting point (°C)**	**Cost (US \$ per tonne)***	**Ref**
1	Zinc oxide	ZnO	Sigma Aldrich	99	81.38	5.61	1975	1234	[5-7]
2	Zirconium (IV)	ZrO_2	Aldrich	99	123.21	5.68	2700	10,000	[8-10]

	oxide (< 100 nm)								
3	Silicon dioxide (< 10 - 20 nm)	SiO_2	Aldrich	99.5	60.08	2.65	1710	2500	11-13
4	Manganese (II) oxide	MnO	Chem supply	> 94	70.93	5.43	1842	8000	14-15
5	Ferric oxide	Fe_2O_3	Aldrich	≤ 100	159.70	5.24	1565	580	16-17
6	Titanium (IV) oxide	TiO_2	Aldrich	99	79.86	4.23	1840	1400	9, 18-19
7	Nickel (II) oxide	NiO	Sigma - Aldrich	99.9	74.69	6.67	1955	5000	20-21
8	Copper (II) oxide	CuO	Aldrich	99	79.54	6.31	1326	2000	22-23
9	Yttrium (III) oxide	Y_2O_3	Aldrich	99.9	225.81	5.01	2400	3000	24-25
10	Cerium (IV) oxide (< 25 nm)	CeO_2	Aldrich	99	172.11	7.22	2600	1500	26-27

*The prices in USD were chosen as an average from a range of given price lists in the market from the references provided in the table.

7.2 Literature review

Pure zinc oxide (ZnO) is a soft white powder but naturally occurs as a rare mineral zincite.[28] It has been considered an attractive material for various applications due to its unique physical and chemical properties. These applications include solar cells, gas sensors, surface acoustic wave devices and light emitters.[29-31] ZnO is also commonly studied as a heterogeneous catalyst among transition metal oxides.[32] It has high melting and boiling points (1975 °C and 2360 °C) and exists as a hexagonal wurtzite structure ($P6_3mc$) under ambient pressure conditions.[12, 31, 33] According to HSC Chemistry software, the reaction between CaH_2 and ZnO is highly exothermic and requires extremely high pressures. The reaction is predicted as shown in 7-2 with $\Delta H = -105$ kJ.mol^{-1}.H_2 at $T = 25$ °C under a pressure of 9.9 x 10^{24} bar.

$CaH_2 + ZnO \rightarrow CaO + Zn + H_2(g)$ 7-2

Zirconium oxide (ZrO_2), also known as zirconia, is a white crystalline oxide of Zr with a monoclinic structure ($P2_1/c$) at room temperature and tetragonal ($P4_2/nmc$) and cubic ($Fm\bar{3}m$) at high temperatures.[34-36] It is a hard material used in ceramics, dentistry, and diamond stimulant.[37] The theoretical thermodynamic predictions from HSC Chemistry software showed the reaction pathway (7-3) with $CaZrO_3$ and Zr metal as the main reaction products. The enthalpy of the reaction was found as $\Delta H = 69$ kJ.mol^{-1}.H_2 at $T_{1bar} = 246$ °C, and hence the reaction is endothermic.

$2CaH_2 + 3ZrO_2 \rightarrow 2CaZrO_3 + Zr + 2H_2(g)$ 7-3

Meerson *et.al.*[38] detailed a reduction reaction between CaH_2 and ZrO_2 at 1000 °C, yielding pure Zr metal and its hydride $ZrH_{0.64}$. A reaction pathway consisting of four steps has been suggested (equation 7-4 to 7-7), which results in an aggregate reaction as expressed in 7-8.

$CaH_2 \rightleftharpoons Ca + H_2$ 7-4

$ZrO_2 + 2H_2 \rightleftharpoons Zr + 2H_2O$ 7-5

$H_2O + Ca \rightleftharpoons CaO + H_2$ 7-6

$Zr + 0.32H_2 \rightleftharpoons ZrH_{0.64}$ 7-7

Then 2 (7-4) + 7-5 + 2 (7-6) + 7-7 gives:

$2CaH_2 + ZrO_2 \rightleftharpoons ZrH_{0.64} + 2CaO + 1.68H_2$ 7-8

Silicon dioxide (SiO_2) also known as silica, exists in a tetrahedral structure and is naturally found as quartz, the second most abundant mineral in the earth's crust.[39] It is the main component in sand and hence applied in the construction industry and suitable for the production of glass, food, cosmetics, pharmaceutical, and semiconductor technology. The SiO_2 nanocomposite (SiO_2 nanoparticles dispersed in lithium carbonate and potassium carbonate solution) has recently attracted attention for solar thermal energy applications, such as enhancing materials' thermal properties and phase change materials (PCMs).[40] SiO_2 also can act as a multiple porous fire-resistant supporting material.[40-43] According to theoretical thermodynamic predictions, the reaction between CaH_2 and SiO_2 is endothermic from room temperature to 780 °C, and above 780 °C, the reaction became exothermic. The reaction can be predicted as follows:

$2CaH_2 + SiO_2 \rightarrow 2CaO + Si + 2H_2(g)$ 7-9

Among the transition metals, due to the range of valance states, Mn has the highest number of oxides such as MnO, Mn_3O_4, Mn_2O_3, MnO_2, MnO_3 and Mn_2O_7, each with varying crystal structures.[44] Manganese oxide materials are highly attractive for electrochemical energy storage applications. The low hysteresis, high theoretical specific capacity and high density make manganese (II) oxide (MnO) a potential anode material for lithium-ion batteries.[45-48] It adopts a rock salt structure. It is also a significant component of fertilisers and food additives.[49] Equations 7-10 and 7-11 illustrate the predicted reaction between CaH_2 and MnO_2 and MnO, respectively. MnO is the selected candidate in this investigation, and according to the thermodynamic predictions, the reaction (7-14) is possible at $T = 25$ °C with $\Delta H = -68$ $kJ.mol^{-1}.H_2$ under high pressure (1.5×10^{17} bar).

$CaH_2 + MnO_2 \rightarrow CaO + Mn + H_2O$ 7-10

$CaH_2 + MnO \rightarrow CaO + Mn + H_2(g)$ 7-11

Iron (III) oxide or ferric oxide (Fe_2O_3) is one of the three principal oxides of iron and the cheapest among all the selected oxides (US $ 580/tonne). Oxides of iron are suitable oxygen carriers; they show multiple phase transitions and are ideal for either chemical looping combustion or hydrogen production.[50-51] The most common form of Fe_2O_3 is α-Fe_2O_3 in the rhombohedral crystal structure. It also possesses a high melting point of 1539 °C and is most important in the steel and iron industries application.[12, 34, 52] According to HSC Chemistry software, the exothermic reaction between CaH_2 and Fe_2O_3, as shown in 7-12, has a $\Delta H = -178$ $kJ.mol^{-1}.H_2$ at $T = 25$ °C under extremely high pressure (1.1×10^{112} bar).

$3CaH_2 + Fe_2O_3 \rightarrow 3CaO + 2Fe + 3H_2(g)$ 7-12

Titanium oxide (TiO_2) or titania has high popularity in the surface science of metal oxides, with its primary uses being as heterogeneous catalysts; in solar cells for the production of hydrogen and electric energy; as a gas sensor; as a corrosion protective coating, and also applications in Li based batteries and electrochromic devices.[53-55] It is comparatively easy to prepare by sputtering and annealing.[53] The theoretical predictions from HSC Chemistry software shows an endothermic reduction reaction between CaH_2 and TiO_2 which produces pure Ti metal (7-13). The enthalpy of the reaction was $\Delta H = 16$ kJ.mol^{-1}.H_2 at $T = 25$ °C at a pressure of 4.3 x 10^5 bar.

$2CaH_2 + TiO_2 \rightarrow 2CaO + Ti + 2H_2(g)$ 7-13

However, Meerson *et.al.* shows an alternate reaction pathway between CaH_2 and TiO_2 that produces $TiH_{0.27}$ at 1000 °C, similar to the reaction between CaH_2 and ZrO_2. The resultant reaction can be written as:

$2CaH_2 + TiO_2 \rightarrow 2CaO + TiH_{0.27} + 1.865H_2(g)$ 7-14

Nickel (II) oxide (NiO) is the principal oxide of nickel and has a rock salt structure.[56] It has found application in semiconducting devices, batteries, solar cells and catalysts due to its peculiar electrical, optical, thermal and magnetic properties.[57-59] NiO is also an attractive material for preparing nickel cermet for the anode layer of fuel cells.[58] The reaction between CaH_2 and NiO from HSC Chemistry software (7-15) with $\Delta H = -213$ kJ.mol^{-1}.H_2 at $T = 25$ °C that requires extremely high pressure (4.6 x 10^{43} bar).

$CaH_2 + NiO \rightarrow CaO + Ni + H_2(g)$ 7-15

Copper (II) oxide or cupric oxide (CuO) is one of the two stable oxides of copper. It is considered an electrode material for next-generation rechargeable Li-ion batteries due to its high theoretical capacity, safety, and is environmentally benign.[60-61] It also has potential application in storage devices, sensors, catalysts and solar energy transfer.[62-63] The predictions from HSC Chemistry show that CaH_2 reduces CuO into pure Cu metal, as shown in equation 7-16.

$CaH_2 + CuO \rightarrow CaO + Cu + H_2(g)$ 7-16

Yttrium (III) oxide (Y_2O_3), also known as yttria, is a *c*-type structured (modified fluorite cubic structure) rare earth oxide, which is stable in air up to 2325 °C.[64-67] Due to its high thermal structural stability, it has promising applications in high-temperature coatings, solid oxide fuel cells and nuclear engineering.[64, 68-72] Theoretical calculations show, at high temperatures, $T_{1bar} = 1180$ °C, the endothermic reaction between CaH_2 and Y_2O_3 occurs as shown in equation 7-17 with $\Delta H = 151$ kJ.mol^{-1}.H_2

$3CaH_2 + Y_2O_3 \rightarrow 3CaO + 2Y + 3H_2(g)$ 7-17

Ceric oxide or cerium(IV) oxide (CeO_2) is also a rare earth metal oxide of cerium, with particular applications in the purification of the element from ores, and as an important commercial product.[73-75] It can be used in the thermochemical water-splitting process for hydrogen production and polishing hard materials with a relative hardness of 6-7 on Moh's hardness scale.[76-79] According to the theoretical predictions, the endothermic reaction between CaH_2 and CeO_2 is endothermic and occurs at $T_{1bar} = 407$ °C with $\Delta H = 95$ kJ.mol^{-1}.H_2.

$$2CaH_2 + CeO_2 \rightarrow 2CaO + Ce + 2H_2(g) \qquad 7\text{-}18$$

Interestingly, no research or literature review is available on these metal oxides on the thermodynamic destabilisation or reaction with CaH_2. Hence, this chapter discusses the synthesis, characterisation, thermal analysis, and suitability of each CaH_2-oxide system as a TES material for CSP applications.

7.3 Results and discussion

7.3.1 Synthesis and characterisation

All chemicals were handled inside an Ar filled MBraun Unilab glovebox maintained at an oxygen and water level of < 1 ppm. CaH_2 (Sigma Aldrich; >95% purity) and each oxide, purchased and purity as shown in Table 7.1, were mixed separately in a 1:1 molar ratio and ball-milled using a planetary ball mill. The samples were sealed inside a stainless-steel vial with a 40:1 ball (equal number of 10 mm and 6 mm diameter balls) to powder ratio and milled for 3 h at a rotational speed of 400 rpm. The XRD patterns of each CaH_2-oxide system after ball milling are displayed in Figure 7.1. All the XRD patterns except Fe_2O_3 were obtained from a Bruker D8 Advance diffractometer using Cu K_α radiation. The XRD analysis of Fe containing samples with Cu radiation creates polychromatic radiation (high background level) due to its fluorescent nature. Hence the diffraction patterns of the CaH_2-Fe_2O_3 system were collected using a Bruker D8 diffractometer with a Co K_α radiation.

The XRD patterns after ball milling help to identify any reactions that occurred between CaH_2 and oxides. However, depending on the oxides' hardness, density, and molar mass, the intensity of the CaH_2 peak varies or is amorphous after ball milling. Moreover, in most cases, the peaks of CaH_2 and oxides overlap. It is evident from Figure 7.1(8), CaH_2 reacted with CuO and reduced CuO to Cu and CaO during ball milling. Moreover, XRD patterns do not show the crystalline peaks of any reaction products for any oxide system except CuO. Due to the nanoparticle size (< 10 nm) of SiO_2 used for the synthesis of the CaH_2-SiO_2 system, it was challenging to identify the crystalline peaks of the SiO_2 compound after ball milling (Figure 7.1(3)). However, in the CaH_2-Y_2O_3 system, due to the hard nature of Y_2O_3 (similar to diamond), it was difficult to locate the CaH_2 peaks after ball milling. Also, after ball milling the CaH_2-CeO_2 system, it was challenging to find the crystalline peaks of both CaH_2 and CeO_2 (Figure 7.1(10)). Ball milling may have reduced the particle size, or due to the relatively hard nature of CeO_2, the compound became amorphous and hence challenging to locate the peaks using XRD analysis.

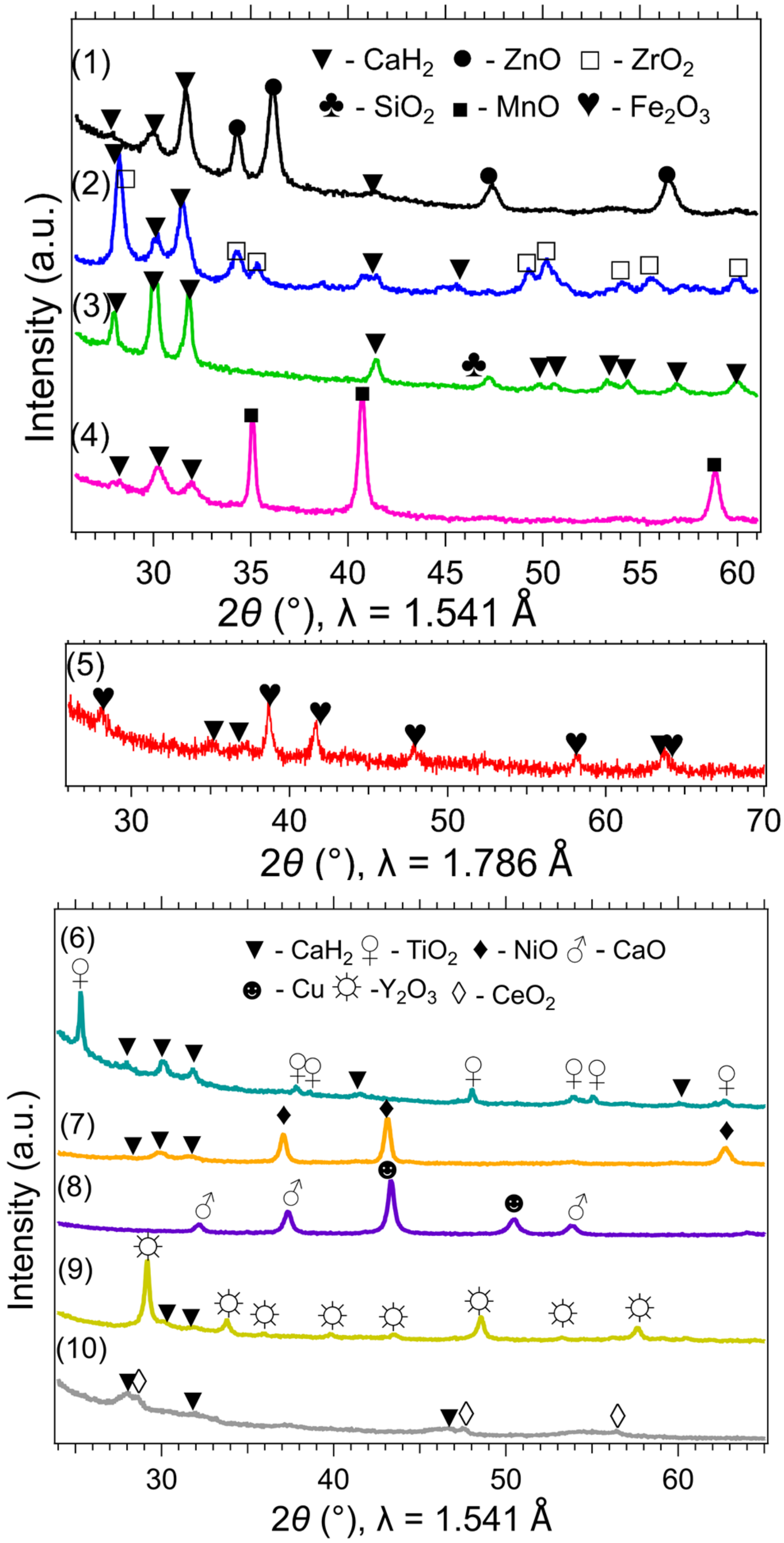

Figure 7.1 *Ex-situ* powder diffraction patterns of as prepared (1) CaH_2-ZnO (black), (2) CaH_2-ZrO_2 (blue), (3) CaH_2-SiO_2 (green), (4) CaH_2-MnO (pink), (5) CaH_2-Fe_2O_3 (red), (6) CaH_2-TiO_2 (cyan), (7) CaH_2-NiO (orange), (8) CaH_2-CuO (purple), (9) CaH_2-Y_2O_3 (yellow) and (10) CaH_2-CeO_2 (grey) in 1:1 molar ratio.

7.3.2 Thermal analysis

7.3.2.1 Differential scanning calorimetry (DSC) & temperature programmed desorption analysis

DSC analysis was performed on the CaH_2- oxide systems using a Netzsch (STA 449 F3 Jupiter) under Ar flow of 40 mL/min using Al_2O_3 crucibles. The Ar was passed through a Zr filter (heated to 200 °C) to reduce oxygen impurities in the gas stream before entering the DSC. The samples were heated from room temperature to 900 °C with a ramp rate of 20 °C/min. The TGA data did not provide helpful information as no increase or decrease in mass was observed. The DSC peaks assist in identifying whether the reaction between CaH_2 and oxide is endothermic or exothermic. Overall an endothermic reaction is required for the material to find use as a TES for CSP application. TPD analysis on each CaH_2- oxide system was performed from room temperature to ≈ 800 °C with a ramp rate of 7 °C/min, with all the measurements starting from the vacuum.

The DSC data of each system is presented in Figure 7.2(a) & (b) and compared with its differential pressure obtained from temperature-programmed desorption (TPD) studies (Figure 7.2(c) & (d). In addition, Figure 7.3(a) & (b) shows the experimental desorbed H_2 wt% vs temperature and (c) & (d) pressure vs temperature. XRD was again conducted after TPD to determine the reaction products (Figure 7.4.1 and 7.4.2).

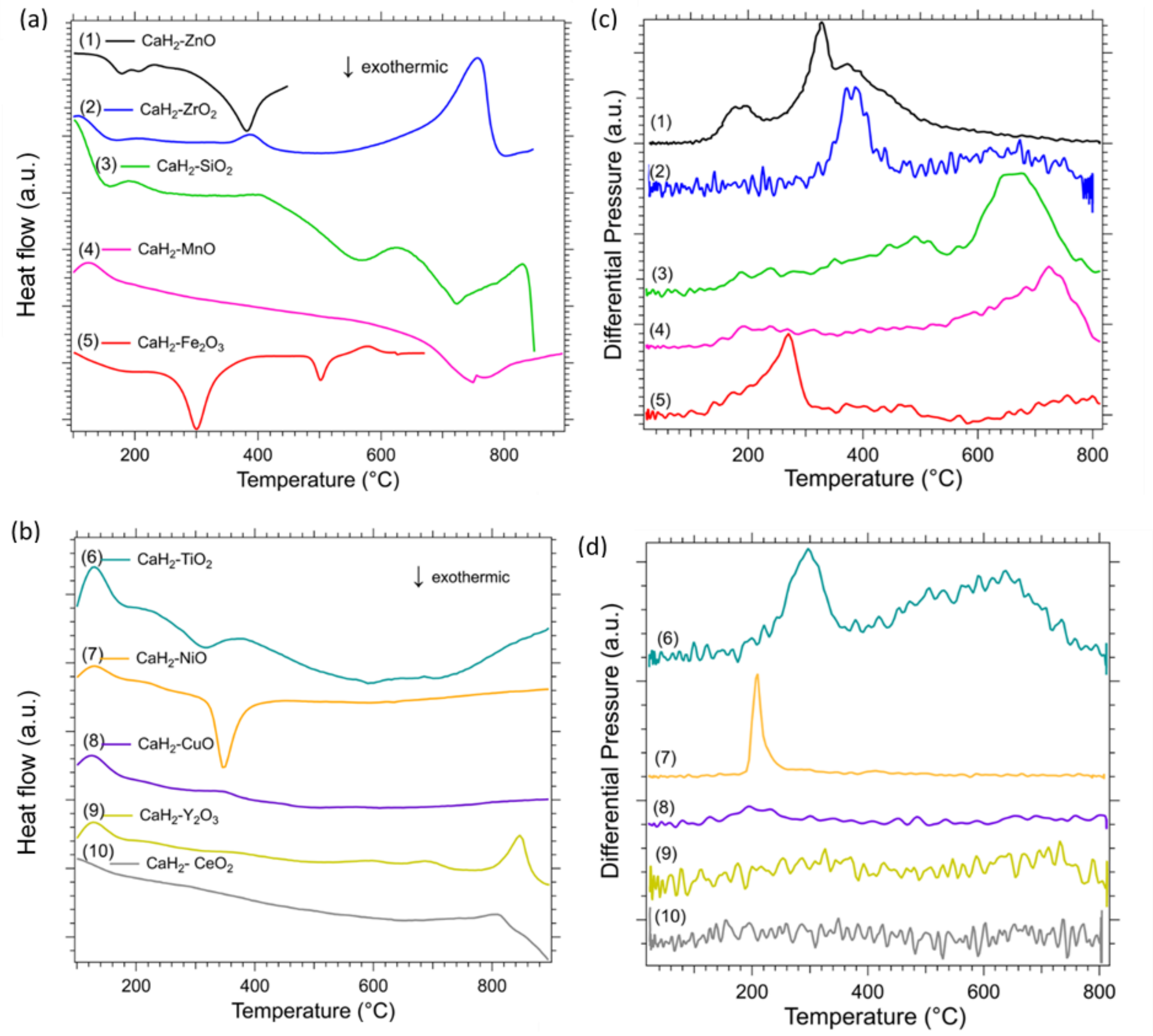

Figure 7.2 (a) &(b) DSC analysis of the CaH_2 and oxide systems with a heating rate of 20 °C/min and (c) &(d) Differential TPD profiles of CaH_2 and oxide systems from room temperature to 800 °C.

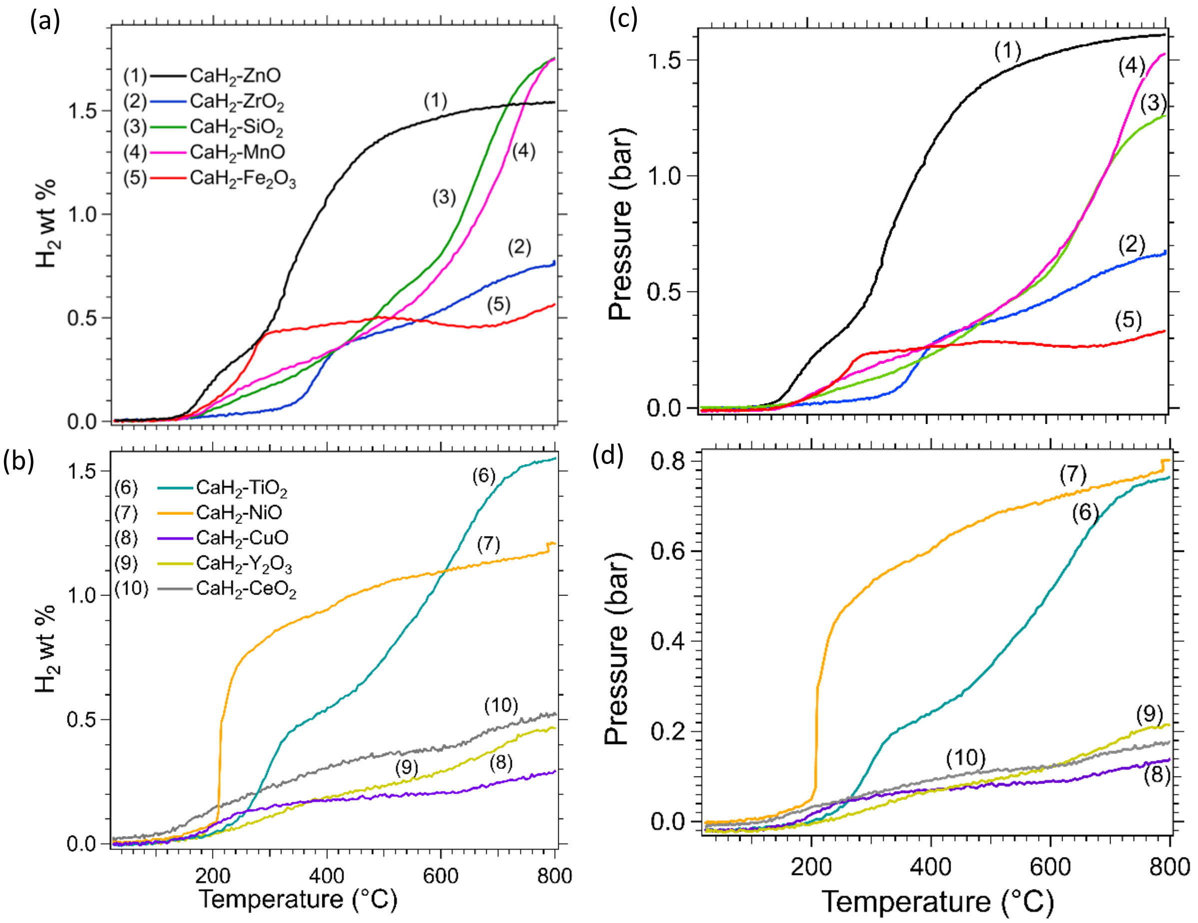

Figure 7.3 TPD profiles, (a) & (b) H_2 wt% vs temperature, (c) & (d) pressure vs temperature, for the CaH_2 and oxide systems heated from room temperature to 800 °C with a ramp rate of 7 °C/min.

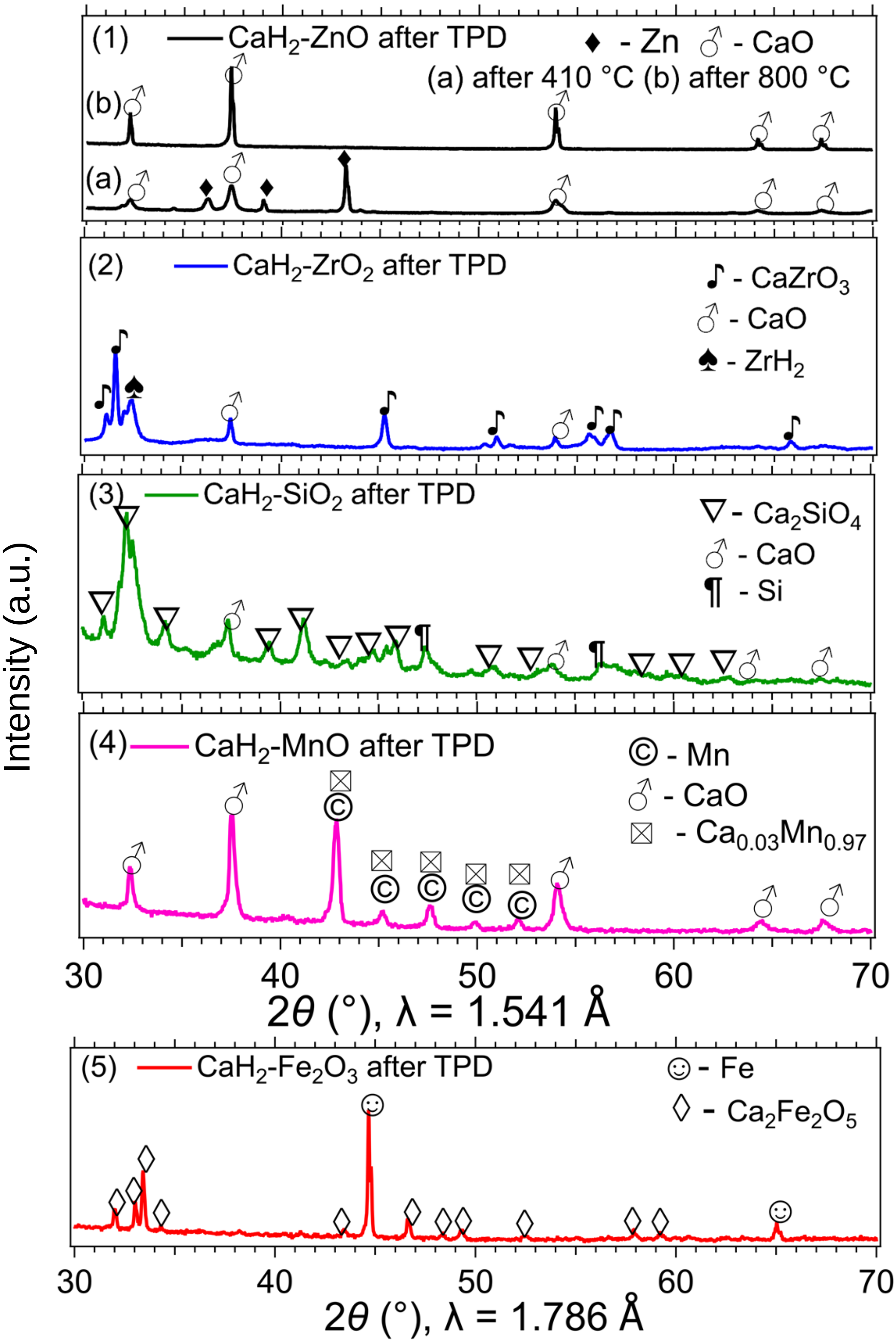

Figure 7.4.1 *Ex-situ* XRD pattern for the (1a) CaH$_2$-ZnO after TPD at 410 °C, (1b) CaH$_2$-ZnO, (2) CaH$_2$-ZrO$_2$, (3) CaH$_2$-SiO$_2$, (4) CaH$_2$-MnO, and (5) CaH$_2$-Fe$_2$O$_3$ after TPD at 800 °C.

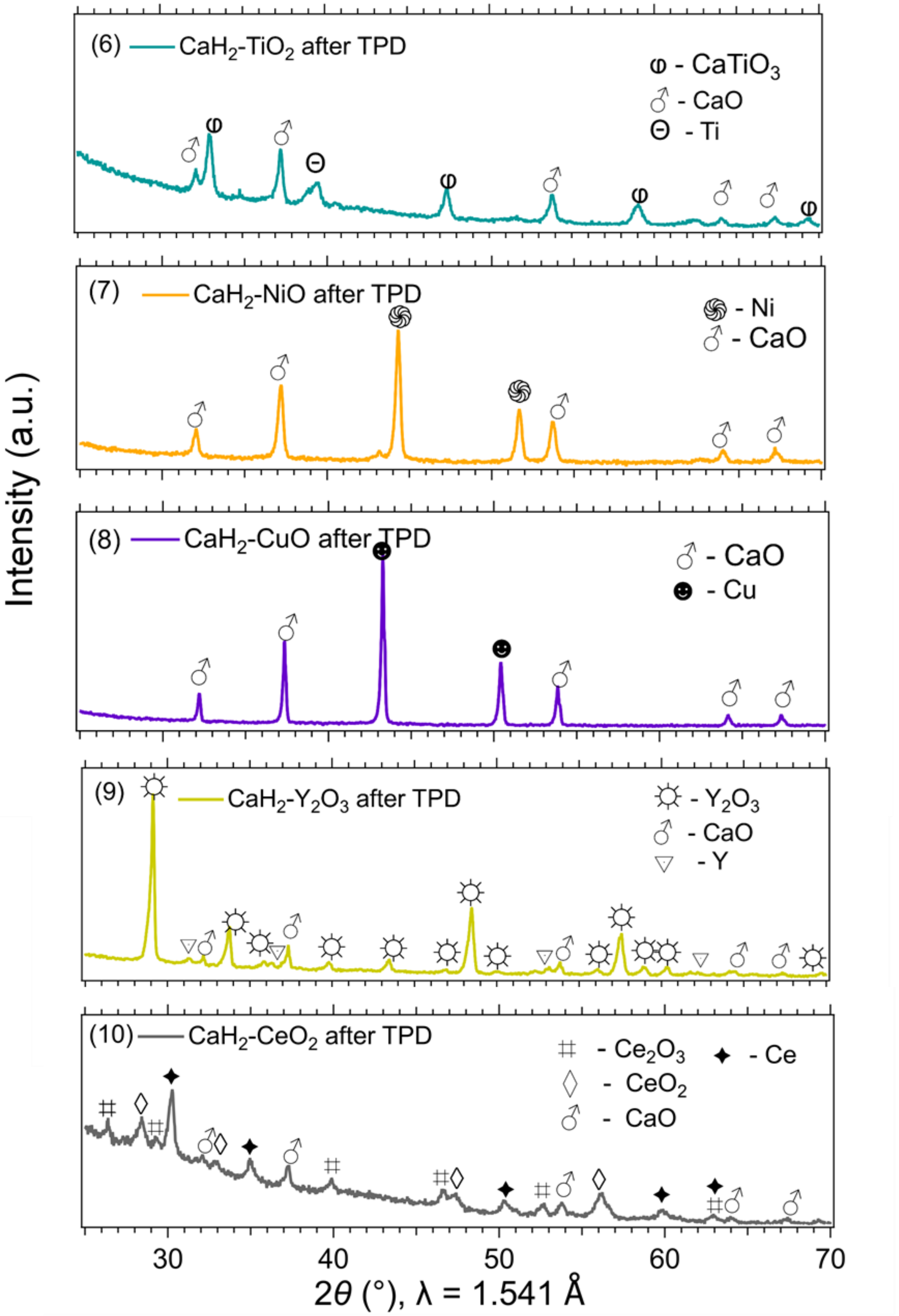

Figure 7.4.2 *Ex-situ* XRD pattern for the (6) CaH_2-TiO_2, (7) CaH_2-NiO, (8) CaH_2-CuO, (9) CaH_2-Y_2O_3, and (10) CaH_2-CeO_2 after TPD at 800 °C.

The significant findings from the DSC, TPD experiment, and subsequent quantitative XRD are listed below:

(1) CaH_2-ZnO - It is clear from the differential TPD profile (Figure 7.2(c(1))), that the reaction between CaH_2 and ZnO started at 100 °C, with the first peak maximum at 200 °C and the second at 330 °C. The maximum hydrogen desorption capacity reached was ≈1.55 wt%, which correlates with the theoretical wt% of 1.6, at ≈ 800 °C (Figure 7.3(a(1))), equivalent to a pressure of 1.61 bar (Figure 7.3(c(1))). DSC analysis (Figure 7.2(a(1))) also shows two exothermic peaks with the first peak maximum at 200 °C that matches with TPD studies. The second peak was obtained centred at 390 °C (broad peak in the temperature range 385 - 411 °C), which contradicts the peak at 330 °C in the TPD curve. This may be due to the Zn melting peak overlapped with a reaction peak (the melting point of Zn is 419 °C). The XRD measured after TPD measured up to 410 °C (Figure 7.4.1(1(a)) shows that the CaH_2 reduced ZnO into Zn and CaO. The corresponding Rietveld refinement (Figure 7.5(a)) provided a composition of CaO and Zn as 68 ± 1 wt% and 28 ± 1 wt%, respectively with some unreacted CaH_2 (2 ± 1 wt%) and ZnO (3 ± 1 wt%). The XRD measured after TPD at 800 °C shows only CaO peaks (Figure 7.4.1(1(b)). This is because zinc evaporates while heating to 800 °C and is seen deposited on the cooler sides of the reactor. The quantitative XRD refinement (Figure 7.5(b)) shows only 100 wt% of CaO. As a result, the reaction between CaH_2 and ZnO is limited to below 420 °C and can be described by equation 7-19 and matches with the theoretically predicted reaction in equation 7-2. The reversibility of the reaction was also tested by performing a hydrogen absorption experiment at 400 °C under an H_2 pressure of 40 bar using a stainless-steel reactor. The XRD after absorption (Figure 7.6) nearly matched with XRD after desorption at 410 °C, indicating the reaction is irreversible.

$$CaH_2 + ZnO \rightarrow CaO + Zn + H_2(g) \qquad \text{7-19}$$

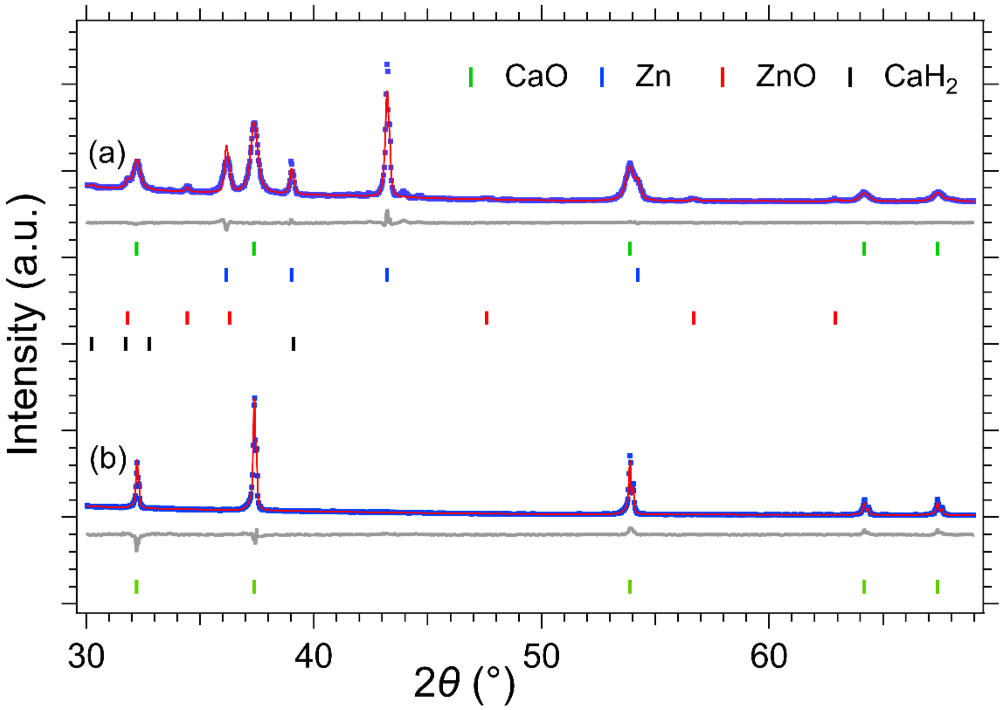

Figure 7.5 Rietveld refinement of CaH_2-ZnO system after TPD at (a) 410 °C (b) 800 °C (Cu K_α , $\lambda = 1.5418$ Å).

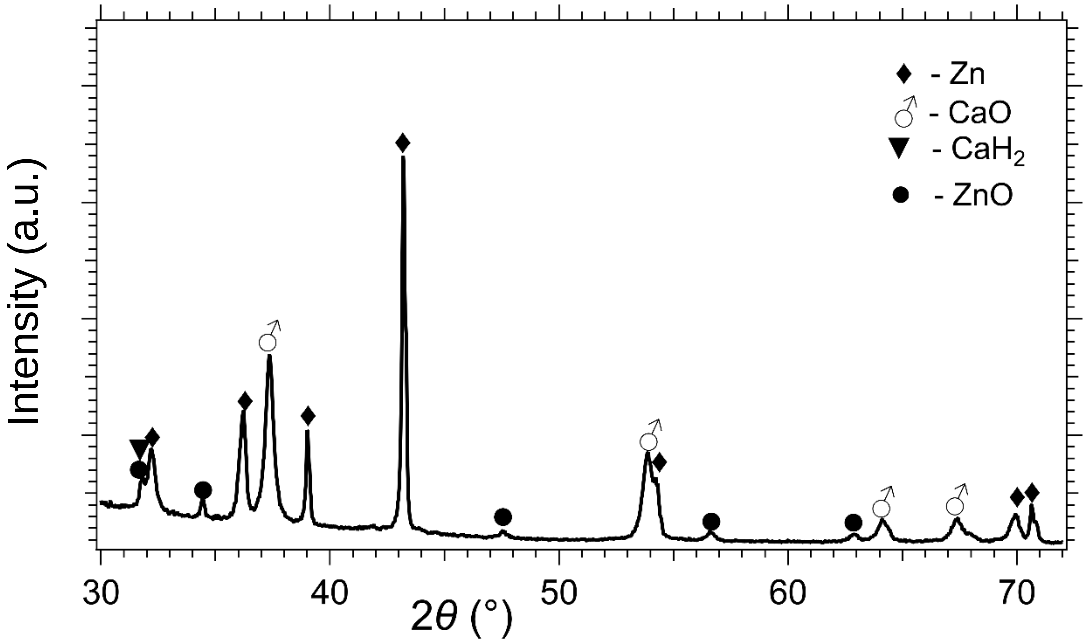

Figure 7.6 *Ex-situ* XRD pattern for CaH_2-ZnO system after absorption 400 °C (Cu K_α, λ = 1.5418 Å).

(2) CaH_2-ZrO_2 - The DSC data (Figure 7.2(a(2)) measured shows two endothermic peaks at 400 °C and 757 °C, while the differential TPD curves (Figure 7.2(c(2)) indicates one significant peak at 400 °C and a broad curve with an onset temperature of 600 °C and a maxima at 720 °C. This two-step reaction pathway was later proven by *in-situ* XRD studies (Section 7.3.2.2). A maximum of 0.75 wt% hydrogen (Figure 7.3(a(2))) was desorbed experimentally (theoretical wt% = 0.6) at ≈ 800 °C with a maximum pressure of 0.68 bar (Figure 7.3(c(2))). In Figure 7.4.1(2), XRD after TPD identified $CaZrO_3$ and ZrH_2 as the main decomposition products. The Rietveld refinement of the data (Figure 7.7) shows $CaZrO_3$, CaO and ZrH_2 with a wt% of 62 ± 2, 18 ± 1 and 20 ± 2, respectively. The reaction can be expressed as shown in 7-20, which combines the two predicted reactions 7-3 and 7-8. Moreover, the reversibility of the reaction 7-20 needs further testing, which requires a temperature above 700 °C as the decomposition peak of ZrH_2 is at 700 °C.[80]

$$2CaH_2 + 2ZrO_2 \rightarrow CaZrO_3 + CaO + ZrH_2 + H_2(g) \qquad 7\text{-}20$$

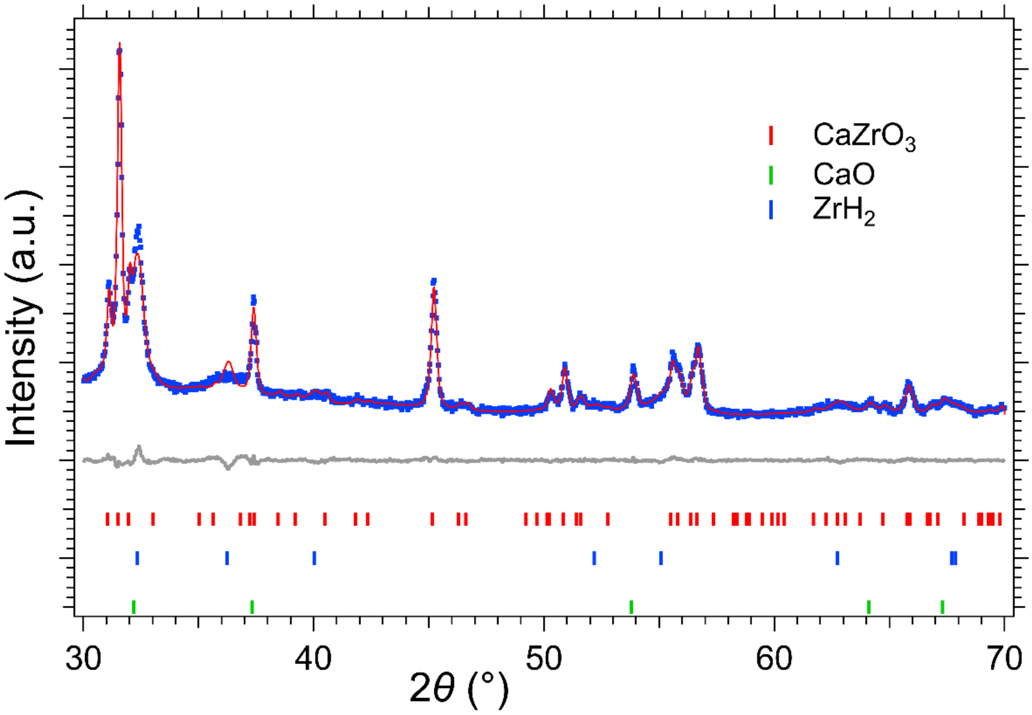

Figure 7.7 Rietveld refinement of CaH_2-ZrO_2 system after TPD (Cu K_α, λ = 1.5418 Å).

(3) CaH_2-SiO_2 - Both the DSC curve (Figure 7.2(a(3))) and the differential TPD profile (Figure 7.2(c(3))) show two steps of reaction. The first one in the TPD was a slow H_2 release process in the range 200 to 600 °C, and the second one (580 - 760 °C), which is centred at 700 °C and was relatively faster and more prominent. The DSC signal showed a small rise at 400 °C and the second (580 - 730 °C) more prominent one peaked at 640 °C. The third peak in the DSC shows the melting of CaH_2 that melts at 815 °C. These observations matched the *in-situ* XRD patterns (discussed in section 7.3.2.2) and identified the two reaction pathways. This system shows the highest capacity of hydrogen desorption of 1.77 wt% up to 800 °C (Figure 7.3(a(3))), equivalent to a pressure of 1.27 bar (Figure 7.3(c(3))). It was noted that the H_2 wt% increased to 1.91 after waiting at 800 °C for 5 hours isothermally. The main decomposition products confirmed using XRD after TPD were Ca_2SiO_4, CaO and Si, as shown in Figure 7.4.1(3). Quantitative Rietveld refinement was performed to compare the as-prepared sample and after TPD at 800 °C samples. It was difficult to determine the exact wt% of SiO_2. The intensity of the crystalline peaks of the SiO_2 (powder size of < 10 nm for synthesis) after ball-milling was too low or became amorphous compared to CaH_2 peaks. Hence, the refinement (Figure 7.8(a)) underestimated the wt% of SiO_2 as 10 ± 2, instead of the expected 58%, while the wt% of CaH_2 was determined as 90 ± 2. However, the quantitative analysis after TPD (Figure 7.8(b)) gives Ca_2SiO_4 as the significant component, with 90 ± 3 wt%, while CaO and Si represent 2 ± 1 and 3 ± 1 wt%, respectively. In addition, the refinement after TPD shows excess SiO_2 (5 ± 3), which was also later proved by *in-situ* studies. Hence, the reaction can be written as shown in 7-21 and the optimised reaction can be written as displayed in 7-22:

$$CaH_2 + SiO_2 \rightarrow \frac{1}{4}Ca_2SiO_4 + \frac{1}{2}CaO + \frac{1}{2}Si + \frac{1}{4}SiO_2 + H_2\ (g) \qquad 7\text{-}21$$

$$4CaH_2 + 3SiO_2 \rightarrow Ca_2SiO_4 + 2CaO + 2Si + 4H_2\ (g) \qquad 7\text{-}22$$

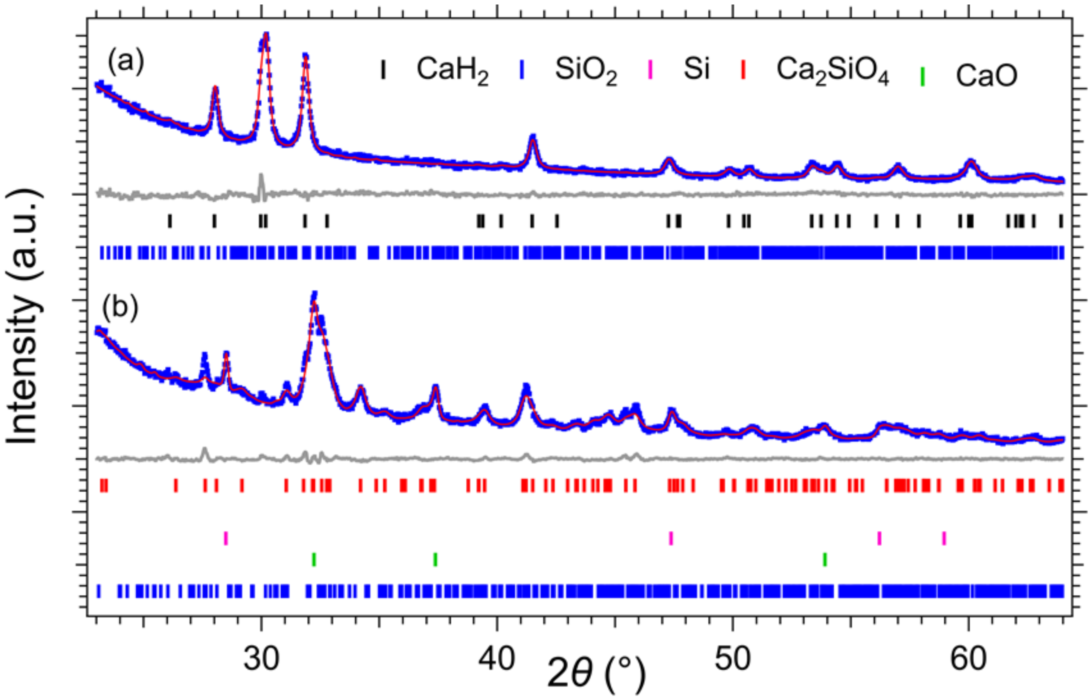

Figure 7.8 Rietveld refinement of CaH$_2$-SiO$_2$ system (a) as prepared (b) after TPD (Cu K$_\alpha$, λ = 1.5418 Å).

(4) CaH$_2$-MnO - DSC studies of this system (Figure 7.2a(4)) show a single exothermic peak at 750 °C that is in good agreement with the TPD profiles (Figure 7.2c(4)). The reaction between CaH$_2$ and MnO started at > 400 °C and reached maximum H$_2$ desorption of 1.77 wt% at 800 °C (agrees with the theoretical value of 1.78 wt%), with an equivalent pressure of 1.52 bar (Figure 7.3(a & c(4))). The XRD after TPD (Figure 7.4.1(4)) and refinement (Figure 7.9) shows Ca$_{0.03}$Mn$_{0.97}$ (27 ± 1 wt%, space group $I\bar{4}3m$), which matches with Mn (16 ± 1 wt%, space group $P4_132$) peaks along with CaO (57 ± 1 wt%). Hence the reaction can be written as shown in 7-23

$$CaH_2 + MnO \rightarrow Ca_{0.97}O + Ca_{0.03}Mn_{0.97} + 0.03Mn + H_2(g) \qquad 7\text{- }23$$

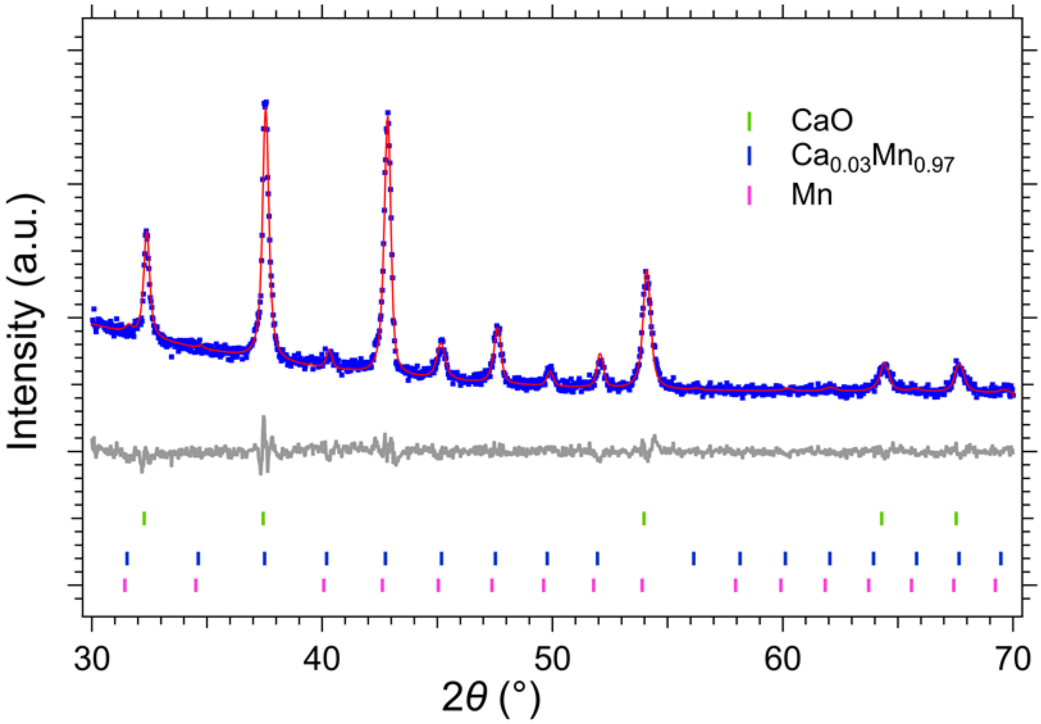

Figure 7.9 Rietveld refinement of CaH_2-MnO system after TPD (Cu K_α, λ = 1.5418 Å).

(5) CaH_2-Fe_2O_3 - Two exothermic peaks at 300 °C and 512 °C were shown by DSC studies (Figure 7.2(a(5))), while the differential TPD analysis revealed only one peak at 280 °C (Figure 7.2(c(5))). The TPD curve (Figure 7.3(a & c(5))) clearly shows that the system reached a maximum H_2 desorption of 0.58 wt% at 800 °C with an equivalent pressure of 0.33 bar. The desorbed H_2 wt% showed a rise from 0.58 to 0.76 after waiting at 800 °C for 5 hours isothermally. The primary decomposition products from XRD after TPD at 800 °C were $Ca_2Fe_2O_5$ and Fe as shown in Figure 7.4.1(5), and the reaction can be expressed as shown in 7-24. It is noted from the literature that $Ca_2Fe_2O_5$ undergoes polymorphic transitions at higher temperatures and hence the second peak in the DSC studies shows the crystal transformation of $Ca_2Fe_2O_5$.[81] Rietveld refinement of the XRD data (Figure 7.10) reveals $Ca_2Fe_2O_5$ and Fe with a wt% of 69 ± 1 and 31 ± 1, respectively. As the quantitative analysis shows no excess Fe_2O_3 or CaH_2 after TPD, the reaction 7-24 can be balanced by adding a $\frac{1}{4}O_2(g)$ as shown in 7-25. Therefore, the reaction between CaH_2 and Fe_2O_3 should release $O_2(g)$ along with $H_2(g)$; however, this needs further testing.

$$CaH_2 + Fe_2O_3 \rightarrow \frac{1}{2}Ca_2Fe_2O_5 + Fe + H_2(g) \qquad 7\text{-}24$$

$CaH_2 + Fe_2O_3 \rightarrow \frac{1}{2}Ca_2Fe_2O_5 + Fe + \frac{1}{4}O_2(g) + H_2(g)$ 7-25

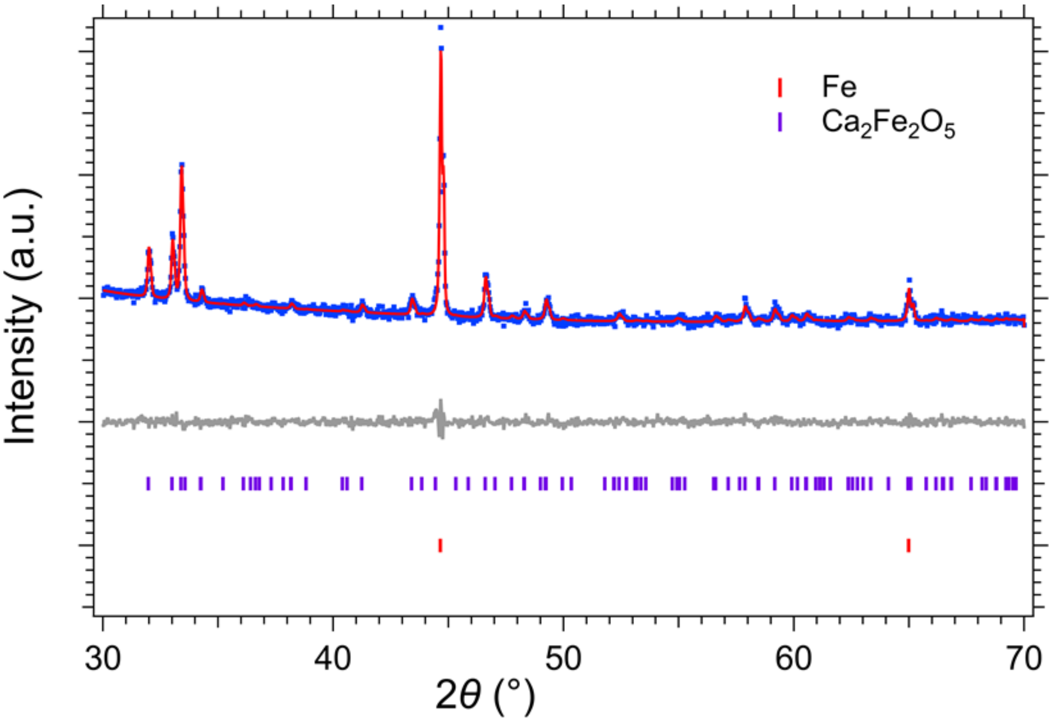

Figure 7.10 Rietveld refinement of CaH_2-Fe_2O_3 system after TPD (Co K_α, λ = 1.789 Å).

(6) CaH_2-TiO_2 - The DSC signal (Figure 7.2(b(6))) obtained was unfortunately not strong enough to distinguish between endothermic or exothermic peaks. However, the differential TPD (Figure 7.2(d(6))) shows a peak at 300 °C that can be compared with an exothermic peak in the DSC analysis at 300 °C. In addition, the TPD profile shows a second slow event from 400 - 800 °C, centred at 640 °C. Figure 7.3(b & d(6)) illustrates a maximum H_2 wt% and pressure obtained after TPD at 800 °C as 1.57 and 0.75 bar, respectively. XRD after TPD confirmed the reaction products as $CaTiO_3$, Ti and CaO, as shown in Figure 7.4.2(6). However, the quantitative Rietveld refinement data (Figure 7.11) determined the composition of the material to be $CaTiO_3$, Ti and CaO as 44 ± 4, 4 ± 3 and 29 ± 2 wt%, respectively, with an excess of unreacted TiO_2 (19 ± 2 wt%). Hence, equation 7-26 shows the reaction between CaH_2 and TiO_2. The optimised form of the reaction 7-26 can be written as shown in 7-27, without excess TiO_2:

$CaH_2 + TiO_2 \rightarrow \frac{1}{4}CaTiO_3 + \frac{3}{4}CaO + \frac{1}{2}Ti + \frac{1}{4}TiO_2 + H_2(g)$ 7-26

$4CaH_2 + 3TiO_2 \rightarrow CaTiO_3 + 3CaO + 2Ti + 4H_2(g)$ 7-27

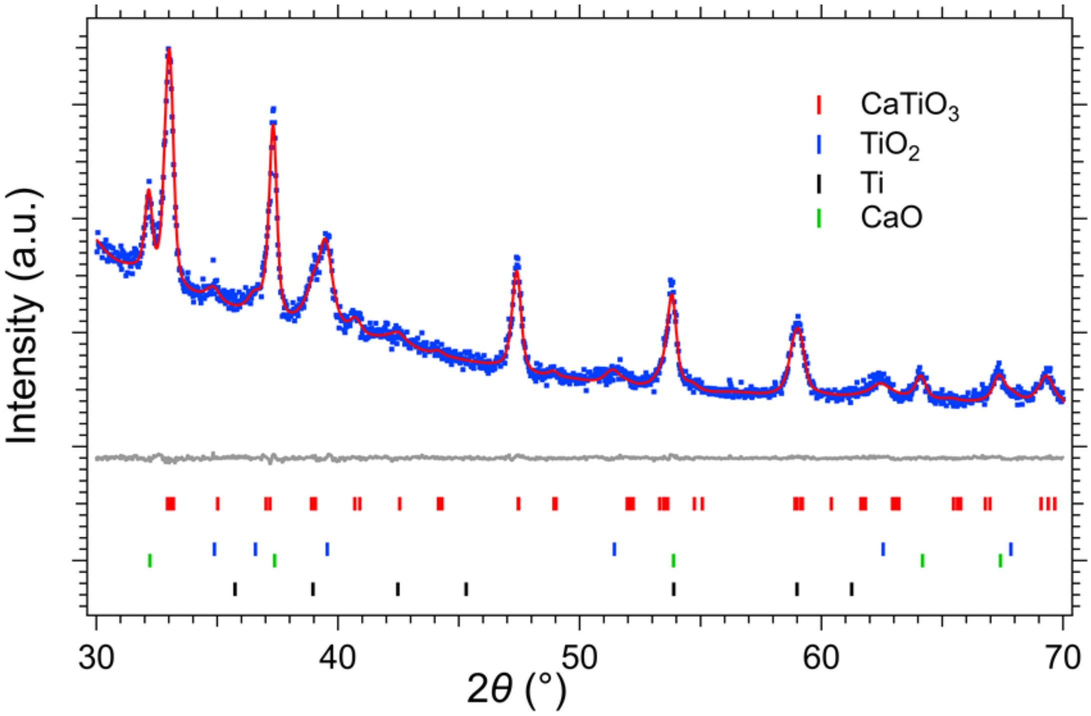

Figure 7.11 Rietveld refinement of CaH_2-TiO_2 system after TPD (Cu K_α , $\lambda = 1.5418$ Å).

(7) CaH_2-NiO - It is clear from the DSC (Figure 7.2(b(7))) and TPD data (Figure 7.2(d(7))) the reaction between CaH_2 and NiO occurs in a single step. The single peak obtained from DSC (340 °C) and TPD (240 °C) differ by a temperature of 100 °C. However, the DSC peak demonstrates the reaction as an exothermic reaction. Figure 7.3(c & d(7)) illustrates the maximum H_2 wt% of 1.2 at 800 °C with an equivalent pressure of 0.8 bar. The system showed an increase in H_2 wt% (1.45) after waiting at 800 °C for 5 hours isothermally. The XRD after TPD (Figure 7.4.2(7)) and corresponding quantitative XRD refinement (Figure 7.12) prove that the CaH_2 reduced NiO into pure Ni (46 ± 1 wt%) and CaO (45 ± 1 wt%). In addition, 5 ± 2 wt% of NiO and 4 ± 2 wt% of CaH_2 were also found unreacted. However, the reaction can be written as shown in 7-28 and exactly matches with the theoretically predicted reaction 7-15:

$CaH_2 + NiO \rightarrow CaO + Ni + H_2(g)$ 7-28

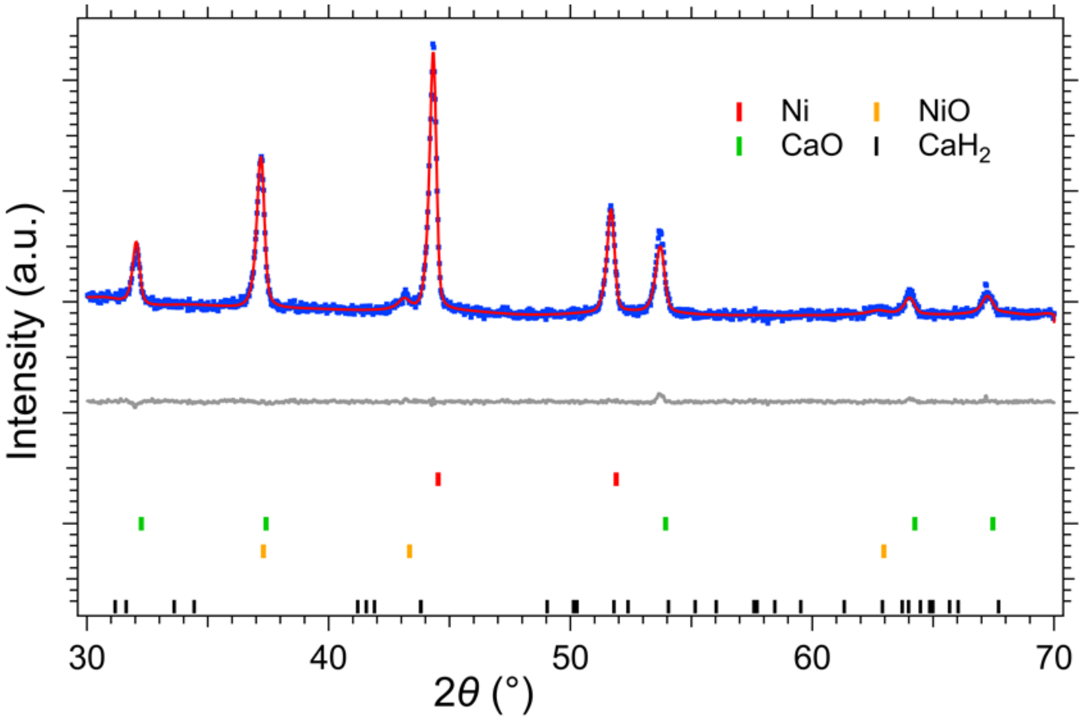

Figure 7.12 Rietveld refinement of CaH_2-NiO system after TPD (Cu K_α, $\lambda = 1.5418$ Å).

(8) CaH_2-CuO - DSC (Figure 7.2(b(8))) and TPD analysis (Figure 7.2(d(8))) did not show any significant peaks of reaction, as expected because all the CaH_2 and CuO had reacted during ball milling, as seen in the XRD after ball-milling (Figure 7.1(8)). The CaH_2 reduced CuO into Cu and formed CaO. The reaction products remained the same as the ball-milled products even after heating up to 800 °C (Figure 7.4.2(8)), which agrees with DSC results. The corresponding refinement (Figure 7.13) confirms the same wt% for CaO and Cu (50 ± 1). The reaction can be written as shown in 7-29 and agrees with the predicted reaction 7-16.

$CaH_2 + CuO \rightarrow CaO + Cu + H_2(g)$ 7-29

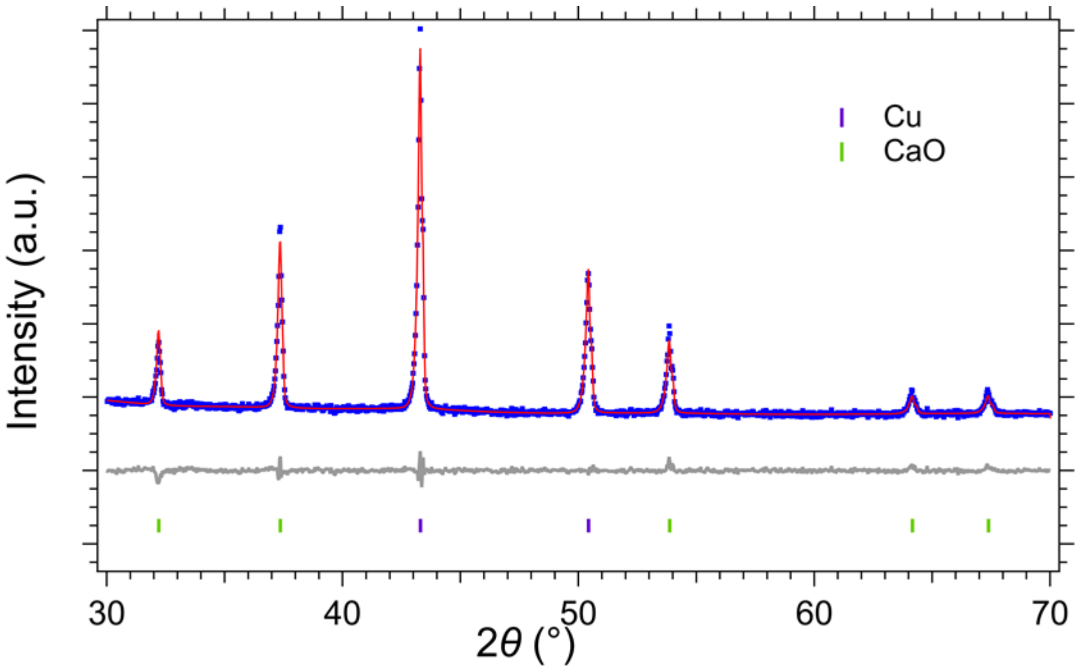

Figure 7.13 Rietveld refinement of CaH_2-CuO system after TPD (Cu K_α, λ = 1.5418 Å).

(9) CaH_2-Y_2O_3 - The DSC signal (Figure 7.2b(9)) and differential TPD profiles (Figure 7.2d(9)) did not show any significant peak until 800 °C. The theoretical predictions showed that Y_2O_3 is a thermally stable compound and that a temperature of > 1000 °C at 1 bar H_2 is required to complete the reaction. The literature also noted that Y_2O_3 is highly stable even at temperatures above 2000 °C and is used as a high-temperature protective coating.[64, 68-72] However, the TPD curve (Figure 7.3(b & d(9))) shows a slow release of H_2 from 200 °C and reaches 0.48 wt% H_2 and pressure of ≈ 0.22 bar at 800 °C , which is close to the theoretical value of 0.7. However, the DSC curve shows an endothermic peak at 846 °C, which could be due to the melting of Ca metal overlapping with the reaction between the CaH_2-Y_2O_3 system. Hence, the reaction could be completed if the temperature were increased to 900 °C. Quantitative refinement of the XRD data (Figure 7.4.2(9)) collected after TPD and on the ball-milled sample was analysed (Figure 7.14). The refinement on the sample after ball milling (Figure 7.14(a))) shows 93 ± 1 wt% Y_2O_3 and 7 ± 1 wt% which contrasts with the expected theoretical values of 85 and 15 wt%. This is due to the amorphous nature of CaH_2 peaks after ball milling. However, the refinement after TPD at 800 °C (Figure 7.14(b))) gives CaO (15 ± 1 wt%) and Y (3 ± 1 wt%) along with excess of Y_2O_3 (70 ± 2 wt%) and CaH_2 (12 ± 1 wt%). This shows that the highest temperature of the reaction applied was not enough to complete the reaction between CaH_2 and Y_2O_3. Hence, according to the XRD refinement after TPD, the reaction can be written as 7-30 and the optimised form of the reaction can be written as shown in 7-31, without excess CaH_2 and Y_2O_3.

$4CaH_2 + 4Y_2O_3 \rightarrow 3CaO + 2Y + CaH_2 + 3Y_2O_3 + 3H_2(g)$ 7-30

$3CaH_2 + Y_2O_3 \rightarrow 3CaO + 2Y + 3H_2(g)$ 7-31

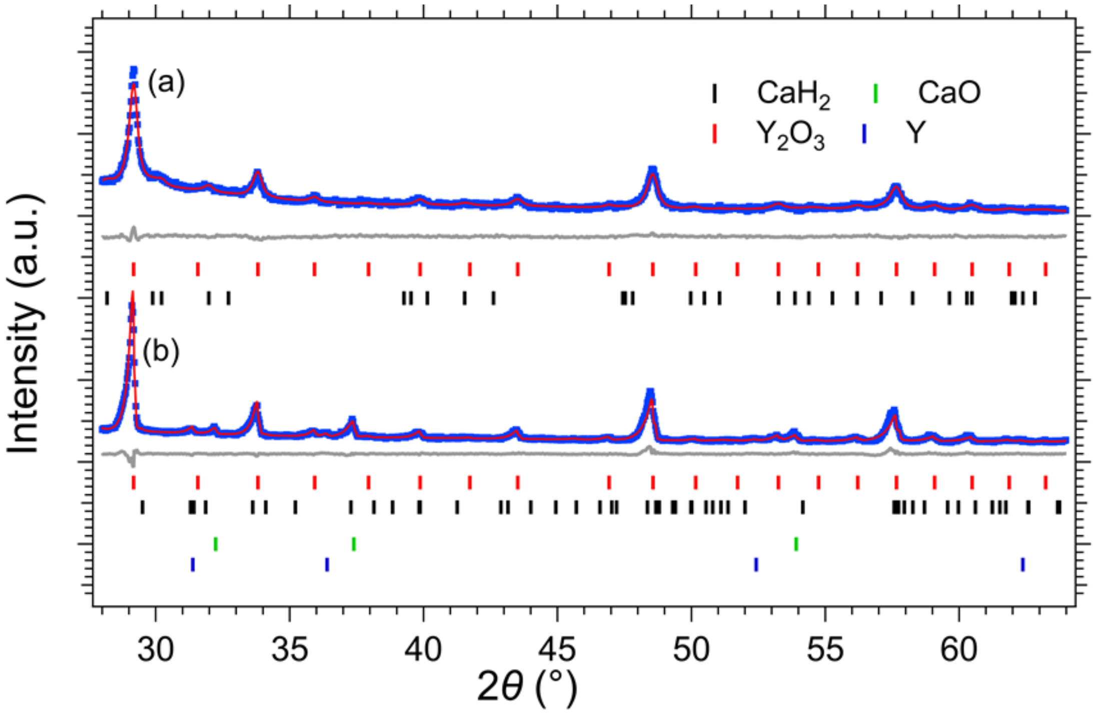

Figure 7.14 Rietveld refinement of CaH_2-Y_2O_3 system (a) as prepared (b) after TPD (Cu K_α, $\lambda = 1.5418$ Å).

(10) CaH_2-CeO_2 - The DSC signal (Figure 7.2b(10)) and differential TPD profiles (Figure 7.2d(10)) did not show any significant peak until 800 °C. The TPD curve (Figure 7.3b & d(10)) reached a maximum desorbed H_2 wt% of 0.52 at 800 °C with a pressure of 0.18 bar , and the DSC shows an endothermic event at 800 °C. It was difficult to locate the peaks in the XRD pattern due to the amorphous nature of the sample after ball milling. However, Figure 7.15 illustrates the Rietveld refinement of the samples after ball milling and TPD at 800 °C. Figure 7.15(a) shows the composition of the sample to be CeO_2 (94 ± 2 wt%) and CaH_2 (6 ± 4 wt%) after ball-milling. It was difficult to find the exact amount of CaH_2 due to the amorphous nature of the particles after ball milling with CeO_2. Moreover, the refinement after TPD (Figure 7.15(b)) shows Ce (18 ± 2 wt%), CaO (30 ± 2 wt%) and Ce_2O_3 (23 ± 1 wt%) with excess CeO_2 (29 ± 1 wt%). It is noted from the literature that when there is a shortage of oxygen, cerium

(IV) oxide (CeO_2) can be reduced to cerium (III) oxide (Ce_2O_3) at high temperatures.[82-83] The wide peak in the DSC at 800 °C could be the combination of the reaction between CaH_2-CeO_2 and the melting of Ce (the melting point of Ce is 795 °C). However, the reaction can be written as:

$$CaH_2 + CeO_2 \rightarrow CaO + \frac{3}{8}Ce + \frac{1}{4}Ce_2O_3 + \frac{1}{8}CeO_2 + H_2(g) \qquad 7\text{-}32$$

The optimised reaction can be written in as shown in 7-33, the reaction could be completed without excess CeO_2 if the initial synthesis were done at a molar ratio of 8:7, CaH_2:CeO_2.

$$8CaH_2 + 7CeO_2 \rightarrow 8CaO + 3Ce + 2Ce_2O_3 + 8H_2(g) \qquad 7\text{-}33$$

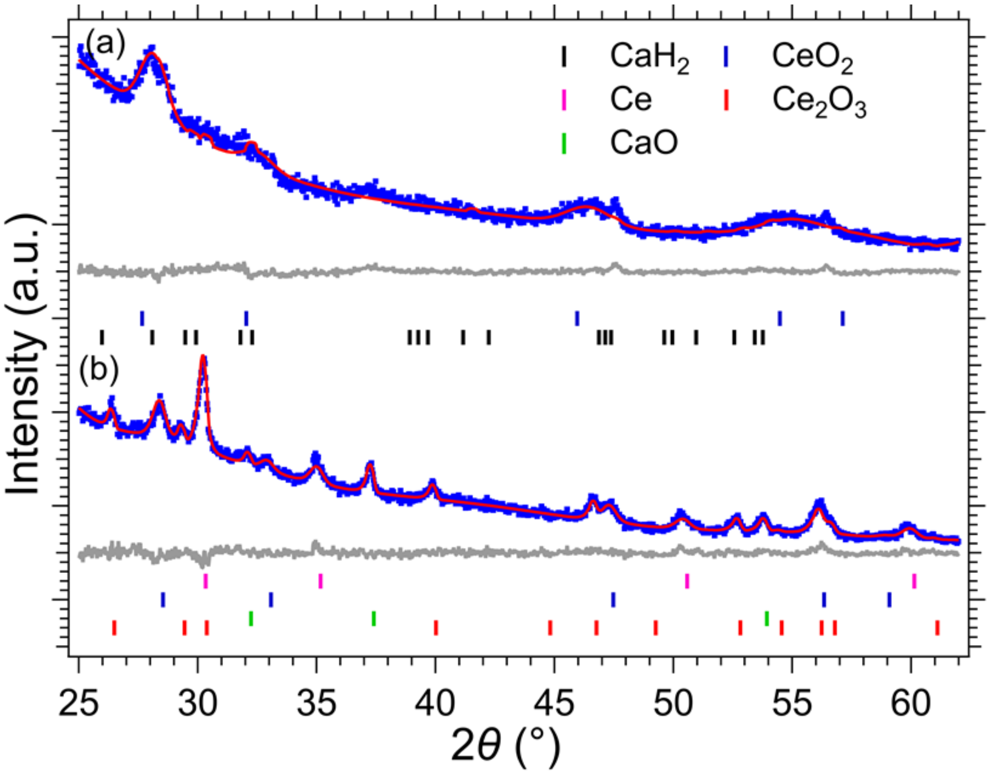

Figure 7.15 Rietveld refinement of CaH_2-CeO_2 system (a) as prepared (b) after TPD (Cu K_α, λ = 1.5418 Å).

7.3.2.2 *In-situ* Xray diffraction studies of CaH_2-SiO_2 and CaH_2-ZrO_2 systems

From the above discussed CaH_2-oxide systems, CaH_2-ZrO_2 and CaH_2-SiO_2 showed the most favourable characteristics as a TES material for CSP applications. Compared to the other systems, from the DSC curves, both these systems release H_2 in endothermic reactions (Figure 7.2(a(2) & (3)). The CaH_2-ZrO_2 system has a high operating temperature (> 740 °C), and CaH_2-SiO_2 has a high desorbed H_2 wt% of 1.76, and SiO_2 is relatively less expensive (US $ 2.5/kg). Therefore, *in-situ* XRD was performed on both CaH_2-ZrO_2 and CaH_2-SiO_2 systems to identify the two steps of reaction pathways, using a Thermo Fisher ARL Equinox 5000 diffractometer ($\lambda = 0.7093$, Mo-K_α, 50 kV, 30 mA). The samples were loaded into a quartz capillary tube, sealed, and then mounted to the sample holder inside an Ar filled glove box. The samples were heated from room temperature to 742 °C with a ramp rate of 5 °C/min using a hot air blower and remained at 742 °C for ten minutes isothermally. The data was collected every 60 s. Figure 7.16 shows the *in-situ* XRD patterns for the CaH_2-ZrO_2 system, and the red line of temperature reading shows the last 10 minutes of isothermal data. It can be seen, from Figure 7.16, that the reaction between CaH_2 and ZrO_2 occurs in a two-step reaction between 400 °C (new peaks at $2\theta \approx 14.5$ and 17 °) and ≈ 720 °C (for instance, $2\theta \approx 10$, 21, 22.5 and 25 °),, which is in good agreement with DSC and TPD profiles.

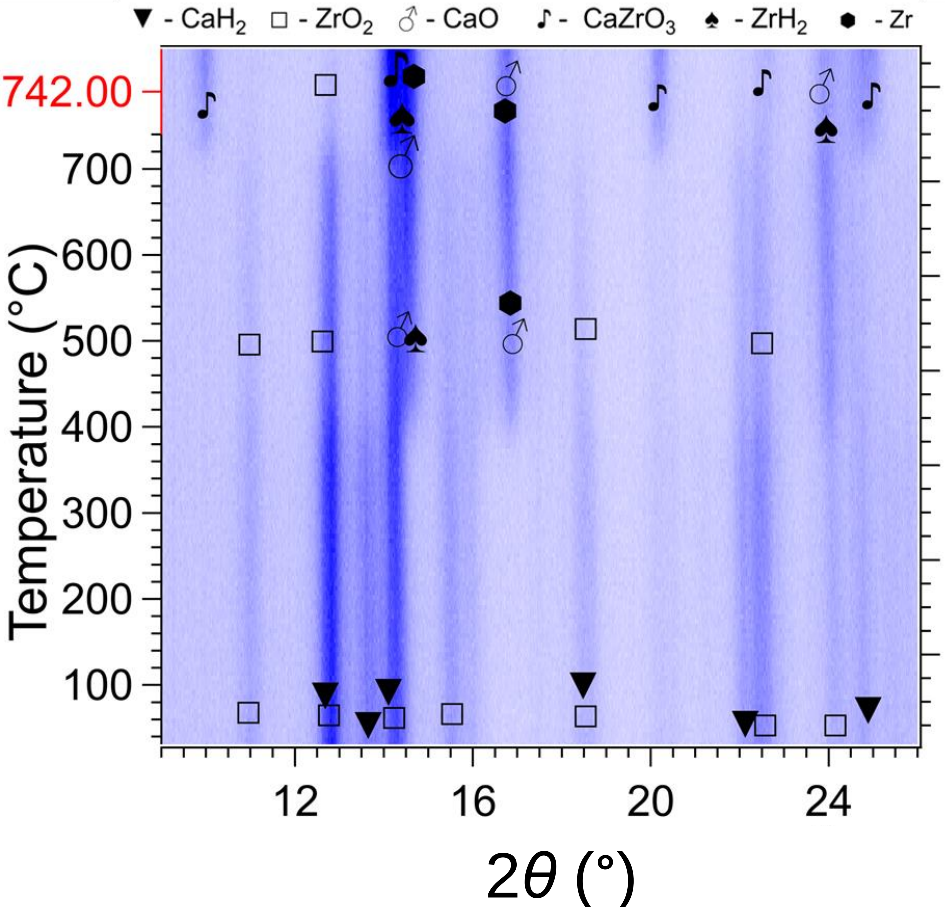

Figure 7.16 *In-situ* XRD patterns for the CaH_2-ZrO_2 system from room temperature to 742 °C ($\lambda = 0.7093$, Mo K_α).

It can be seen from Figure 7.16 that the first reaction starts at ≈ 400 °C, and the new reaction products formed are ZrH_2 and Zr and CaO at $2\theta \approx 14.5$ and 17 °, respectively. It was also noted that excess CaH_2 and ZrO_2 were present with these products. Therefore, the first reaction can be written as follows:

$$2CaH_2 + 2ZrO_2 \rightarrow \frac{7}{4}CaO + \frac{7}{16}Zr + \frac{7}{16}ZrH_2 + \frac{1}{4}CaH_2 + \frac{9}{8}ZrO_2 + \frac{21}{16}H_2(g) \qquad 7\text{-}34$$

At 720 °C, the second reaction and a new product, $CaZrO_3$ (peaks at $2\theta \approx 10$, 14, 21, 22.5 and 25 °), along with CaO, Zr and ZrH_2, was found. Unfortunately, due to the maximum temperature limitation (742 °C) for the *in-situ* instrument used, it was not possible to record the complete reaction. However, the second reaction products can be compared with XRD after TPD at ≈ 800 °C (Figure 7.4.1(2)), which shows that all the Zr reacted to form $CaZrO_3$ and can be written as follows:

$$2CaH_2 + 2ZrO_2 \rightarrow CaZrO_3 + CaO + ZrH_2 + H_2(g) \qquad 7\text{-}35$$

The CaH_2-SiO_2 system is similar to the CaH_2-ZrO_2 system having two reaction steps that match with the DSC and TPD studies, as shown in the *in-situ* analysis in Figure 7.17. The first reaction between CaH_2 and SiO_2 occur in the temperature range of 200 and 600 °C. At ≈ 200 °C, it is clear from Figure 7.17 that the CaO and Si are the new products formed with excess unreacted CaH_2 and SiO_2. Hence the first step of reaction can be expressed as shown in 7-36:

$$CaH_2 + SiO_2 \rightarrow \frac{1}{2}CaO + \frac{1}{4}Si + \frac{1}{2}CaH_2 + \frac{3}{4}SiO_2 + \frac{1}{2}H_2(g) \qquad 7\text{-}36$$

The second reaction starts at ≈ 600 °C, and all the CaH_2 and SiO_2 are reacted at 740 °C with the main decomposition product as Ca_2SiO_4 as shown in Figure 7.17, which is correlated with XRD after TPD analysis (Figure 7.4.1(3)). The second reaction step can be expressed as given in 7-37, and the optimised reaction can be written in a 4:3 molar ratio as written in 7-38.

$$CaH_2 + SiO_2 \rightarrow \frac{1}{4}Ca_2SiO_4 + \frac{1}{2}CaO + \frac{1}{2}Si + \frac{1}{4}SiO2 + H_2(g) \qquad 7\text{-}37$$

$$4CaH_2 + 3SiO_2 \rightarrow Ca_2SiO_4 + 2CaO + 2Si + 4H_2(g) \qquad 7\text{-}38$$

Therefore, adding ZrO_2 and SiO_2 to CaH_2 reduces the decomposition temperature to 755 °C (Figure 7.2(3)) and 740 °C (Figure 7.6), respectively. However, the thermodynamic properties and cycling stability of these systems need to be tested.

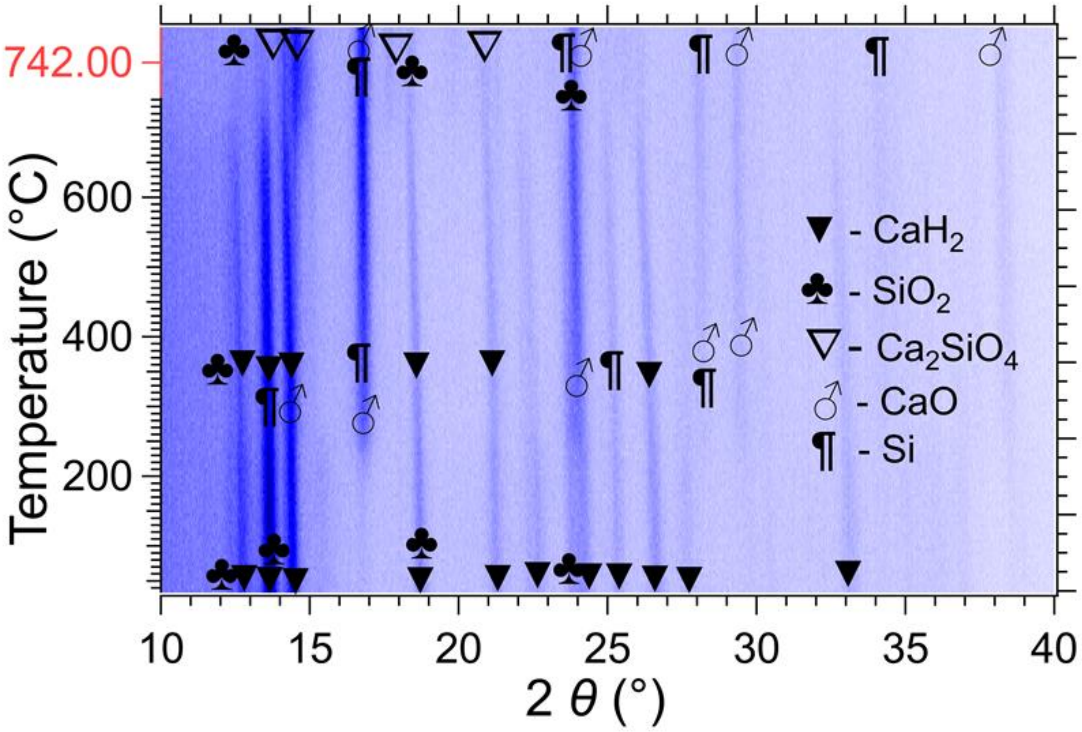

Figure 7.17 *In-situ* XRD patterns for the CaH_2-SiO_2 system from room temperature to 742 °C (λ = 0.7093, Mo K_α).

7.4 Summary

The CaH_2 and different metal oxides were synthesised separately in a 1:1 molar ratio, and the effect of these oxides on the thermodynamic destabilisation of CaH_2 for the CSP application was investigated. All the oxides can be used for the thermodynamic destabilisation of CaH_2. The reactions can be either exothermic or endothermic, which is confirmed using DSC analysis, and an endothermic reaction is favourably required for the TES application. The XRD after TPD verified the reaction products. The CaH_2 reduces ZnO, MnO, NiO, and CuO into corresponding Zn, Mn, Ni, and Cu metals. In addition, the CaH_2 reduced Fe_2O_3 into $CaFe_2O_5$ and pure Fe, which could release O_2(g) along with H_2(g) that needs to be tested. The reaction of CaH_2 with Y_2O_3 was incomplete, and it requires an operating temperature of ≈1000 °C to finish the reaction. The reaction of CaH_2 with CeO_2 also requires a higher operating temperature, and conversion of CeO_2 into Ce_2O_3 makes it challenging. The CaH_2 - ZrO_2, CaH_2 - SiO_2 systems showed the most promising results. The *in-situ* XRD studies of CaH_2-ZrO_2, CaH_2-SiO_2 systems showed a two-step reaction which is in good agreement with DSC and TPD investigation. The cycling stability of CaH_2-ZnO was tested and found to be irreversible. It can be noted that the exothermic reduction reactions are hard to reverse. However, the experimental thermodynamic values and the cycling capacity of the systems are unknown and need to be tested. Moreover, the samples need to be resynthesised in the optimised molar ratios to obtain optimum results while determining the thermodynamic properties and the H_2 desorption absorption cycles. A complete summary of the findings is concluded in Table 7.2.

Table 7.2. Summary of the results of the CaH_2-oxide systems.

	Sample in 1:1 molar ratio	**The reaction pathways**	**Theoretical H_2 wt%**	**Practical H_2 wt% at 800 °C**	**Desorbed H_2 Pressure (bar)**	**Comments**
1	CaH_2 + ZnO	$CaH_2 + ZnO \rightarrow CaO + Zn + H_2(g)$	1.6	1.55	1.61	Operating temperature 200 - 410 °C. The destabilisation was achieved. Exothermic and irreversible.
2	CaH_2 + ZrO_2	$2CaH_2 + 2ZrO_2 \rightarrow CaZrO_3 + CaO + ZrH_2 + H_2(g)$	0.6	0.75	0.68	Two-step endothermic reaction. Operating temperature 400 - 790 °C. The destabilisation was achieved. The formation of ZrH_2 may affect the reversibility of the system, which

						requires further testing.
3	CaH_2 + SiO_2	$CaH_2 + SiO_2 \rightarrow \frac{1}{4} Ca_2SiO_4 + \frac{1}{2} CaO + \frac{1}{2} Si + \frac{1}{4} SiO_2 + H_2(g)$ Optimised reaction in 4:3 molar ratio $4CaH_2 + 3SiO_2 \rightarrow Ca_2SiO_4 + 2CaO + 2Si + 2H_2(g)$	1.97	1.77	1.27	Two-step endothermic reaction. Operating temperature 200 - 760 °C. The destabilisation was achieved. The cycling capacity needs to be tested. However, the TPD analysis shows slow kinetics.
4	CaH_2 + MnO	$CaH_2 + MnO \rightarrow Ca_{0.97}O + 0.03Mn + Ca_{0.03}Mn_{0.97} + H_2(g)$	1.78	1.77	1.52	Operating temperature 600 - 750 °C. The destabilisation was achieved. Exothermic, needs further investigation.
5	CaH_2 + Fe_2O_3	$CaH_2 + Fe_2O_3 \rightarrow \frac{1}{2}Ca_2Fe_2O_5 + Fe + \frac{1}{4}O_2(g) + H_2(g)$	0.9	0.58	0.33	The destabilisation was achieved. Operating temperature 200 - 320 °C.

						Releases oxygen. Exothermic and irreversible
6	CaH_2 + TiO_2	$CaH_2 + TiO_2 \rightarrow \frac{1}{4}CaTiO_3 + \frac{3}{4}CaO + \frac{1}{2}Ti + \frac{1}{4}TiO_2 + H_2(g)$ Optimised reaction in 4:3 molar ratio $4CaH_2 + 3TiO_2 \rightarrow CaTiO_3 + 3CaO + 2Ti + 4H_2(g)$	1.65	1.57	0.75	Operating temperature 200 - 720 °C. The destabilisation was achieved. Excess TiO_2 found unreacted. Comparatively high H_2 wt%. Needs more investigation that need to be synthesised in 4:3 molar ratio.
7	CaH_2 + NiO	$CaH_2 + NiO \rightarrow CaO + Ni + H_2(g)$	1.72	1.2	0.8	Operating temperature 200 - 300 °C. The destabilisation was achieved. Exothermic, low-temperature reaction.
8	CaH_2 + CuO	$CaH_2 + CuO \rightarrow CaO + Cu + H_2(g)$	1.65	0.14	0.29	Exothermic reaction occurred at room temperature during ball milling.

9	CaH_2 + Y_2O_3	$4CaH_2 + 4Y_2O_3 \rightarrow 3CaO + 2Y + CaH_2 + 3Y_2O_3 + 3H_2(g)$ Optimised reaction in 3:1 molar ratio $CaH_2 + Y_2O_3 \rightarrow 3CaO + 2Y + H_2(g)$	0.56	0.48	0.22	Reaction was not completed. Needs higher temperature ≈ 1000 °C. Further testing at high temperatures required.
10	CaH_2 + CeO_2	$CaH_2 + CeO_2 \rightarrow CaO + \frac{3}{8}Ce + \frac{1}{4}Ce_2O_3 + \frac{1}{8}CeO_2 + H_2(g)$ Optimised reaction in 8:7 molar ratio $8CaH_2 + 7CeO_2 \rightarrow 8CaO + 3Ce + 2Ce_2O_3 + 8H_2(g)$	0.9	0.52	0.18	Conversion of CeO_2 to Ce_2O_3 and formation of pure Ce. Excess CeO_2 found. Needs further investigation.

7.5 References

1. Alexander, P. P., Reduction of Ores by Metallic Calcium. US Patents: **1936**.
2. Cech, R., Cobalt-Rare Earth Intermetallic Compounds Produced by Calcium Hydride Reduction of Oxides. *J. Met.*, **1974**, *26*, 32-35.
3. Alexander, P., Hydride Process. *Met. Alloys*, **1938**, *9*.

4. Perkin, F. M.; Pratt, L., Reducing Action of Metallic Calcium and Calcium Hydride Upon Metallic Oxides, Sulphides, and Halogen Salts. *Trans. Faraday Soc.* **1908**, *3*, 179-185.
5. Alibaba ZnO Prices. https://www.alibaba.com/product-detail/China-Manufacturer-High-purity-all-Grades_1600108326834.html?spm=a2700.themePage.1019987796157.64.47d8233dYTEXYH (accessed December **2021**).
6. Su, X.; Zhang, Z.; Zhu, M., Melting and Optical Properties of ZnO Nanorods. *Appl. Phys. Lett.*, **2006**, *88*, 061913.
7. Klimm, D.; Ganschow, S.; Schulz, D.; Fornari, R., The Growth of ZnO Crystals from the Melt. *J. Cryst. Growth*, **2008**, *310*, 3009-3013.
8. Alibaba ZrO_2 Prices. https://www.alibaba.com/product-detail/Zirconium-Price-Powder-Zirconium-Oxide-Price_1600271235988.html?spm=a2700.7735675.normal_offer.d_title.17533edcizg2er&s=p (accessed December **2021**).
9. Fushimi, S.; Ikeda, T., Phase Equilibrium in the System PbO-TiO_2-ZrO_2. *J. Am. Ceram. Soc.* **1967**, *50*, 129-132.
10. Wyers, G.; Cordfunke, E., Phase Relations in the System Li_2O-ZrO_2. *J. Nucl. Mater.*, **1989**, *168*, 24-30.
11. Alibaba SiO_2 Prices. https://www.alibaba.com/product-detail/Powder-Silica-Silicon-Dioxide-Price-Dioxide_62203293674.html?spm=a2700.7735675.normal_offer.d_title.71189f1bjGA6kV&s=p (accessed December **2021**).
12. Haynes, W. M., Crc Handbook of Chemistry and Physics; *CRC press*, **2014**.
13. Bowen, N.; Greig, J., The System: Al2o3. Sio2. *J. Am. Ceram. Soc.*, **1924**, *7*, 238-254.
14. Alibaba MnO Prices. https://www.alibaba.com/product-detail/High-purity-Industrial-grade-battery-grade_1600331300729.html?spm=a2700.7724857.normal_offer.d_title.76ea3414sfRBLg (accessed December 2021).
15. Wu, P.; Eriksson, G.; Pelton, A. D., Critical Evaluation and Optimization of the Thermodynamic Properties and Phase Diagrams of the CaO-FeO, CaO-MgO, CaO-MnO, FeO-MgO, FeO-MnO, and MgO-MnO Systems. *J. Am. Ceram. Soc.*, **1993**, *76*, 2065-2075.
16. Alibaba Fe_2O_3 Prices. https://www.alibaba.com/product-detail/Ferric-Oxide-Red-Iron-OxideGranular_60677022615.html?spm=a2700.7724857.normal_offer.d_title.42e576d83tyySe&s=p (accessed December 2021).
17. Goto, Y.; Takada, T., Phase Diagram of the System BaO-Fe_2O_3. *J. Am. Ceram. Soc.*, **1960**, *43*, 150-153.

18. Alibaba TiO_2 Prices.https://www.alibaba.com/product-detail/Nano-TiO_2-Powder-TiO_2-TiO_2-Manufacturer_62224961294.html?spm=a2700.galleryofferlist.normal_offer.d_title.9fbb46e8nNTNLR&s=p (accessed December **2021**).
19. Collins, D. R.; Smith, W.; Harrison, N. M.; Forester, T. R., Molecular Dynamics Study of TiO_2 Microclusters. *J. Mater. Chem.*, **1996**, *6*, 1385-1390.
20. Alibaba NiO Priceshttps://ditaichem.en.made-in-china.com/product/ejWEUzadYrVf/China-High-Quality-Nickel-Oxide-with-Good-Price.html (accessed December 2021).
21. Phillips, B.; Hutta, J.; Warshaw, I., Phase Equilibria in the System NiO-Al_2O_3-SiO_2. *J. Am. Ceram. Soc.*, **1963**, *46*, 579-583.
22. Alibaba CuO Prices. https://qdsalus.en.made-in-china.com/product/rSzmDUElTfkg/China-Copper-Oxide-with-Good-Price.html (accessed December **2021**).
23. Liang, J.; Chen, Z.; Wu, F.; Xie, S., Phase Diagram of SrO□ CaO□ CuO Ternary System. *Solid State commun.*, **1990**, *75*, 247-252.
24. Alibaba Y_2O_3 Prices. https://www.alibaba.com/product-detail/Rare-earth-yttrium-oxide-powdercas_1600277535173.html?spm=a2700.galleryofferlist.normal_offer.d_title.3a2e4cb6YBjaPJ&s=p (accessed December **2021**).
25. Cockayne, B., The Uses and Enigmas of the Al_2O_3-Y_2O_3 Phase System. *J. Less-Common Met.*, **1985**, *114*, 199-206.
26. Alibaba CeO_2 Prices. https://www.alibaba.com/product-detail/Cerium-High-Purity-99-99-Cerium_1600294108142.html?spm=a2700.7735675.normal_offer.d_title.4b131e90L2d0SN&s=p (accessed December **2021**).
27. Yoshimoto, M.; Shimozono, K.; Maeda, T.; Ohnishi, T.; Kumagai, M.; Chikyow, T.; Ishiyama, O.; Shinohara, M.; Koinuma, H., Room-Temperature Epitaxial Growth of CeO_2 Thin Films on Si (111) Substrates for Fabrication of Sharp Oxide/Silicon Interface. *Jpn. J. Appl. Phys.,*, **1995**, *34*, L688.
28. Klingshirn, C., ZnO: Material, Physics and Applications. *Chem. Phys. Chem.*, **2007**, *8*, 782-803.
29. Miloua, R.; Kebbab, Z.; Miloua, F.; Benramdane, N., Ab Initio Investigation of Phase Separation in Ca1- xZnxO Alloys. *Phys. Lett. A*, **2008**, *372*, 1910-1914.
30. Sha, X.; Tian, F.; Li, D.; Duan, D.; Chu, B.; Liu, Y.; Liu, B.; Cui, T., Ab Initio Investigation of Cao-Zno Alloys under High Pressure. *Sci. Rep.*, **2015**, *5*, 1-8.
31. Xia, L.; Liu, Z.; Taskinen, P., Phase Equilibrium Study of the CaO-ZnO System. *J. Am. Ceram. Soc.*, **2016**, *99*, 3809-3815.

32. Kumar, D.; Ali, A., Transesterification of Low-Quality Triglycerides over a Zn/Cao Heterogeneous Catalyst: Kinetics and Reusability Studies. *Energy Fuels*, **2013**, *27*, 3758-3768.

33. Semiconductors, W. B., Fundamental Properties and Modern Photonic and Electronic Devices/Eds. *K. Takahashi, A. Yoshikawa, A. Sandhu. New York*, **2007**.

34. Greenwood, N. N.; Earnshaw, A., Chemistry of the Elements; *Elsevier*, **2012**.

35. Doufar, N.; Benamira, M.; Lahmar, H.; Trari, M.; Avramova, I.; Caldes, M., Structural and Photochemical Properties of Fe-doped ZrO_2 and Their Application as Photocatalysts with Tio2 for Chromate Reduction. *J. Photochem. Photobiol., A*,, **2020**, *386*, 112105.

36. Wang, D.; Guo, Y.; Liang, K.; Tao, K., Crystal Structure of Zirconia by Rietveld Refinement. *Sci. China, Ser. A: Math., Phys., Astron.*, **1999**, *42*, 80.

37. Wang, S.; Zhang, J.; Luo, D.; Gu, F.; Tang, D.; Dong, Z.; Tan, G.; Que, W.; Zhang, T.; Li, S., Transparent Ceramics: Processing, Materials and Applications. *Prog. Solid State Chem.*, **2013**, *41*, 20-54.

38. Meerson, G.; Kolchin, O., Mechanism of the Reduction of Zirconium and Titanium Oxides by Calcium Hydride. *Sov. J. At. Energy*, **1957**, *2*, 305-312.

39. Iler, K. R., The Chemistry of Silica. Solubility, polymerization, colloid and surface properties and biochemistry of silica, **1979**.

40. Shin, D.; Banerjee, D., Enhanced Thermal Properties of Sio2 Nanocomposite for Solar Thermal Energy Storage Applications. *Int. J. Heat Mass Transfer*, **2015**, *84*, 898-902.

41. Fang, G.; Li, H.; Chen, Z.; Liu, X., Preparation and Properties of Palmitic Acid/Sio2 Composites with Flame Retardant as Thermal Energy Storage Materials. *Sol. Energy Mater. Sol. Cells*, **2011**, *95*, 1875-1881.

42. Liu, Y.-L.; Wei, W.-L.; Hsu, K.-Y.; Ho, W.-H., Thermal Stability of Epoxy-Silica Hybrid Materials by Thermogravimetric Analysis. *Thermochim. Acta*, **2004**, *412*, 139-147.

43. Liu, P.; Su, Z., Thermal Stabilities of Polystyrene/Silica Hybrid Nanocomposites Via Microwave-Assisted *in-Situ* Polymerization. *Mater. Chem. Phys.*, **2005**, *94*, 412-416.

44. Hu, Y.; Wu, Y.; Wang, J., Manganese-Oxide-Based Electrode Materials for Energy Storage Applications: How Close Are We to the Theoretical Capacitance? *Adv. Mater.*, **2018**, *30*, 1802569.

45. Sun, X.; Xu, Y.; Ding, P.; Chen, G.; Zheng, X.; Zhang, R.; Li, L., The Composite Sphere of Manganese Oxide and Carbon Nanotubes as a Prospective Anode Material for Lithium-Ion Batteries. *J. Power Sources*, **2014**, *255*, 163-169.

46. Zhong, K.; Xia, X.; Zhang, B.; Li, H.; Wang, Z.; Chen, L., MnO Powder as Anode Active Materials for Lithium Ion Batteries. *J. Power Sources,* **2010**, *195*, 3300-3308.
47. Zhong, K.; Zhang, B.; Luo, S.; Wen, W.; Li, H.; Huang, X.; Chen, L., Investigation on Porous Mno Microsphere Anode for Lithium Ion Batteries. *J. Power Sources,* **2011**, *196*, 6802-6808.
48. Sun, B.; Chen, Z.; Kim, H.-S.; Ahn, H.; Wang, G., Mno/C Core-Shell Nanorods as High Capacity Anode Materials for Lithium-Ion Batteries. *J. Power Sources,* **2011**, *196*, 3346-3349.
49. Esmaeilnejad, A.; Mahmoudi, P.; Zamanian, A.; Mozafari, M., Synthesis of Titanium Oxide Nanotubes and Their Decoration by Mno Nanoparticles for Biomedical Applications. *Ceram. Int.,* **2019**, *45*, 19275-19282.
50. Cuadrat, A.; Abad, A.; Adánez, J.; De Diego, L.; García-Labiano, F.; Gayán, P., Behavior of Ilmenite as Oxygen Carrier in Chemical-Looping Combustion. *Fuel Process. Technol.,* **2012**, *94*, 101-112.
51. Ismail, M.; Liu, W.; Chan, M. S.; Dunstan, M. T.; Scott, S. A., Synthesis, Application, and Carbonation Behavior of Ca2fe2o5 for Chemical Looping H2 Production. *Energy Fuels,* **2016**, *30*, 6220-6232.
52. Vujtek, M.; Zboril, R.; Kubinek, R.; Mashlan, M., Ultrafine Particles of Iron (Iii) Oxides by View of Afm-Novel Route for Study of Polymorphism in Nano-World. *Sci Tech Ed Micro.,* **2003**, *1*, 1-8.
53. Zheng, M.; Gu, M.; Jin, Y.; Jin, G., Preparation, Structure and Properties of Tio2-Pvp Hybrid Films. *Mater. Sci. Eng., B,* **2000**, *77*, 55-59.
54. Henrich, V. E.; Cox, P. A., The Surface Science of Metal Oxides; Cambridge university press, **1996**.
55. Alderman, O.; Skinner, L.; Benmore, C.; Tamalonis, A.; Weber, J., Structure of Molten Titanium Dioxide. *Phys. Rev., B,* **2014**, *90*, 094204.
56. Greenwood, N. N.; Earnshaw, A. Chemistry of the Elements Oxford Pergamon Press; ISBN 0-08-022057-6: **1984**.
57. Al-Ghamdi, A.; Mahmoud, W. E.; Yaghmour, S. J.; Al-Marzouki, F., Structure and Optical Properties of Nanocrystalline Nio Thin Film Synthesised by Sol-Gel Spin-Coating Method. *J. Alloys Compd.,* **2009**, *486*, 9-13.
58. Danjumma, S. G.; Abubakar, Y.; Suleiman, S., Nickel Oxide (Nio) Devices and Applications: A Review. *J. Eng. Res. Technol,* **2019**, *8*, 12-21.

59. Jamwal, G.; Prakash, J.; Chandran, A.; Gangwar, J.; Srivastava, A.; Biradar, A. In Effect of Nickel Oxide Nanoparticles on Dielectric and Optical Properties of Nematic Liquid Crystal, *AIP Conference Proceedings*, AIP Publishing LLC: **2015**; p 030065.

60. Zhang, Q.; Zhang, K.; Xu, D.; Yang, G.; Huang, H.; Nie, F.; Liu, C.; Yang, S., Cuo Nanostructures: Synthesis, Characterization, Growth Mechanisms, Fundamental Properties, and Applications. *Prog. Mater. Sci.,*, **2014**, *60*, 208-337.

61. Song, M.-K.; Park, S.; Alamgir, F. M.; Cho, J.; Liu, M., Nanostructured Electrodes for Lithium-Ion and Lithium-Air Batteries: The Latest Developments, Challenges, and Perspectives. *Mater. Sci. Eng. R: Reports,* **2011**, *72*, 203-252.

62. Singh, J.; Kaur, G.; Rawat, M., A Brief Review on Synthesis and Characterization of Copper Oxide Nanoparticles and Its Applications. *J. Bioelectron. Nanotechnol,* **2016**, *1*.

63. Aparna, Y.; Rao, K. E.; Subbarao, P. S. In Synthesis and Characterization of Cuo Nano Particles by Novel Sol-Gel Method, *Proceedings of the 2nd International Conference on Environment Science and Biotechnology*, **2012**.

64. Mudavakkat, V.; Atuchin, V.; Kruchinin, V.; Kayani, A.; Ramana, C., Structure, Morphology and Optical Properties of Nanocrystalline Yttrium Oxide (Y_2O_3) Thin Films. *Opt. Mater.,* **2012**, *34*, 893-900.

65. Lacroix, B.; Paumier, F.; Gaboriaud, R. J., Crystal Defects and Related Stress in Y 2 O 3 Thin Films: Origin, Modeling, and Consequence on the Stability of the C-Type Structure. *Phys. Rev. B,* **2011**, *84*, 014104.

66. Swamy, V.; Dubrovinskaya, N.; Dubrovinsky, L., High-Temperature Powder X-Ray Diffraction of Yttria to Melting Point. *J. Mater. Res.,* **1999**, *14*, 456-459.

67. O'Connor, B.; Valentine, T., A Neutron Diffraction Study of the Crystal Structure of the C-Form of Yttrium Sesquioxide. *Acta Crystallographica Section B: Structural Crystallography and Crystal Chemistry,* **1969**, *25*, 2140-2144.

68. Xiang, X.; Zu, X.; Zhu, S.; Zhang, C.; Wang, Z.; Wang, L.; Ewing, R., Xps and Optical Studies of Xe+-Implanted and Annealed Ysz Single Crystals. *Nucl. Instrum. Methods Phys. Res., Sect. B,* **2006**, *250*, 382-385.

69. Zhu, S.; Zu, X.; Wang, L.; Ewing, R., Cesium Ion Implantation in Single Crystal Yttria-Stabilised Zirconia (YSZ) and Polycrystalline $MgAl_2O_4$-YSZ. *MRS Online Proc. Libr.,* **2002**, *713*.

70. Zhu, S.; Zu, X.; Wang, L.; Ewing, R., Nanodomains of Pyrochlore Formed by Ti Ion Implantation in Yttria-Stabilised Zirconia. *Appl. Phys. Lett.,* **2002**, *80*, 4327-4329.

71. Wang, L.; Zhu, S.; Ewing, R., Us Department of Energy's Nuclear Engineering Education Research: Highlights of Recent and Current Research-Iii. 1. Behavior of Fission Products in YSZ-Based Inert Matrix Fuel. *Trans. Am. Nucl. Soc.*, **2001**, *84*, 103-104.

72. Huang, H.; Nakamura, M.; Su, P.; Fasching, R.; Saito, Y.; Prinz, F. B., High-Performance Ultrathin Solid Oxide Fuel Cells for Low-Temperature Operation. *J. Electrochem. Soc.*, **2006**, *154*, B20.

73. Patnaik, P., Handbook of Inorganic Chemicals; *McGraw-Hill New York*, 2003; Vol. 529.

74. Lide, D. R., Standard Thermodynamic Properties of Chemical Substances. *CRC Handbook of Chemistry and Physics*, **1992**.

75. Fronzi, M.; Assadi, M. H. N.; Hanaor, D. A., Theoretical Insights into the Hydrophobicity of Low Index CeO_2 Surfaces. *Appl. Surf. Sci.*, **2019**, *478*, 68-74.

76. Kodama, T.; Kondoh, Y.; Kiyama, A.; Shimizu, K.-I. In Hydrogen Production by Solar Thermochemical Water-Splitting/Methane-Reforming Process, *ASME 2003 International Solar Energy Conference*, 2003; pp 121-128.

77. Belkhir, N.; Bouzid, D.; Herold, V., Wear Behavior of the Abrasive Grains Used in Optical Glass Polishing. *J. Mater. Process. Technol.*, **2009**, *209*, 6140-6145.

78. Savio, G.; Meneghello, R.; Concheri, G., A Surface Roughness Predictive Model in Deterministic Polishing of Ground Glass Moulds. *Int. J. Mach. Tools Manuf* **2009**, *49*, 1-7.

79. Chen, Y.; Long, R.; Chen, Z., Preparation and Polishing Performance of CeO_2@ SiO_2 Composite Abrasives. *Mater. Rev.* **2010**, *24*, 35-38.

80. Zhang, J.; Li, Y.-c.; Huang, J.-y.; Wu, J.-x.; Liu, Q.; Wu, S.-z.; Gao, Z.-r.; Zhang, S.; Yang, L., The Effect of Al Particle Size on Thermal Decomposition, Mechanical Strength and Sensitivity of Al/ZrH_2/PtFe Composite. *Def. Technol.*, **2021**, *17*, 829-835.

81. Krüger, H.; Kahlenberg, V.; Petříček, V.; Phillipp, F.; Wertl, W., High-Temperature Structural Phase Transition in $Ca_2Fe_2O_5$ Studied by *in-situ* X-Ray Diffraction and Transmission Electron Microscopy. *J. Solid State Chem.*, **2009**, *182*,1515-1523.

82. Xiao, W.; Guo, Q.; Wang, E., Transformation of Ceo2 (1 1 1) to Ce_2O_3 (0 0 0 1) Films. *Chem. Phys. Lett.* **2003**, *368*, 527-531.

83. Höcker, J.; Krisponeit, J.-O.; Schmidt, T.; Falta, J.; Flege, J. I., The Cubic-to-Hexagonal Phase Transition of Cerium Oxide Particles: Dynamics and Structure. *Nanoscale* **2017**, *9*, 9352-9358.

Chapter 8

Conclusions and future perspectives

The need for clean energy and a focus on zero emissions has promoted tremendous progress in the solar energy development sector, including PV and CSP. Energy storage technology illuminates the mismatch in time between solar power supply and peak power demand. Long term electric energy storage using batteries has been proven to be economically unviable compared to thermal energy storage (TES) systems. Concentrated Solar Power (CSP) plants integrated with a thermal battery is a prominent way to overcome the intermittent nature of solar energy and provide a continuous energy supply. Moreover, the next-generation CSP plants require a TES material that can operate above 600 °C to increase efficiency and reduce cost. Metal hydrides are ideal TES candidates as they can operate above 600 °C. Therefore, this thesis has focused on solar energy storage using high-temperature metal hydride for CSP applications. The primary material chosen as a high-temperature metal hydride was calcium hydride due to its attractive properties, including high energy densities and operating temperature. A brief literature review about TES systems for CSP application, high-temperature metal hydrides, thermodynamic destabilisation of CaH_2 and experimental methods used in this thesis was discussed in the first two chapters.

The next section of the thesis determined the thermodynamic properties (both solid and molten) and the desorption reaction kinetics of CaH_2. Little research has been conducted in recent years to find the thermodynamic properties of pure CaH_2, with the prior studies conducted in the 1960s. Moreover, each former investigator reported conflicting thermodynamic results and conclusions. It was challenging to determine the thermodynamic properties of pure CaH_2 due to the very low-pressure (< 0.01 bar) or high temperature (> 1000 °C) requirements, volatile nature of Ca, the solid solubility of CaH_2 in Ca and vice versa and the poor reaction kinetics ($E_a = 203 \pm 12$ kJ.mol^{-1}). The experimental thermodynamic values of molten CaH_2 and solid CaH_2 were determined as ΔH_{des} (molten CaH_2) = 216 ± 10 kJ.mol^{-1}.H_2, ΔS_{des} (molten CaH_2) = 177 ± 9 J.K^{-1}.mol^{-1}.H_2, T_{des} 1 bar (molten CaH_2) = 947 ± 48 °C and ΔH_{des} (solid CaH_2) = 172 ± 12 kJ.mol^{-1}. H_2, ΔS_{des} (solid CaH_2) = 144 ± 10 J.K^{-1}.mol^{-1}. H_2 T_{des} 1 bar (solid CaH_2) = 921 ± 63 °C, respectively.

The following four chapters detailed the thermodynamic destabilisation of CaH_2 using additives. Chapters 4 and 5 are peer-reviewed published articles that describe the addition of Al_2O_3 and Zn to CaH_2 altered its desorption pathway and reduced the temperature of desorption to 636 °C and 597 °C at 1 bar of H_2 pressure, respectively. The initial synthesis of CaH_2 - Al_2O_3 was in a 1:1 molar ratio, and the system degraded faster during cycling (after 3rd cycle mixture lost its 90% H_2 storage capacity) due to the presence of excess Al_2O_3. Hence synthesis was carried out in a 2:1 molar ratio, i.e., reduced the amount of Al_2O_3 in half, which improved the cycling capacity of the system. The reaction occurred in a single step, and $Ca_{12}Al_{14}O_{33}$ was the main product with $\Delta H_{des} = 100 \pm 2$ kJ.mol^{-1}.H_2. The sintering of the materials and slow reaction rates are the main issues addressed with this system. Moreover, in future, the addition of some catalysts (Ni, salts etc.) can be tested to improve the kinetics and cycling ability of the system. The CaH_2 - 3Zn system showed excellent reaction kinetics, and the desorption was completed in less than three hours. The reaction between CaH_2 and Zn yielded three different calcium zinc alloys, $CaZn_{13}$, $CaZn_{11}$ and $CaZn_5$, at 190, 390 and 590 °C. The enthalpy of reaction was determined as $\Delta H_{des} = 131 \pm 4$ kJ.mol^{-1}.H_2 and exhibited a consistent ten H_2 desorption/absorption cycles (80% of initial capacity retained). The system degrades due to the evaporation of Zn from the calcium zinc alloys, especially at high temperatures (> 600 °C). Therefore, the system may be suitable for low-temperature operations. However, the material showed no significant sintering after heating which is confirmed by scanning electron microscopy. Hence, in future, the design of an appropriate sample holder, such as closed iron tubes, to avoid Zn escaping from the alloys could improve the cycling stability of the system and its potential as a thermal battery.

According to theoretical predictions, the CaH_2 - 2C system (Chapter 6) was most promising due to its high theoretical gravimetric energy density (2072 kJ.kg^{-1}) compared with other selected systems. Unfortunately, the release of methane gas made the system degrade faster. The system lost its reversibility with a 90% loss in storage capacity after the first cycle. The availability of unreacted C to react with CaH_2 to form CaC_2 and H_2(g) decreased after each desorption. The formation of methane and possible different reaction pathways between CaH_2 and C made the system impractical as a thermal battery for CSP application. The system could be used for methane production. However, this may also be less favourable commercially due to the high cost associated with these materials than the current market price of methane.

The metal oxides are cheaper and more stable (with high melting and boiling points) than pure metals. Hence, in the Chapter 7, investigated the performance of several commonly available oxides (ZnO, Fe_2O_3, ZrO_2, MnO, SiO_2, TiO_2, CuO, NiO, Y_2O_3 and CeO_2) on the thermodynamic destabilisation of CaH_2. The endothermic desorption is a favourable condition for TES application. Also, the exothermic reduction reactions are hard to reverse. However, CaH_2 - ZnO, CaH_2 - Fe_2O_3 and CaH_2 - NiO releases H_2 below 500 °C, whereas the CaH_2 - CuO system reacted entirely while ball-milling at room temperature. CaH_2 reduced MnO and TiO_2 into Mn, CaO, $CaTiO_3$ and Ti, respectively at 750 °C and 640 °C. CaH_2 - Y_2O_3 requires a higher temperature (≈ 1000 °C) to complete the reaction. Moreover, in CaH_2 - CeO_2 system, CaH_2 reduced CeO_2 into Ce, CaO and Ce_2O_3. However, the XRD refinement found an excess of CeO_2 unreacted after TPD at 800 °C. Moreover, CaH_2 - ZrO_2 and CaH_2 - SiO_2 were determined as the most promising systems due to their high operating temperature (> 600 °C). In addition, the formation of ZrH_2 from the reaction between CaH_2 and ZrO_2, along with $CaZrO_3$, requires a temperature of > 700 °C to reverse (the decomposition temperature of ZrH_2 is 700 °C). Furthermore, a kinetic study of different materials and cycling stability need to be verified to determine their feasibility as a TES material.

This thesis studied the destabilised CaH_2 systems operating in the temperature range 600 - 800 °C. Moreover, the investigation proved that the thermodynamic destabilisation of CaH_2 can be achieved by adding the selected elements (Zn & C) and oxides (Al_2O_3, ZnO, Fe_2O_3, ZrO_2, MnO, SiO_2, TiO_2, CuO, NiO, Y_2O_3 and CeO_2). These destabilised calcium hydride systems can be competitive high-temperature thermochemical energy storage material and promising solutions for the CSP plants. For example, the CaH_2-Al_2O_3 system has an operating temperature of T_{des} 1 bar = 636 °C, and the cost of the material is US \$9.7 kWh_{th}, hence deeming it as a highly promising thermal battery for the next generation CSP application.

Furthermore, as the research to find a practically suitable high-temperature material for next-generation CSP plants continues, CaH_2 with other additives or complex metal hydrides can be investigated for CSP application. Metal hydride research is multifaceted and effectively stores large amounts of hydrogen safely. Also, thermochemical energy storage materials, especially high-temperature materials, have various applications rather than CSP. They can be used in industries for waste heat recovery, transportation, space heating, buildings, and fuel cell applications.

Appendix I

Permission of reproduction from the copyright owner

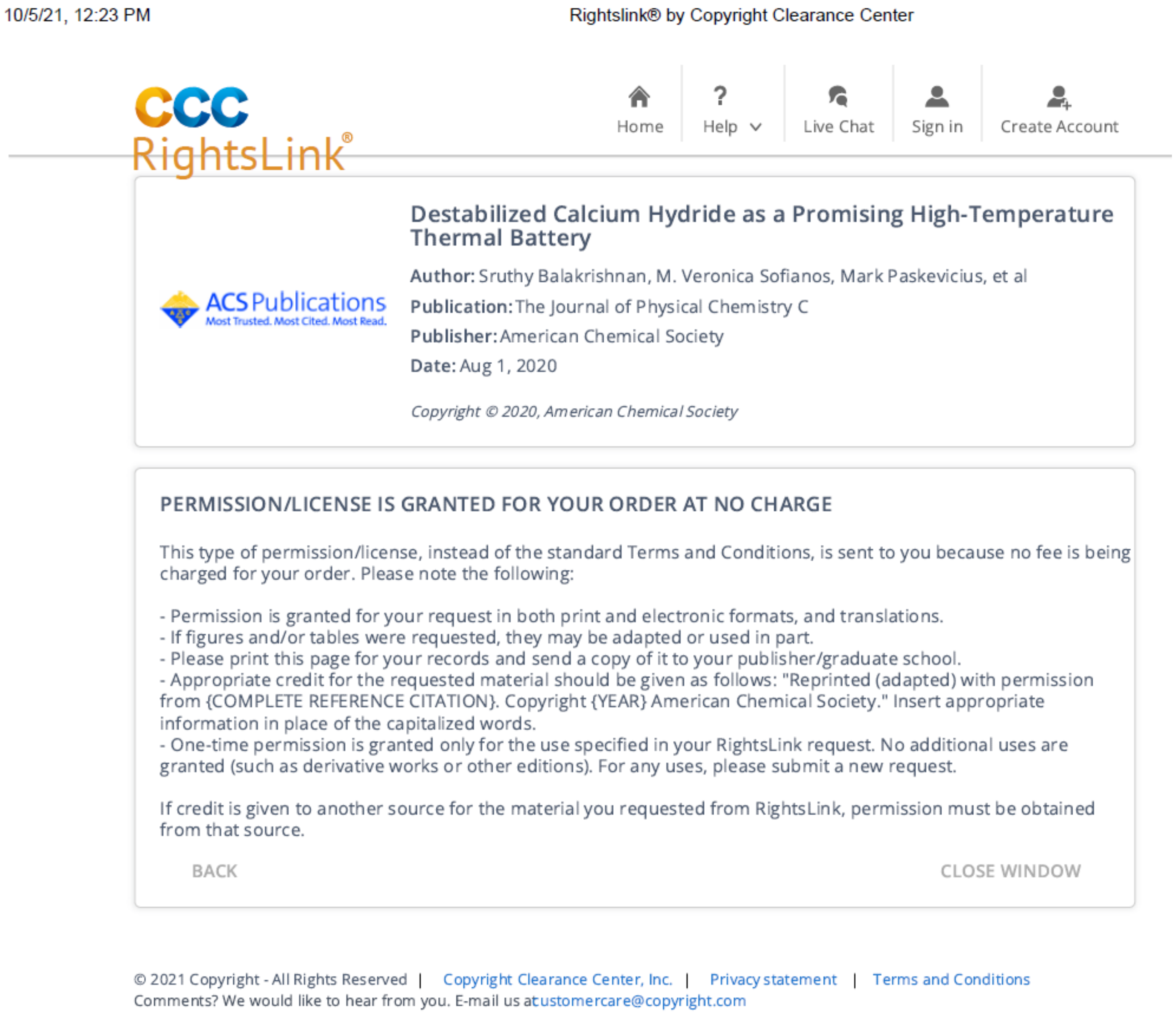

10/5/21, 12:23 PM Rightslink® by Copyright Clearance Center

Destabilized Calcium Hydride as a Promising High-Temperature Thermal Battery

Author: Sruthy Balakrishnan, M. Veronica Sofianos, Mark Paskevicius, et al

Publication: The Journal of Physical Chemistry C

Publisher: American Chemical Society

Date: Aug 1, 2020

Copyright © 2020, American Chemical Society

PERMISSION/LICENSE IS GRANTED FOR YOUR ORDER AT NO CHARGE

This type of permission/license, instead of the standard Terms and Conditions, is sent to you because no fee is being charged for your order. Please note the following:

- Permission is granted for your request in both print and electronic formats, and translations.
- If figures and/or tables were requested, they may be adapted or used in part.
- Please print this page for your records and send a copy of it to your publisher/graduate school.
- Appropriate credit for the requested material should be given as follows: "Reprinted (adapted) with permission from {COMPLETE REFERENCE CITATION}. Copyright {YEAR} American Chemical Society." Insert appropriate information in place of the capitalized words.
- One-time permission is granted only for the use specified in your RightsLink request. No additional uses are granted (such as derivative works or other editions). For any uses, please submit a new request.

If credit is given to another source for the material you requested from RightsLink, permission must be obtained from that source.

S. Balakrishnan, M.V. Sofianos, T.D Humphries, M. Paskevicius, and C.E. Buckley, Thermochemical energy storage performance of zinc destabilised calcium hydride at high temperatures, *J.* Phys. Chem. Chem. Phys., **22,** 2020, 25780-25788. https://doi.org/10.1039/D0CP04431H

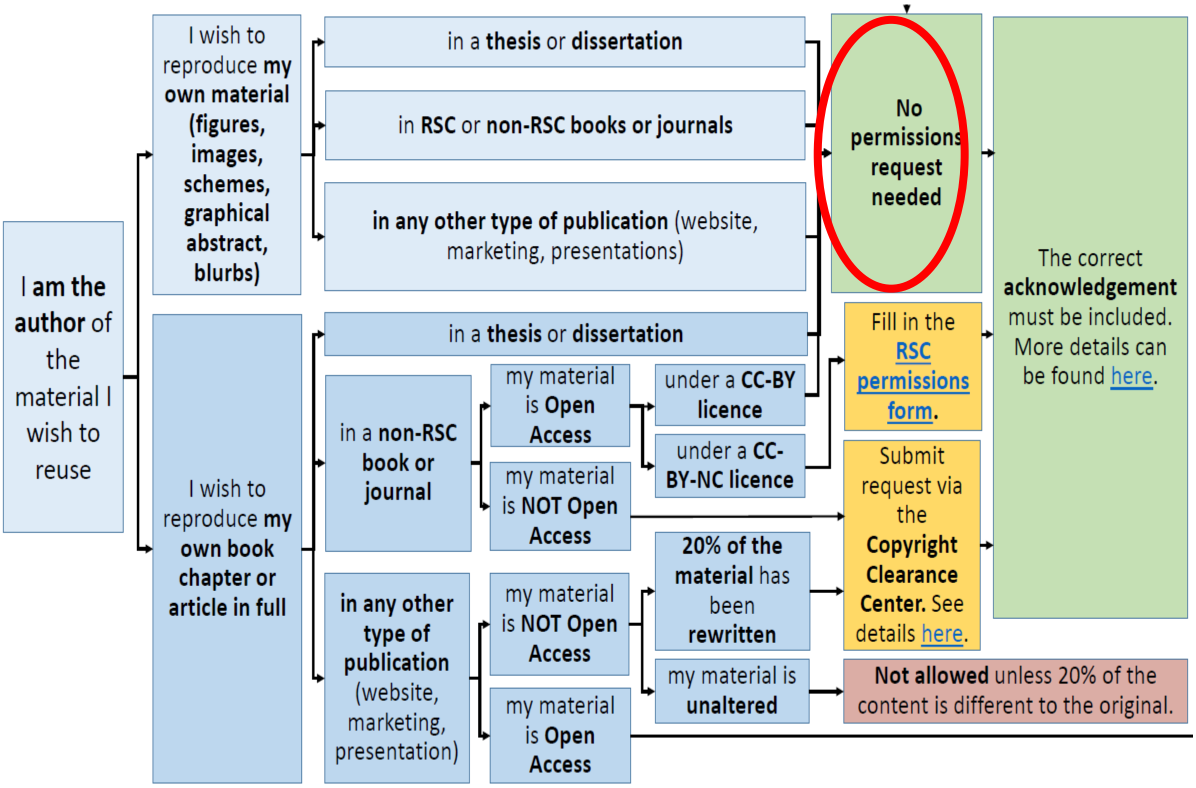

Appendix II

Co-author attribution statement

Chapter 4: S. Balakrishnan, M.V. Sofianos, M. Paskevicius, M.R. Rowles and C.E. Buckley, Destabilised Calcium Hydride as a Promising High-Temperature Thermal Battery, *J. Phys. Chem. C*, 2020, **124**, 17512-17519. https://doi.org/10.1021/acs.jpcc.0c04754

	Conception & design	Experiments conduction & data acquisition	Data processing & analysis	Interpretation & discussion	Manuscript writing, revision	Final approval
Sruthy Balakrishnan	☒	☒	☒	☒	☒	☒
I acknowledge these represent my contribution to the above research output Signature :						
M.Veronica Sofianos	☒	☐	☒	☒	☒	☒
I acknowledge these represent my contribution to the above research output Signature :						
Mark Paskevicius	☒	☐	☐	☒	☒	☒
I acknowledge these represent my contribution to the above research output Signature :						
Matthew R Rowles	☐	☒	☒	☐	☒	☒
I acknowledge these represent my contribution to the above research output Signature :						
Craig E Buckley	☒	☐	☐	☒	☒	☒
I acknowledge these represent my contribution to the above research output Signature :						

Chapter 5: S. Balakrishnan, M.V. Sofianos, T.D Humphries, M. Paskevicius, and C.E. Buckley, Thermochemical energy storage performance of zinc destabilised calcium hydride at high temperatures, *J.* Phys. Chem. Chem. Phys.**,** **22,** 2020, 25780-25788. https://doi.org/10.1039/D0CP04431H

	Conception & design	Experiments conduction & data acquisition	Data processing & analysis	Interpretation & discussion	Manuscript writing, revision	Final approval
Sruthy Balakrishnan	☒	☒	☒	☒	☒	☒
I acknowledge these represent my contribution to the above research output Signature :						
M.Veronica Sofianos	☒	☐	☐	☒	☒	☒
I acknowledge these represent my contribution to the above research output Signature :						
Terry D Humphries	☐	☐	☐	☒	☒	☐
I acknowledge these represent my contribution to the above research output Signature :						
Mark Paskevicius	☒	☐	☐	☒	☒	☒
I acknowledge these represent my contribution to the above research output Signature :						
Craig E Buckley	☒	☐	☐	☒	☒	☒
I acknowledge these represent my contribution to the above research output Signature :						

All reasonable efforts have been made to acknowledge the owners of copyright material. I would love to hear from any copyright owners that have been omitted or incorrectly acknowledged.

****